UNIVERSITÀ DI SIENA 1240

Dipartimento di Scienze fisiche, della Terra e dell'ambiente

Dottorato in Scienze e tecnologie ambientali, geologiche e polari

35° Ciclo

Coordinatore: Prof. Simone Bastianoni

Analysis of ablation areas in Antarctica through remote sensing

Settore scientifico disciplinare: *GEO/04 Geografia Fisica e Geomorfologia*

Candidato
Dr. Giacomo Traversa
Università degli Studi di Siena

Firma digitale del candidato

GIACOMO
TRAVERSA
26.04.2023
16:09:16
GMT+01:00

Tutori
Prof. Massimo Frezzotti
Università degli Studi Roma 3

Prof. Franco Talarico
Università degli Studi di Siena

Co-tutore
Prof.ssa Guglielmina Adele Diolaiuti
Università degli Studi di Milano

Anno accademico di conseguimento del titolo di Dottore di ricerca
2021/22

Università degli Studi di Siena
Dottorato in Scienze e tecnologie ambientali, geologiche e polari
35° Ciclo

Data dell'esame finale
12 Maggio 2023

Commissione giudicatrice
Pier Lorenzo Fantozzi, PA, UniSI (membro interno)
Luca Vittuari, PO, UniBO (membro esterno)
Maria Cristina Salvatore, PA, UniPI (membro esterno)

Supplente
Barbara Delmonte, PA, UniMIB

Analysis of ablation areas in Antarctica through remote sensing

Analisi delle aree di ablazione in Antartide tramite telerilevamento

Index

Abstract

The PhD thesis intends to study and map those areas in Antarctica involved in surficial ablation processes linked to the wind action (wind-scouring phenomenon, i.e., erosion and sublimation of snow and ice for the effect of katabatic winds). In fact, Antarctica shows a meanly positive mass balance and the analysis of ablation areas, which can show near-zero or negative surface mass balance in the case of glazed snow and blue ice respectively, becomes fundamental since an eventual expansion would have consequences also on continental mass balance, leading to effects on sea-level rise. To glazed snow and blue ice, the study of snow megadunes is added, since these landforms are associated to the presence of glazed snow (characterizing their leeward flanks) and they present m/km variations leading to impacts on snow accumulation processes. All these surfaces and landforms optically behave differently to surrounding snow, the main surface of Antarctica, showing a lower albedo and so can be investigated from the space. Therefore, remote sensing, i.e., the study of globes through satellite imagery, has a key role in this research project and allows mapping and temporal-spatial analyses of these areas. Albedo was analysed using both already available data of Moderate Resolution Imaging Spectroradiometer (MODIS) and data that needed different calibration steps, i.e., Landsat-mission imagery. In the second case, a new model for its calculation was validated for broadband albedo and is under evaluation for narrowband albedo. MODIS was used for determining blue ice optical properties, which show an albedo of 0.50-0.70 and Landsat instead was applied in snow-glazed analyses, as its higher spatial resolution allowed to detect the slightly lower albedo that these surfaces have in respect to surrounding snow (maximum -0.04 in near-infrared wavelengths). Additionally, the other investigated meteorological parameters were wind, which can be studied using reanalysis atmospheric models or using a model derived from sastrugi (peculiar landforms parallel to prevailing wind direction) and thermal brightness temperature (from Landsat 8 TIRS). The use of these parameters allowed the automatic mapping of both glazed snow and blue ice, leading to their spatial and temporal analyses. Finally, the morphological analyses of megadunes provided the most relevant results of the thesis, confirming through a comparison of in-situ GPS/GPR measurements (It-ITASE traverse of 1999) and remote data (REMA DEM), their “antidunal” formation and allowing to precisely quantify their migration. These results were furtherly supported through an analysis of feature tracking on Landsat and Sentinel-2 images, which provided analogous results. In conclusion, this PhD thesis provides new and significant information about the ablation areas in Antarctica, as well as confirms and quantifies what was previously hypothesized. This information will be of fundamental importance for surface mass balance studies and for a better understanding of the role of Antarctica on the global climatic system.

Riassunto

La tesi di dottorato si propone di studiare e mappare quelle aree dell'Antartide interessate da processi di ablazione superficiale collegati all'effetto del vento (fenomeno del *wind-scouring*, i.e., erosione e sublimazione della neve e del ghiaccio per effetto dei venti catabatici). Infatti, l'Antartide presenta un bilancio di massa mediamente positivo e l'analisi delle aree di ablazione, che possono presentare un bilancio di massa superficiale nullo o negativo nel caso delle *glazed snow* e del ghiaccio blu rispettivamente, diventa fondamentale dal momento che un'eventuale loro espansione inciderebbe sul bilancio di massa continentale, con relative implicazioni sull'innalzamento del livello marino. A queste forme del rilievo, si è aggiunta anche l'analisi delle megadune di neve, poiché queste forme sono associate alla presenza del *glazed snow* (presente sul loro fianco sottovento) e le loro variazioni di pochi m/km portano a impatti sui processi di accumulo nevoso. Tutte le superfici e le forme del rilievo citate si comportano da un punto di vista spettrale in maniera differente rispetto la neve, principale copertura caratterizzante il continente Antartico, presentando un'albedo mediamente minore, il che le rende anche visibili dallo spazio. Quindi il telerilevamento, ovvero lo studio del globo tramite immagini satellitari ricopre un ruolo chiave nel progetto di ricerca e ne rende possibile la mappatura e l'analisi temporale e spaziale. L'albedo è stata quindi analizzata utilizzando sia dati già disponibili del sensore *Moderate Resolution Imaging Spectroradiometer* (MODIS) che con dati che prevedessero diverse fasi di calibrazione, ovvero quelli della missione Landsat. Nel secondo caso, un nuovo metodo è stato validato per calcolare l'albedo a banda larga ed è in corso di definizione quello per l'albedo spettrale. MODIS è stato usato per determinare le proprietà ottiche del ghiaccio blu, che mostra un'albedo di 0.50-0.70 e Landsat invece per le *glazed snow*, dal momento che la sua più alta risoluzione spaziale permetteva di individuarne l'albedo leggermente inferiore rispetto la neve circostante (con un massimo di -0.04 nelle lunghezze d'onda del vicino infrarosso). Inoltre, gli altri fattori meteorologici investigati sono stati il vento, che può essere studiato con modelli atmosferici di rianalisi o con un modello derivato dai sastrugi (peculiari forme del rilievo paralleli alla direzione dei venti dominanti) e la temperatura di brillanza termica (da Landsat 8 TIRS). L'unione di questi parametri ha permesso la mappatura automatica sia delle superfici di *glazed snow* che di ghiaccio blu, consentendone le loro analisi spaziali e temporali. Infine, l'analisi morfologica delle megadune ha fornito i risultati più importanti della tesi, confermando tramite un confronto di dati di terreno (dalla traversa It-ITASE del 1999) e da remoto (REMA DEM), la loro formazione "anti-dunale" e ha permesso di quantificare con precisione la loro migrazione. Questi risultati sono inoltre supportati da un'analisi di *feature tracking* applicata ad immagini Landsat e Sentinel-2, che hanno fornito risultati analoghi. In conclusione, la presente tesi di dottorato ha così fornito nuovi e

significative informazioni sulle aree di ablazione in Antartide, oltreché confermare e quantificare quanto precedentemente ipotizzato. Queste informazioni saranno così di fondamentale importanza per gli studi sul bilancio di massa superficiale e per una migliore comprensione del ruolo dell'Antartide nel sistema climatico terrestre.

Chapter 1: Introduction

1.1 Antarctica in the Global Climate System

Antarctica is considered to be the heat sink of the Southern Hemisphere, presenting a relevant control over the circulation of the atmosphere at mid-high latitudes (King and Turner, 1998). The net cooling which is present at these high latitudes results partly from simple geometry, in consideration that these areas receive less solar radiation at the top of the atmosphere (TOA), meanly over a year, than the tropics. However snow and ice surfaces, widely present in these regions, give rise to strong positive feedback. In fact, the presence of snow and ice, which show a high albedo (also called bi-hemispherical reflectance and defined as the ratio of the radiant flux reflected from a unit surface area into the whole hemisphere to the incident radiant flux of hemispherical angular extent, Schaepman-Strub et al., 2006, in the approximate spectral range 350–3000 nm, Grenfell, 2011), increases the cooling by reflecting a higher portion of the solar radiation than do rock or ocean surfaces. Then, a decrease or increase in temperature in the Polar Regions is expected to result in an increase or decrease in ice coverage, that will subsequently strengthen the original temperature change. Such a mechanism, i.e., ice-albedo feedback, can be a relevant process in creating variations and changes in the polar climate, bringing to an impact also on the global climate system. In contradiction to the Northern Hemisphere, which presents wide areas of seasonal snow cover which is able to quickly reply to changes in temperature, contributing to this feedback, Antarctica shows a permanent ice sheet (at millennial timescale), widely covered in snow. In Antarctica, the sea ice around the continent has the highest potential in contributing to climate variability and change. In contrast to Arctic sea-ice, Antarctic pack ice is unconstrained by surrounding land masses and shows higher yearly variations in terms of extent, thus affecting the atmospheric circulation of the Southern Ocean.

Antarctica represents a considerable feature in a hemisphere otherwise mainly free of large-scale orography. An atmospheric and ocean barrier is represented by the Antarctic Peninsula, exerting an important effect on the circulation of the Southern Hemisphere. Nevertheless, the inner continental ice sheets have even a bigger significance in this context. In fact, the important cooling which takes place over the dome-shaped ice sheets produces a persistent katabatic circulation (Fig. 1), with cold air flowing down from the inner areas towards the coasts. In fact, the air in proximity of the surface, which is negative buoyant (it cools radiatively relative to the upward air), will accelerate down over a sloping surface in response to the buoyancy force. This resulting flow, called katabatic wind (persistent and directional-steady winds blowing down from the high interior plateau), will be also turned by the Coriolis force, retarded by the surface friction, and respond to free-atmosphere pressure

gradients. However, even on moderate slopes which are widely present in the inner continent, where the stability of near-surface air is relevant, the wind will be first controlled by katabatic forcing. In Antarctica (as well as in Greenland), the mix of continuous cooling of the surface for most of the year and the vast sloping surfaces brings to a large-scale katabatic circulation to develop, which dominates the low-level circulation over the entire continent (King and Turner, 1998).

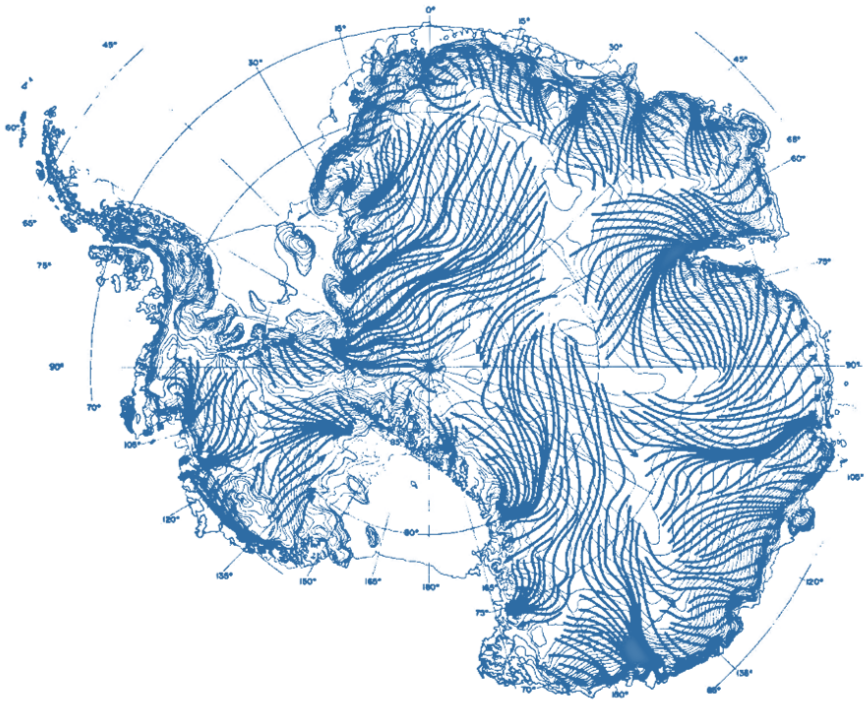

Figure 1. Map showing annual wind directions (open arrows) and sastrugi orientations (bold arrows) with contour lines in the background. Modified from Parish and Bromwich (1987).

Recently, Antarctic climate and mass balance have been highlighted by the Special Report on the Ocean and Cryosphere in a Changing Climate (Meredith et al., 2019) by the Intergovernmental Panel on Climate Change (IPCC) among the main uncertainties for the climate system and sea level projections, considering that the ice sheets of Antarctica hold enough water to raise global sea level by 58 m (Fretwell et al., 2013). The ice sheets drain the ice to the oceans across a system of glaciers and ice streams (Rignot et al., 2011), each one with a considerable inland catchment. Mass variations of grounded ice sheets occur owing to differences between surface net snow accumulation, meltwater runoff and ice discharge into the ocean. Reductions in the thickness (Shepherd et al., 2010) and extent (Cook and Vaughan, 2010) of floating ice shelves have disrupted inland ice flow, causing retreat (Rignot et al., 2014; Konrad et al., 2018), quickening (Joughin et al., 2002; Rignot et al., 2004) and drawdown (Shepherd et al., 2002; Scambos et al., 2004) of several marine-terminating ice streams.

1.2 Mass Balance

The Antarctic Ice Sheet (AIS) mass loss and its contribution to the sea level budget is the consequence of the difference of two similar (comparable magnitude) fluxes: ice flow discharging in the ocean and net snow accumulation on the ice sheet surface, i.e., the Surface Mass Balance (SMB). The whole ice sheet mass balance (SMB minus ice flow discharging) can be calculated using different approaches, not only in Antarctica, such as satellite altimetry, gravimetry, or the input–output method (which consists in separately modelling ice dynamics and SMB, Shepherd et al., 2018). All these methods are complementary and need SMB estimates. SMB (Fig.2a) usually was considered to be the sum of gained mass (mainly snowfall accumulation and some riming, Fig. 2b), mass losses (mainly surface and drifting snow sublimation, some liquid water run-off), and drifting snow transport (defined as the horizontal advection of the drifting snow), which can cause either gain or loss of mass (Agosta et al., 2019) and provides mass input to the surface of the Antarctic Ice Sheet. The mass gain represented by snowfall accumulation is of an order of magnitude larger than all of the other SMB fluxes at the continental scale (Lenaerts et al., 2012). The biggest difference is found along the ice sheet margins because of the cyclonic activity of the Southern Ocean and of the orographic raising of fairly warm and moist air masses (Van Wessem et al., 2014a; Favier et al., 2017). Ice sheet SMB varies significantly across multiple scales of time (hourly to decadal) and space (metres to hundreds of kilometres) (Agosta et al., 2012), and it is knowingly difficult to observe and represent in atmospheric models (Agosta et al., 2019). In addition, seen the difficulties in gaining access to the inner part of the ice sheet, only few field measurements on past and current conditions are present.

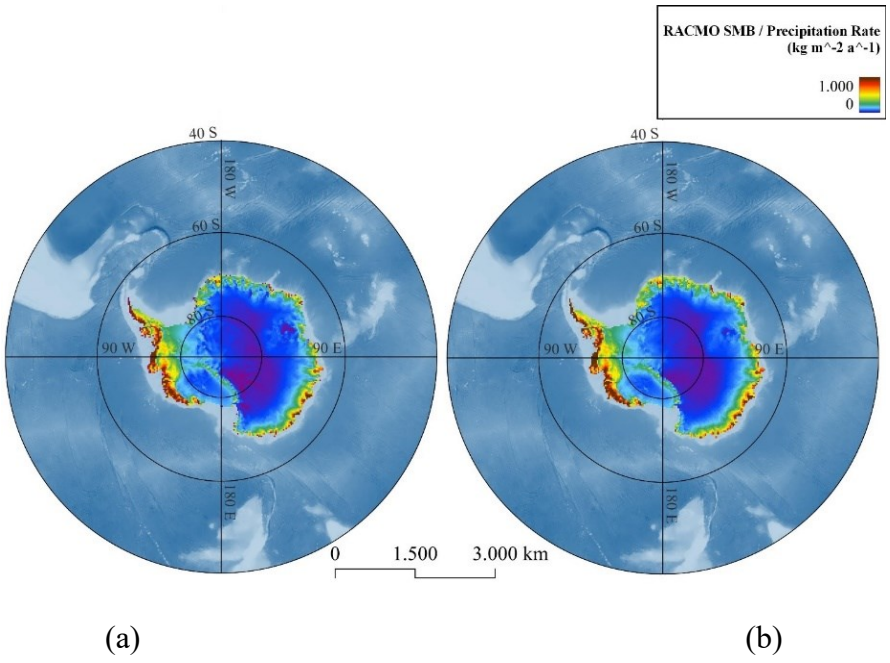

Figure 2. RACMO models (van Wessem et al., 2018) of SMB (a) and precipitation rate (b) at 35 km of spatial resolution in kg m^{-2} a^{-1}. ETOPO1 elevation model in the background (Amante and Eakins, 2009).

1.3 Ablation areas in Antarctica

In Antarctica the ablation areas are defined as those areas presenting a value of SMB ≤ 0 kg m^{-2} a^{-1}. In contrast to Greenland, which experiences strong seasonal melting, Antarctica lacks developed ablation areas (van den Broeke et al., 2006). Nevertheless, ablation areas are present (Fig. 3a) and is witnessed by vast occurrence of blue ice areas (BIAs), where the 70– 100 m thick firn layer has been removed (strongly negative SMB, at least two times of local accumulation) and the blue glacier ice appears at the surface (Bintanja, 1999; Winther et al., 2001). BIAs have a cover of about 1.7% at continental scale (Hui et al., 2014). Another ablation areas are the wind glaze areas (or wind crust or glazed snow areas, 11.2 ± 1.7% of East Antarctic Ice-Sheet, EAIS above 1500 m of altitude, Scambos et al., 2012), showing near-zero or slightly negative SMB (loss equal to accumulation or one and half time). This latter surface is also related to the presence of another peculiar Antarctic landforms, i.e., the snow megadunes (Frezzotti et al., 2002a), covering 775,000 km^2 circa of the EAIS (Fahnestock et al., 2000).

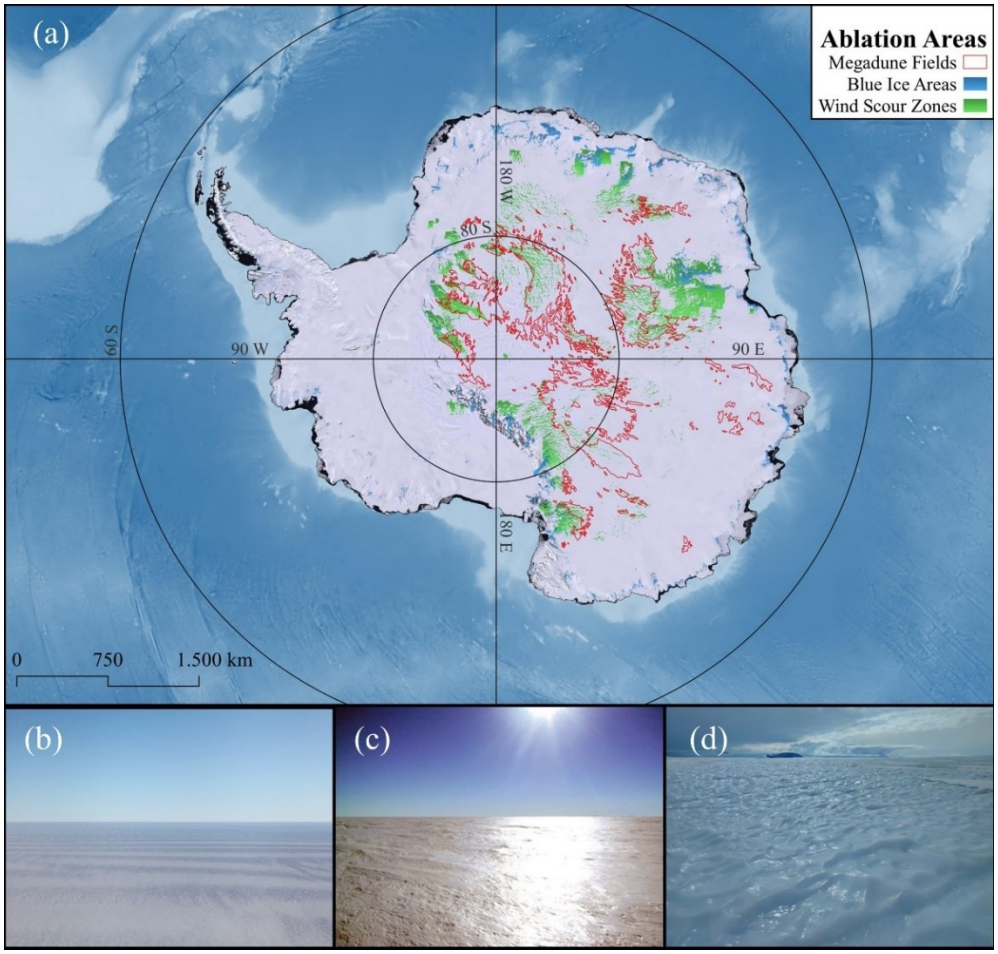

Figure 3. polygons of ablation areas in Antarctica (a), i.e., blue ice (blue, Hui et al., 2014), wind scour (green, Scambos et al., 2012) and megadune fields (red perimeter, Fahnestock et al., 2000). LIMA mosaic in the background (Bindschadler et al., 2008). Underneath photos represent a megadune field (b, over the plateau between Concordia and McMurdo Stations, photo by G. Picard) , glazed snow (c, Scambos et al., 2012) and blue ice (Nansen Ice Shelf, photo by G. Traversa).

1.3.1 Snow glaze areas

Snow glaze areas were firstly mentioned in 1912 by R. F. Scott in his diary: "Monday 29th January… The loose snow has been swept into heaps, hard and wind tossed. The rest has a glazed appearance, the loose drifting snow no doubt acting on it, polishing it like a sand blast." (Scott, 1913). Snow glazed areas (or wind glaze areas) are formed by a peculiar wind-topography interaction effect of persistent katabatic winds on areas of near-zero net surface accumulation and low temperatures on EAIS and are localized on leeward sloped of undulations and megadunes of the ice-sheet (Fahnestock et al., 2000; Frezzotti et al., 2002a, b; Scambos et al., 2012). Thus, wind glaze areas are relevant considering their SMB, that is near-zero (Scambos et al., 2012). They are mainly located in EAIS in confluence areas of katabatic winds (Scarchilli et al., 2010) and, morphologically, are represented as irregular to elongated patches of few hectometres / few kilometres in linear dimensions of wind polished glaze surface covering a coarsely recrystallized firn layer (Watanabe, 1978; Goodwin, 1990; Frezzotti et al., 2002a; Albert et al., 2004, Fig 3c). In contradiction with dune areas, characterized by rough surfaces with the presence of sastrugi (Fahnestock et al., 2000), wind glaze are flat and smooth, with scarcity of sastrugi forms (Scambos et al., 2012). However, snow glaze surfaces show deep cracks that are more evident in early summer season (Watanabe, 1978; Frezzotti et al., 2002a; Albert et al., 2004; Courville et al., 2007), caused by repeated thermal cycles (thermal expansion and contraction of snow or firn layers), and patterns in polygonal form, correlated to a long-term hiatus in accumulation of snow (Watanabe, 1978). At the end of summer, with cooling season, surfaces tend therefore to change their appearances also in remote-sensing data for wind erosion and sublimation effect. Fortunately, the spectral differences between glaze areas and surrounding snow make their identification easier from outer space, considering their lower albedo (Fujii et al., 1987; Frezzotti et al., 2002a). Spectral differences lead to temperature implications, showing a temperature that is mainly higher than on snow surface (Fujii et al., 1987). According to Frezzotti et al. (2002a), their formation is the result of an increased average inversion wind speed owed to an increase in local surface slope in the downwind direction. Thus, an increase in slope over a distance slightly higher than the inversion layer thickness (100-300m circa according to Connolley, 1996) can accelerate the flow that could lead to an increase in blowing-snow transport, a rise in surface and sublimation of snow due to adiabatic heating and compression (Neumann et al., 2005; Scarchilli et al., 2010), and to a steep temperature-gradient metamorphism (Gow, 1965). This cycle can annually remove most of (or the entirety of) the precipitated or wind-deposited snow that may temporarily accumulate (Scambos et al., 2012). Thus, a recrystallization on the ice crust, caused by the sublimation and upward transport of water vapor, occurs (Fujii and Kusunoki, 1982). In some coastal zones or slope convergence areas, Scarchilli et al. (2010) found that up to 50% of precipitation is removed by these

combined processes (i.e. blowing-snow sublimation and snow transport). Nevertheless, the persistence of snow glaze areas is possible only with steady wind intensity and direction, typical of zones between 1500 m and 3500 m a.s.l. (Parish and Bromwich, 1991; Fahnestock et al., 2000), otherwise only temporal intermittent glaze areas can take place (Goodwin, 1990), lacking of typical surface cracks.

1.3.2 Snow megadunes

Since their similarity with transverse sand megadunes, Swithinbank (1988) firstly described these aeolian features as megadunes. Megadune fields cover several square kilometre areas, mainly located on EAIS plateau (Fig. 3a, b). The reason behind their location is the uncommon snow accumulation and redistribution processes, leading therefore to a crucial role in SMB and ice core interpretation. In fact, in such inland areas, constancy of climatic conditions could play a key role, since accumulation is very low and wind intensity and direction is very stable and these conditions could affect firn recrystallization, favouring standing-wave mechanism (Fahnestock et al., 2000) and a high grade of metamorphism (Albert et al., 2004; Courville et al., 2007; Scambos et al., 2012; Dadic et al., 2013). In general, megadune fields are present in those areas where a slightly steeper regional slope occurs in conjunction with persistent katabatic winds. Morphologically, these features stand for 2-4 m amplitude waves of 2-5 km wavelength due to variable accumulation (Swithinbank, 1988; Fahnestock et al., 2000; Frezzotti et al., 2002b, 2005; Arcone et al., 2012a, b), in a range of 25% (leeward faces, characterized by the presence of wind glaze surfaces, as described later) and 120% (windward faces, covered by huge sastrugi up to 1.5 m height) of accumulation in adjacent non-megadune areas (Frezzotti et al., 2002b). For these reasons, dunes and sastrugi are fundamental in order to evaluate the orientation of wind direction, since the dunes are perpendicular to prevailing wind direction and sastrugi are parallel (Mather, 1962; Parish and Bromwich, 1991; Fahnestock et al., 2000). In addition, looking at the sedimentary structure of buried megadunes, observed near deep ice core drilling site areas (e.g. Vostok Station, Ekaykin et al., 2015), it could be possible to observe a windward surface migration (uphill), in contradiction with sand megadune (downward) (Frezzotti et al., 2002b, Fig. 4), typical of “antidunal” forms (Prothero and Schwab, 2004).

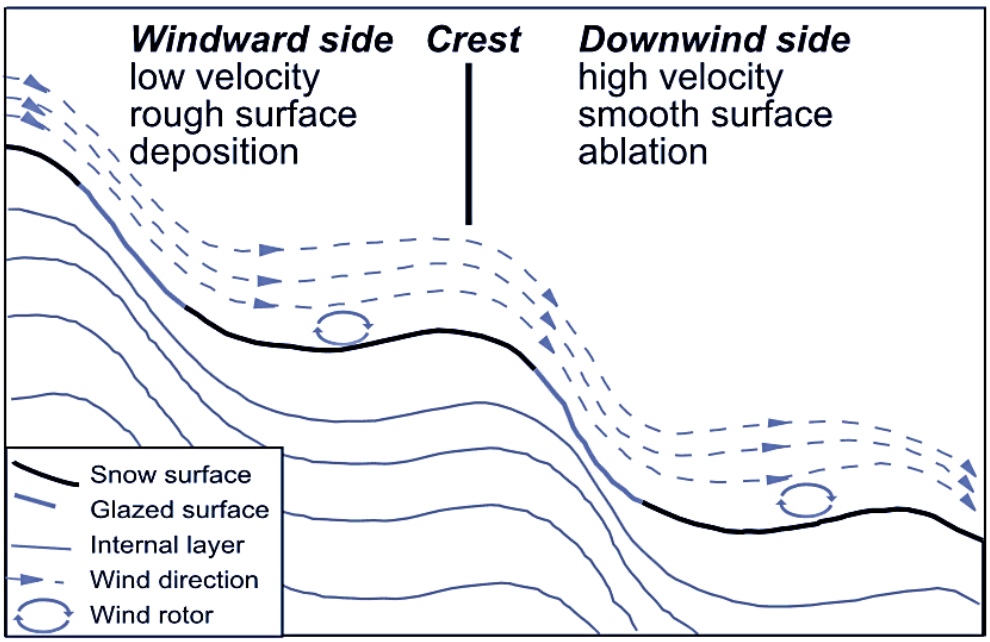

Figure 4. Summarizing of megadune growth processes, modified from Frezzotti et al. (2002a), modified.

This uphill migration is owed to different accumulation between windward (high accumulation) and leeward (near-zero accumulation) sides, leading, in addition, to differences in physical snow features and surface roughness (Fahnestock et al., 2000; Albert et al., 2004; Courville et al., 2007). According to Dadic et al. (2013), who took advantage of superficial-flow theory for sediments in water (Núñez-González and Martín-Vide, 2011) and atmospheric flow modelling, previous parameters, i.e. persistent katabatic winds, strong stability and spatial variability in surface roughness, are the primary controllers of upwind accumulation and migration of megadune, where the latter one represents the main factor that influences their velocity. Frezzotti et al. (2002b) pointed out that slope in the prevailing wind direction (SPWD) is, topographically, the most important characteristic of megadune, as they formed in a SPWD range of 0.13-0.22m km^{-1} and 1-1.5m km^{-1}. An increase or decrease in topographic slope (i.e., change in elevation over a certain distance) would not allow the megadune formation. SPWD, that is continuous and homogenous, the strength of surface inversion during winter temperatures (Phillpot and Zillman, 1970) and a mean low accumulation (Vaughan et al., 1999; Scambos et al., 2012), create consequently the perfect environment for megadune development. In association with snow dunes, peculiar surface features, called snow glaze areas, take place on the leeward slope of the megadunes (Section 1.3.1), creating a self-reinforcing of transverse glaze stripes and accumulating ridges that leads to glaze-dunes long trains (Frezzotti et al., 2002a; Scambos et al., 2012).

1.3.3 Blue Ice Areas

BIAs cover approximately 1-1.7% of Antarctic continent, presenting a negative SMB (Bintanja, 1999; Winther et al., 2001; Hui et al., 2014) and they are usually located in proximity of the coast or mountainous zones, in sloping areas (Winther et al., 2001, Fig. 3a, d). Historically, the first glaciological and geomorphological surveys on BIAs were carried out in the early fifties in Dronning Maud Land (Autenboer and Adie, 1964; Worsfold, 1967; Juckes, 1972), but then their interest increased significantly after the discovery of several meteorites trapped inside (Yoshida et al., 1971), which show ages up to 2.5 Ma. These meteorites are mainly located at altitudes over 2000 m a.s.l., suggesting that high-altitude BIAs are also the most stable ones (Cassidy et al., 1992). Geomorphologically, we can distinguish four types of BIAs (Bintanja, 1999, Fig. 5a): i) associated to nunataks or located on the edge of barriers which help the snow accumulation, with lengths that can be 50-100 times higher than barrier height (Takahashi et al., 1992); ii) located along valley glaciers, emerging by the effect of catabatic wind erosion; iii) located on relatively sloping surfaces where a wind effect similar to type ii is encountered; iv) located at the bottom of mountains and due to the effect of wind acceleration which removes/sublimate snow/firn/ice from the surface. In general, most of the BIAs in Antarctica are of type i, even if other types show averagely wider areas. Their formation can be divided into four main phases (Bintanja, 1999, Fig. 5b): i) rock is in depth below ice and does not have any influence on the surface, ii) ice-flow is affected by mountain presence becoming steeper and katabatic winds become stronger eroding snow and exposing bare ice, iii) nunatak emerges and on its leeward flank ice thickness decreases and blue ice enlarges by effect of snow erosion and sublimation, iv) further ice lowering releases completely the nunatak, increasing turbulences, sublimation and snow transport. In addition, progressive loss of blue ice mass is owed to its lower albedo (0.50-0.70, Bintanja and Van Den Broeke, 1995; Bintanja, 1999; Reijmer et al., 2001) than surrounding snow (0.80-0.85, Grenfell et al., 1994), increasing the available energy for sublimation/melting. An increase in wind action on leeward flanks can additionally lead to an enlargement of their surface.

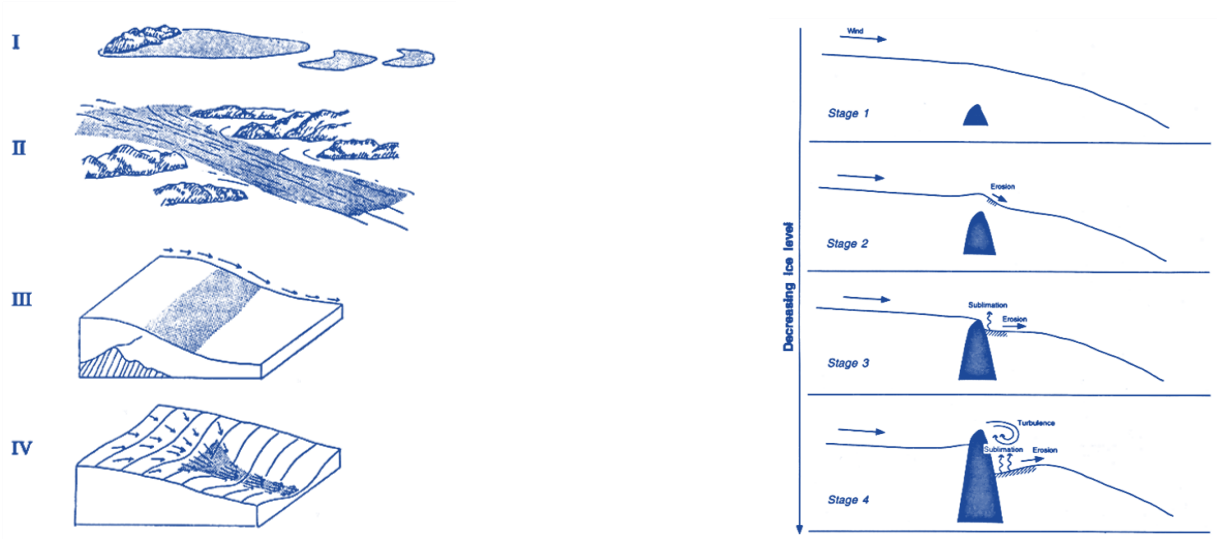

(a) (b)

Figure 5. illustration of four types of BIAs (a) and of their formation stages (b) from Bintanja (1999), modified.

1.4 Study areas

In order to analyse the ablation areas in Antarctica, i.e., snow-glaze areas (and megadunes) and BIAs, we focused on certain regions of the continent which present vast surfaces of these peculiar landforms. The considered areas cover most of the continent and are distributed at different latitudes and longitudes, even if all of them are included in the EAIS. In fact, the studied regions (Fig. 6) are: Victoria Land (*i*), Dronning Maud Land (*ii*), Mac. Robertson Land (*iii*) and the Antarctic plateau (*iv*).

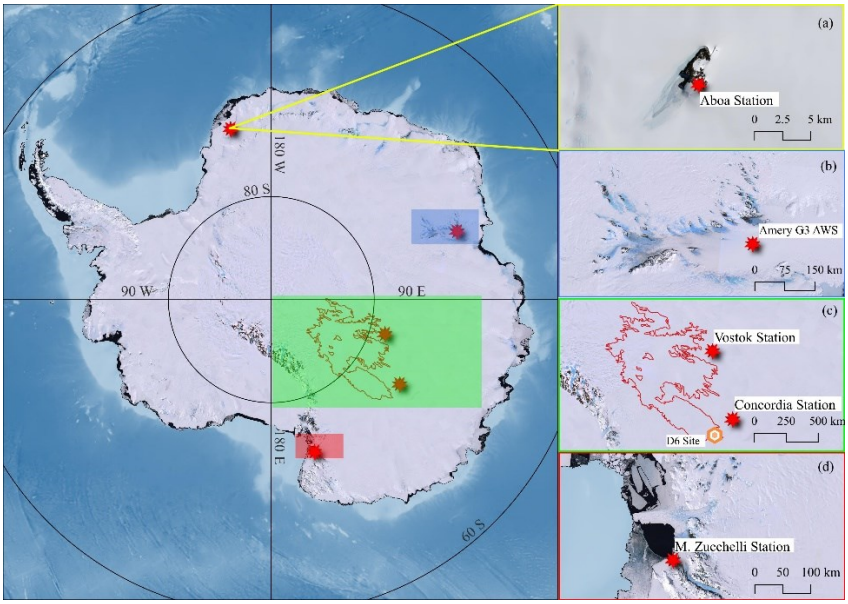

Figure 6. Locations of the different study areas where black and white dots stand for research stations and AWSs. In details: Dronning Maud Land (a), Mac. Robertson Land (b), Antarctic plateau (c) showing the major megadune field (red perimeter polygon) and D6 drill site (orange dot), and the Victoria Land (d).

In detail: *i* was analysed especially in the area of Terra Nova Bay where Italian Mario Zucchelli Station is (MZS; 74° 42' S, 164° 07' E). In fact, this area is characterised by the presence of large covering of blue ice (Benoit, 1995; Folco et al., 2006), mainly present on the David, Reeves, Priestley and Rennick Glaciers and Nansen Ice Shelf, as well as on the lee sides of nunataks at southernmost David Glacier, Mesa Range and Outback Nunataks. In this area a relative cover in glazed snow (Frezzotti, 1998) is also present in the southern part of the bay. On the other side of the continent is the Finnish Aboa Station (*ii*), distant about 130 km from the ocean (73° 03' S, 13° 25' W) on a nunatak of the Kraul Mountains. There, vast cover of BIAs are knowingly present (Rasmus, 2006; Järvinen et al., 2014). Another area strongly characterized by the presence of blue ice is *iii* (Yu et al., 2012; Markov et al., 2019), especially over Prydz Bay (Amery Ice Shelf, the third largest ice shelf of the continent; 69° 45' S, 71° 00' E), where temperature above 0°C are not rare during summers and surface meltwater systems (streams, ponds, etc.) are then current (Spergel et al., 2021; Tuckett et al., 2021), even directly on BIAs. Last but not least, glazed snow is widely persistent over the Antarctic plateau at the highest latitudes (*iv*), in relation with snow megadune fields, where climatic conditions are characterised by extremely low temperatures (mean annual temperatures from –45° to –60°C), extremely low snow precipitation (<30 mm water equivalent per year, w.e.a^{-1}; Van Wessem et al., 2014; Agosta et al., 2019) and nearly constant katabatic wind direction and wind speed (6–12 m s^{-1}; Courville et al., 2007). In particular, here we focused on two sites of the hugest megadune field, respectively near Concordia and Vostok Stations (150 and 300 km of distance respectively). The choice of analysing these two areas was due to the fact that past field campaigns were carried out with two different traverse expeditions, i.e., Italian-International TransAntarctic Scientific Expedition (It-ITASE) in 1998-1999 and East Antarctic International Ice Sheet Traverse (EAIIST) in 2018-19. It-ITASE area is 150 km East of Concordia Station (75°54' S, 131°36' E) and EAIIST area is situated 300 km East of Vostok Station (80°47' S, 122°19' E). The survey data of the second area (EAIIST, https://www.eaiist.com/en/) are under processing whereas the in-situ observations of the first traverse It-ITASE are available (Frezzotti et al., 2002b, a, 2004, 2005; Proposito et al., 2002; Vittuari et al., 2004). The EAIIST area is in the middle of the megadune area; thus, megadunes are well defined and continuous on satellite images in optical and microwave bands, whereas the It-ITASE area is at the North-West limit of the megadune field where this morphology is discontinuous and disappears, thus representing the developing threshold of the environmental conditions (morphology, climatology, glaciology) determining megadune formation.

1.5 State of the art and open issues

In general, ablation areas depend on different factors in Antarctica (Lenaerts et al., 2019), which are surface melt (occurring when the surface temperature reaches the melting point or at small depth caused by penetration of solar radiation), evaporation (occurring when liquid water is exposed at the ice sheet surface), sublimation (surface sublimation or drifting snow/blowing snow sublimation) and snow erosion (no sublimation occurs and snow redeposits in areas where the flow convergences and/or decelerates).

Van den Broeke et al. (2006) described three types of these peculiar surfaces for the Antarctic continent based on these features: erosion-driven ablation area (averagely 2000-3200 m a.s.l.), the sublimation-driven ablation area (occurring at elevations <2000 m, rather at the foot of steep topographic barriers, where temperature and wind speed are high and relative humidity low) and the melt-driven ablation area (mainly in the northern Antarctic Peninsula). In the first group are included the snow glaze areas, which are, as previously discussed, mainly related with the presence of sloping surfaces, such as on the leeward flanks of snow megadunes (Frezzotti et al., 2002a). Previous works have already studied megadune fields and thus glazed snow in Antarctica using ground penetrating radar (GPR; Frezzotti et al., 2002b; Arcone et al., 2012a, b; Das et al., 2013; Ekaykin et al., 2015), atmospheric models (Dadic et al., 2013; Palm et al., 2011, 2017) and remote sensing. Remote sensing was used both at high resolution (Frezzotti et al., 2002a, b), based on satellites of the Landsat family, and lower spatial resolution by using other images (Das et al., 2013), such as Radarsat/MODIS (Fahnestock et al., 2000; Arcone et al., 2012a; Scambos et al., 2012) and AVHRR (Fahnestock et al., 2000). These studies allowed to hypothesize the upwind accumulation and migration of megadunes (Dadic et al., 2013), by burying the glazed surface of the leeward face (Frezzotti et al., 2002b; Ekaykin et al., 2015), with typical “antidune” processes similar to those observed on fluvial and ocean bedforms (Prothero and Schwab, 2004), as well as describing their optical (Fahnestock et al., 2000; Frezzotti et al., 2002a; Scambos et al., 2012) and thermal (Fujii et al., 1987) properties. Previous attempts tried also to manually or automatically map the landforms (Fahnestock et al., 2000; Das et al., 2013). However, a detailed analysis of megadune physical parameters and their migration over time is still lacking. Additionally, in spite of the importance of the glazed surfaces of megadunes for the SMB of Antarctica, a remote sensing characterization of their physical properties and spatial distribution, and a quantitative analysis of their migration is currently lacking, as well as a precise automatic methodology for mapping them, which could allow a detailed temporal analysis.

The blue ice, which can be included in the second type of ablation areas (sublimation-driven) was first studied with field measurements (Autenboer and Adie, 1964; Worsfold, 1967; Juckes, 1972) and then from remote (Orheim and Lucchitta, 1990; Winther et al., 2001; Hui et al., 2014), providing

interesting results on their SMB role, formation and surface morphology and spectral characteristics. Nevertheless, most of the previous attempts focused only on specific regions of the continent (e.g., Dronning Maud Land; Bintanja and Van Den Broeke, 1995; Bintanja, 1999) and glaciological analyses are lacking for many regions (e.g., Victoria Land), despite of their knowingly existence. In addition, a detailed temporal analysis of blue ice extent is lacking, both at continental and regional scale; the role of meteorological parameters (i.e., wind, temperature and snowfall) and altitude results to be not satisfactorily clear and above all a strong uncertainty of its continental extent was encountered, as different results were obtained by several studies (~ 1% of the Antarctic surface, Bintanja, 1999, versus ~ 1.7 %, Hui et al., 2014).

1.6 Aims of the study

In contrast with field-based methodologies, which are limited in time and space, remote sensing allows performing large-scale analyses over otherwise remote areas, at a good temporal and spatial resolution. Therefore, the surfaces of ablation areas can be studied in detail, improving our knowledge about their evolution in time and then their role in Antarctica in the global climate system.

The present thesis aims to improve the understanding of the previously discussed open issues (see subsection 1.5) by taking advantage of remote sensing techniques and products, from satellite and other sources. For these reasons, this study focuses on different regions of Antarctica, where vast covers of glazed snow, megadunes and blue ice are present. In this context, this Ph.D. thesis pursues the following objectives:

1. identification of those key-parameters (e.g., albedo) fundamental for the analysis of ablation areas and which are totally or partially shared from all of them, with the aim of calculating and validating them in the most proper way for the specific context of Antarctic continent, and, as regards specifically the albedo, more in general for polar ice sheets, including then also Greenland Ice Sheet;
2. analyse and update the knowledge on glazed snow surfaces and megadunes, by using the most recent satellite images and products, as well as new techniques in order to fulfil the gaps remained from the past efforts;
3. prove previous hypothesized theories and provide new information about snow megadunes in Antarctica, such as a quantitative analysis of their migration (by assessing different feature tracking techniques), the characterization of their physical properties and spatial distribution and a precise automatic methodology for mapping the associated glazed snow surfaces, which could allow a detailed temporal analysis;

4. mapping of BIAs at continental scale to evaluate their extent and, regarding, providing a temporal analysis both at continental and regional scales;
5. analyse the role of key-meteorological parameters on BIA presence/extent, such as albedo (both broadband and narrowband from field and remote approaches), wind (both intensity and direction), temperature and evaluate a possible role of altitude.

To this end, several remote sensing approaches and applications were tested and developed, using satellite images and product and field observations (from weather stations), as described in the next chapter.

Chapter 2: Data and Methods

2.1 Data

This section of the thesis presents the remote and field data used for the analysis of ablation areas, divided into three main categories, i.e., satellite data (mainly optical data), meteorological observations from remote product (climatic reanalysis) and Automatic Weather Stations (AWSs), and topographic measurements, above all based on Digital Elevation Models (DEMs). During the research, also different datasets form *Quantarctica* repository (Matsuoka et al., 2021) were essential for carrying out specific needs.

2.1.1 Satellite data

With the aim of calculating and analysing significant optical parameters of the ablation surfaces, e.g., albedo and temperature, but also for other relevant analyses (e.g., glacier velocity estimation), different remote sources were used in the present research. These sources present various characteristics, such as different spatial and temporal resolution of the acquired data (images), some provide certain parameters already available and some needed specific processing steps to calculate these parameters. In this context and considering the aims of this thesis, four main satellite datasets were chosen, in consideration of their different properties, which are: Landsat family satellites, Sentinel-2, the sensor Moderate Resolution Imaging Spectroradiometer (MODIS) on board of Terra (EOS AM-1) and Aqua (EOS PM-1) satellites and the Advanced Spaceborne Thermal Emission and Reflection Radiometer (ASTER) sensor on Terra. All of them are sun-synchronous near-polar satellites (satellite that observe different portions of Earth, by passing over them after a certain period, i.e., temporal resolution, where each image is taken at the same local time). In detail, looking at the characteristics of each dataset, Landsat is an enterprise for acquisition of satellite imagery of Earth (NASA-USGS joint program) which includes nine launched satellites, sharing similar features. The first Landsat mission was launched in 1972, being the first Earth Observation (EO) satellite having the aim of monitoring the Earth's land. Even if Landsat 6 failed in achieving the orbit, Landsat series is the longest continuous imaging programme for the Earth. In fact, Landsat 1, 2 and 3 were launched in the 70', Landsat 4 and 5 (which carried the Multi Spectral Scanner, MSS, and Thematic Mapper, TM, instruments) in the 80', Landsat 7 (carrying the Enhanced Thematic Mapper Plus instrument, ETM+) at the end of 90', Landsat 8 in 2013 (Operational Land Imager, OLI, and Thermal InfraRed Sensor, TIRS, instruments) and Landsat 9 in 2021 (similar instruments than Landsat 8, but presenting an enhanced radiometric resolution, i.e., 14-bit against 12-bit). However, the scan line corrector of

Landsat 7 failed few years after its launch, in 2003, causing a degradation of data acquisitions, resulting in linear gaps on the images starting from that year. For this reason, when possible, the use of Landsat 5 imagery, which end date was in 2011, could fill the gap of Landsat 7 between 2003 to the beginning of the following decade. In this context, the only year with no degraded data remained approximately the 2012. The different Landsat satellites present different bands with several spatial and spectral resolutions, as follows:

- Landsat 1-5 MSS: four bands with 60 m spatial resolution, covering visible and near infrared (VNIR) wavelengths (0.50-1.10 μm);
- Landsat 4-5 TM: six bands with 30 m spatial resolution VNIR wavelengths (0.45-2.35 μm) and one with 120 m for Thermal InfraRed band (TIR, 10.40-12.50 μm);
- Landsat 7 ETM+: same VNIR and TIR bands of TM (TIR band having 60 m spatial resolution), plus an eighth panchromatic band having 15 m spatial resolution (0.52-0.90 μm);
- Landsat 8-9 OLI-TIRS: eight VNIR-ShortWave-InfraRed (SWIR) bands (0.43-2.29 μm) with 30 m spatial resolution, two TIR bands with 100 m s.r. (10.6-12.51 μm) and a panchromatic band with 15 m s.r. (0.50-0.68 μm, Zanter, 2019).

Another help to fill the gap in the first decade of second millennium is represented by ASTER (an USA-Japan team development), whose first acquisitions are dated back to 2000. This sensor, the only high spatial resolution on Terra satellite, presents fourteen bands divided into: four bands in the VNIR wavelengths (0.52-0.86 μm) with 15 m s.r., six SWIR bands (1.60-2.43 μm) with 30 m s.r. and five TIR bands (8.13-11.7 μm) with 90 m s.r.

The last considered high spatial resolution mission is the Copernicus Sentinel-2, two satellites (Sentinel 2A and 2B) from the European Space Agency (ESA), launched in 2015. These satellites carry a Multi Spectral Instrument (MSI) which provide thirteen bands for each acquisition, divided into ten for VNIR wavelengths (0.44-0.95 μm) at 10-20-60 m s.r. and three bands of SWIR (1.38-2.19 μm) at 20-60 m s.r.

In the end, the last instrument which was used in the present research is MODIS, aboard the Terra and Aqua satellites, which present 36 spectral bands (250-500-1000 m spatial resolution, 0.62-14.39 μm spectral resolution) and a constant 1-2-day temporal resolution for the entire Earth's surface (the other satellites present a more heterogenous temporal resolution, especially at high latitudes where the acquisitions become more inconstant). In detail, in the present thesis, three products of this sensor were taken into account, as they provide already-calculated albedo values. These products are MOD10A1, MYD10A1 and MCD43A3, all having 500 m of spatial resolution and a daily temporal resolution. The main differences between these products are that: MOD10A1 derives from Terra and

MYD10A1 from Aqua and they share similar properties; on the other hand, MCD43A3 dataset is produced daily using 16 days of Terra and Aqua data at 500 m resolution, where data are temporally weighted to the ninth day of the 16th day. Additionally, this product provides black sky albedo (directional hemispherical reflectance, that is inherent to specific locations and is linked with the structure and optical properties of the land cover, Schaaf et al., 2011) and white sky albedo (bi-hemispherical reflectance) values. For a higher detail of used scenes and bands, see the following chapters.

2.1.2 Meteorological observations

In the present research, meteorological observations were obtained from two main types of datasets: field measurements, i.e., AWSs and in-situ stations, and reanalysis data. In the first case, different AWS and in-situ stations were taken into account and the investigated parameters were the albedo, temperature and wind, both its intensity and direction. In this context, different sources were used and in details they were investigated: ***i*** seven AWSs owned by the *Institute for Marine and Atmospheric Research Utrecht* (IMAU), distributed over the Dronning Maud Land and the Antarctic Peninsula (Jakobs et al., 2020), ***ii*** two AWSs owned by the *Finnish Meteorological Institute* (FMI) in proximity of Aboa Station (Dronning Maud Land), ***iii*** three in-situ stations from the *World Radiation Monitoring Center – Baseline Surface Radiation Network* (WRMC – BSRN, Driemel et al., 2018), i.e., Concordia, Neumayer and Shōwa Stations (respectively located in Dome C, Dronning Maud Land and in proximity of Cosmonaut Sea) and ***iv*** an AWS (Amery G3), part of the *Australian Antarctic Data Centre* (AADC), located on the Amery Ice Shelf in the Mac. Robertson Land. To these Antarctic stations, ***v*** also four AWSs all over the Greenland Ice Sheet from the *Program for Monitoring of the Greenland Ice Sheet* (PROMICE, Van As et al., 2011) were considered for the validation of an albedo model for Greenland Ice Sheet, as well as for Antarctica. The ***i***, ***ii***, ***iii*** and ***v*** acquire albedo values (equipped with *Kipp & Zonen* radiometers CNR1 and CNR4 and pyranometers CM22, CMP22 and CMP21) useful as comparison and validation to the results obtained from satellites and ***iv*** provides temperature and wind values in an area characterized by the presence of BIAs (Budd, 1966; Markov et al., 2019). Seen the scarcity of wind available data from field observations, climatic reanalysis data were analysed and the choice fell on ERA5 atmospheric reanalysis climate dataset (Hersbach et al., 2020), distributed by the *European Centre for Medium-Range Weather Forecasts* (ECMWF). The product *ERA5 hourly data on single levels* (DOI: 10.24381/cds.adbb2d47) is the fifth generation ECMWF reanalysis for the global climate and weather from 1959 onwards and provides hourly estimates for a large number of atmospheric, ocean-wave and land-surface quantities (Hesrbach et al., 2018). This dataset was used to calculate raster maps of

velocity and direction of wind (0.25° of spatial resolution for atmospheric data), as results of the combination of 10 m u and v wind components (eastward and northward respectively, at a height of ten metres above the surface of the Earth). In ERA5 u and v and wind velocity are calculated as:

$$u = -|\vec{V}| \sin \varphi$$
$$v = -|\vec{V}| \cos \varphi \quad (1)$$
$$\vec{V} = \sqrt{u^2 + v^2}$$

Finally, different *Regional Atmospheric Climate Model* (RACMO) products were used, such as temperature and wind speed (Van Wessem et al., 2014b), or SMB and total precipitation rate (Van Wessem et al., 2014a).

2.1.3 Topographic measurements

As seen in Sec. 2.1.2 for climatic data, also in this case both field measurements and remote observations were considered. In the first case, GPR and Global Positioning System (GPS) from the It-ITASE traverse from 1999 were used, providing the topography of a portion of the major megadune field, 150 km E of Concordia Station (detailly, in D6-core-site area, Fig. 6c; Vittuari et al., 2004) in January of that year, as well as the paleo-topography (and thus also the paleo-dunes) of the corresponding area, identifiable across the different firn layers. In addition to these field data, also the most recent and highest resolution DEM of Antarctica was used, i.e., *Reference Elevation Model of Antarctica* (REMA) DEM (Howat et al., 2019), essential as comparison with field measurements, for the topographic correction of satellite albedo and for calculating various topographic parameters, e.g., slope, aspect, etc. REMA is built from hundreds of thousands of individual stereoscopic DEMs obtained from couples of submeter (0.32 to 0.5 m) resolution Maxar satellite imagery, containing data from WorldView-1, WorldView-2, and WorldView-3, and a few from GeoEye-1, acquired between 2009 and 2017, mostly collected in 2015 and 2016, over the austral summer seasons (mainly December to March). Each single DEM was vertically registered to satellite altimetry measurements from Cryosat-2 and ICESat, bringing to absolute uncertainties of less than a metre over most of its area (relative uncertainties of decimetres). REMA comprises around 98% of the contiguous continental landmass extending to maximum of 88° S circa. Above and beyond this lack in South Pole area, some voids exist. Its resolution is 8 m spatial resolution, even if 2 m-stripes can be used for some areas (mainly West Antarctica). On the other side, in order to apply the topographic correction on satellite albedo also over the Arctic Ice Sheet, *Greenland Mapping Project* (GIMP) DEM (Howat et al., 2014) was employed. GIMP DEM is composed of a combination of ASTER and SPOT-5 DEMs (Korona et al., 2009) for the ice sheet boundary and margin south of circa 82.5° N,

and AVHRR photoclinometry in the inner ice sheet and far north (Scambos and Haran, 2002). The final product has 30-90 m of spatial resolution, depending on areas covered by SPOT-5 or AVHRR respectively.

2.2 Methods

The Methods section of the thesis includes the main methodologies applied on the different datasets with the aim of providing the most precise and reliable results, taking advantage of new and renowned techniques. In the thesis context, three main methodological sections are present, i.e., the calculation of the albedo and thermal brightness temperature starting from satellite imagery; wind calculation and validation and the subsequent estimation of the key parameter SPWD and dune and glacier movement calculation from both field and remote datasets and a combination of them.

2.2.1 Albedo and thermal brightness temperature

In order to calculate narrowband and broadband albedo and thermal brightness temperature from remote, Landsat-family satellites were used, as they allow a study of the ice sheet in fined detail than other lower resolution imagery. The other reason why the choose fell on Landsat was that albedo models based on it already exist (Reijmer et al., 2001; Klok et al., 2003; Shuai et al., 2011; Wang et al., 2014; Fugazza et al., 2016; Naegeli et al., 2017), even if not yet tested or applied on the ice sheets. In detail, the present research based its albedo retrieval on the model proposed by Klok et al. (2003) and more recently adjusted by Fugazza et al. (2016). These models include different steps of correction, from raw satellite data to final albedo. The first step is the radiometric calibration, which allow the back-scale process from the quantized digital number (DN dimensionless) to the radiance, using the coefficients taken from meta-data file, in accordance with the following formula (Λ_b is the radiance at satellite level in a given band):

$$\Lambda_b = DN_b * gain + offest \tag{2}$$

Then, the so calculated radiance needed to be converted to Top-of-Atmosphere (TOA) reflectance ($\rho_{TOA,b}$) with the formula:

$$\rho_{TOA,b} = \frac{\pi * d^2 * \Lambda_b}{E_{sun,b} * \cos SZA} \tag{3}$$

where d is the distance between Sun and Earth (depending on the day of the year), $E_{sun,b}$ is the specific band mean exoatmospheric solar irradiance (W m^{-2}) and SZA the Solar Zenith Angle. However, as Landsat 8-9 OLI do not provide the solar irradiance values, another algorithm is requested in order to calculate the TOA reflectance and it is as follows:

$$\rho_{TOA,b} = \frac{M_\rho * Q_{cal} + A_\rho}{\cos SZA} \quad (4)$$

where M_ρ and A_ρ are respectively the band-specific multiplicative rescaling and additive factors in the Metadata file and Q_{cal} is the quantized and calibrated standard product pixel values (DN).
After these initial steps, the TOA reflectance needed three additional correction steps. The first one is the correction of reflectance for atmospheric interference using the 6S radiative transfer model (Vermote et al., 1997) in GRASS GIS software. The algorithm requires used-defined parameters to be run, which are: ***i*** satellite source, ***ii*** date, time and central coordinates, ***iii*** atmospheric model, ***iv*** aerosol model, ***v*** aerosol optical thickness (AOT) at 550 nm (estimating the attenuation of direct solar irradiance by aerosols) and ***vi*** the target elevation (from DEMs). Then, the effect of the topography requires a correction, i.e., topographic correction. Different models are available and here c-factor, cosine and Minnaert were considered. All these models require a first step of calculation, i.e., the calculation of an illumination model, representing the cosine of the solar incident angle (through DEM), calculated as:

$$\cos i = \cos s * \cos SZA + \sin s * \sin SZA * \cos(SAA - o) \quad (5)$$

where *i* is the incident angle, *s* the terrain slope angle, SAA the Solar Azimuth Angle and *o* the aspect angle. In detail, the c-factor, cosine and Minnaert methods are respectively described as follows:

$$ref_c = ref_O \frac{\cos z + c}{\cos i + c} \quad (6)$$

$$ref_c = \frac{ref_O * \cos z}{\cos i} \quad (7)$$

$$ref_c = ref_O * (\frac{\cos z}{\cos i})^k \quad (8)$$

where ref_c is the corrected reflectance, ref_O is the original reflectance, c is equal to $a\ m^{-1}$ from

$$ref_O = a + m * \cos i \quad (9)$$

and k is obtained by linear regression of

$$\ln(ref_O) = \ln(ref_c) - k * \ln(\frac{\cos i}{\cos z}) \quad (10)$$

Once applied the atmospheric and topographic corrections, the reflectance needed to be corrected for the anisotropy, which increases with increasing wavelength and incident angles (Greuell and de Ruyter de Wildt, 1999), as ice and snow are non-Lambertian surfaces, i.e., reflected radiation is different for any given direction. The formula for this correction is:

$$\alpha_{s,b} = \frac{\rho_{s,b}}{f} \quad (11)$$

where $\alpha_{s,b}$ is the albedo in a specific band (narrowband albedo), f is the anisotropic correction factor and $\rho_{s,b}$ is the reflectance corrected until topographic step. f was calculated from the Bidirectional Reflectance Distribution Functions (BRDFs) over ice and snow using different models (Greuell and de Ruyter de Wildt, 1999; Reijmer et al., 2001; Ren et al., 2021) and in accordance with the different wavelengths of the satellite bands. In this context, the Normalized Difference Snow Index (NDSI) was used to discriminate between ice and snow, setting the threshold on 0.45 (Ren et al., 2021). The NDSI was calculated as follows (*B* stands for *band*):

$$NDSI = \frac{B_{Green} - B_{SWIR_1}}{B_{Green} + B_{SWIR_1}} \quad (12)$$

The last remaining step is the narrowband to broadband albedo conversion, which is possible taking advantage of three already existing equations: Knap (Knap et al., 1999), Reijmer (Reijmer et al., 2001) and Liang (Liang, 2001) algorithms, defined as follows:

$$\alpha_{Knap} = 0.726\alpha_{Green} - 0.322{\alpha_{Green}}^2 - 0.051\alpha_{NIR} + 0.581{\alpha_{NIR}}^2 \quad (13)$$

$$\alpha_{Reijmer} = 0.509\alpha_{Green} + 0.309\alpha_{NIR} \quad (14)$$

$$\alpha_{Liang} = 0.356\alpha_{Blue} + 0.130\alpha_{Red} + 0.373\alpha_{NIR} + 0.085\alpha_{SWIR_1} + 0.072\alpha_{SWIR_2} - 0.0018 \quad (15)$$

As regards the calculation of the TOA thermal brightness temperature, the first TIR band of Landsat was used (10.60 – 11.19 μm). Using the spectral radiance of that band (L_λ, where only radiometric calibration was applied) and the two band-specific thermal conversion constants ($K_{1,2}$) from meta-data file, the following formula was employed:

$$T = \frac{K_2}{\ln(\frac{K_1}{L_\lambda} + 1)} \quad (16)$$

2.2.2 Wind and Slope in the Prevailing Wind Direction

The SPWD is one of the most important and peculiar features that characterizes the megadune fields (Frezzotti et al., 2002b) and depends mainly on three parameters: wind direction, topographic slope and aspect of the field. As regards the first parameter, i.e., wind direction, ERA5 provides it as showed in Sec. 2.1.2. Five classes were further created, considering wind speed values above certain thresholds, which are: >3 m s^{-1}, >5 m s^{-1}, >7 m s^{-1} and >11 m s^{-1}. These thresholds were chosen based on the interactions between wind and snow: snow transportation by saltation (within 0.3 m in elevation) starts at wind speeds between 2 and 5 m s^{-1}, transportation by suspension (drift snow) starts at velocities > 5 m s^{-1} (within 2 m) and blowing snow (snow transportation higher than 2 m) starts at velocities between 7 and 11 m s^{-1} (see Frezzotti et al., 2004 and references therein). The threshold wind speed at which the sublimation of blowing snow starts to contribute substantially to katabatic flows in a feedback mechanism appears to be 11 m s^{-1} (Kodama et al., 1985; Wendler et al., 1993). Since ERA5 is a reanalysis dataset derived from a combining of models and observations with a low spatial resolution (0.25°), we tried to take advantage of sastrugi directions to derive wind orientation, as they are parallel (Mather, 1962; Parish and Bromwich, 1991; Fahnestock et al., 2000). A sastrugi-based wind direction file would be more accurate as representative of the local prevalent wind conditions, and it was fundamental to check the results obtained by ERA5. In this context, we used Landsat 8 OLI imagery considering its high resolution (30 m) and in detail its NIR band because differences between snow and megadunes (glazed surfaces, dunes and sastrugi) are better seen, since solar radiation is strongly absorbed in this part of the spectrum and, in contrast with the visible bands, here feature differences are heightened (Frezzotti et al., 2002b). In addition, in order to heighten the discrepancies among morphologies and better identify the sastrugi, a pre-processing step was applied by using a high pass filter with a length scale of 150 m implemented through a Fast Fourier Transform. Then, the edge detection algorithm, *i.edge* of GRASS software, was used, which detects a wide range of edges in raster maps and produces edge and angle maps (Canny, 1986), with specific thresholds (between 10 and 35) and Kernel radius (5) values, with the aim of excluding other features and heighten sastrugi only. The obtained angle raster map presented only pixels along sastrugi morphologies. However, since Landsat 8 provides images for Antarctica in Polar Stereographic coordinate system (EPSG: 3031), the obtained values of angles did not represent correct and real sastrugi direction and the raster map needed to be converted into a polyline shapefile. After having cleaned the angle map from errors and artefacts, on ArcMap software it was utilized a thinning process and then the conversion to polyline (with minimum length equal to 400). Subsequently the obtained polyline shapefile has been simplified with *Simplify line* tool and finally converted into another coordinate system. In order to provide the best and realistic angle of sastrugi direction, a

conformal projection was necessary, as it maintains the angles. Thus, for our specific case, the UTM zone 51 S coordinate system (EPSG: 32751) and UTM zone 52 S (EPSG: 32752) for 069119 and 081114 tiles respectively, were chosen. Now, with *GetPolylineAzimuth* module (that uses the arc tangent) on ArcMap software, we obtained the correct sastrugi angles in degrees (it was necessary to add 180° to obtain the result). In some cases, a definitive cleaning was required. Once obtained the correct sastrugi angle file, we converted back the polyline shapefile into raster, maintaining the 30m spatial resolution of initial Landsat images and then projected it in Polar Stereographic coordinate system. With the aim of obtaining a complete raster of wind direction, comparable to the one of ERA5, we applied a surface interpolation (*r.fillnulls* module on GRASS software with bi-linear interpolation) in order to fill the entire area, also the part not included in sastrugi coverage.

Once having the wind speed directions, both from ERA5 and sastrugi-derived, the approach of Scambos et al. (2012) to calculate SPWD was implemented. This method calculated the dot product between the slope derived from the REMA DEM and the wind direction. The algorithm was applied to ERA5 and sastrugi-based wind directions resampled at 120 m spatial resolution, and the REMA DEM was resampled to match ERA5 and sastrugi-based wind directions using bilinear interpolation.

2.2.3 Dune and glacier movement estimation

In order to analyse and estimate the movement of snow dunes, two approaches were used and subsequently compared. In fact, on the base of sedimentary structure of buried megadunes by using GPR and GPS, Frezzotti et al. (2002b) and Ekaykin et al. (2015) demonstrated that the migration of the megadunes and ice sheet surface flow have a similar intensity but opposite directions and that megadunes migrates upwind with time (bury of glazed surface of the leeward face).

Based on this assumptions, megadune migration can be provided and quantified by three different components, i.e.: ice-flow (If) direction (correlated mainly to topographic slope), sedimentological migration (Ms, caused by sedimentological processes linked to deposition and ablation of snow), and the result of these processes, the absolute migration (Ma). The relation of these components is shown in the following formula:

$$\overrightarrow{M_a} = \overrightarrow{M_s} + \overrightarrow{If} \tag{17}$$

In order to calculate these features, both an in-situ-based and a remote-based approaches can be applied. In fact, during the It-ITASE traverse at the D6 site, megadunes were surveyed by means of GPR-GPS to measure ice velocity and surface elevation. By comparing these measurements with the REMA DEM (2014), it was possible to calculate the change in surface morphology due to sedimentological migration of the megadunes. On the other hand, remotely, the feature tracking

module IMCORR (Fahnestock et al., 1992; Scambos et al., 1992) was run in System for Automated Geoscientific Analyses (SAGA GIS) on pairs of Landsat 8 and Sentinel-2 images over the two megadune study sites. This algorithm is an image-to-image cross correlation and co-registration algorithm based on the normalised cross-covariance method (Bernstein, 1983), used to find the displacements of moving features. In this algorithm, for each small image chip chosen from a reference image, a corresponding chip is investigated in a larger search area inside a second image, providing displacement intensity (which can be converted to annual displacement) and direction. Before the application of the IMCORR module, each pair of images was pre-processed by using a low pass filter with a length scale of 150 m implemented through a Fast Fourier Transform (FFT) in order to smooth the sastrugi presence and highlight megadune features. Then, the so obtained displacement values were balanced by means of the corresponding time period, obtaining the absolute migration of the megadunes in m a^{-1}. These results (remote and in-situ) were then processed with the MEaSUREs ice-flow velocity product (the highest-resolution digital mosaic of ice motion in Antarctica, Rignot et al., 2017) and the ice flow measurements taken during the It-ITASE traverse (Vittuari et al., 2004). Finally, applying Eq. 1, all the megadune migration components could be calculated.

Together with IMCORR module, other feature-tracking and machine-learning based algorithms were applied (on Landsat, Sentinel-2 and ASTER imagery) to estimate the glacier displacements and directions. Again, field measurements of GPS were considered as comparison with remote data. See section 6.2 for details.

References

Agosta, C., Favier, V., Genthon, C., Gallée, H., Krinner, G., Lenaerts, J. T., and van den Broeke, M. R.: A 40-year accumulation dataset for Adelie Land, Antarctica and its application for model validation, Climate dynamics, 38, 75–86, 2012.

Agosta, C., Amory, C., Kittel, C., Orsi, A., Favier, V., Gallée, H., van den Broeke, M. R., Lenaerts, J. T. M., van Wessem, J. M., van de Berg, W. J., and Fettweis, X.: Estimation of the Antarctic surface mass balance using the regional climate model MAR (1979–2015) and identification of dominant processes, The Cryosphere, 13, 281–296, https://doi.org/10.5194/tc-13-281-2019, 2019.

Albert, M., Shuman, C., Courville, Z., Bauer, R., Fahnestock, M., and Scambos, T.: Extreme firn metamorphism: impact of decades of vapor transport on near-surface firn at a low-accumulation glazed site on the East Antarctic plateau, Annals of Glaciology, 39, 73–78, https://doi.org/10.3189/172756404781814041, 2004.

Amante, C. and Eakins, B. W.: ETOPO1 arc-minute global relief model: procedures, data sources and analysis, 2009.

Anslow, F. S., Hostetler, S., Bidlake, W. R., and Clark, P. U.: Distributed energy balance modeling of South Cascade Glacier, Washington and assessment of model uncertainty, Journal of Geophysical Research: Earth Surface, 113, https://doi.org/10.1029/2007JF000850, 2008.

Arcone, S. A., Jacobel, R., and Hamilton, G.: Unconformable stratigraphy in East Antarctica: Part I. Large firn cosets, recrystallized growth, and model evidence for intensified accumulation, J. Glaciol., 58, 240–252, https://doi.org/10.3189/2012JoJ11J044, 2012a.

Arcone, S. A., Jacobel, R., and Hamilton, G.: Unconformable stratigraphy in East Antarctica: Part II. Englacial cosets and recrystallized layers, J. Glaciol., 58, 253–264, https://doi.org/10.3189/2012JoG11J045, 2012b.

Autenboer, T. van and Adie, R. J.: The geomorphology and glacial geology of the Sor-Rondane, Dronning Maud Land, Antarctic Geology, 81–103, 1964.

Azzoni, R. S., Senese, A., Zerboni, A., Maugeri, M., Smiraglia, C., and Diolaiuti, G. A.: Estimating ice albedo from fine debris cover quantified by a semi-automatic method: the case study of Forni Glacier, Italian Alps, The Cryosphere, 10, 665–679, https://doi.org/10.5194/tc-10-665-2016, 2016.

Benoit, P. H.: Meteorites as surface exposure time markers on the blue ice fields of Antarctica: episodic ice flow in Victoria Land over the last 300,000 years, Quaternary Science Reviews, 14, 531–540, 1995.

Bernstein, R.: Image geometry and rectification, Manual of Remote Sensing (R. N. Colwell, Ed.), 881–884, 1983.

Bindschadler, R., Vornberger, P., Fleming, A., Fox, A., Mullins, J., Binnie, D., Paulsen, S., Granneman, B., and Gorodetzky, D.: The Landsat Image Mosaic of Antarctica, Remote Sensing of Environment, 112, 4214–4226, https://doi.org/10.1016/j.rse.2008.07.006, 2008.

Bintanja, R.: On the glaciological, meteorological, and climatological significance of Antarctic blue ice areas, Reviews of Geophysics, 37, 337–359, 1999.

Bintanja, R. and Van Den Broeke, M. R.: The surface energy balance of Antarctic snow and blue ice, Journal of Applied Meteorology and Climatology, 34, 902–926, 1995.

Brock, B. W., Mihalcea, C., Kirkbride, M. P., Diolaiuti, G., Cutler, M. E. J., and Smiraglia, C.: Meteorology and surface energy fluxes in the 2005–2007 ablation seasons at the Miage debris-covered glacier, Mont Blanc Massif, Italian Alps, Journal of Geophysical Research: Atmospheres, 115, https://doi.org/10.1029/2009JD013224, 2010.

van den Broeke, M., van de Berg, W. J., van Meijgaard, E., and Reijmer, C.: Identification of Antarctic ablation areas using a regional atmospheric climate model, Journal of Geophysical Research: Atmospheres, 111, https://doi.org/10.1029/2006JD007127, 2006.

Budd, W.: The dynamics of the Amery ice shelf, Journal of Glaciology, 6, 335–358, 1966.

Canny, J.: A computational approach to edge detection, IEEE Transactions on pattern analysis and machine intelligence, 679–698, 1986.

Carenzo, M., Pellicciotti, F., Mabillard, J., Reid, T., and Brock, B. W.: An enhanced temperature index model for debris-covered glaciers accounting for thickness effect, Advances in Water Resources, 94, 457–469, https://doi.org/10.1016/j.advwatres.2016.05.001, 2016.

Cassidy, W., Harvey, R., Schutt, J., Delisle, G., and Yanai, K.: The meteorite collection sites of Antarctica, Meteoritics, 27, 490–525, 1992.

Connolley, W. M.: The Antarctic temperature inversion, International Journal of Climatology: A Journal of the Royal Meteorological Society, 16, 1333–1342, 1996.

Cook, A. J. and Vaughan, D. G.: Overview of areal changes of the ice shelves on the Antarctic Peninsula over the past 50 years, The cryosphere, 4, 77–98, 2010.

Courville, Z. R., Albert, M. R., Fahnestock, M. A., Cathles, L. M., and Shuman, C. A.: Impacts of an accumulation hiatus on the physical properties of firn at a low-accumulation polar site, J. Geophys. Res., 112, F02030, https://doi.org/10.1029/2005JF000429, 2007.

Dadic, R., Mott, R., Horgan, H. J., and Lehning, M.: Observations, theory, and modeling of the differential accumulation of Antarctic megadunes: ACCUMULATION OF ANTARCTIC MEGADUNES, J. Geophys. Res. Earth Surf., 118, 2343–2353, https://doi.org/10.1002/2013JF002844, 2013.

Das, I., Bell, R. E., Scambos, T. A., Wolovick, M., Creyts, T. T., Studinger, M., Frearson, N., Nicolas, J. P., Lenaerts, J. T. M., and van den Broeke, M. R.: Influence of persistent wind scour on the surface mass balance of Antarctica, Nature Geosci, 6, 367–371, https://doi.org/10.1038/ngeo1766, 2013.

Driemel, A., Augustine, J., Behrens, K., Colle, S., Cox, C., Cuevas-Agulló, E., Denn, F. M., Duprat, T., Fukuda, M., Grobe, H., Haeffelin, M., Hodges, G., Hyett, N., Ijima, O., Kallis, A., Knap, W., Kustov, V., Long, C. N., Longenecker, D., Lupi, A., Maturilli, M., Mimouni, M., Ntsangwane, L., Ogihara, H., Olano, X., Olefs, M., Omori, M., Passamani, L., Pereira, E. B., Schmithüsen, H., Schumacher, S., Sieger, R., Tamlyn, J., Vogt, R., Vuilleumier, L., Xia, X., Ohmura, A., and König-Langlo, G.: Baseline Surface Radiation Network (BSRN): structure and data description (1992–2017), Earth Syst. Sci. Data, 10, 1491–1501, https://doi.org/10.5194/essd-10-1491-2018, 2018.

Ekaykin, A. A., Lipenkov, V. Ya., and Shibaev, Yu. A.: Spatial Distribution of the Snow Accumulation Rate Along the Ice Flow Lines Between Ridge B and Lake Vostok, Lëd i sneg, 52, 122, https://doi.org/10.15356/2076-6734-2012-4-122-128, 2015.

Fahnestock, M. A., Scambos, T. A., and Bindschadler, R. A.: Semi-automated ice velocity determination from satellite imagery, Eos, 73, 493, 1992.

Fahnestock, M. A., Scambos, T. A., Shuman, C. A., Arthern, R. J., Winebrenner, D. P., and Kwok, R.: Snow megadune fields on the East Antarctic Plateau: Extreme atmosphere-ice interaction, Geophysical research letters, 27, 3719–3722, https://doi.org/10.1029/1999GL011248, 2000.

Favier, V., Krinner, G., Amory, C., Gallée, H., Beaumet, J., and Agosta, C.: Antarctica-Regional Climate and Surface Mass Budget, Curr Clim Change Rep, 3, 303–315, https://doi.org/10.1007/s40641-017-0072-z, 2017.

Folco, L., Welten, K. C., Jull, A. J. T., Nishiizumi, K., and Zeoli, A.: Meteorites constrain the age of Antarctic ice at the Frontier Mountain blue ice field (northern Victoria Land), Earth and Planetary Science Letters, 248, 209–216, https://doi.org/10.1016/j.epsl.2006.05.022, 2006.

Foster, L. A., Brock, B. W., Cutler, M. E. J., and Diotri, F.: A physically based method for estimating supraglacial debris thickness from thermal band remote-sensing data, Journal of Glaciology, 58, 677–691, https://doi.org/10.3189/2012JoG11J194, 2012.

Fretwell, P., Pritchard, H. D., Vaughan, D. G., Bamber, J. L., Barrand, N. E., Bell, R., Bianchi, C., Bingham, R. G., Blankenship, D. D., and Casassa, G.: Bedmap2: improved ice bed, surface and thickness datasets for Antarctica, The Cryosphere, 7, 375–393, 2013.

Frezzotti, M.: Surface wind field of Victoria Land (Antarctica) from surveys of aeolian morphologic features, Terra Antartica Reports, 1, 43–45, 1998.

Frezzotti, M., Flora, O., and Urbini, S.: The Italian ITASE expedition from Terra Nova station to Talos Dome, 1998.

Frezzotti, M., Gandolfi, S., Marca, F. L., and Urbini, S.: Snow dunes and glazed surfaces in Antarctica: new field and remote-sensing data, Ann. Glaciol., 34, 81–88, https://doi.org/10.3189/172756402781817851, 2002a.

Frezzotti, M., Gandolfi, S., and Urbini, S.: Snow megadunes in Antarctica: Sedimentary structure and genesis, Journal of Geophysical Research: Atmospheres, 107, ACL 1-1-ACL 1-12, https://doi.org/10.1029/2001JD000673, 2002b.

Frezzotti, M., Pourchet, M., Flora, O., Gandolfi, S., Gay, M., Urbini, S., Vincent, C., Becagli, S., Gragnani, R., and Proposito, M.: New estimations of precipitation and surface sublimation in East Antarctica from snow accumulation measurements, Climate Dynamics, 23, 803–813, https://doi.org/10.1007/s00382-004-0462-5, 2004.

Frezzotti, M., Pourchet, M., Flora, O., Gandolfi, S., Gay, M., Urbini, S., Vincent, C., Becagli, S., Gragnani, R., and Proposito, M.: Spatial and temporal variability of snow accumulation in East Antarctica from traverse data, Journal of Glaciology, 51, 113–124, https://doi.org/10.3189/172756505781829502, 2005.

Frezzotti, Ma., Capra, A., and Vittuari, L.: Comparison between glacier ice velocities inferred from GPS and sequential satellite images, Annals of Glaciology, 27, 54–60, 1998b.

Fugazza, D., Senese, A., Azzoni, R. S., Maugeri, M., and Diolaiuti, G. A.: Spatial distribution of surface albedo at the Forni Glacier (Stelvio National Park, Central Italian Alps), Cold Regions Science and Technology, 125, 128–137, https://doi.org/10.1016/j.coldregions.2016.02.006, 2016.

Fujii, Y. and Kusunoki, K.: The role of sublimation and condensation in the formation of ice sheet surface at Mizuho Station, Antarctica, Journal of Geophysical Research: Oceans, 87, 4293–4300, 1982.

Fujii, Y., Yamanouchi, T., Suzuki, K., and Tanaka, S.: Comparison of the Surface Conditions of the Inland Ice Sheet, Dronning Maud Land. Antarctica. Derived from Noaa AVHRR Data with Ground Observation, Annals of Glaciology, 9, 72–75, https://doi.org/10.3189/S0260305500000410, 1987.

Fyffe, C. L., Reid, T. D., Brock, B. W., Kirkbride, M. P., Diolaiuti, G., Smiraglia, C., and Diotri, F.: A distributed energy-balance melt model of an alpine debris-covered glacier, Journal of Glaciology, 60, 587–602, https://doi.org/10.3189/2014JoG13J148, 2014.

Gjermundsen, E. F., Mathieu, R., Kääb, A., Chinn, T., Fitzharris, B., and Hagen, J. O.: Assessment of multispectral glacier mapping methods and derivation of glacier area changes, 1978–2002, in the central Southern Alps, New Zealand, from ASTER satellite data, field survey and existing inventory data, J. Glaciol., 57, 667–683, https://doi.org/10.3189/002214311797409749, 2011.

Goodwin, I. D.: Snow accumulation and surface topography in the katabatic zone of Eastern Wilkes Land, Antarctica, Antartic science, 2, 235–242, https://doi.org/10.1017/S0954102090000323, 1990.

Gow, A. J.: On the accumulation and seasonal stratification of snow at the South Pole, Journal of Glaciology, 5, 467–477, 1965.

Grenfell, T. C.: Albedo, Encyclopedia of Snow, Ice and Glaciers, edited by: Singh, V., Singh, P., and Haritahya, U., Springer, the Netherlands, 2011.

Grenfell, T. C., Warren, S. G., and Mullen, P. C.: Reflection of solar radiation by the Antarctic snow surface at ultraviolet, visible, and near-infrared wavelengths, Journal of Geophysical Research: Atmospheres, 99, 18669–18684, 1994.

Greuell, W. and de Ruyter de Wildt, M.: Anisotropic reflection by melting glacier ice: Measurements and parametrizations in Landsat TM bands 2 and 4, Remote Sensing of Environment, 70, 265–277, 1999.

Guglielmin, M.: Ground surface temperature (GST), active layer and permafrost monitoring in continental Antarctica, Permafrost and Periglacial Processes, 17, 133–143, 2006.

Guglielmin, M., Ellis-Evans, C. J., and Cannone, N.: Active layer thermal regime under different vegetation conditions in permafrost areas. A case study at Signy Island (Maritime Antarctica), Geoderma, 144, 73–85, https://doi.org/10.1016/j.geoderma.2007.10.010, 2008.

Hartmann, D. L.: Global Physical Climatology, 2° edizione., Elsevier Science, Amsterdam ; Boston, 498 pp., 2015.

Heid, T. and Kääb, A.: Evaluation of existing image matching methods for deriving glacier surface displacements globally from optical satellite imagery, Remote Sens. Environ., 118, 339–355, 2012.

Hersbach, H., Bell, B., Berrisford, P., Hirahara, S., Horányi, A., Muñoz-Sabater, J., Nicolas, J., Peubey, C., Radu, R., Schepers, D., Simmons, A., Soci, C., Abdalla, S., Abellan, X., Balsamo, G., Bechtold, P., Biavati, G., Bidlot, J., Bonavita, M., Chiara, G., Dahlgren, P., Dee, D., Diamantakis, M., Dragani, R., Flemming, J., Forbes, R., Fuentes, M., Geer, A., Haimberger, L., Healy, S., Hogan, R. J., Hólm, E., Janisková, M., Keeley, S., Laloyaux, P., Lopez, P., Lupu, C., Radnoti, G., Rosnay, P., Rozum, I., Vamborg, F., Villaume, S., and Thépaut, J.: The ERA5 Global Reanalysis, Q J R Meteorol Soc, qj.3803, https://doi.org/10.1002/qj.3803, 2020.

Howat, I. M., Negrete, A., and Smith, B. E.: The Greenland Ice Mapping Project (GIMP) land classification and surface elevation data sets, The Cryosphere, 8, 1509–1518, https://doi.org/10.5194/tc-8-1509-2014, 2014.

Howat, I. M., Porter, C., Smith, B. E., Noh, M.-J., and Morin, P.: The Reference Elevation Model of Antarctica, The Cryosphere, 13, 665–674, https://doi.org/10.5194/tc-13-665-2019, 2019.

Hui, F., Ci, T., Cheng, X., Scambos, T. A., Liu, Y., Zhang, Y., Chi, Z., Huang, H., Wang, X., and Wang, F.: Mapping blue-ice areas in Antarctica using ETM+ and MODIS data, Annals of Glaciology, 55, 129–137, 2014.

Jakobs, C. L., Reijmer, C. H., Smeets, C. J. P. P., Trusel, L. D., van de Berg, W. J., van den Broeke, M. R., and van Wessem, J. M.: A benchmark dataset of in situ Antarctic surface melt rates and energy balance, J. Glaciol., 66, 291–302, https://doi.org/10.1017/jog.2020.6, 2020.

Järvinen, O., Mattila, O.-P., Sinisalo, A., and Leppäranta, M.: Snow Research in the Dronning Maud Land within the Finnish Antarctic Research Program in 1989-2014., Geophysica, 50, 2014.

Joughin, I., Tulaczyk, S., Bindschadler, R., and Price, S. F.: Changes in West Antarctic ice stream velocities: observation and analysis, Journal of Geophysical Research: Solid Earth, 107, EPM-3, 2002.

Juckes, L. M.: The geology of north-eastern Heimefrontfjella, Dronning Maud Land, British Antarctic Survey, 1972.

Kaser, G., Fountin, A., and Jansson, P.: A manual for monitoring the mass balance of mountain glaciers, UNESCO-IHP, Paris, 2003.

King, J. C. and Turner, J.: Antarctic meteorology and climatology, Polar Record, 34, 256–257, https://doi.org/10.1017/S0032247400025754, 1998.

Klok, E. L., Greuell, W., and Oerlemans, J.: Temporal and spatial variation of the surface albedo of Morteratschgletscher, Switzerland, as derived from 12 Landsat images, Journal of Glaciology, 49, 491–502, https://doi.org/10.3189/172756503781830395, 2003.

Knap, W. H., Reijmer, C. H., and Oerlemans, J.: Narrowband to broadband conversion of Landsat TM glacier albedos, International Journal of Remote Sensing, 20, 2091–2110, 1999.

Kodama, Y., Wendler, G., and Gosink, J.: The effect of blowing snow on katabatic winds in Antarctica, Annals of Glaciology, 6, 59–62, https://doi.org/10.3189/1985AoG6-1-59-62, 1985.

Konrad, H., Shepherd, A., Gilbert, L., Hogg, A. E., McMillan, M., Muir, A., and Slater, T.: Net retreat of Antarctic glacier grounding lines, Nature Geoscience, 11, 258–262, 2018.

Korona, J., Berthier, E., Bernard, M., Rémy, F., and Thouvenot, E.: SPIRIT. SPOT 5 stereoscopic survey of polar ice: reference images and topographies during the fourth International Polar Year (2007–2009), ISPRS journal of photogrammetry and remote sensing, 64, 204–212, 2009.

Kraaijenbrink, P. D. A., Shea, J. M., Litt, M., Steiner, J. F., Treichler, D., Koch, I., and Immerzeel, W. W.: Mapping Surface Temperatures on a Debris-Covered Glacier With an Unmanned Aerial Vehicle, Frontiers in Earth Science, 6, 2018.

Lenaerts, J. T., Van den Broeke, M. R., Van de Berg, W. J., Van Meijgaard, E., and Kuipers Munneke, P.: A new, high-resolution surface mass balance map of Antarctica (1979–2010) based on regional atmospheric climate modeling, Geophysical Research Letters, 39, 2012.

Lenaerts, J. T., Medley, B., van den Broeke, M. R., and Wouters, B.: Observing and modeling ice sheet surface mass balance, Reviews of Geophysics, 57, 376–420, 2019.

Liang, S.: Narrowband to broadband conversions of land surface albedo I: Algorithms, Remote sensing of environment, 76, 213–238, https://doi.org/10.1016/S0034-4257(00)00205-4, 2001.

Markov, A., Polyakov, S., Sun, B., Lukin, V., Popov, S., Yang, H., Zhang, T., Cui, X., Guo, J., Cui, P., Zhang, L., Greenbaum, J., Mirakin, A., Voyevodin, A., Boronina, A., Sukhanova, A., Deshovykh, G., Krekhov, A., Zarin, S., Semyonov, A., Soshchenko, V., and Mel'nik, A.: The conditions of the formation and existence of "Blue Ice Areas" in the ice flow transition region from the Antarctic ice sheet to the Amery Ice Shelf in the Larsemann Hills area, Polar Science, 22, 100478, https://doi.org/10.1016/j.polar.2019.08.004, 2019.

Mather, K. B.: Further observations on sastrugi, snow dunes and the pattern of surface winds in Antarctica, Polar Record, 11, 158–171, https://doi.org/10.1017/S0032247400052888, 1962.

Matsuoka, K., Skoglund, A., Roth, G., de Pomereu, J., Griffiths, H., Headland, R., Herried, B., Katsumata, K., Le Brocq, A., Licht, K., Morgan, F., Neff, P. D., Ritz, C., Scheinert, M., Tamura, T., Van de Putte, A., van den Broeke, M., von Deschwanden, A., Deschamps-Berger, C., Van Liefferinge, B., Tronstad, S., and Melvær, Y.: Quantarctica, an integrated mapping environment for Antarctica, the Southern Ocean, and sub-Antarctic islands, Environmental Modelling & Software, 140, 105015, https://doi.org/10.1016/j.envsoft.2021.105015, 2021.

Meredith, M., Sommerkorn, M., Cassotta, S., Derksen, C., Ekaykin, A., Hollowed, A., Kofinas, G., Mackintosh, A., Melbourne-Thomas, J., and Muelbert, M. M. C.: Polar Regions. Chapter 3, IPCC Special Report on the Ocean and Cryosphere in a Changing Climate, 2019.

Messerli, A. and Grinsted, A.: Image georectification and feature tracking toolbox: ImGRAFT, Geoscientific Instrumentation, Methods and Data Systems, 4, 23–34, 2015.

Mihalcea, C., Mayer, C., Diolaiuti, G., D'Agata, C., Smiraglia, C., Lambrecht, A., Vuillermoz, E., and Tartari, G.: Spatial distribution of debris thickness and melting from remote-sensing and meteorological data, at debris-covered Baltoro glacier, Karakoram, Pakistan, Annals of Glaciology, 48, 49–57, https://doi.org/10.3189/172756408784700680, 2008a.

Mihalcea, C., Brock, B. W., Diolaiuti, G., D'Agata, C., Citterio, M., Kirkbride, M. P., Cutler, M. E. J., and Smiraglia, C.: Using ASTER satellite and ground-based surface temperature measurements to derive supraglacial debris cover and thickness patterns on Miage Glacier (Mont Blanc Massif, Italy), Cold Regions Science and Technology, 52, 341–354, https://doi.org/10.1016/j.coldregions.2007.03.004, 2008b.

Minora, U., Senese, A., Bocchiola, D., Soncini, A., D'agata, C., Ambrosini, R., Mayer, C., Lambrecht, A., Vuillermoz, E., Smiraglia, C., and Diolaiuti, G.: A simple model to evaluate ice melt over the ablation area of glaciers in the Central Karakoram National Park, Pakistan, Ann. Glaciol., 56, 202–216, https://doi.org/10.3189/2015AoG70A206, 2015.

Müller, F. and Keeler, C. M.: Errors in Short-Term Ablation Measurements on Melting Ice Surfaces, Journal of Glaciology, 8, 91–105, https://doi.org/10.3189/S0022143000020785, 1969.

Naegeli, K., Damm, A., Huss, M., Wulf, H., Schaepman, M., and Hoelzle, M.: Cross-Comparison of Albedo Products for Glacier Surfaces Derived from Airborne and Satellite (Sentinel-2 and Landsat 8) Optical Data, Remote Sensing, 9, 110, https://doi.org/10.3390/rs9020110, 2017.

Nakawo, M. and Young, G. J.: Field Experiments to Determine the Effect of a Debris Layer on Ablation of Glacier Ice, Annals of Glaciology, 2, 85–91, https://doi.org/10.3189/172756481794352432, 1981.

Neumann, T. A., Waddington, E. D., Steig, E. J., and Grootes, P. M.: Non-climate influences on stable isotopes at Taylor Mouth, Antarctica, Journal of Glaciology, 51, 248–258, 2005.

Nicholson, L. and Benn, D. I.: Calculating ice melt beneath a debris layer using meteorological data, Journal of Glaciology, 52, 463–470, https://doi.org/10.3189/172756506781828584, 2006.

Nicholson, L. and Benn, D. I.: Properties of natural supraglacial debris in relation to modelling sub-debris ice ablation, Earth Surface Processes and Landforms, 38, 490–501, https://doi.org/10.1002/esp.3299, 2013.

Núñez-González, F. and Martín-Vide, J. P.: Analysis of antidune migration direction, Journal of Geophysical Research: Earth Surface, 116, https://doi.org/10.1029/2010JF001761, 2011.

Orheim, O. and Lucchitta, B.: Investigating climate change by digital analysis of blue ice extent on satellite images of Antarctica, Annals of Glaciology, 14, 211–215, 1990.

Osterkamp, T. E.: Establishing long-term permafrost observatories for active-layer and permafrost investigations in Alaska: 1977–2002, Permafrost and Periglacial Processes, 14, 331–342, https://doi.org/10.1002/ppp.464, 2003.

Palm, S. P., Yang, Y., Spinhirne, J. D., and Marshak, A.: Satellite remote sensing of blowing snow properties over Antarctica, J. Geophys. Res., 116, D16123, https://doi.org/10.1029/2011JD015828, 2011.

Palm, S. P., Kayetha, V., Yang, Y., and Pauly, R.: Blowing snow sublimation and transport over Antarctica from 11 years of CALIPSO observations, The Cryosphere, 11, 2555–2569, https://doi.org/10.5194/tc-11-2555-2017, 2017.

Parish, T. R. and Bromwich, D. H.: The surface windfield over the Antarctic ice sheets, Nature, 328, 51–54, https://doi.org/10.1038/328051a0, 1987.

Parish, T. R. and Bromwich, D. H.: Continental-scale simulation of the Antarctic katabatic wind regime, Journal of Climate, 4, 135–146, https://doi.org/10.1175/1520-0442(1991)004<0135:CSSOTA>2.0.CO;2, 1991.

Phillpot, H. R. and Zillman, J. W.: The surface temperature inversion over the Antarctic continent, Journal of Geophysical Research, 75, 4161–4169, 1970.

Proposito, M., Becagli, S., Castellano, E., Flora, O., Genoni, L., Gragnani, R., Stenni, B., Traversi, R., Udisti, R., and Frezzotti, M.: Chemical and isotopic snow variability along the 1998 ITASE

traverse from Terra Nova Bay to Dome C, East Antarctica, Annals of Glaciology, 35, 187–194, https://doi.org/10.3189/172756402781817167, 2002.

Prothero, D. R. and Schwab, F.: Sedimentary geology, Macmillan, 2004.

Quincey, D. J., Copland, L., Mayer, C., Bishop, M., Luckman, A., and Belò, M.: Ice velocity and climate variations for Baltoro Glacier, Pakistan, Journal of Glaciology, 55, 1061–1071, 2009.

Ragettli, S., Pellicciotti, F., Immerzeel, W. W., Miles, E. S., Petersen, L., Heynen, M., Shea, J. M., Stumm, D., Joshi, S., and Shrestha, A.: Unraveling the hydrology of a Himalayan catchment through integration of high resolution in situ data and remote sensing with an advanced simulation model, Advances in Water Resources, 78, 94–111, https://doi.org/10.1016/j.advwatres.2015.01.013, 2015.

Rasmus, K.: Field measurements of the total and spectral albedo of snow and ice in Dronning Maud Land, Antarctica, Geophysica, 42, 17–34, 2006.

Reijmer, C. H., Bintanja, R., and Greuell, W.: Surface albedo measurements over snow and blue ice in thematic mapper bands 2 and 4 in Dronning Maud Land, Antarctica, Journal of Geophysical Research: Atmospheres, 106, 9661–9672, 2001.

Ren, S., Miles, E., Jia, L., Menenti, M., Kneib, M., Buri, P., McCarthy, M., Shaw, T., Yang, W., and Pellicciotti, F.: Anisotropy Parameterization Development and Evaluation for Glacier Surface Albedo Retrieval from Satellite Observations, Remote Sensing, 13, 1714, https://doi.org/10.3390/rs13091714, 2021.

Rignot, E., Casassa, G., Gogineni, P., Krabill, W., Rivera, A. U., and Thomas, R.: Accelerated ice discharge from the Antarctic Peninsula following the collapse of Larsen B ice shelf, Geophysical research letters, 31, 2004.

Rignot, E., Mouginot, J., and Scheuchl, B.: Ice flow of the Antarctic ice sheet, Science, 333, 1427–1430, 2011.

Rignot, E., Mouginot, J., Morlighem, M., Seroussi, H., and Scheuchl, B.: Widespread, rapid grounding line retreat of Pine Island, Thwaites, Smith, and Kohler glaciers, West Antarctica, from 1992 to 2011, Geophysical Research Letters, 41, 3502–3509, 2014.

Rignot, E., Mouginot, J., and Scheuchl, B.: MEaSUREs InSAR-based Antarctica ice velocity map, version 2, Boulder, CO: NASA DAAC at the National Snow and Ice Data Center, 2017.

Rounce, D. R. and McKinney, D. C.: Debris thickness of glaciers in the Everest area (Nepal Himalaya) derived from satellite imagery using a nonlinear energy balance model, The Cryosphere, 8, 1317–1329, https://doi.org/10.5194/tc-8-1317-2014, 2014.

Rounce, D. R., King, O., McCarthy, M., Shean, D. E., and Salerno, F.: Quantifying Debris Thickness of Debris-Covered Glaciers in the Everest Region of Nepal Through Inversion of a Subdebris Melt Model, Journal of Geophysical Research: Earth Surface, 123, 1094–1115, https://doi.org/10.1029/2017JF004395, 2018.

Rounce, D. R., Hock, R., McNabb, R. W., Millan, R., Sommer, C., Braun, M. H., Malz, P., Maussion, F., Mouginot, J., Seehaus, T. C., and Shean, D. E.: Distributed Global Debris Thickness Estimates Reveal Debris Significantly Impacts Glacier Mass Balance, Geophysical Research Letters, 48, e2020GL091311, https://doi.org/10.1029/2020GL091311, 2021.

Rozenstein, O., Qin, Z., Derimian, Y., and Karnieli, A.: Derivation of Land Surface Temperature for Landsat-8 TIRS Using a Split Window Algorithm, Sensors, 14, 5768–5780, https://doi.org/10.3390/s140405768, 2014.

Scambos, T. A. and Haran, T.: An image-enhanced DEM of the Greenland ice sheet, Annals of Glaciology, 34, 291–298, 2002.

Scambos, T. A., Dutkiewicz, M. J., Wilson, J. C., and Bindschadler, R. A.: Application of image cross-correlation to the measurement of glacier velocity using satellite image data, Remote Sensing of Environment, 42, 177–186, https://doi.org/10.1016/0034-4257(92)90101-O, 1992.

Scambos, T. A., Bohlander, J. A., Shuman, C. A., and Skvarca, P.: Glacier acceleration and thinning after ice shelf collapse in the Larsen B embayment, Antarctica, Geophysical Research Letters, 31, 2004.

Scambos, T. A., Frezzotti, M., Haran, T., Bohlander, J., Lenaerts, J. T. M., Van Den Broeke, M. R., Jezek, K., Long, D., Urbini, S., Farness, K., Neumann, T., Albert, M., and Winther, J.-G.: Extent of low-accumulation “wind glaze” areas on the East Antarctic plateau: implications for continental ice mass balance, J. Glaciol., 58, 633–647, https://doi.org/10.3189/2012JoG11J232, 2012.

Scarchilli, C., Frezzotti, M., Grigioni, P., De Silvestri, L., Agnoletto, L., and Dolci, S.: Extraordinary blowing snow transport events in East Antarctica, Climate Dynamics, 34, 1195–1206, 2010.

Schaaf, C. L. B., Liu, J., Gao, F., and Strahler, A. H.: MODIS albedo and reflectance anisotropy products from Aqua and Terra, Land Remote Sensing and Global Environmental Change: NASA's Earth Observing System and the Science of ASTER and MODIS, 11, 549–561, 2011.

Schaepman-Strub, G., Schaepman, M. E., Painter, T. H., Dangel, S., and Martonchik, J. V.: Reflectance quantities in optical remote sensing—Definitions and case studies, Remote sensing of environment, 103, 27–42, https://doi.org/10.1016/j.rse.2006.03.002, 2006.

Schauwecker, S., Rohrer, M., Huggel, C., Kulkarni, A., Ramanathan, A., Salzmann, N., Stoffel, M., and Brock, B.: Remotely sensed debris thickness mapping of Bara Shigri Glacier, Indian Himalaya, Journal of Glaciology, 61, 675–688, https://doi.org/10.3189/2015JoG14J102, 2015.

Scott, R. F.: Scott's Last Expedition...: Vol. I. Being the Journals of Captain RF Scott, RN, CVO Vol II., Being the Reports of the Journeys and the Scientific Work Undertaken by Dr. EA Wilson and the Surviving Members of the Expedition, Arranged by Leonard Huxley, Dodd, Mead, 1913.

Senese, A., Diolaiuti, G., Mihalcea, C., and Smiraglia, C.: Energy and Mass Balance of Forni Glacier (Stelvio National Park, Italian Alps) from a Four-Year Meteorological Data Record, Arctic, Antarctic, and Alpine Research, 44, 122–134, https://doi.org/10.1657/1938-4246-44.1.122, 2012.

Senese, A., Maugeri, M., Ferrari, S., Confortola, G., Soncini, A., Bocchiola, D., and Diolaiuti, G. A.: Modelling shortwave and longwave downward radiation and air temperature driving ablation at the Forni glacier (Stelvio National Park, Italy), Geografia Fisica e Dinamica Quaternaria, 39, 89–100, 2016.

Senese, A., Maugeri, M., Meraldi, E., Verza, G. P., Azzoni, R. S., Compostella, C., and Diolaiuti, G.: Estimating the snow water equivalent on a glacierized high elevation site (Forni Glacier, Italy), The Cryosphere, 12, 1293–1306, https://doi.org/10.5194/tc-12-1293-2018, 2018.

Senese, A., Manara, V., Maugeri, M., and Diolaiuti, G. A.: Comparing Measured Incoming Shortwave and Longwave Radiation on a Glacier Surface with Estimated Records from Satellite and Off-Glacier Observations: A Case Study for the Forni Glacier, Italy, Remote Sensing, 12, 3719, https://doi.org/10.3390/rs12223719, 2020.

Senese, A., Leidi, M., and Diolaiuti, G. A.: A new enhanced temperature index model including net solar and infrared radiation, Geografia Fisica e Dinamica Quaternaria, 44, 3–12, 2021.

Shepherd, A., Wingham, D. J., and Mansley, J. A.: Inland thinning of the Amundsen Sea sector, West Antarctica, Geophysical Research Letters, 29, 2–1, 2002.

Shepherd, A., Wingham, D., Wallis, D., Giles, K., Laxon, S., and Sundal, A. V.: Recent loss of floating ice and the consequent sea level contribution, Geophysical Research Letters, 37, 2010.

Shepherd, A., Ivins, E., Rignot, E., Smith, B., van den Broeke, M., Velicogna, I., Whitehouse, P., Briggs, K., Joughin, I., Krinner, G., Nowicki, S., Payne, T., Scambos, T., Schlegel, N., A, G., Agosta, C., Ahlstrøm, A., Babonis, G., Barletta, V., Blazquez, A., Bonin, J., Csatho, B., Cullather, R., Felikson, D., Fettweis, X., Forsberg, R., Gallee, H., Gardner, A., Gilbert, L., Groh, A., Gunter, B., Hanna, E., Harig, C., Helm, V., Horvath, A., Horwath, M., Khan, S., Kjeldsen, K. K., Konrad, H., Langen, P., Lecavalier, B., Loomis, B., Luthcke, S., McMillan, M., Melini, D., Mernild, S., Mohajerani, Y., Moore, P., Mouginot, J., Moyano, G., Muir, A., Nagler, T., Nield, G., Nilsson, J., Noel, B., Otosaka, I., Pattle, M. E., Peltier, W. R., Pie, N., Rietbroek, R., Rott, H., Sandberg-Sørensen, L., Sasgen, I., Save, H., Scheuchl, B., Schrama, E., Schröder, L., Seo, K.-W., Simonsen, S., Slater, T., Spada, G., Sutterley, T., Talpe, M., Tarasov, L., van de Berg, W. J., van der Wal, W., van Wessem, M., Vishwakarma, B. D., Wiese, D., Wouters, B., and The IMBIE team: Mass balance of the Antarctic Ice Sheet from 1992 to 2017, Nature, 558, 219–222, https://doi.org/10.1038/s41586-018-0179-y, 2018.

Shuai, Y., Masek, J. G., Gao, F., and Schaaf, C. B.: An algorithm for the retrieval of 30-m snow-free albedo from Landsat surface reflectance and MODIS BRDF, Remote Sensing of Environment, 115, 2204–2216, https://doi.org/10.1016/j.rse.2011.04.019, 2011.

Spergel, J. J., Kingslake, J., Creyts, T., van Wessem, M., and Fricker, H. A.: Surface meltwater drainage and ponding on Amery Ice Shelf, East Antarctica, 1973–2019, J. Glaciol., 1–14, https://doi.org/10.1017/jog.2021.46, 2021.

Swithinbank, C.: Antarctica, US Government Printing Office, 1988.

Takahashi, S., Endoh, T., Azuma, N., and Meshida, S.: Bare ice fields developed in the inland part of Antarctica, Proceedings of the NIPR Symposium on Polar Meteorology and Glaciology, 5, 128–139, 1992.

Tarca, G. and Guglielmin, M.: Using ground-based thermography to analyse surface temperature distribution and estimate debris thickness on Gran Zebrù glacier (Ortles-Cevedale, Italy), Cold Regions Science and Technology, 196, 103487, https://doi.org/10.1016/j.coldregions.2022.103487, 2022.

Tuckett, P. A., Ely, J. C., Sole, A. J., Lea, J. M., Livingstone, S. J., Jones, J. M., and van Wessem, J. M.: Automated mapping of the seasonal evolution of surface meltwater and its links to climate on the Amery Ice Shelf, Antarctica, The Cryosphere, 15, 5785–5804, https://doi.org/10.5194/tc-15-5785-2021, 2021.

Van As, D., Ahlstrøm, A. P., Andersen, M. L., Citterio, M., Edelvang, K., Gravesen, P., Machguth, H., and Nick, F. M.: Programme for Monitoring of the Greenland Ice Sheet (PROMICE): first temperature and ablation records, Geological Survey of Denmark and Greenland Bulletin, 23, 73–76, 2011.

Van Wessem, J. M., Reijmer, C. H., Morlighem, M., Mouginot, J., Rignot, E., Medley, B., Joughin, I., Wouters, B., Depoorter, M. A., Bamber, J. L., Lenaerts, J. T. M., Van De Berg, W. J., Van Den Broeke, M. R., and Van Meijgaard, E.: Improved representation of East Antarctic surface mass balance in a regional atmospheric climate model, J. Glaciol., 60, 761–770, https://doi.org/10.3189/2014JoG14J051, 2014a.

Van Wessem, J. M., Reijmer, C. H., Lenaerts, J. T. M., Van de Berg, W. J., Van den Broeke, M. R., and Van Meijgaard, E.: Updated cloud physics in a regional atmospheric climate model improves the modelled surface energy balance of Antarctica, The Cryosphere, 8, 125–135, 2014b.

Van Wyk de Vries, M. and Wickert, A. D.: Glacier Image Velocimetry: an open-source toolbox for easy and rapid calculation of high-resolution glacier velocity fields, The Cryosphere, 15, 2115–2132, https://doi.org/10.5194/tc-15-2115-2021, 2021.

Vaughan, D. G., Bamber, J. L., Giovinetto, M., Russell, J., and Cooper, A. P. R.: Reassessment of net surface mass balance in Antarctica, Journal of climate, 12, 933–946, 1999.

Vermote, E. F., Tanré, D., Deuze, J. L., Herman, M., and Morcette, J.-J.: Second simulation of the satellite signal in the solar spectrum, 6S: An overview, IEEE transactions on geoscience and remote sensing, 35, 675–686, https://doi.org/10.1109/36.581987, 1997.

Vittuari, L., Vincent, C., Frezzotti, M., Mancini, F., Gandolfi, S., Bitelli, G., and Capra, A.: Space geodesy as a tool for measuring ice surface velocity in the Dome C region and along the ITASE traverse, Annals of Glaciology, 39, 402–408, https://doi.org/10.3189/172756404781814627, 2004.

Wang, J., Ye, B., Cui, Y., He, X., and Yang, G.: Spatial and temporal variations of albedo on nine glaciers in western China from 2000 to 2011, Hydrological Processes, 28, 3454–3465, https://doi.org/10.1002/hyp.9883, 2014.

Watanabe, O.: Distribution of surface features of snow cover in Mizuho Plateau, http://id.nii.ac.jp/1291/00000854/, 1978.

Wendler, G., André, J. C., Pettré, P., Gosink, J., and Parish, T.: Katabatic winds in Adélie coast, Antarctic meteorology and climatology: studies based on automatic weather stations, 61, 23–46, https://doi.org/10.1029/AR061p0023, 1993.

van Wessem, J. M., van de Berg, W. J., Noël, B. P. Y., van Meijgaard, E., Amory, C., Birnbaum, G., Jakobs, C. L., Krüger, K., Lenaerts, J. T. M., Lhermitte, S., Ligtenberg, S. R. M., Medley, B., Reijmer, C. H., van Tricht, K., Trusel, L. D., van Ulft, L. H., Wouters, B., Wuite, J., and van den Broeke, M. R.: Modelling the climate and surface mass balance of polar ice sheets using RACMO2 – Part 2: Antarctica (1979–2016), The Cryosphere, 12, 1479–1498, https://doi.org/10.5194/tc-12-1479-2018, 2018.

Winther, J.-G., Jespersen, M. N., and Liston, G. E.: Blue-ice areas in Antarctica derived from NOAA AVHRR satellite data, J. Glaciol., 47, 325–334, https://doi.org/10.3189/172756501781832386, 2001.

Worsfold, R. J.: Physiography and glacial geomorphology of Heimefrontfjella, Dronning Maud Land, British Antarctic Survey Bulletin, 11, 49–57, 1967.

Yoshida, M., OMOTO, K., NARUSE, R., and AGETA, Y.: Discovery of meteorites near Yamato mountains, east Antarctica, 南極資料, 39, 62–65, 1971.

Yu, J., Liu, H., Wang, L., Jezek, K. C., and Heo, J.: Blue ice areas and their topographical properties in the Lambert glacier, Amery Iceshelf system using Landsat ETM+, ICESat laser altimetry and ASTER GDEM data, Antarctic Science, 24, 95–110, https://doi.org/10.1017/S0954102011000630, 2012.

Zanter, K.: Landsat 8 (L8) data users handbook, Landsat Science Official Website, 2019.

Zhang, T., Stamnes, K., and Bowling, S. A.: Impact of Clouds on Surface Radiative Fluxes and Snowmelt in the Arctic and Subarctic, Journal of Climate, 9, 2110–2123, https://doi.org/10.1175/1520-0442(1996)009<2110:IOCOSR>2.0.CO;2, 1996.

Chapter 3: Albedo

3.1 Presentation of the chapter

Given the importance of albedo as a key meteorological parameter, its relevance for the energy balance and in the present study as an important proxy for the definition and identification of ablation areas in Antarctica, the first part of the PhD thesis was dedicated in finding and validating a new methodology able to accurately calculate albedo from remote sensing data. This was possible by starting from existing methodologies, which however have not been deeply investigated on the ice sheets. For this reason, taking advantage of a consistent dataset of satellite and in-situ measurements, an initial evaluation of each step of correction from radiance to albedo, passing by reflectance, was carried out. These analyses are part of an article and a short note, focused respectively on ***i*** radiometric calibration, atmospheric correction, topographic correction, and conversion from narrowband to broadband albedo and ***ii*** anisotropic correction. The two publications are: "Traversa, G., Fugazza, D., Senese, A., & Frezzotti, M. (2021). Landsat 8 OLI broadband albedo validation in Antarctica and Greenland. Remote Sensing, 13(4), 799, doi: 10.3390/rs13040799" (Section 3.2) and "Traversa, G., & Fugazza, D. (2021). Evaluation of Anisotropic Correction Factors for the Calculation of Landsat 8 Oli Albedo on the Ice Sheets. Geografia Fisica E Dinamica Quaternaria, 44(1), 91-95, doi: 10.4461/GFDQ.2021.44.8" (Section 3.3).

3.2 Article "Landsat 8 OLI Broadband Albedo Validation in Antarctica and Greenland" (Traversa et al., 2021a)

Giacomo Traversa [1,2], Davide Fugazza [2,*], Antonella Senese [2] and Massimo Frezzotti [3]

[1] Department of Physical Sciences, Earth and Environment (DSFTA), Università Degli Studi Di Siena, 53100 Siena, Italy; giacomo.traversa@student.unisi.it

[2] Department of Environmental Science and Policy (ESP), Università Degli Studi Di Milano, 20133 Milan, Italy; antonella.senese@unimi.it

[3] Department of Science, Università Degli Studi Roma Tre, 00146 Rome, Italy; massimo.frezzotti@uniroma3.it

* Correspondence: davide.fugazza@unimi.it; Tel.: +39-(02)-5031-5566

Abstract: The albedo is a fundamental component of the processes that govern the energy budget, and particularly important in the context of climate change. However, a satellite-based high-resolution (30 m) albedo product which can be used in the polar regions up to 82.5◦ latitude during the summer seasons is lacking. To cover this gap, in this study we calculate satellite-based broadband albedo from Landsat 8 OLI and validate it against broadband albedo measurements from in situ stations located on the Antarctic and Greenland icesheets. The model to derive the albedo from raw satellite data includes an atmospheric and topographic correction and conversion from narrow-band to broadband albedo, and at each step different options were taken into account, in order to provide the best combination of corrections. Results, after being cleaned from anomalous data, show a good agreement with in situ albedo measurements, with a mean absolute error between in situ and satellite albedo of 0.021, a root mean square error of 0.026, a standard deviation of 0.015, a correlation coefficient of 0.995 ($p < 0.01$) and a bias estimate of −0.005. Considering the structure of the model, it could be applied to data from previous sensors of the Landsat family and help construct a record to analyze albedo variations in the polar regions.

1. Introduction

The albedo has a relevant role in the energy budget studies above all at the Poles, where it is generally high owing to the large fraction of surface area covered with snow and ice. Variations from these high albedo values could deeply affect the surface mass balance, leading to serious consequences, considering that the Antarctic and Greenland ice sheets have a crucial role on sea level control. The albedo (α), also called bi-hemispherical reflectance, is defined as the ratio of the radiant flux reflected from a unit surface area into the whole hemisphere to the incident radiant flux of hemispherical angular extent [1] in the approximate spectral range 350–3000 nm [2]. On the ice sheets, it depends on different factors, i.e., snow metamorphism, including changes in the size and shape of snow grains [3–7], snow density and stratification, the occurrence of various surface morphologies owing to strong and persistent winds (e.g., sastrugi, snow dunes and wind glaze areas), or the presence of blue ice [8–10]. In turn, the rate of snow metamorphism is influenced by temperature, relative humidity and wind [11–13]. Historically, the albedo has been acquired, especially on the ice sheets and ice shelves, by

instruments mounted on automatic weather stations (AWSs), that record measures of albedo at a hourly or subhourly temporal resolution [14–18]. However, while the surface covered by these punctual records can approximate a Landsat satellite pixel [19], it cannot be considered representative of a large area, i.e., an entire glacier or ice sheet [20]. Alternatively, during field campaigns, distributed measurements can be acquired by using portable radiometers [21,22]. However, many of these instruments would be required to cover such a wide area as a glacier, more so an ice sheet. In this context, remote sensing acquires relevance. NASA already provides a series of albedo products obtained by combining observations from the Moderate Resolution Imaging Spectroradiometer (MODIS) sensors on board the Terra and Aqua satellites. MODIS was used in the past to study the ice sheets, both in Greenland [23–25] and in Antarctica [6,26,27], but its spatial resolution is too coarse (i.e., at most, 500 m) to satisfactorily represent albedo variability of local features of the ice sheet (e.g., blue ice, wind glaze zones). The Landsat family of satellites provides data at a higher resolution (30 m) and thus allows researchers to study the ice sheet surfaces in finer detail. Many albedo models based on Landsat data exist [19,28–33], but none of them has been thoroughly tested on the ice sheets. For these reasons, the purpose of our study is to provide a model to derive broadband albedo of ice and snow-covered surfaces from satellite data at a high spatial resolution (i.e., 30 m), and validate it against ground observations from in situ stations located on the ice sheets, in order to support future ice sheet studies. In our research, we start from the model proposed by Klok et al. (2003) [29] and recently adjusted by Fugazza et al. (2016) [19]. The model includes several correction steps to derive albedo from the raw satellite data, and at each step we evaluate different possible inputs and parameters to provide the most suitable set of corrections. We take advantage from data acquired by the Landsat 8 OLI sensor, available from 2013 for latitudes up to ±82.5◦. The entirety of our satellite data was then validated using different available in situ albedo datasets in both Antarctica (IMAU [18] and BSRN [17] datasets) and Greenland (PROMICE AWSs [16]).

2. Materials and Methods

Landsat 8 OLI data for the period 2013–2020 were downloaded from the Landsat Collection 2 dataset from the USGS Earth Explorer website (https://earthexplorer.usgs. gov/ (accessed date 19 February 2021)). The data are preprocessed by USGS to obtain an absolute geolocation accuracy of 12 m, orthorectified using global digital elevation model sources and radiometrically calibrated. The spatial resolution of Landsat 8 image bands is 30 m except for band 8 (panchromatic, 15 m spatial resolution) and the two thermal bands 10–11 (100 m). Bands 2, 4, 5, 6, 7 (i.e., blue, red, near-infrared and shortwave-infrared) were used to comply with Liang's broadband albedo algorithm [34] while Band 3 was used for the evaluation of another broadband albedo model [35]. In each case, we used only

those satellite images where cloud cover was absent or low (<10%), that covered the in situ station and corresponded by date and time with ground observations (in situ stations report hourly data). Cloud cover is reported in the Landsat metadata, as determined by the CFMask (C code of the function of mask) algorithm [36]. However, since CFMask may be inaccurate over bright targets such as snow, an additional visual check for each analyzed image was necessary. Additionally, we excluded coastal scenes where measurements of aerosol optical thickness (AOT) were not available and scenes with exceedingly high values of solar zenith angle (SZA, >80◦). Only polar "spring–summer" periods were considered: October-March in Antarctica and April-August in Greenland. The final dataset includes 86 scenes (53 in Antarctica and 33 in Greenland). To calculate the albedo, we started from other albedo models available in literature and applied in other regions of Earth [19,29,31,32], such as the Alps, and modified them to obtain the best results in the polar regions, for instance by adding a pixel-specific correction for the SZA. The statistics used to validate satellite albedo against AWS observations were the mean absolute error (MAE), the standard deviation (STD), the root–mean–square Error (RMSE), the bias-removed root–mean–square error (BRRMSE), the bias estimate (BE) [22] and the correlation coefficient (Cc), where the last one is defined as follows:

$$Cc = \frac{\sum(x-\bar{x})(y-\bar{y})}{\sqrt{\sum(x-\bar{x})^2 \sum(y-\bar{y})^2}} \quad (1)$$

where *x* and *y* are the first and the second sets of measurements and *x* and *y* their averages. As concerns the BE, it is calculated as:

$$BE = \frac{1}{N}\sum(y-x) \quad (2)$$

where *N* is defined as the sample size. The MAE is estimated as:

$$MAE = \frac{1}{N}\sum|y-x| \quad (3)$$

The RMSE is described as:

$$RMSE = \left[\frac{1}{N}\sum(y-x)^2\right]^{0.5} \quad (4)$$

and the BRRMSE as:

$$BRRMSE = \left[\frac{1}{N}\sum(y-x-BE)^2\right]^{0.5} \quad (5)$$

The first part of this section describes the steps followed to process the original satellite images to obtain albedo: radiometric calibration, zenith, atmospheric and topographic corrections, and narrowband to broadband conversion. While other studies [19,32,33] have also employed bidirectional reflectance distribution functions (BRDF) to correct for the anisotropic reflectance of snow/ice surfaces under varying illumination conditions, we omit this step because of the lack of a

directly applicable method to include BRDF corrections for such high albedo and SZA as are normally found on the icesheets. At each step of the process to derive albedo from satellite data, different variants of the same corrections were proposed, in order to obtain the combination of corrections that provides the lowest statistical errors and highest correlation with in situ observations. The complete proposed model, and all the variants for each step, are shown in the workflow in Figure 1.

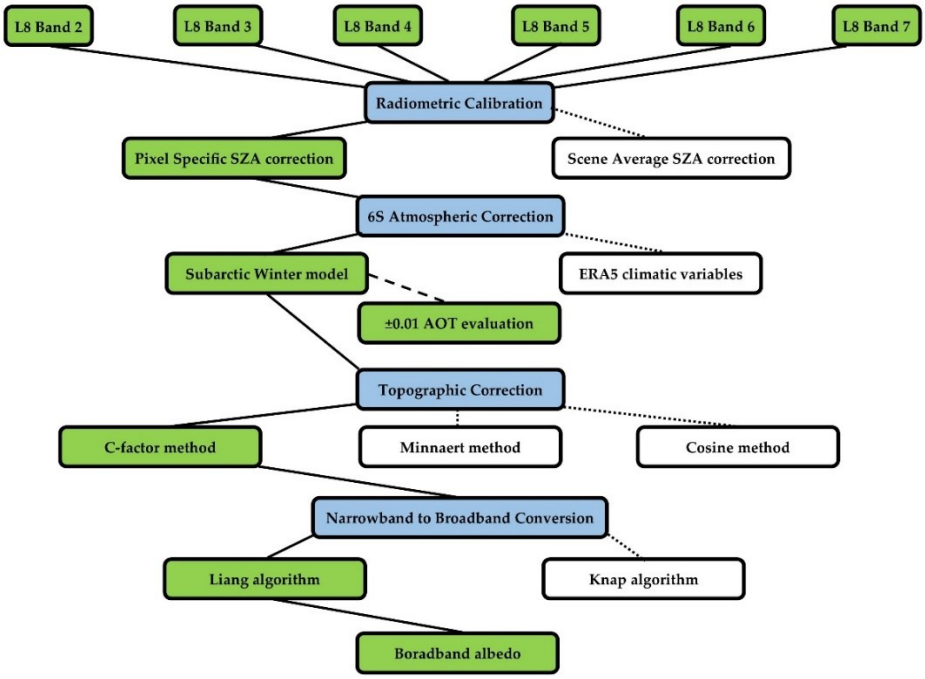

Figure 1. Workflow of albedo calculation through the main 4 steps (blue boxes), with each cor-responding tested variant (best ones in green boxes, others evaluated in white boxes); solid lines stand for best workflow, dotted lines for other tested variants and dashed line for the evaluation of different AOT values.

2.1. Satellite Data Processing

2.1.1. Radiometric Calibration and SZA Correction

In order to be stored and transmitted efficiently, radiance measured by the Landsat sensor is converted to a quantized digital number (DN, dimensionless) and needs to be scaled back to the original value. First, Landsat DNs in each band were converted to top of atmosphere (TOA) reflectance, following the Landsat 8 (L8) Data User Handbook [37] using the rescaling coefficients in the metadata as follows:

$$\rho_\lambda' = M_\rho Q_{cal} + A_\rho \quad (6)$$

where ρ_{λ}' is the TOA planetary reflectance in band λ (without SZA correction), M_{ρ} is the band-specific multiplicative rescaling factor, A_{ρ} the band-specific additive factor from the Metadata file and Q_{cal} is the quantized and calibrated standard product pixel values (DN). Two possible corrections were then evaluated: one using an average SZA correction for each scene, and the other using the SZA band generated from the Angle file of Landsat 8 (scene average SZA). The zenith correction on TOA reflectance is calculated as:

$$\rho_{\lambda} = \frac{\rho_{\lambda}'}{\cos(\theta_{SZA})} = \frac{\rho_{\lambda}'}{\sin(\theta_{SEA})} \quad (7)$$

where ρ_{λ} is the TOA reflectance in band λ with correction for the SZA, θ_{SEA} is the local sun elevation angle in degrees and θ_{SZA} is the local SZA ($\theta_{SZA} = 90° - \theta_{SEA}$) provided either as the average value for the scene (obtained from the metadata) or in the solar zenith band for each single pixel. A pixel-specific correction could be relevant to calculate the albedo in polar regions since the SZA can vary across a Landsat scene (±2◦) and the scene-average SZA might not be sufficient to provide an accurate model of albedo in the study area, especially when SZA is very high (>60°) [38].

2.1.2. Atmospheric Correction

For the retrieval of surface reflectance, we carried out a correction of reflectance for atmospheric interference using the 6S radiative transfer code [39]. This correction was performed using GRASS i.atcorr tool, which provides standard atmospheric profiles, but also accepts user defined values to characterize the atmospheric layer above a given area. The required inputs are: (i) the geometrical conditions, that is the satellite source (in our case Landsat 8 OLI); (ii) date, time and central coordinates (longitude and latitude); (iii) the atmospheric model; (iv) an aerosol model, where we selected the continental one; (v) visibility (km) or aerosol optical thickness (AOT) at 550 nm to estimate attenuation of direct solar irradiance by aerosols. As regards the atmospheric model, we tested two possible models: subarctic winter, which was chosen despite the fact that our scenes only cover the summer period because it best resembles the climatological conditions of the polar areas, and a scene specific model with user-defined values. The inputs for the userdefined model are altitude (m), pressure (hPa), temperature (◦C), H2O and O3 density (g/m3), which were retrieved from the ERA5 [40] atmospheric reanalysis global climate dataset produced by the European Centre for Medium-Range Weather Forecasts (ECMWF). AOT is generally very low for the Antarctic continent, from observations in the AERONET Aerosol Robotic Network datasets (https://aeronet.gsfc.nasa.gov/cgi-bin/draw_map_ display_aod_v3 (accessed date 19 February 2021)),

based on 7 stations distributed across the continent, i.e., Marambio (64.240◦S, 56.625◦W), ARM WAIS (79.471◦S, 112.083◦W), Utsteinen (71.950◦S, 23.333◦E), Vechernaya Hill (67.660◦S, 46.158◦E), Progress (69.378◦S, 76.389◦E), South Pole Obs NOAA (90.000◦S, 70.300◦E) and ARM McMurdo (77.849◦S, 166.730◦E), that provide AOT between the summer seasons 2013–2020. Here, the AOT ranges from 0.01 to 0.03, showing an average of 0.02. This value was used for the entire continent, given the low variability of AOT across Antarctica (both coastal areas and inland) and the absence of other ground stations in the vicinity of the in situ stations and corresponding LANDSAT scenes. Regarding the Greenland Ice Sheet, AOT is more heterogeneous: in the inland, given the lack of available AOT values from aerosol observing networks, we used data from the Modern-Era Retrospective analysis for Research and Applications, Version 2 reanalysis product (MERRA-2, [41]). On the dates analyzed, the AOT from MERRA-2 is on average 0.02, and such value was therefore applied in the inland of Greenland. In the coastal zones, AOT shows a larger variability; thus, we selected AOT measurements from the closest stations from the AERONET network. To test the sensitivity of the albedo model to the chosen AOT values, we compared the albedo obtained with the selected values with two additional runs obtained by adding and subtracting 0.01 to the AOT (e.g., in Antarctica, we provide two comparisons with models retrieved using an AOT of 0.01 or 0.03). Finally, vi) the mean target elevation a.s.l. (km) was derived from the Reference Elevation Model of Antarctica (REMA) Digital Terrain Model (DEM) [42] for Antarctica, resampled to 30 m spatial resolution and the Greenland Ice Mapping Project (GIMP) DEM [43] for the Greenland icesheet, also resampled to 30 m. This correction provides a surface reflectance dataset lacking topographic correction.

2.1.3. Topographic Correction

To compute the topographic correction of surface reflectance, different methods are available in GRASS GIS i.topo.corr tool, and we compared the following ones: c-factor, cosine and Minnaert. The first step is to produce an illumination model, which represents the cosine of the solar incident angle starting from the DEM. The formula is:

$$\cos i = \cos s \cos z + \sin s \sin z \cos(a - o) \quad (8)$$

where: i is the incident angle, s is the terrain slope angle, z is the SZA, a the solar azimuth angle and o the terrain aspect angle. Once the illumination model is calculated, it is possible to apply the topographic correction. The c-factor method is based on the following formula:

$$ref_c = ref_o \frac{\cos z + c}{\cos i + c} \quad (9)$$

where refc is the corrected reflectance, refo is the original reflectance, c is equal to a m^{-1} from

$$ref_o = a + m\cos i \quad (10)$$

In summary, the tool needs a DEM and a value of SZA and solar azimuth angle, which are available from the Landsat metadata. The cosine method is the simplest topographic correction, since it is represented by the following algorithm:

$$ref_c = \frac{ref_o * \cos z}{\cos i} \quad (11)$$

while the Minnaert method is described by:

$$ref_c = ref_o * \left(\frac{\cos z}{\cos i}\right)^k \quad (12)$$

where k is obtained by linear regression of

$$\ln(ref_o) = \ln(ref_c) - k * \ln\left(\frac{\cos i}{\cos z}\right) \quad (13)$$

2.1.4. Narrowband to Broadband Albedo Conversion

The final step concerns the estimation of broadband albedo (α), i.e., the albedo integrated over the entire solar spectrum. In our model, we used Liang albedo algorithm [34], which considers bands 2, 4, 5, 6 and 7 of the Landsat 8 OLI sensor, as suggested also by Naegeli et al. (2017) [32]. The algorithm is:

$$\alpha = 0.356\alpha_2 + 0.130\alpha_4 + 0.373\alpha_5 + 0.085\alpha_6 + 0.072\alpha_7 - 0.0018 \quad (14)$$

where α_x is the specific reflectance (equal to ref_c) of each band (and x the band number). The main advantage of this algorithm is that it considers contribution from a wider range of the spectrum than the others, allowing to capture the albedo changes due to changes in grain size, which have particularly large impact on near-infrared and shortwave infrared wavelengths [44]. We also evaluated the Knap algorithm [35], which is represented by the following equation:

$$\alpha = 0.726\alpha_3 - 0.322\alpha_3^2 - 0.051\alpha_5 + 0.581\alpha_5^2 \quad (15)$$

2.2. In Situ Broadband Albedo Data

With the intention of validating our satellite derived albedo after the correction process, we considered broadband albedo data from in situ stations located on the Antarctic and Greenland Ice Sheets (Figure 2). In detail, for the Antarctica we used broadband albedo from 7 AWSs owned by the Institute for Marine and Atmospheric Research Utrecht (IMAU) [18] in different zones of the

Antarctic continent (Dronning Maud Land and Antarctic Peninsula) from 2013 to 2018 and 3 in situ stations from the World Radiation Monitoring Center Baseline Surface Radiation Network (WRMC-BSRN, [17]), i.e., Concordia (DOM, [45]), Neumayer (GVN, [46]) and Syowa (SYO, [47]) Stations (respectively, located in Dome C, Dronning Maud Land and in proximity of Cosmonaut Sea). Regarding the 7 IMAU AWSs, they are equipped with Kipp and Zonen CNR1 or CNR4 radiometers, with a stated accuracy of ±10%. The sensor acquisition rate is 6 min, but the albedo values are then calculated as a 24 h moving average (in order to reduce errors due to sensor tilt and rime formation) [18]. The three BSRN stations are equipped with Kipp and Zonen pyranometers, respectively, CM22 for Concordia St., CMP22 for Neumayer St. and CMP21 for Syowa St. In each of the three BSRN stations, the pyranometer is situated at a height of 2 m and the sensor acquisition rate is 1 min, reporting separately the shortwave downwelling and upwelling radiation [45–47], from which we derived the albedo as a 24 h moving average for consistency with measurements from the IMAU network. On 9 out of 20 dates, the SZA at Neumayer and Syowa was higher than 60◦, and the albedo appeared to increase compared to the dates with lower SZA (0.79 ± 0.027 at Neumayer and 0.76 ± 0.049 at Syowa when the SZA was < 60◦ compared to 0.88 ± 0.010 and 0.81 ± 0.035 when it was > 60◦). This also led to much higher in situ albedo (up to 0.11) compared to satellite-derived albedo on these dates. We therefore assumed in situ albedo to be overestimated when the SZA was higher than 60◦; in fact, this influence of high SZA on the albedo measured at in situ stations is well known and caused by an underestimation of the incoming radiation flux owing to the imperfect cosine response of the upward looking pyranometer [38]. To correct the values from these stations, we adopted the algorithm proposed by Briegleb et al. (1986) [48], derived by a scheme proposed by Dickinson (1983) [49], which normalizes albedo to a SZA of 60◦. The algorithm was originally developed for vegetated surfaces and TOA reflectance, but was also used to estimate surface albedo by Pinker and Laszlo (1992) [50]. It is described as follows:

$$\alpha_{60} = \alpha_{SZA} \frac{1+2d\cos\theta_{SZA}}{1+d} \quad (16)$$

where α_{60} is the normalized albedo considering SZA = 60°, α_{SZA} is the albedo measured at the in situ station at a specific SZA and d is equal to a constant, which varies between 0.1 and 0.4 depending on the type of surface and its dependence on SZA. [48,51,52]. We set d to 0.4 following Yang et al. (2008) [52], who suggests using this value for surface types with a high SZA dependence.

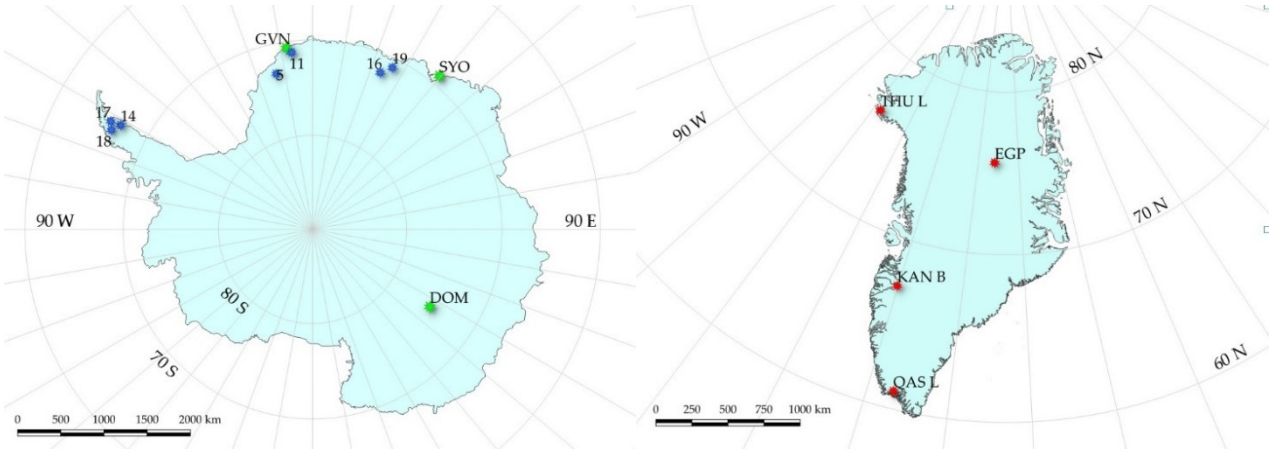

(a) **(b)**

Figure 2. Location of the in situ stations employed in this study, in Antarctica (IMAU–Institute for Marine and Atmospheric Research Utrecht in blue and BSRN–Baseline Surface Radiation Network in green) on the left (a) and in Greenland (PROMICE–Programme for Monitoring of the Greenland Ice Sheet in red) on the right (b).

As regards the Greenland Ice Sheet, we used 4 AWSs of the Program for Monitoring of the Greenland Ice Sheet (PROMICE) [16], equipped with Kipp and Zonen CNR1 or CNR4 radiometers, acquiring data every 10 minutes (hourly averages transmitted). The stated accuracy is < 10% [53]. Again, even if some data are available since 2011, we analyzed albedo measurements acquired between 2014 and 2018. In Table 1 further information about all the used in situ stations are reported and Figure 2 shows their locations. In general, all the satellite values of albedo used for the validation with the in situ data were averages of the 9 pixels surrounding the station, where the station is located in the center pixel. The only exception is represented by the Syowa Station, as it is in proximity of uncovered rock (distance lower than Landsat pixel resolution). For this station, we performed a comparison of a 9-pixel area NW of the station (approximately 60 m) to avoid rock disturbance. We also compared the average of the 4 surrounding pixels and the value of the specific pixel of the station. In both study areas, not all available in situ stations from the IMAU, WRMC-BSRN and PROMICE networks have been considered in this research, as for some of them we could not obtain a sufficient number of Landsat scenes for validation, owing to the absence of AOT values from nearby AERONET stations or excessive cloud cover in specific dates, also confirmed by the cloud cover value of the station datasets.

Table 1. Details of in situ stations considered in this study with the respective number of L8 scenes used for validation. * indicates dates excluded from the comparison (see Section 3.5). AWS stands for Automatic Weather Station, SZA for Solar zenith angle, DOM for Concordia Station, GVN for Neumayer Station, SYO for Syowa Station, EGP for EastGRIP Station, KAN B for Kangerlussuaq Station, QAS L for Quassimiut low Station and THU L for Thule low Station.

Dataset	In Situ Stations	Coordinates (Lat°; Long°)	Elevation (m a.s.l.)	Period	Landsat Scene	Landsat Dates	SZA (Deg)	Surface Type

IMAU								
	AWS 05	-73.10; -13.17	360	1998-2014	178112	21/11/2013	62	Snow
						07/12/2013	61	
	AWS 11	-71.17; -6.80	690	2007-2019	178110	07/12/2013*	58	Snow
						24/01/2014*	63	
						27/01/2015*	66	
						28/02/2015*	76	
						15/02/2016*	71	
						12/10/2016*	74	
						16/01/2017*	63	
	AWS 14	-67.02; -61.50	50	2009-2015	217107	13/02/2015	68	Snow
	AWS 16	-71.95; 23.33	1300	2009-2015	156111	27/11/2013	64	Snow
						30/01/2014	69	
						03/03/2014	79	
						13/10/2014	76	
						29/10/2014	70	
						14/11/2014	66	
						16/10/2015	74	
						17/11/2015	65	
						03/12/2015	63	
	AWS 17	-65.93; -61.85	50	2011-2016	217106	11/10/2015	70	Snow
	AWS 18	-66.40; -63.73	70	2014-2018	217107	11/10/2015*	71	Snow
						03/12/2017*	58	
						03/10/2018*	74	
	AWS 19	-70.95; 26.27	50	2014-2016	156110	16/10/2015	76	Snow
						17/11/2015	67	
						03/12/2015	64	
BSRN								
	DOM	-75.10; 123.38	3233	2006-2020	089113	24/11/2014	61	Snow
						12/02/2015	70	
						29/12/2015	60	
						28/10/2016	68	
						18/12/2017	59	
						20/02/2018	73	
						21/10/2019	71	
	GVN	-70.65; -8.25	42	1992-2020	178110	07/12/2013	56	Snow
						29/12/2015	56	
						15/02/2016	67	
						02/03/2016	72	
						12/10/2016	70	
						16/01/2017	59	
						05/12/2018	56	
						09/01/2020	57	
	SYO	-69.01; 39.59	18	1994-2019	148109	12/10/2014	69	Snow
						28/10/2014	63	
						13/11/2014	59	
						29/11/2014	56	
						16/11/2015	58	
						03/01/2016	55	
						07/03/2016	73	
						04/12/206	55	
						22/02/2017	68	
						20/10/2017	66	
						08/01/2018	56	
						23/10/2018	65	
PROMICE								

EGP	75.62; -35.97	2660	2016-2019	007006	26/07/2016	57	Snow
					26/05/2017	55	
					11/06/2017	53	
					29/07/2017	57	
					29/05/2018	54	
KAN B	67.13; -50.18	350	2011-2019	007013	29/04/2013*	52	Rock
					31/05/2013	45	
					19/08/2013	55	
					06/08/2014	51	
					23/05/2016	46	
					08/06/2016	44	
					10/07/2016	45	
					26/07/2016	48	
					10/05/2017	49	
					27/06/2017	44	
					29/07/2017	49	
					14/08/2017	53	
QAS L	61.03; -46.85	280	2007-2019	002017	02/07/2014	39	Ice
					03/08/2014	45	
					03/06/2015	40	
					21/06/2016	39	
					05/04/2017	56	
					07/05/2017	45	
					24/06/2017	39	
					10/05/2018	44	
					13/07/2018	41	
					29/07/2018	44	
					29/05/2019	41	
THU L	76.40; -68.27	570	2010-2019	032005	04/07/2014	54	Ice
					04/05/2015	61	
					20/05/2015	57	
					23/07/2015	57	
					24/08/2015	66	

3. Results and Discussion

The results are displayed in five different subsections: the first concerns the validation of the albedo retrieval method in comparison with all in situ stations; then, each specific station dataset is considered, i.e., (i) IMAU AWSs [18] and (ii) BSRN stations [17] in Antarctica and (iii) PROMICE AWSs [16] in Greenland. Finally, we discuss possible reasons of discrepancy between satellite derived albedo and in situ observations.

3.1. Method Validation

As described in Section 2, in order to validate the different combinations of input data or correction approaches for obtaining accurate albedo from satellite data, we compared different albedo values

calculated following the same procedure, but varying the required inputs or parameters, as shown in the workflow of Figure 1. The specific statistics of the best combination and of each correction step are shown in Table 2. Examining the differences in albedo when changing inputs and parameters in the workflow, firstly, we calculated the albedo applying the pixel-specific SZA or scene average SZA corrections. The difference between the albedo calculated with the average and pixel specific SZA was very low, as the two datasets differed statistically (MAE) by 0.003, with only slightly worse values when using the average SZA, probably because of the low range of possible SZA within a Landsat image (±2◦). The small statistical differences between the correction with scene-average and pixel specific SZA suggests that the pixel-specific SZA correction step is not crucial for albedo retrieval at high latitudes, although it did provide slightly better results. As regards the atmospheric correction, we compared the albedo retrieved by using ERA5 climatic variables, against the one obtained when using the subarctic winter model in GRASS GIS. Again, the statistics were very similar, even if the atmospheric correction using the atmospheric model based on ERA5 variables showed slightly worse results. The standard deviation between in situ and satellite albedo processed by using ERA5 data was 0.030, the RMSE 0.041 and the BE increased to 0.011. (Best model: 0.029, 0.040 and 0.005, respectively). In addition, the statistics for the validation with Antarctic observations were worse since the MAE increased to 0.028, while the MAE for Greenland stations was slightly better (0.028). In this context, we demonstrated that the use of an available generic model for atmospheric correction, i.e., subarctic winter, provided the same, or even better, results than using detailed parameters, e.g., from ERA5 dataset. This might be caused by an incorrect representation of atmospheric layers at high latitudes in ERA5, given the scarcity of ground observations in the polar areas. Thus, the use of specific parameters in the 6S model might not be necessary at such high latitudes.

Table 2. Statistics of the albedo retrieval procedure, with the best combination in the first row and all other variants used for comparison (86 values). Statistics are: mean absolute error (MAE), standard deviation (STD), bias estimate (BE), correlation coefficient (Cc), root–mean–square error (RMSE) and bias-removed root–mean–square error (BRRMSE). Correlation is always significant at the 99% confidence level.

Dataset	MAE tot	MAE Antarctica	MAE Greenland	STD	BE	Cc	RMSE	BRRMSE
Proposed model	0.027	0.026	0.029	0.029	0.005	0.987	0.040	0.039
Ave. SZA c.	0.030	0.028	0.033	0.029	0.003	0.986	0.042	0.041
ERA5	0.028	0.028	0.028	0.030	0.011	0.987	0.041	0.040
AOT -0.01	0.028	0.027	0.030	0.029	0.007	0.987	0.040	0.040
AOT +0.01	0.028	0.026	0.031	0.028	0.002	0.987	0.040	0.040
Cosine c.	0.026	0.026	0.027	0.025	0.009	0.990	0.036	0.035

Minnaert c.	0.027	0.025	0.030	0.028	0.007	0.988	0.039	0.038
Knap a.	0.047	0.043	0.053	0.039	0.040	0.984	0.061	0.046
1 pixel	0.028	0.027	0.030	0.030	0.004	0.986	0.041	0.041
4 pixels	0.028	0.026	0.031	0.031	0.005	0.986	0.042	0.041

We also compared the results obtained by adding or subtracting 0.01 from the applied value of AOT. In fact, in the 6S model used for atmospheric correction, we simplified the AOT parameter by using a mean of 0.02 in Antarctica, considering that the parameter is constant throughout the average summer season, especially in the inland. According to Klok et al. (2003) [29], the uncertainty in AOT can propagate to the final albedo retrieval, leading to an error of 0.01. Thus, with the aim of minimizing the uncertainty, future research could better quantify AOT at the poles with specific campaigns. We did not find large differences among the three runs with different AOT, even if the default model provided always better statistics, especially compared to the albedo obtained when lowering the AOT by 0.01, apart from the BE. Nevertheless, looking at the two satellite albedo datasets obtained by varying the AOT by ±0.01, it is evident that an error of this magnitude in AOT should not cause a significant error in the calculated albedo. In addition, the strong correlation (0.985 99% confidence) between the proposed model and the one obtained when adding +0.01 to the AOT might suggest that AOT in Antarctica is well represented by an average range of 0.02–0.03. As regards the topographic correction, in addition to the c-factor method, we also calculated the albedo by using two other methods: the cosine and the Minnaert methods. The cosine method showed good results, with statistics similar to the c-factor. Here, even if the model is more basic than c-factor (see Section 2.1.3) and the BE was higher by 0.004 and MAE by 0.001, the STD turned out to be slightly lower (0.025), as did the RMSE (0.036) and BRRMSE (0.035). Minimal statistical differences were also found between the c-factor and Minnaert method. However, looking at highly sloped areas (>15◦) facing the same direction as the solar azimuth, e.g., mountain zones (Figure 3), the albedo from the cosine and Minnaert algorithms show some relevant problems.

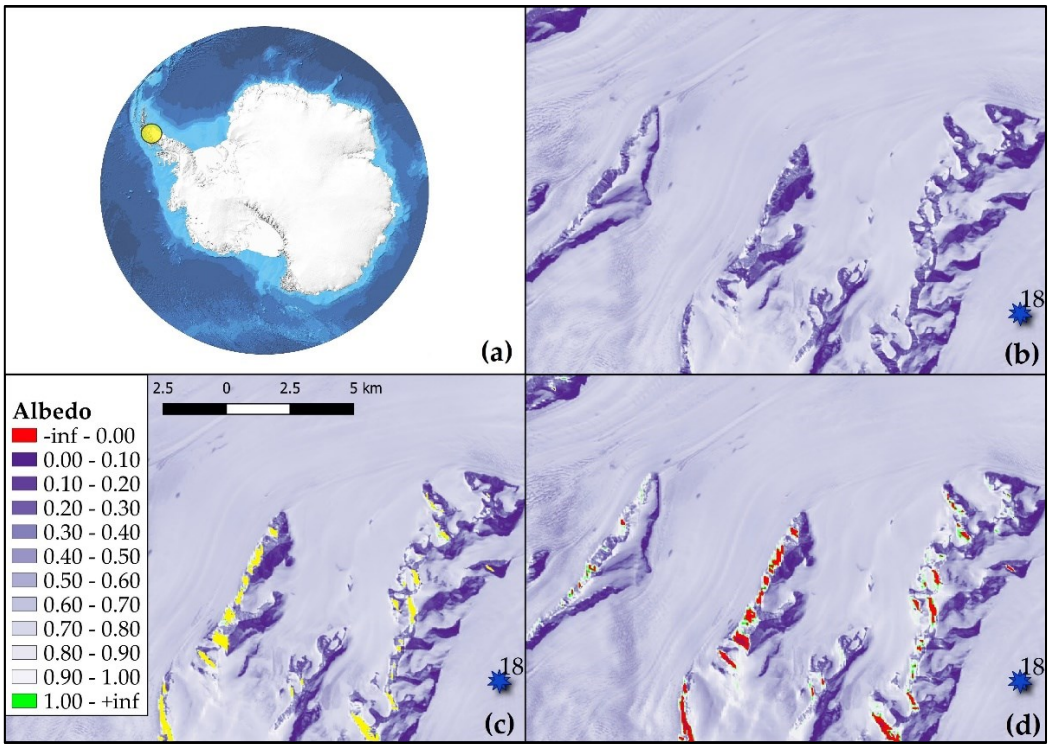

Figure 3. (a) International bathymetric chart of the Southern Ocean (IBCSO, [54]) showing the mountainous area in the Antarctic Peninsula (within the yellow circle) in proximity of IMAU AWS 18; (b–d) broadband albedo raster maps of the yellow area, respectively calculated using: the c-factor method (b), Minnaert method (c) and the cosine method (d). No-data: represented in yellow.

In fact, compared to the c-factor method which provides albedo values for all kind of surfaces (Figure 3b), the Minnaert method cannot process area with high acclivity, which result in no data (yellow areas in Figure 3c). This is probably because Equation (12) uses a power function that can lead the values to overflow outside the possible ranges of floating-point numbers; in contrast, the cosine method overestimated or underestimated albedo in these zones (with values much higher than 1 or much lower than 0, green and red areas in Figure 3d, respectively). In view of these differences, even if these sloped areas are quite uncommon across the ice sheets, we suggest using the c-factor method, since it provides at the same time results that are in agreement with in situ observations, while being able to obtain albedo values also for sloped surfaces, e.g., the ones represented in Figure 3. Further still, we tested two separate algorithms to convert narrowband to broadband albedo: the Liang and Knap algorithms [34,35]. Broadband albedo calculated using the Knap algorithm (αKnap) showed much worse statistics than the conversion using Liang algorithm (αLiang). The MAE for αKnap was 0.047, almost doubled compared to the MAE for αLiang (0.027). Furthermore, for αKnap the STD was 0.039, the RMSE increased to 0.061 and the BE to 0.040. In summary, the comparison between the two albedo datasets calculated using either Liang algorithm [34] or Knap algorithm [35], showed clear results in support of Liang algorithm. This is probably because Knap algorithm considers a

lower number of bands than Liang algorithm (2 bands vs. 5), and might not be able to adequately represent albedo changes due to changes in grain size in the near-infrared and shortwave infrared wavelengths. Moreover, we checked whether there were any significant differences when considering 9, 4 or 1 pixels in the satellite image around the in situ station. Once more, the three datasets were very similar and the use of 9 pixels shows a minor improvement in results. The general statistics present only variations of a few thousandths. This might depend on the great homogeneity of the polar areas, characterized by wide, highly reflective surfaces. In summary, our proposed model, i.e., the best combination of corrections reported in green in Figure 1 and in the first row in Table 2, showed a RMSE and a BRRMSE of 0.040 and 0.039 respectively, a BE of 0.005, an STD of 0.029, a correlation of 0.987 ($p < 0.01$) between in situ and satellite data and a MAE of 0.027. The MAE from the validation of satellite- albedo using in situ data was lower for the Antarctic Ice Sheet (IMAU and BSRN in situ stations, 53 scenes), than in the Greenland Ice sheet (PROMICE AWSs, 33 scenes), with a value of 0.026 against 0.029.

3.2. IMAU AWSs (Antarctica)

We considered seven IMAU AWSs in Antarctica [18], obtaining data consistent with Landsat 8 temporal range (2013–present). These AWSs provide broadband albedo, thus we compared the data with those calculated using Liang algorithm [34]. The total MAE between AWS observations and satellite derived albedo was 0.033 and STD was 0.026, based on 26 measurements. However, such an MAE might be due to the high MAE at AWS 11 (0.043 MAE) and 18 (0.077 MAE), which generally showed larger differences in comparison with the other stations. In fact, no other AWS reached a MAE of 0.040. AWSs 5 and 11 are situated in western Dronning Maud Land, in proximity of the sea (Atlantic Ocean). 2 Landsat scenes were used for comparison with AWS 5, resulting in a MAE of 0.020 and 0.030 (thus a mean of 0.025); here, satellite albedo was generally slightly lower than AWS albedo. For AWS 11, we considered 7 Landsat scenes. The MAE of the difference between satellite and in situ albedo on these 7 dates was 0.043 and in every case the satellite derived albedo was lower than ground observations, and was on average 0.80, consistently with the typical Antarctic snow albedo [11,23]. AWS-based albedo had much higher values, even higher than 0.85 (which is typical of fresh snow). All dates of this station were affected by cloud cover, which was always >20%, which might explain the higher values compared to satellite-derived albedo, as the albedo is usually larger under clouds than in clear-sky conditions [55,56]. AWSs 14, 17 and 18 are situated in the northern part of Antarctic peninsula. AWS 14 and 17 had 1 coincident Landsat scene; at AWS14, Landsat derived and in situ albedo showed the same value, while the MAE was 0.030 at AWS 17.

The albedo from 3 Landsat scenes was used for comparison with AWS 18, showing the highest absolute difference (0.077), as visible in Figure 4a. In fact, while the observations from AWS18 showed a value typical of dry snow (>0.80), satellite derived albedo was always lower, showing values more typical of metamorphosized or wet snow (0.70–0.77, [57]). In particular, the MAE was 0.115, recorded on 11 October 2015. On that date, the satellite image showed lower albedo values in the proximity of the AWS, even typical of blue ice [58] while a value of 0.83 was measured at the AWS. The large difference at AWS 18 could be caused by the variations in surface conditions at the AWS, an inaccurate location recorded for this AWS due to ice flow, or residual sensor tilt that was not corrected by the 24 h moving average. This AWS is located at the base of an outlet glacier, where surface conditions could vary significantly over time: blue ice exposure can occur at the beginning of the summer season due to the effect of winter wind scouring, while in summer snow/ice melt can lead to the presence of superficial water. In addition, according to MEaSUREs ice flow velocity map (mostly derived from 2007–2016 data at 450 m spatial resolution [59]), the flow velocity of ice is 141 m/yr around the AWS, which might lead to a shift in the location of the station over time. Finally, the last two AWSs (16 and 19) are situated in central-eastern Dronning Maud Land. AWS 16, used to validate the albedo from 9 Landsat scenes, showed a low MAE, 0.016. In addition, for 4 of these scenes, the error was even lower than 0.010. AWS 19 showed a MAE of 0.031 between AWS observations and satellite derived albedo, based on the validation of 3 Landsat scenes. Considering AWS16 and AWS19, we did not detect a bias between in situ and satellite data, since sometimes satellite-derived albedo underestimated in situ observations, sometimes overestimated them.

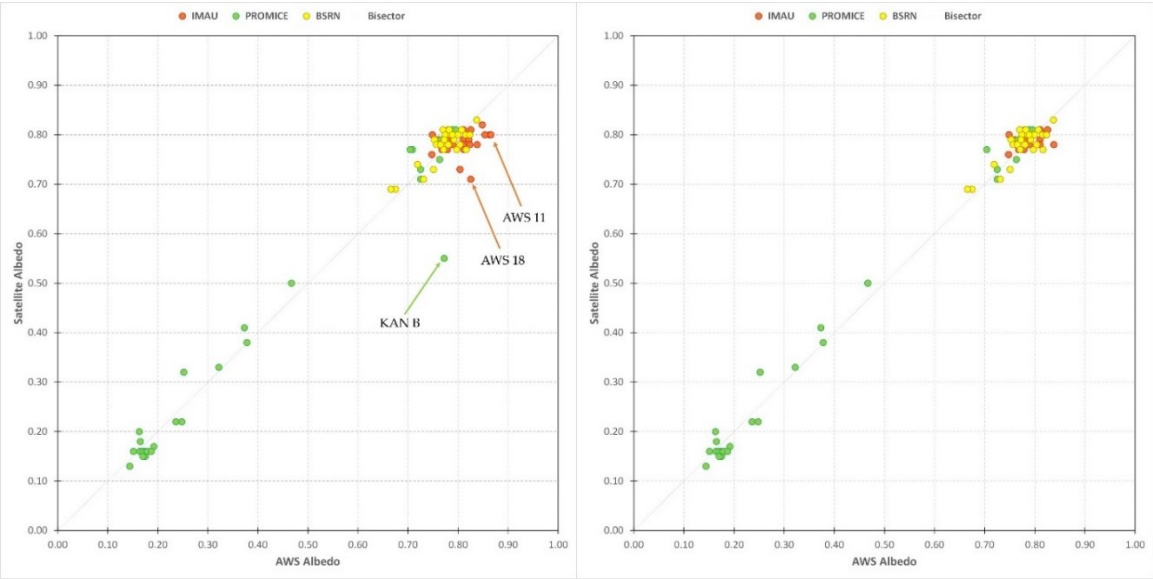

Figure 4. The plots show the validation of satellite retrieved albedo (Landsat 8 OLI) using in situ observations: (a) IMAU in red, BSRN in yellow (Antarctica) and PROMICE in green (Greenland), (b) cleaned dataset. The arrows indicate the anomalous data.

3.3. BSRN AWSs (Antarctica)

The best statistics were found for the validation of satellite albedo against BSRN in situ stations, based on a dataset of 27 Landsat scenes. In fact, the MAE for this dataset was 0.020 and the STD 0.012. 3 in situ stations were used for validation: DOM, GVN and SYO. The first one, DOM at Concordia Station, is the only one situated in the inner part of the continent and 7 dates were found to be suitable for the validation of satellite albedo, showing a MAE of 0.028, the highest of all three in situ stations. Here, 6 satellite-derived albedo values out of 7 were lower than field observations. In contrast, SYO showed no bias while at GVN satellite albedo was higher for most dates. At Neumayer and Syowa stations, the MAE was lower than 0.020: 0.019 and 0.015, respectively. 8 Landsat scenes were validated with data from GVN, and 12 with data from SYO (the most numerous dataset with KAN B AWS, see Section 3.4). As regards SYO in situ station, none of the data used for validation showed an absolute error greater than 0.030, while GVN station showed only one date with an absolute error > 0.030, on 16 January 2017.

3.4 PROMICE AWSs (Greenland)

As concerns the Greenland ice-sheet, we compared Landsat derived albedo with data from 4 PROMICE AWSs [16], obtaining a dataset with 33 dates. In this case, the MAE be-tween AWS measurements and satellite derived albedo was 0.029 and its standard deviation was 0.038. The only AWS situated in the inland is the EastGRIP Greenland site (EGP) AWS, at an average altitude of 2660 m a.s.l. Five dates were considered for EGP, resulting in a MAE of 0.020. Kangerlussuaq on land station (KAN B), on the South-West of the ice-sheet, showed albedo values typical of rock (< 0.20). A good agreement was found between albedo from this AWS and the one obtained from Landsat, except for the albedo from the first date used for validation (29 April 2013), that diverged from all the others, showing an absolute error of 0.222. Thus, the final MAE for the entire AWS is 0.035. Qassimiut low station (QAS L), in the southernmost area of Greenland, showed a MAE of 0.024, based on 11 dates. The last considered station was the Thule low AWS (THU L), on the North-Western tip of Greenland. As for EGP, since the station is located at high lati-tude (over 75o N), we could validate fewer Landsat 8 images (5). The MAE here was quite high, i.e., 0.034.

3.4. Analysis of the Cleaned Dataset

As discussed in the previous subsections, some of the scenes presented strong anomalies in the validation of satellite albedo using AWS observations from the IMAU dataset. In detail, AWSs 11

and 18 showed the largest differences. The former always shows high values typical of fresh snow (>0.85), which tend to be very unusual in Antarctica, and in fact, previous studies found lower albedo values for snow on the Antarctic plateau, around 0.80 or just slightly higher [3,11,27]. Moreover, high values of longwave-equivalent cloud cover (20–30%) were recorded at AWS 11 on several dates, even if the satellite imagery was cloudfree (according to the Landsat Metadata and visual check). Longwave equivalent cloud cover is not an observed value of cloudiness but is modelled from hourly values of downward longwave radiation and air temperature (at 2 m) [56,60]. According to Munneke et al. (2011) [61], this modeled cloud cover could differ from observed cloudiness (e.g., from satellite), leading to differences in modeled and observed net shortwave radiation at the surface and thus in albedo. In general, clouds have a relevant effect on albedo [62], especially when it is very high (e.g., for snowy surfaces, [44]). They alter the broadband albedo of a snow surface mainly by filtering out radiation at near-infrared (IR) wavelengths (>800 nm) more effectively than radiation in the visible region, thus changing the spectral composition of incoming radiation. The spectrally integrated albedo increases because the spectral albedo for visible wavelengths is higher than for near-IR wavelengths [56]. Cloudiness has been proposed as an explanation for higher variability in albedo measured at weather stations on the Antarctic shores [11], where most AWSs showing anomalous results are located. In addition to this cloud-cover issue, another station presented anomalous observations, with a MAE of 0.077, i.e., IMAU AWS 18 (see Section 3.2). In order to clean our dataset from the stations that showed anomalous data, we decided to exclude from the IMAU dataset AWS 11 (7 data) and 18 (3 data), providing a 43-scene dataset for Antarctica. Removing from the statistical calculations these 10 albedo values from AWS11 and AWS18, the MAE of Antarctic area dropped to 0.021. As concerns the Greenland Ice Sheet, one case of Landsat-derived albedo presented a large difference compared to field measurements, i.e., KAN B AWS on 29 April 2013, when the albedo observed at the station was much lower than the satellite derived one (0.55 against 0.77, a difference of 0.222). By examining the AWS dataset, we found high albedo variability in the week of satellite image acquisition, due to a snowfall event at the end of the boreal winter on the otherwise rocky surface where the station is located. In fact, albedo changed by more than 0.500 over a few days and since the PROMICE stations record hourly averages, such a difference can lead to an inaccurate validation of Landsat-derived albedo. Excluding the albedo from this date from the comparison, the MAE dropped to 0.023, based on a 32-scene dataset. In general, excluding from the total statistics all these outliers, i.e., the data of 10 scenes in the Antarctic dataset and of 1 scene in the Greenland dataset, we obtained improved statistics for a 75-scene dataset (Figure 4b): a MAE of 0.021, STD of 0.015, RMSE of 0.026, BBRMSE of 0.025, a BE of −0.005 and a correlation coefficient of 0.995, with $p < 0.01$ (Table 3). Comparing these results with previous studies on polar

ice sheets, Gusain et al. (2018) [63] found that MODIS albedo (from the MOD43B3 product) always overestimated AWS measurements in Antarctica, with a correlation coefficient of 0.86, a BE of 0.01 and a RMSE of 0.09; similar results were found by Stroeve et al. (2006) [64] in Greenland (RMSE > 0.06, BE < 0.02); Liang et al. (2005) [25] also reported a higher BE, slightly < 0.02 in Greenland. In other Earth regions (i.e., United States of America), Li et al. (2018) [65] found a lower BE and RMSE using higher spatial resolution satellite images (Sentinel-2A) compared to MODIS. Higher spatial resolution images are in fact less impacted by the spatial distribution of landscape features and structural changes across the surface (typical of coarser resolution images) and they are able to detect micro-scale differences as well.

Table 3. Statistics of the validation of satellite-albedo with in situ observations for the cleaned dataset, with the best option and all other variants used for comparison (75 values). Statistics are: mean absolute error (MAE), standard deviation (STD), bias (BE), correlation coefficient (Cc), root–mean–square error (RMSE) and bias-removed root–mean–square error (BRRMSE). Correlation is always significant at the 99% confidence level.

Dataset	MAE tot	MAE Antarctica	MAE Greenland	STD	BE	Cc	RMSE	BRRMSE
Proposed model	0.021	0.020	0.023	0.015	-0.005	0.995	0.026	0.025
Ave. SZA c.	0.024	0.022	0.027	0.017	-0.006	0.994	0.030	0.029
ERA5	0.021	0.021	0.022	0.016	0.001	0.995	0.026	0.026
AOT -0.01	0.022	0.020	0.024	0.015	-0.002	0.995	0.026	0.026
AOT +0.01	0.023	0.021	0.025	0.015	-0.007	0.995	0.027	0.027
Cosine c.	0.021	0.021	0.022	0.014	0.001	0.995	0.026	0.026
Minnaert c.	0.021	0.019	0.025	0.015	-0.002	0.995	0.026	0.026
Knap a.	0.040	0.035	0.047	0.029	0.032	0.992	0.049	0.037
1 pixel	0.022	0.021	0.024	0.017	-0.006	0.994	0.028	0.027
4 pixels	0.022	0.019	0.025	0.016	-0.004	0.995	0.027	0.027

Concerning possible reasons of discrepancies between our final satellite dataset and the in situ observations, surely relevant is the fact that data from in situ stations may represent local features that are averaged up in satellite-derived products with larger footprints, a problem that is likely to increase when coarser resolution data (e.g., MODIS, 500 m) are used in place of Landsat. In fact, our satellite data presented generally more constant values than the ones measured by the stations. Other sources of uncertainty for in situ albedo observations employed in this study include the intrinsic instrument measurement uncertainty, residual tilt errors, shifts in the station location over time and the correction of SZA dependence for albedo measured at GVN and SYO stations, using a formula that was originally developed for vegetated surfaces. However, this latter uncertainty only concerns 9 out of 86 measurements in our validation data set. While observations from ground stations are usually

considered the most accurate and the standard method to assess the accuracy of satellite-derived products, our study shows that observations from AWSs might still be affected by large uncertainty, and that using manned stations (such as those from the BSRN network) might be more appropriate for validation. Besides, ground stations might show values that are not completely representative of their surroundings, and their use for validation of satellite data on the icesheets should be carefully evaluated. As regards satellite-derived albedo, topographic correction and the related geolocation accuracy are considered to be the most important sources of errors, with an uncertainty up to 5% [29], depending on the incorrect co-registration of each DEM, even if in Antarctica such issue could be less relevant as large variations in altitude and slope are limited to very few areas. In addition, using Landsat 8 imagery, the DEMs proposed in this research represent the only available choices to maintain a similar spatial resolution between Landsat and DEM datasets. In fact, all other existing products in polar areas have a much coarser resolution (an order of magnitude larger), which would require down sampling to obtain a 30 m spatial resolution, likely introducing larger uncertainty. A further correction not implemented in this study is anisotropic correction using BRDF models, which can be important in the retrieval of albedo from satellite data; its lack in our model could have negatively affected our satellite derived albedo and the observed differences might also be caused by its absence, according to Knap et al. (1999) [66]. While an anisotropic effect is certainly present on ice and snow surfaces in the polar regions, it has been omitted in this study because of the lack of a directly applicable correction model for Landsat data for such high values of albedo and SZA as are normally found on the ice sheets. In future research, approaches combining Landsat data with BRDF from MODIS, as done e.g., by He et al. (2018) [67], could be tested to evaluate whether including the anisotropic correction actually improves the agreement between satellite-derived albedo and in situ observations.

4. Conclusions

In this study, we employed the methodology proposed by Klok et al. (2003) [29] and also used by Fugazza et al. (2016) [19] to derive broadband albedo from Landsat 8 OLI satellite data at 30 m spatial resolution and validate it using observations from in situ stations located on the Antarctic and Greenland Ice Sheets. This model could allow future research to study local surface features by an optical point of view, considering that previous attempts provided only coarser resolution products (≥250 m) based on MODIS observations [6,23–26]. To validate satellite derived albedo, we performed a comparison between Landsat-retrieved albedo and different ground-based datasets, for a total of 86 scenes, while Fugazza et al. (2016) [19] only compared satellite albedo against data from

one AWS and Wang et al. (2014) [27] performed a satellite inter-comparison between Landsat and MODIS albedo, following the method proposed by Klok et al. (2003) [29]. The difference from the latter research lies in a more detailed correction for the SZA, taking into account pixel-specific values, and in the narrowband to broadband albedo conversion. In fact, we found that Liang algorithm [34] provided better ground truth validation in the polar regions than Knap algorithm from the comparison with in situ observations [35]. The final proposed workflow (Figure 1) was obtained after we tested different variants of the model, by changing inputs and parameters at each stage of the albedo calculation, i.e., with average or pixel-specific SZA correction, atmospheric correction using a pre-defined model or with specific parameters from a reanalysis product, three different topographic correction approaches and two different algorithms for conversion of narrowband to broadband albedo. These comparisons allowed us to define the combination of corrections that could provide the best agreement with ground observations by in situ stations. Three ground observation datasets were employed: (i) a dataset of seven AWSs from IMAU [18] located on the Antarctic Peninsula and Dronning Maud Land (Antarctica) and providing broadband albedo from 2014 to 2018, (ii) three stations from BSRN [17], located in three different areas of the continent, i.e., DOM (Dome C area), SYO (in the proximity of Cosmonaut sea) and GVN (Dronning Maud Land) from 2013 to present and iii) a dataset from PROMICE [16] of four AWSs located on the Greenland icesheet (both inland and coastal and southern and northern areas) from 2013 to 2019. In total, using data from 14 different in situ stations, we compared 86 albedo measurements on the Greenland and Antarctic icesheets, 33 in Greenland and 53 in Antarctica, obtaining a MAE between ground observations and satellite derived albedo of 0.027. In detail, the validation for stations on the Antarctic Ice Sheet showed a lower value compared to the Greenland Ice Sheet, with a MAE of 0.026 against 0.029. However, excluding 10 anomalous albedo values from the IMAU dataset and one from PROMICE, we compared a cleaned 75-scene dataset, which showed a lower MAE of 0.021 (0.020 for Antarctica and 0.023 for Greenland), a STD of 0.015, a RMSE of 0.026 and BRRMSE of 0.025, a BE of −0.005 and a correlation coefficient of 0.995 ($p < 0.01$). Our study provides relevant findings for future polar sciences analysis at high resolution; to further extend and validate it, our model could be tested on previous satellites of the Landsat family, i.e., Landsat 5 ETM and Landsat 7 ETM+ as well as other satellite products at a similar spatial resolution, e.g., Sentinel 2 or ASTER.

Author Contributions: Conceptualization, G.T., D.F. and A.S.; Data curation, G.T.; Formal analysis, G.T.; Investigation, G.T.; Methodology, G.T. and D.F.; Project administration, M.F.; Software, G.T. and D.F.; Supervision, A.S. and M.F.; Validation, G.T., D.F. and A.S.; Visualization, G.T.; Writing Original draft, G.T., D.F., A.S. and M.F. All authors have read and agreed to the published version of the manuscript.

Funding: Researchers involved in the study were supported by: MNA–National Antarctic Museum of Italy (PhD Scholarship of G. Traversa), DARA–Department for Regional Affairs and Autonomies–of the Italian Presidency of the Council of Ministers and by Sanpellegrino Levissima Spa.

Institutional Review Board Statement: Not applicable.

Informed Consent Statement: Not applicable.

Data Availability Statement: All data used in this study are openly available. PROMICE AWS data are available from https://www.promice.org/PromiceDataPortal/#Automaticweatherstations at 10.22008/promice/data/aws; IMAU data from https://doi.pangaea.de/10.1594/PANGAEA.910473; BSRN data are available from: https://dataportals.pangaea.de/bsrn/; Landsat 8 data are available from: https://earthexplorer.usgs.gov/.

Acknowledgments: We are grateful to Michele Citterio of the Geological Survey of Denmark and Greenland (GEUS) for his precious suggestions, which have improved the manuscript, and in general to GEUS for its important AWS data on Greenland Ice Sheet. In addition, we thank Stan Jakobs and all his colleagues from the Institute for Marine and Atmospheric Research Utrecht (IMAU) for their data and assistance. Conflicts of Interest: The authors declare no conflict of interest.

References

1. Schaepman-Strub, G.; Schaepman, M.E.; Painter, T.H.; Dangel, S.; Martonchik, J.V. Reflectance Quantities in Optical Remote Sensing—Definitions and Case Studies. Remote Sens. Environ. 2006, 103, 27–42. [CrossRef]

2. Grenfell, T.C. Albedo. Encyclopedia of Snow, Ice and Glaciers; Singh, V., Singh, P., Haritahya, U., Eds.; Springer: Dordrecht, The Netherlands, 2011.

3. Grenfell, T.C.; Warren, S.G.; Mullen, P.C. Warren Reflection of Solar Radiation by the Antarctic Snow Surface at Ultraviolet, Visible, and near-Infrared Wavelengths. J. Geophys. Res. 1994, 99, 18669–18684. [CrossRef]

4. Gay, M.; Fily, M.; Genthon, C.; Frezzotti, M.; Oerter, H.; Winther, J.-G. Snow Grain-Size Measurements in Antarctica. J. Glaciol. 2002, 48, 527–535. [CrossRef]

5. Warren, S.G.; Brandt, R.E.; Grenfell, T.C. Visible and Near-Ultraviolet Absorption Spectrum of Ice from Transmission of Solar Radiation into Snow. Appl. Opt. 2006, 45, 5320–5334. [CrossRef] [PubMed]

6. Gallet, J.-C.; Domine, F.; Arnaud, L.; Picard, G.; Savarino, J. Vertical Profile of the Specific Surface Area and Density of the Snow at Dome C and on a Transect to Dumont D'Urville, Antarctica—Albedo Calculations and Comparison to Remote Sensing Products. Cryosphere 2011, 5, 631–649. [CrossRef]

7. Picard, G.; Libois, Q.; Arnaud, L.; Verin, G.; Dumont, M. Development and Calibration of an Automatic Spectral Albedometer to Estimate Near-Surface Snow SSA Time Series. Cryosphere 2016, 10, 1297–1316. [CrossRef]

8. Frezzotti, M.; Gandolfi, S.; Marca, F.L.; Urbini, S. Snow Dunes and Glazed Surfaces in Antarctica: New Field and Remote-Sensing Data. Ann. Glaciol. 2002, 34, 81–88. [CrossRef]

9. Scambos, T.A.; Frezzotti, M.; Haran, T.; Bohlander, J.; Lenaerts, J.T.M.; Van Den Broeke, M.R.; Jezek, K.; Long, D.; Urbini, S.; Farness, K.; et al. Extent of Low-Accumulation "wind Glaze" Areas on the East Antarctic Plateau: Implications for Continental Ice Mass Balance. J. Glaciol. 2012, 58, 633–647. [CrossRef]

10. Das, I.; Bell, R.E.; Scambos, T.A.; Wolovick, M.; Creyts, T.T.; Studinger, M.; Frearson, N.; Nicolas, J.P.; Lenaerts, J.T.M.; van den Broeke, M.R. Influence of Persistent Wind Scour on the Surface Mass Balance of Antarctica. Nat. Geosci. 2013, 6, 367–371. [CrossRef]

11. Pirazzini, R. Surface Albedo Measurements over Antarctic Sites in Summer. J. Geophys. Res. 2004, 109, D20118. [CrossRef]

12. Picard, G.; Domine, F.; Krinner, G.; Arnaud, L.; Lefebvre, E. Inhibition of the Positive Snow-Albedo Feedback by Precipitation in Interior Antarctica. Nat. Clim. Chang. 2012, 2, 795–798. [CrossRef]

13. Lenaerts, J.T.M.; Lhermitte, S.; Drews, R.; Ligtenberg, S.R.M.; Berger, S.; Helm, V.; Smeets, C.; Van Den Broeke, M.R.; Van De Berg, W.J.; Van Meijgaard, E. Meltwater Produced by Wind–Albedo Interaction Stored in an East Antarctic Ice Shelf. Nat. Clim. Chang. 2017, 7, 58–62. [CrossRef]

14. Rusin, N.P. Meteorological and Radiational Regime of Antarctica. Jerus. Isr. Program Sci. Transl. 1961.

15. Bintanja, R.; Van Den Broeke, M.R. The Surface Energy Balance of Antarctic Snow and Blue Ice. J. Appl. Meteorol. Climatol. 1995, 34, 902–926. [CrossRef]

16. van As, D.; Ahlstrøm, A.P.; Andersen, M.L.; Citterio, M.; Edelvang, K.; Gravesen, P.; Machguth, H.; Nick, F.M. Programme for Monitoring of the Greenland Ice Sheet (PROMICE): First Temperature and Ablation Records. Geol. Surv. Den. Greenl. Bull. 2011, 23, 73–76.

17. Driemel, A.; Augustine, J.; Behrens, K.; Colle, S.; Cox, C.; Cuevas-Agulló, E.; Denn, F.M.; Duprat, T.; Fukuda, M.; Grobe, H.; et al. Baseline Surface Radiation Network (BSRN): Structure and Data Description (1992–2017). Earth Syst. Sci. Data 2018, 10, 1491–1501. [CrossRef]

18. Jakobs, C.L.; Reijmer, C.H.; Smeets, C.J.P.P.; Trusel, L.D.; van de Berg, W.J.; van den Broeke, M.R.; van Wessem, J.M. A Benchmark Dataset of in Situ Antarctic Surface Melt Rates and Energy Balance. J. Glaciol. 2020, 66, 291–302. [CrossRef]

19. Fugazza, D.; Senese, A.; Azzoni, R.S.; Maugeri, M.; Diolaiuti, G.A. Spatial Distribution of Surface Albedo at the Forni Glacier (Stelvio National Park, Central Italian Alps). Cold Reg. Sci. Technol. 2016, 125, 128–137. [CrossRef]

20. Azzoni, R.S.; Senese, A.; Zerboni, A.; Maugeri, M.; Smiraglia, C.; Diolaiuti, G.A. Estimating Ice Albedo from Fine Debris Cover Quantified by a Semi-Automatic Method: The Case Study of Forni Glacier, Italian Alps. Cryosphere 2016, 10, 665–679. [CrossRef]

21. Brock, B.W.; Willis, I.C.; Sharp, M.J. Measurement and Parameterization of Albedo Variations at Haut Glacier d'Arolla, Switzerland. J. Glaciol. 2000, 46, 675–688. [CrossRef]

22. Senese, A.; Maugeri, M.; Ferrari, S.; Confortola, G.; Soncini, A.; Bocchiola, D.; Diolaiuti, G. Modelling Shortwave and Longwave Downward Radiation and Air Temperature Driving Ablation at the Forni Glacier (Stelvio National Park, Italy). Geogr. Fis. Dinam. Quat. 2016, 39, 89–100.

23. Stroeve, J.; Box, J.E.; Wang, Z.; Schaaf, C.; Barrett, A. Re-Evaluation of MODIS MCD43 Greenland Albedo Accuracy and Trends. Remote Sens. Environ. 2013, 138, 199–214. [CrossRef]

24. Box, J.E.; van As, D.; Steffen, K. Greenland, Canadian and Icelandic Land-Ice Albedo Grids (2000–2016). Geol. Surv. Den. Greenl. Bull. 2017, 4, 53–56. [CrossRef]

25. Liang, S. Mapping Daily Snow/Ice Shortwave Broadband Albedo from Moderate Resolution Imaging Spectroradiometer (MODIS): The Improved Direct Retrieval Algorithm and Validation with Greenland in Situ Measurement. J. Geophys. Res. 2005, 110, D10109. [CrossRef]

26. Hui, F.; Ci, T.; Cheng, X.; Scambos, T.A.; Liu, Y.; Zhang, Y.; Chi, Z.; Huang, H.; Wang, X.; Wang, F. Mapping Blue-Ice Areas in Antarctica Using ETM+ and MODIS Data. Ann. Glaciol. 2014, 55, 129–137. [CrossRef]

27. Traversa, G.; Fugazza, D.; Senese, A.; Diolaiuti, G.A. Preliminary Results on Antarctic Albedo from Remote Sensing Observations. Geogr. Fis. Din. Quat. 2019, 42, 245–254.

28. Reijmer, C.H.; Bintanja, R.; Greuell, W. Surface Albedo Measurements over Snow and Blue Ice in Thematic Mapper Bands 2 and 4 in Dronning Maud Land, Antarctica. J. Geophys. Res. Atmos. 2001, 106, 9661–9672. [CrossRef]

29. Klok, E.L.; Greuell, W.; Oerlemans, J. Temporal and Spatial Variation of the Surface Albedo of Morteratschgletscher, Switzerland, as Derived from 12 Landsat Images. J. Glaciol. 2003, 49, 491–502. [CrossRef]

30. Shuai, Y.; Masek, J.G.; Gao, F.; Schaaf, C.B. An Algorithm for the Retrieval of 30-m Snow-Free Albedo from Landsat Surface Reflectance and MODIS BRDF. Remote Sens. Environ. 2011, 115, 2204–2216. [CrossRef]

31. Wang, J.; Ye, B.; Cui, Y.; He, X.; Yang, G. Spatial and Temporal Variations of Albedo on Nine Glaciers in Western China from 2000 to 2011. Hydrol. Process. 2014, 28, 3454–3465. [CrossRef]

32. Naegeli, K.; Damm, A.; Huss, M.; Wulf, H.; Schaepman, M.; Hoelzle, M. Cross-Comparison of Albedo Products for Glacier Surfaces Derived from Airborne and Satellite (Sentinel-2 and Landsat 8) Optical Data. Remote Sens. 2017, 9, 110. [CrossRef]

33. Fugazza, D.; Senese, A.; Azzoni, R.S.; Maugeri, M.; Maragno, D.; Diolaiuti, G.A. New Evidence of Glacier Darkening in the Ortles-Cevedale Group from Landsat Observations. Glob. Planet. Chang. 2019, 178, 35–45. [CrossRef]

34. Liang, S. Narrowband to Broadband Conversions of Land Surface Albedo I: Algorithms. Remote Sens. Environ. 2001, 76, 213–238. [CrossRef]

35. Knap, W.H.; Reijmer, C.H.; Oerlemans, J. Narrowband to Broadband Conversion of Landsat TM Glacier Albedos. Int. J. Remote Sens. 1999, 20, 2091–2110. [CrossRef]

36. Foga, S.; Scaramuzza, P.L.; Guo, S.; Zhu, Z.; Dilley, R.D., Jr.; Beckmann, T.; Schmidt, G.L.; Dwyer, J.L.; Hughes, M.J.; Laue, B. Cloud Detection Algorithm Comparison and Validation for Operational Landsat Data Products. Remote Sens. Environ. 2017, 194, 379–390. [CrossRef]

37. Zanter, K. Landsat 8 (L8) Data Users Handbook. In Landsat Sci. Off. Website. Available online: https://www.usgs.gov/media/ files/landsat-8-data-users-handbook (accessed on 19 February 2021).

38. Picard, G.; Libois, Q.; Arnaud, L.; Vérin, G.; Dumont, M. Estimation of Superficial Snow Specific Surface Area from Spectral Albedo Time-Series at Dome C, Antarctica. Cryosphere Discuss 2016, 1–39. [CrossRef]

39. Vermote, E.F.; Tanré, D.; Deuze, J.L.; Herman, M.; Morcette, J.-J. Second Simulation of the Satellite Signal in the Solar Spectrum, 6S: An Overview. IEEE Trans. Geosci. Remote Sens. 1997, 35, 675–686. [CrossRef]

40. Hersbach, H.; Bell, B.; Berrisford, P.; Hirahara, S.; Horányi, A.; Muñoz-Sabater, J.; Nicolas, J.; Peubey, C.; Radu, R.; Schepers, D.; et al. The ERA5 Global Reanalysis. Q. J. R. Meteorol. Soc. 2020, 146, 1999–2049. [CrossRef]

41. Gelaro, R.; McCarty, W.; Suárez, M.J.; Todling, R.; Molod, A.; Takacs, L.; Randles, C.A.; Darmenov, A.; Bosilovich, M.G.; Reichle, R. The Modern-Era Retrospective Analysis for Research and Applications, Version 2 (MERRA-2). J. Clim. 2017, 30, 5419–5454. [CrossRef] [PubMed]

42. Howat, I.M.; Porter, C.; Smith, B.E.; Noh, M.-J.; Morin, P. The Reference Elevation Model of Antarctica. Cryosphere 2019, 13, 665–674. [CrossRef]

43. Howat, I.M.; Negrete, A.; Smith, B.E. The Greenland Ice Mapping Project (GIMP) Land Classification and Surface Elevation Data Sets. Cryosphere 2014, 8, 1509–1518. [CrossRef]

44. Wiscombe, W.J.; Warren, S.G. A Model for the Spectral Albedo of Snow. I: Pure Snow. J. Atmos. Sci. 1980, 37, 2712–2733. [CrossRef]

45. Lupi, A. Basic and Other Measurements of Radiation at Concordia Station; Institute of Atmospheric Sciences and Climate of the Italian National Research Council: Bologna, Italy, 2020.

46. Schmithüsen, H. Basic and Other Measurements of Radiation at Neumayer Station; Alfred Wegener Institute, Helmholtz Centre for Polar and Marine Research: Bremerhaven, Germany, 2020.

47. Ogihara, H. Basic and Other Measurements of Radiation at Station Syowa; National Institute of Polar Research: Tokyo, Japan, 2019.

48. Briegleb, B.P.; Minnis, P.; Ramanathan, V.; Harrison, E. Comparison of Regional Clear-Sky Albedos Inferred from Satellite Observations and Model Computations. J. Clim. Appl. Meteorol. 1986, 25, 214–226. [CrossRef]

49. Dickinson, R.E. Land surface processes and climate—Surface albedos and energy balance. In Advances in Geophysics, Proceedings of the A Symposium Commemorating the Two-Hundredth Anniversary of the Academy of Sciences of Lisbon, Lisbon, Portugal, 12–14 October 1981; Academic Press: Cambridge, MI, USA, 1983; Volume 25, pp. 305–353.

50. Pinker, R.T.; Laszlo, I. Modeling Surface Solar Irradiance for Satellite Applications on a Global Scale. J. Appl. Meteorol. Climatol. 1992, 31, 194–211. [CrossRef]

51. Wang, Z.; Barlage, M.; Zeng, X.; Dickinson, R.E.; Schaaf, C.B. The Solar Zenith Angle Dependence of Desert Albedo. Geophys. Res. Lett. 2005, 32. [CrossRef]

52. Yang, F.; Mitchell, K.; Hou, Y.-T.; Dai, Y.; Zeng, X.; Wang, Z.; Liang, X.-Z. Dependence of Land Surface Albedo on Solar Zenith Angle: Observations and Model Parameterization. J. Appl. Meteor. Climatol. 2008, 47, 2963–2982. [CrossRef]

53. Citterio, M.; Van As, D.; Ahlstrøm, A.P.; Andersen, M.L.; Andersen, S.B.; Box, J.E.; Charalampidis, C.; Colgan, W.T.; Fausto, R.S.; Nielsen, S.; et al. Automatic Weather Stations for Basic and Applied Glaciological Research. GEUS Bull. 2015, 69–72. [CrossRef]

54. Arndt, J.E.; Schenke, H.W.; Jakobsson, M.; Nitsche, F.O.; Buys, G.; Goleby, B.; Rebesco, M.; Bohoyo, F.; Hong, J.; Black, J.; et al. The International Bathymetric Chart of the Southern Ocean (IBCSO) Version 1.0—A New Bathymetric Compilation Covering Circum-Antarctic Waters. Geophys. Res. Lett. 2013, 40, 3111–3117. [CrossRef]

55. Yamanouchi, T. Variations of Incident Solar Flux and Snow Albedo on the Solar Zenith Angle and Cloud Cover, at Mizuho Station, Antarctica. J. Meteorol. Soc. Jpn. Ser. II 1983, 61, 879–893. [CrossRef]

56. Munneke, P.K.; Reijmer, C.H.; Van den Broeke, M.R. Assessing the Retrieval of Cloud Properties from Radiation Measurements over Snow and Ice. Int. J. Climatol. 2011, 31, 756–769. [CrossRef]

57. Cuffey, K.M.; Paterson, W.S.B. The Physics of Glaciers; Academic Press: Amsterdam, The Netherlands, 2010.

58. Bintanja, R. On the Glaciological, Meteorological, and Climatological Significance of Antarctic Blue Ice Areas. Rev. Geophys. 1999, 37, 337–359. [CrossRef]

59. Rignot, E.; Mouginot, J.; Scheuchl, B. MEaSUREs InSAR-Based Antarctica Ice Velocity Map, Version 2; NASA DAAC at the National Snow and Ice Data Center: Boulder, CO, USA, 2017.

60. Jakobs, C.L.; Reijmer, C.H.; Kuipers Munneke, P.; König-Langlo, G.; Van Den Broeke, M.R. Quantifying the Snowmelt-Albedo Feedback at Neumayer Station, East Antarctica. Cryosphere 2019, 13, 1473–1485. [CrossRef]

61. Munneke, P.K.; van den Broeke, M.R.; Lenaerts, J.T.M.; Flanner, M.G.; Gardner, A.S.; van de Berg, W.J. A New Albedo Parameterization for Use in Climate Models over the Antarctic Ice Sheet. J. Geophys. Res. Atmos. 2011, 116. [CrossRef]

62. Oerlemans, J. The Microclimate of Valley Glaciers; Igitur, Utrecht Publishing & Archiving Services: Utrecht, The Netherlands, 2010.

63. Gusain, H.S.; Singh, D.K.; Mishra, V.D.; Arora, M.K. Estimation of Net Radiation Flux of Antarctic Ice Sheet in East Dronning Maud Land, Antarctica, During Clear Sky Days Using Remote Sensing and Meteorological Data. Remote Sens. Earth Syst. Sci. 2018, 1, 89–99. [CrossRef]

64. Stroeve, J.C.; Box, J.E.; Haran, T. Evaluation of the MODIS (MOD10A1) Daily Snow Albedo Product over the Greenland Ice Sheet. Remote Sens. Environ. 2006, 105, 155–171. [CrossRef]

65. Li, Z.; Erb, A.; Sun, Q.; Liu, Y.; Shuai, Y.; Wang, Z.; Boucher, P.; Schaaf, C. Preliminary Assessment of 20-m Surface Albedo Retrievals from Sentinel-2A Surface Reflectance and MODIS/VIIRS Surface Anisotropy Measures. Remote Sens. Environ. 2018, 217, 352–365. [CrossRef]

66. Knap, W.H.; Brock, B.W.; Oerlemans, J.; Willis, I.C. Comparison of Landsat TM-Derived and Ground-Based Albedos of Haut Glacier d'Arolla, Switzerland. Int. J. Remote Sens. 1999, 20, 3293–3310. [CrossRef]

67. He, T.; Liang, S.; Wang, D.; Cao, Y.; Gao, F.; Yu, Y.; Feng, M. Evaluating Land Surface Albedo Estimation from Landsat MSS, TM, ETM+, and OLI Data Based on the Unified Direct Estimation Approach. Remote Sens. Environ. 2018, 204, 181–196. [CrossRef]

3.3 Short Note "Evaluation of Anisotropic Correction Factors for the Calculation of Landsat 8 Oli Albedo on the Ice Sheets" (Traversa & Fugazza, 2021)

Giacomo Traversa [1,2*] & Davide Fugazza [2]

[1] Department of Physical Sciences, Earth and Environment (DSFTA), Università Degli Studi Di Siena, 53100 Siena, Italy;

[2] Department of Environmental Science and Policy (ESP), Università Degli Studi Di Milano, 20133 Milan, Italy;

* Corresponding author: G. Traversa (giacomo.traversa@student.unisi.it)

Abstract: The calculation of ice and snow albedo on the ice sheets from remote sensing has always been an important objective in climate research, especially at a high spatial resolution. In this study, a model of albedo retrieval based on Landsat 8 OLI satellite data is validated by comparing ground observations from Antarctica and Greenland, with a particular focus on the anisotropic correction of satellite data. Different correction factors for the anisotropy of snow and ice were considered, as well as two different conversion formulas from narrowband to broadband albedo. Our findings point out that existing anisotropic-correction models are unable to adequately account for albedo variations at high solar zenith angles, which is a relevant factor in Greenland and especially in Antarctica. Thus, the present study suggests that the anisotropic correction may be omitted when calculating ice and snow albedo on the ice sheets, as on average worse statistics were found when using the correction.

1. Introduction

On the Antarctic Ice Sheet (AIS) and Greenland Ice Sheet (GrIS), where snow is the main type of surface, the albedo (or bi-hemispherical reflectance, Schaepman-Strub & alii, 2006) has an important impact on the surface energy balance. Specifically, in the polar regions, the albedo depends on various factors, i.e., snow metamorphism (Grenfell & Warren, 1994; Gay & alii, 2002; Warren & alii, 2006; Gallet & alii, 2011), snow density and stratigraphy and snow roughness, owed to the presence of different peculiar morphologies and surfaces (e.g., sastrugi, glazed snow, blue ice) (Bintanja, 1999; Frezzotti & alii, 2002; Scambos & alii, 2012; Traversa & alii, 2021a, 2022). Additionally, the rate of snow metamorphism is affected by temperature, relative humidity, wind and the overburden pressure (Pirazzini, 2004; Picard & alii, 2012; van Kampenhout & alii, 2017). While field campaigns for albedo acquisition using e.g., Automatic Weather Stations (AWSs) require a relevant logistic economical effort for Antarctica and Greenland, the calculation of this variable from remote sensing allows covering large areas and can exploit free imagery. Thus, this work aims at contributing to the knowledge of albedo variations of ice- and snow-covered surfaces from remote sensing and it complements a recent paper by Traversa & alii (2021b), which provided a model (based on previous

studies, Klok & alii, 2003; Fugazza & alii, 2016) to retrieve the albedo on the ice sheets based on Landsat imagery. The model by Traversa & alii (2021b) included 1) conversion from raw satellite data to radiance and reflectance; 2) atmospheric correction; 3) topographic correction; 4) conversion from narrowband to broadband albedo. An anisotropic correction step was lacking in this model, compared e.g. to the study of Naegeli & alii (2017) or Fugazza & alii (2019) which used a similar approach to calculate the albedo and its variations on Alpine glaciers. The anisotropic correction can be important because satellites can only measure radiance in a specific direction, but ice and snow do not reflect isotropically but rather show a higher amount of forward scattering compared to the other directions (Reijmer & alii, 2001). Based on such premises, this study evaluates different albedo retrievals from Landsat 8 OLI calculated by implementing anisotropic correction factors, and then converting anisotropically corrected narrowband albedo to broadband albedo using algorithms developed by (Knap & alii, 1999) and (Liang, 2001). The comparison between the different approaches has recently become possible as new correction factors for snow and ice at high Solar Zenith Angle (SZA) have been developed for Liang algorithm (Ren & alii, 2021), in addition to the existing ones based on Knap algorithm (Lucht & alii, 2000; Reijmer & alii, 2001). We then compare the two final albedo products against the values obtained in the previous study, lacking anisotropic correction (Traversa & alii, 2021b) and validate both methods through comparison with field observations from a network of weather stations.

2. Data and Methods

With respect to the satellite database used in this work, we included Landsat 8 OLI imagery acquired between 2013 and 2020 from Collection 2 products downloaded from the USGS Earth Explorer website (https://earthexplorer.usgs.gov/) (spatial resolution 30 m). We used bands 2-3-4-5-6 and 7, respectively: Blue, Green, Red, near-infrared (NIR) and the two shortwave-infrared (SWIR) bands which are required in spectral to broadband albedo conversion (Knap & alii, 1999; Liang, 2001). The Knap algorithm uses bands 3 and 5, while Liang algorithm uses bands 2 and 4-7. Each satellite band was processed through four corrections steps: radiometric, atmospheric, topographic and anisotropic correction. For the first three steps, see Traversa & alii (2021b) for further information, considering that a pixel-specific solar zenith angle was used for the radiometric correction, a sub-arctic winter model for the atmospheric correction and the cosine method for the topographic correction. Regarding the anisotropic correction, two different approaches were used to comply with Knap and Liang algorithms for narrowband to broadband albedo conversion. For Knap algorithm, bands 3 and 5 were corrected using the coefficients developed by Greuell & de Ruyter de Wildt (1999) for ice and

Reijmer & alii (2001) for snow. For the Liang algorithm, the coefficients developed by Ren & alii (2021) were used for bands 2 and 4-7. To discriminate between ice and snow, we followed the approach by Ren & alii (2021), i.e., by setting a threshold of 0.45 on the Normalized Difference Snow Index (NDSI). Additionally, we set pixels with a NDSI < 0 to non-icy areas. Here, the reflectance was assumed isotropic, and no anisotropic correction was applied. After calculating the anisotropic correction, the spectral albedo values for each scene were converted into broadband albedo using the two algorithms. We define $\alpha_{Knap,anis}$ as the final albedo calculated using anisotropic correction coefficients from Greuell and de Wildt (1999) and Reijmer & alii (2001) and Knap algorithm for broadband conversion. We describe as $\alpha_{Liang,anis}$ the final albedo calculated using anisotropic correction coefficients from Ren & alii (2021) and Liang algorithm for broadband conversion, while $\alpha_{Liang,na}$ is the albedo calculated without anisotropic correction. We compared all three albedo products to albedo observations from weather stations using three different datasets (Greenland: PROMICE AWSs, Van As & alii, 2011; Antarctica: IMAU AWSs, Jakobs & alii, 2020, and BSRN Stations, Driemel & alii, 2018). 64 scenes (21 in Greenland and 43 in Antarctica) were compared between 2013 and 2020 (for a detailed description of stations and scenes, see the final dataset of Traversa & alii, 2021b) and the statistics used to estimate the performance of the three models were: correlation coefficients (Cc or R), bias estimate (BE), mean absolute error (MAE), root-mean-square error (RMSE) and bias-removed-root-mean-square error (BRRMSE) (as defined in Traversa & alii, 2021b).

3. Results

In the comparison of the three models against ground observations, $\alpha_{Liang,na}$ presents the best statistics, showing a MAE of 0.022 (lower in Antarctica, with 0.020, against 0.026 for Greenland), an STD of 0.016, a BE of -0.007, a coefficient of correlation of 0.99 and RMSE and BRRMSE respectively of 0.027 and 0.026. Applying the anisotropic correction (Ren & alii, 2021), the statistics were worse and most of the times the errors increased two- to threefold compared to the previous case. The MAE of $\alpha_{Liang,anis}$ increases to 0.065 (in this case, Greenland has a lower MAE of 0.047, compared to 0.074 in Antarctica), an STD of 0.045, BE of -0.065 (more than 9 times higher than without the correction), a coefficient of correlation of 0.976, a RMSE of 0.080 and a BRRMSE of 0.047. In comparison, the albedo values from $\alpha_{Knap,anis}$ showed better statistics than $\alpha_{Liang,anis}$, However, these statistics were all worse than , showing values of MAE, STD, BE, R, RMSE and BRRMSE respectively of: 0.040 (0.047 in Antarctica and 0.027 in Greenland), 0.034, 0.016, 0.962, 0.053 and 0.051. All the statistics are summarized in table 1.

4. Discussion

Compared to the findings of Traversa & alii (2021b), Knap algorithm performs better than Liang algorithm when the anisotropic correction is applied, as all the calculated statistics, except for BRRMSE, are significantly better.

Tab. 1: Statistics of the validation of satellite-albedo with in-situ observations (64 scenes), with the three proposed models. Correlation is always significant at the 99% confidence level.

Dataset	MAE tot	AIS MAE	GrIS MAE	STD	BE	R	RMSE	BRRMSE
$\alpha_{Liang,na}$	0.022	0.020	0.026	0.016	-0.007	0.990	0.027	0.026
$\alpha_{Liang,anis}$	0.065	0.074	0.047	0.045	-0.065	0.976	0.080	0.047
$\alpha_{Knap,anis}$	0.040	0.047	0.027	0.034	0.016	0.962	0.053	0.051

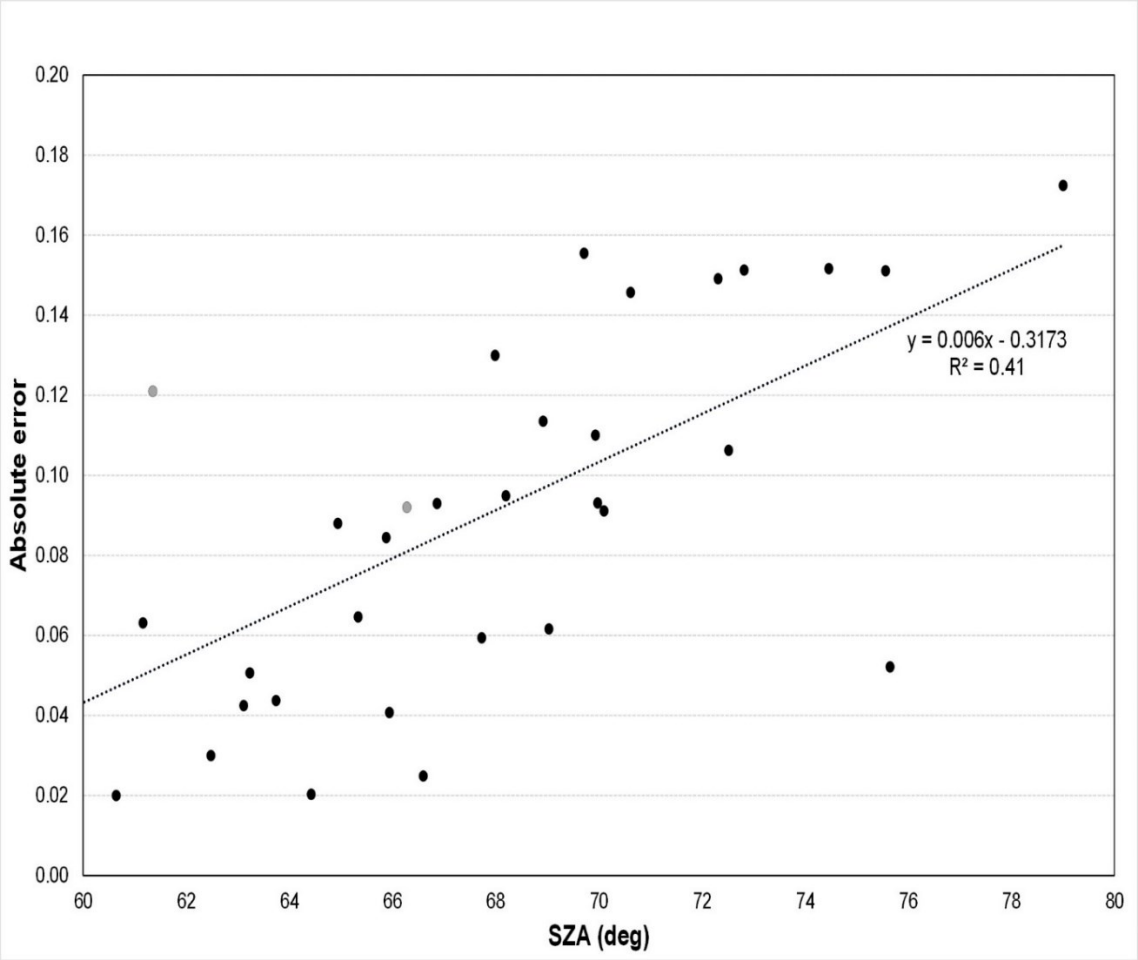

Fig. 1. Plot showing SZA (x) and absolute error (y) of scenes having SZA > 60° (α_(Liang,anis)), demonstrating the correlation between the two parameters (grey dots for GrIS and black dots for AIS).

Nevertheless, worse results were obtained in comparison to the model proposed by Traversa & alii (2021b), which used Liang conversion to broadband albedo without any correction for anisotropy. In detail, looking at the MAE for the AIS and GrIS, it is evident how the statistics were worse especially for Antarctica, while in Greenland only slight differences were found between $\alpha_{Liang,na}$ and $\alpha_{Knap,anis}$ (0.026 vs 0.027). What mostly diverges between the scenes used for satellite albedo validation in Antarctica and Greenland is the SZA, which tends to be generally higher on the AIS than on the GrIS (on average 65° and 50° respectively), due to the different latitude range (between 59° and 84° N for Greenland and between 63° and 90° S for Antarctica). In fact, anisotropy is strongly related to SZA and tends to increase with higher angles (Warren & alii, 1998). Anisotropic correction factors developed for Knap algorithm were not tested with such high SZA values (maximum SZA was given as 60° in Reijmer & alii, 2001), while the factors developed by Ren & alii (2021). In detail, in this study, 70% of Landsat scenes in Antarctica had a SZA > 60° compared to just 10% in Greenland. Calculating the correlation between the difference between ground and satellite albedo of each scene and the corresponding SZA, we found no correlation when using the albedo obtained in the previous model without anisotropic correction (Traversa & alii, 2021b), i.e. a correlation coefficient of -0.04, a much higher value for $\alpha_{Knap,anis}$, i.e. 0.25 and a significant (at 99% confidence level) correlation for αLiang,anis: 0.67 (fig. 1). The effect of the SZA could therefore explain the larger differences found for the Antarctic continent and the lower ones in Greenland, as in the second case the average latitude of ground observations is lower, as is the corresponding SZA. In fact, out of 32 scenes having SZA ≥ 60°, only 2 are located on the GrIS and 30 on AIS. These findings highlight how the present anisotropic-correction models do not adequately compensate for the SZA, which is particularly relevant in polar regions (Traversa & alii, 2019). Nevertheless, it is also evident that the anisotropic-correction factors for snow and ice proposed for Knap algorithm by Reijmer & alii (2001) provide reliable results when SZA is lower than 60°, in accordance with the findings of Fugazza & alii (2016).

5. Conclusions

The present study intends to evaluate the use of anisotropic correction for calculating broadband albedo on the ice-sheets (AIS and GrIS), through a comparison between Landsat 8 OLI imagery, corrected following the model of Traversa & alii (2021b), and three different datasets of ground observations from AWSs and manned weather stations (Van As & alii, 2011; Driemel & alii, 2018; Jakobs & alii, 2020). Three models were taken into account: one using Liang algorithm for narrowband to broadband conversion, without anisotropic correction (Traversa & alii, 2021b) and two models with anisotropic correction (Reijmer & alii, 2001; Ren & alii, 2021) using Knap and

Liang algorithm for conversion to broadband albedo. The statistics were all better in the first case, and a significant correlation was found between the difference between ground and satellite albedo and the SZA when using anisotropic correction factors developed for Liang algorithm, particularly at high SZA (> 60°). Thus, considering that on Greenland and particularly the AIS the SZA can be higher than 60°, our findings suggest that the anisotropic correction may be omitted for these polar areas. and a model that does not include this correction, e.g., Traversa model (Traversa & alii, 2021b), would be more efficient at present to calculate broadband albedo on the ice-sheets from satellite data from Landsat 8 OLI. More research is needed to develop anisotropic correction factors which can adequately represent ice sheet albedo at high SZA.

References

Bintanja R. (1999) - On the glaciological, meteorological, and climatological significance of Antarctic blue ice areas. Reviews of Geophysics, 37 (3), 337-359.

Driemel A., Augustine J., Behrens K., Colle S., Cox C., Cuevas- Agulló E., Denn F.M., Duprat T., Fukuda M., Grobe H., Haeff elin M., Hodg es G., Hyett N., Ijima O., Kallis A., Knap W., Kustov V., Long C.N., Longenecker D., Lupi A., Maturilli M., Mimouni M., Ntsangw ane L., Ogihara H., Olano X., Olefs M., Omori M., Passamani L., Pereira E.B., Schmithüsen H., Schumacher S., Sieger R., Tamlyn J., Vogt R., Vuilleumier L., Xia X., Ohmura A. & König-Langlo G. (2018) - Baseline Surface Radiation Network (BSRN): structure and data description (1992- 2017). Earth System Science Data, 10 (3), 1491-1501. doi: 10.5194/ essd-10-1491-2018.

Frezzott i M., Gandolfi S., Marca F.L. & Urbini S. (2002) - Snow dunes and glazed surfaces in Antarctica: new field and remote-sensing data. Annals of Glaciology, 34, 81-88. doi: 10.3189/172756402781817851

Fugazza D., Senese A., Azzoni R.S., Maugeri M. & Diolaiuti G.A. (2016) - Spatial distribution of surface albedo at the Forni Glacier (Stelvio National Park, Central Italian Alps). Cold Regions Science and Technology, 125, 128-137. doi: 10.1016/j.coldregions.2016.02.006

Fugazza D., Senese A., Azzoni R.S., Maugeri M., Maragno D. & Diolaiuti G.A. (2019) - New evidence of glacier darkening in the Ortles-Cevedale group from Landsat observations. Global and Planetary Change, 178, 35-45. doi: 10.1016/j.gloplacha.2019.04.014

Gallet J.-C., Domine F., Arnaud L., Picard G. & Savarino J. (2011) - Vertical profile of the specific surface area and density of the snow at Dome C and on a transect to Dumont D'Urville, Antarctica –

albedo calculations and comparison to remote sensing products. The Cryosphere, 5 (3), 631-649. doi: 10.5194/tc-5-631-2011

Gay M., Fily M., Genthon C., Frezzott i M., Oerter H. & Winther J.-G. (2002) - Snow grain-size measurements in Antarctica. Journal of Glaciology, 48 (163), 527-535.

Grenfell T.C. & Warren S.G. (1994) - Reflection of solar radiation by the Antarctic snow surface at ultraviolet, visible, and near-infrared wavelengths. Journal of Geophysical Research: Atmosphere, 99 (D9), 18669-18684.

Greuell W. & de Ruyter de Wildt M. (1999) - Anisotropic reflection by melting glacier ice: Measurements and parametrizations in Landsat TM bands 2 and 4. Remote Sensing of Environment, 70 (3), 265-277.

Jakobs C.L., Reijmer C.H., Smeets C.J.P.P., Trusel L.D., van de Berg W.J., van den Broeke M.R. & van Wessem J.M. (2020) - A benchmark dataset of in situ Antarctic surface melt rates and energy balance. Journal of Glaciology, 66 (256), 291-302. doi: 10.1017/jog.2020.6

Klok E.L., Greuell W. & Oerlemans J. (2003) - Temporal and spatial variation of the surface albedo of Morteratschgletscher, Switzerland, as derived from 12 Landsat images. Journal of Glaciology, 49 (167), 491-502. doi: 10.3189/172756503781830395.

Knap W.H., Reijmer C.H. & Oerlemans J. (1999) - Narrowband to broadband conversion of Landsat TM glacier albedos. International Journal of Remote Sensing, 20 (10), 2091-2110.

Liang S. (2001) - Narrowband to broadband conversions of land surface albedo I: Algorithms. Remote sensing of environment, 76 (2), 213-238. doi: 10.1016/S0034-4257(00)00205-4

Lucht W., Schaaf C.B. & Strahler A.H. (2000) - An algorithm for the retrieval of albedo from space using semiempirical BRDF models. IEEE Transactions on Geoscience and Remote sensing, 38 (2), 977-998.

Naegeli K., Damm A., Huss M., Wulf H., Schaepman M. & Hoelzle M. (2017) - Cross-Comparison of Albedo Products for Glacier Surfaces Derived from Airborne and Satellite (Sentinel-2 and Landsat 8) Optical Data. Remote Sensing, 9 (2), 110. doi: 10.3390/rs9020110

Picard G., Domine F., Krinner G., Arnaud L. & Lefebvre E. (2012) - Inhibition of the positive snow-albedo feedback by precipitation in interior Antarctica. Nature Climate Change, 2 (11), 795-798.

Pirazzini R. (2004) - Surface albedo measurements over Antarctic sites in summer. Journal of Geophysical Research, 109 (D20), D20118. doi: 10.1029/2004JD004617

Reijmer C.H., Bintanja R. & Greuell W. (2001) - Surface albedo measurements over snow and blue ice in thematic mapper bands 2 and 4 in Dronning Maud Land, Antarctica. Journal of Geophysical Research: Atmospheres, 106 (D9), 9661-9672.

Ren S., Miles E., Jia L., Menenti M., Kneib M., Buri P., McCarthy M., Shaw T., Yang W. & Pellicciott i F. (2021) – Anisotropy Parameterization Development and Evaluation for Glacier Surface Albedo Retrieval from Satellite Observations. Remote Sensing, 13, 1714. doi: 10.3390/rs13091714

Scambos T.A., Frezzott i M., Haran T., Bohlander J., Lenaerts J.T.M., Van Den Broeke M.R., Jezek K., Long D., Urbini S., Farness K., Neumann T., Albert M. & Winther J.-G. (2012) – Extent of low-accumulation 'wind glaze' areas on the East Antarctic plateau: implications for continental ice mass balance. Journal of Glaciology, 58 (210), 633-647. doi: 10.3189/2012JoG11J232.

Schaepman-Strub G., Schaepman M.E., Painter T.H., Dangel S. & Martonchik J.V. (2006) - Reflectance quantities in optical remote sensing—Definitions and case studies. Remote sensing of environment, 103 (1), 27-42. doi: 10.1016/j.rse.2006.03.002.

Traversa G., Fugazza D., Senese A. & Diolaiuti G.A. (2019) – Preliminary results on Antarctic albedo from remote sensing observations. Geografia Fisica e Dinamica Quaternaria, 42 (2), 245-254. doi: 10.4461/GFDQ.2019.42.14.

Traversa G., Fugazza D. & Frezzott i M. (2021a) - Analysis of Megadune Fields in Antarctica. IEEE, 2021 IEEE International Geoscience and Remote Sensing Symposium IGARSS, 5513-5516. doi: 10.1109/IGARSS47720.2021.9554827.

Traversa G., Fugazza D., Senese A. & Frezzott i M. (2021b) – Landsat 8 OLI Broadband Albedo Validation in Antarctica and Greenland. Remote Sensing, 13 (4), 799. doi: 10.3390/rs13040799

Traversa G., Fugazza D. & Frezzott i M. (2022) - Megadunes in Antarctica: migration and evolution from remote and in situ observations. The Cryosphere Discussions, 1-30. doi: 10.5194/tc-2022-11.

Van As D., Ahlstrøm A.P., Andersen M.L., Citt erio M., Edelvang K., Gravesen P., Machguth H. & Nick F.M. (2011) - Programme for Monitoring of the Greenland Ice Sheet (PROMICE): first temperature and ablation records. Geological Survey of Denmark and Greenland Bulletin, 23, 73-76.

van Kampenhout L., Lenaerts J.T., Lipscomb W.H., Sacks W.J., Lawrence D.M., Slater A.G. & van den Broeke M.R. (2017) – Improving the representation of polar snow and firn in the Community Earth System Model. Journal of Advances in Modeling Earth Systems, 9 (7), 2583-2600.

Warren S.G., Brandt R.E. & O'Rawe Hinton P. (1998) - Effect of surface roughness on bidirectional reflectance of Antarctic snow. Journal of Geophysical Research: Planets, 103 (E11), 25789-25807.

Warren S.G., Brandt R.E. & Grenfell T.C. (2006) - Visible and near-ultraviolet absorption spectrum of ice from transmission of solar radiation into snow. Applied Optics, 45 (21), 5320-5334.

3.4 Conclusion of the chapter

In conclusion of the chapter focused on albedo and in particular in the definition of a methodology to calculate it using Landsat imagery, it is provided a method for broadband albedo, validated against a large number of in-situ measurements in both Greenland and Antarctic ice sheets. This method presents a low uncertainty of about ±0.02 α (MAE). In detail, looking at the different correction step: it is suggested the use of the SZA band for radiometric calibration instead of using an averaged SZA value for the entire scene (even if just a slight improvement exists); there are no significant identified advantages in using a self-defined model for atmospheric correction in 6S algorithm, as the statistics remain unvaried when using the already existing sub-arctic winter model. However, in the atmospheric correction, the AOT value is of relevance, even if a slight variation of this parameter in the order of ±0.01 resulted not so relevant and from our survey a low value of 0.02 could be considered as meanly representative for Antarctica. Then, an evident improvement using the Liang algorithm instead of Knap algorithm was evident in both Antarctica and Greenland. Finally, with the present knowledge, it is suggested avoiding the application of snow and ice factors for anisotropic correction, as they resulted to be dependent to high SZA values (>60°), which are however often present at these high latitudes, especially in the Antarctic continent. Future efforts could focus on narrowband albedo over single bands of Landsat, as well as on the applicability of this methodology on other analogous satellites, such as Sentinel-2.

Chapter 4: Megadunes and wind crust

4.1 Presentation of the chapter

In the present chapter a detailed survey of Antarctic snow megadunes is carried out, in consideration of their glaciological and geomorphological interest and their link with ablation areas, i.e., wind crust. In particular, the focus is on their optical properties, i.e., albedo and brightness temperature, whose analyses is possible by using high resolution satellite images from Landsat 8 OLI-TIRS and Sentinel-2, and on their migration. The optical properties, together with the SPWD, were then used to identify a methodology to automatically detect wind crust, taking advantage of their peculiar characteristics in respect to the surrounding snow. In the second case, a combination of remote (REMA DEM) and field measurements (GPS-GPR) was used, as well as Landsat and Sentinel-2 imagery for detecting and defining the different components of the migration. An initial survey of the first optical analyses is part of a published conference proceeding; a more detailed optical analyses, wind-crust automatic detection methodology and above all megadunes migration is then included in another article. The publications are: “Traversa, G., Fugazza, D., & Frezzotti, M. (2021). Analysis of Megadune Fields in Antarctica. In 2021 IEEE International Geoscience and Remote Sensing Symposium IGARSS (pp. 5513-5516). IEEE, doi: 10.1109/IGARSS47720.2021.9554827” (Section 4.2) and “Traversa, G., Fugazza, D., and Frezzotti, M. (2023). Megadunes in Antarctica: migration and characterization from remote and in situ observations, The Cryosphere, 17, 427–444, https://doi.org/10.5194/tc-17-427-2023” (Section 4.3).

4.2 Conference proceeding "Analysis of Megadune Fields in Antarctica" (Traversa et al., 2021b)

Giacomo Traversa [1,2], Davide Fugazza [2], and Massimo Frezzotti [3]

[1] Department of Physical Sciences, Earth and Environment (DSFTA), Università Degli Studi Di Siena, 53100 Siena, Italy;

[2] Department of Environmental Science and Policy (ESP), Università Degli Studi Di Milano, 20133 Milan, Italy;

[3] Department of Science, Università Degli Studi Roma Tre, 00146 Rome, Italy

Abstract: In this research, we present new and updated properties of the megadune fields, which are largely distributed on the Antarctic plateau. We used mainly Landsat 8 OLI imagery in order to characterize the megadune fields using visible and Near Infrared bands. Focusing on two areas where megadunes occur, we provide detailed albedo measurements, both broadband and near-infrared, differentiating their upwind and downwind parts. In addition, we calculated their brightness temperature. Using the wind surface morphology obtained from Landsat 8 OLI images and the REMA DTM, we also calculated the Slope in the Prevailing Wind Direction at about ten meters scale, which provided information about the formation of snow glazed surfaces. Finally, we studied the upwind migration of the megadunes and compared these results with other remote-sensing products and in-situ measurements.

1. Introduction

Snow megadune fields are a peculiar feature observed on East Antarctic Ice Sheet (EAIS) and on the Martian North Pole [1]–[3]. The area of Antarctic Megadunes, covering about 550,000 km^2, is one of the most inhospitable, unexplored and undocumented territories on Earth, comprising the most extensive desert and coldest area of our planet. This study concerns the analysis of megadune fields on the EAIS. These morphologies are originated from the peculiar interaction between snow accumulation, metamorphism, and wind-driven ablation process (glazed surfaces). The Slope along Wind Direction (SPWD) is the main driver of the formation of the transverse dune, tens of km long, characterized by a snow surface on the upwind flank and a glazed surface on the downwind flank [4]. Megadunes are relevant for Surface Mass Balance (SMB), as their downwind part, covered by snow glazed surfaces, has near-zero SMB, due to katabatic wind driven ablation process [5], [6]. This study focuses on two specific areas of the Antarctic Plateau (Fig. 1 left), respectively located 300 km East of the Russian Vostok Station and 150 km East of the French-Italian Concordia Station, where megadunes are largely present. The research takes advantage of remote sensing imagery, in order to provide new relevant analysis on these very peculiar morphologies.

2. Materials and Methods

Due to the remoteness and harsh environmental condition, remote sensing is the most suited methodology for the analysis of megadune fields.

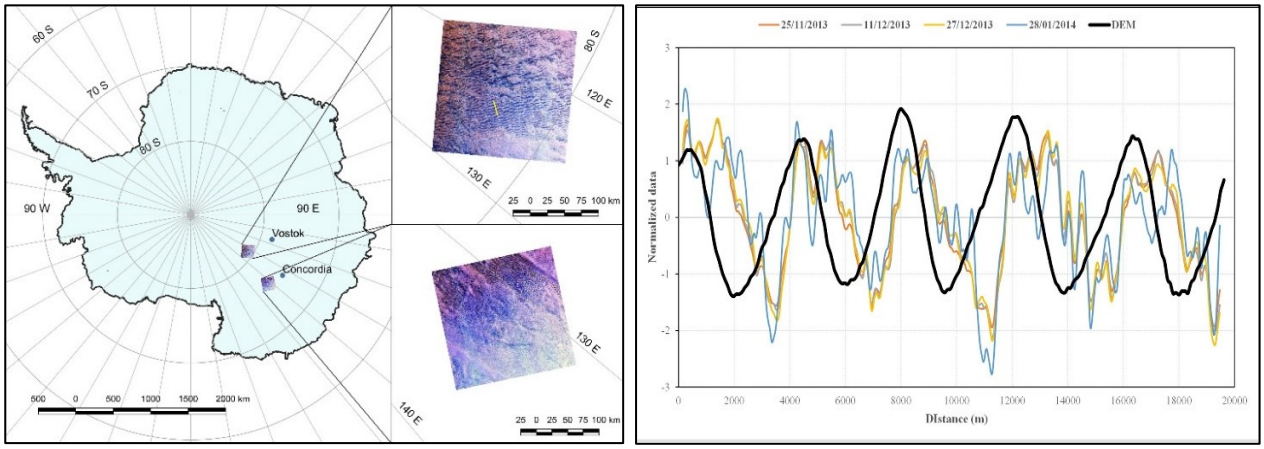

Figure 1: study area locations showing the transect AB in yellow (left) and normalized NIR albedo and normalized-detrended topography plot of the transect (right).

We employed Landsat imagery (above all Landsat 8 OLI) for optical analysis, by calculating broadband albedo, near-infrared spectral albedo, and brightness temperature. As concerns the albedo calculation, we implemented the method originally proposed by Klok et al. 2003 [7] and then adjusted by Fugazza et al. 2016 [8] and for polar regions by Traversa et al. 2021 [9]. The albedo calculation includes four main steps: radiometric calibration (including solar zenith angle correction), atmospheric and topographic corrections and narrowband to broadband albedo conversion (using Liang's algorithm [10]). Regarding the brightness temperature, we calculated it from the two thermal bands of Landsat 8 TIR. To these optical properties, we added also a characterization based on wind properties, the location of macro-relief features (glazed surfaces, transverse dunes, megadunes, glazed surface and sastrugi fields), whose direction and extent were determined by satellite image analysis. Prevalent wind direction was obtained at large scale (pixel size 30 m) based on sastrugi, and validated against small scale wind direction (pixel size 30 km) derived from ERA5 [11] (European center for meteorological weather forecast Re-Analysis) and was then used to calculate SPWD. The sastrugi are morphologies parallel to the prevailing wind (katabatic winds) and are therefore useful to derive the wind direction also at local scale [4]. Their direction was obtained by applying an edge-finding algorithm on a Principal Component Analysis of false colour Landsat 8 bands (NIR, Red and Green). The SPWD was calculated using REMA [12] as the terrain model, taking advantage of its high spatial resolution (pixel size 8 m). Finally, we studied the absolute migration of megadunes during the past 20 years, that is the result of the sedimentological migration and the ice-flow. The last parameter was

obtained by MEaSUREs ice-flow velocity product [13] and GPS measurements from the 1998 Italian Traverse [14]. Additionally, during this Italian traverse, GPS and GPR data along different transects were acquired; these data were used in conjunction with the REMA DSM to obtain the sedimentological migration of the dunes. Regarding the absolute migration, we took advantage of Landsat 7 ETM+ and Landsat 8 OLI images (20-year span), by utilizing a feature tracking module (IMCORR, [15], [16]). As comparison, in order to validate these results, we also calculated the migration over a shorter period, by only using Landsat 8 OLI imagery (6-year span). Seven line transects (parallel to the wind direction, e.g., Fig. 1 right) and thirty control polygons, distributed in the two areas, were utilized for statistics and surface characterizations.

3. Results and discussion

With the aim of characterizing megadune fields in Antarctica, firstly the albedo provides interesting results. Snow glazed surfaces show slightly lower albedo with respect to the snow surface present in the upwind dune flank and surrounding snow plateau (see Fig. 1 right). The comparison of albedo observations and SPWD demonstrated their strong correlations ($r > 0.8$ for NIR spectral albedo). However, the difference between snow glazed surfaces and snow is higher considering NIR spectral albedo. To a "higher" amount of solar radiation absorbed by the surface, corresponds also a different brightness temperature on snow glazed surfaces. In fact, these zones show higher brightness temperature compared to the upwind part of the dune characterized by snow surface. In addition, the SPWD changes suddenly in proximity of glazed surfaces, becoming positive (on the rest of the area it tends to be negative). The correlation coefficients between SPWD and albedo and brightness temperature are very high, in particular with NIR albedo, and in general much higher than with topographic slope. All these findings allow better understanding the characteristics of megadune fields and their glazed areas and would improve their automatic detection. In addition, we decided to focus on the calculation of megadune absolute migration. By implementing IMCORR feature tracking module, we obtained results, both over the long and short period, in accordance with the vectorial sum of ice-flow (MEaSUREs or GPS) and the sedimentological migration (derived from 1998 Italian traverse and REMA DSM), resulting in a superficial speed around 10 m/yr. Thus, we discovered that the intensity of sedimentary migration is about one order of magnitude higher than the ice-flow. In addition, the study confirmed the "antidunal" sedimentological formation [2] of the megadunes that migrate with time in direction opposite to the SPWD.

4. Conclusions

This analysis of megadune fields on the Antarctic plateau confirmed and described previous hypothesized theories on such unique landforms, by providing updated and new results regarding their optical properties, both of albedo (spectral and broadband) and brightness temperature, as well as of SPWD and topographic slope. All this information is of relevance for mapping megadunes and especially their leeward flank, covered in snow glaze surfaces and thus important for the surface mass balance of the Antarctic continent. In addition, detailed analysis on megadune migration and all its components is here proposed, by using remote sensing data validated with field measurements.

References

[1] M. A. Fahnestock, T. A. Scambos, C. A. Shuman, R. J. Arthern, D. P. Winebrenner, and R. Kwok, 'Snow megadune fields on the East Antarctic Plateau: Extreme atmosphere-ice interaction', Geophysical research letters, vol. 27, no. 22, pp. 3719–3722, 2000.

[2] M. Frezzotti, S. Gandolfi, and S. Urbini, 'Snow megadunes in Antarctica: Sedimentary structure and genesis', Journal of Geophysical Research: Atmospheres, vol. 107, no. D18, p. ACL 11-ACL 1-12, 2002, doi: 10.1029/2001JD000673.

[3] C. Herny et al., 'Sedimentation waves on the Martian North Polar Cap: Analogy with megadunes in Antarctica', Earth and Planetary Science Letters, vol. 403, pp. 56–66, Oct. 2014, doi: 10.1016/j.epsl.2014.06.033.

[4] M. Frezzotti, S. Gandolfi, F. L. Marca, and S. Urbini, 'Snow dunes and glazed surfaces in Antarctica: new field and remotesensing data', Ann. Glaciol., vol. 34, pp. 81–88, 2002, doi: 10.3189/172756402781817851.

[5] T. A. Scambos et al., 'Extent of low-accumulation "wind glaze" areas on the East Antarctic plateau: implications for continental ice mass balance', J. Glaciol., vol. 58, no. 210, pp. 633–647, 2012, doi: 10.3189/2012JoG11J232.

[6] I. Das et al., 'Influence of persistent wind scour on the surface mass balance of Antarctica', Nature Geosci, vol. 6, no. 5, pp. 367371, May 2013, doi: 10.1038/ngeo1766.

[7] E. L. Klok, W. Greuell, and J. Oerlemans, 'Temporal and spatial variation of the surface albedo of Morteratschgletscher, Switzerland, as derived from 12 Landsat images', Journal of Glaciology, vol. 49, no. 167, pp. 491–502, 2003.

[8] D. Fugazza, A. Senese, R. S. Azzoni, M. Maugeri, and G. A. Diolaiuti, ‘Spatial distribution of surface albedo at the Forni Glacier (Stelvio National Park, Central Italian Alps)’, Cold Regions Science and Technology, vol. 125, pp. 128–137, May 2016, doi: 10.1016/j.coldregions.2016.02.006.

[9] G. Traversa, D. Fugazza, A. Senese, and M. Frezzotti, ‘Landsat 8 OLI Broadband Albedo Validation in Antarctica and Greenland’, Remote Sensing, vol. 13, no. 4, p. 799, 2021.

[10] S. Liang et al., ‘Narrowband to broadband conversions of land surface albedo: II. Validation’, Remote Sensing of Environment, vol. 84, no. 1, pp. 25–41, 2003.

[11] H. Hersbach et al., ‘The ERA5 Global Reanalysis’, Q J R Meteorol Soc, p. qj.3803, May 2020, doi: 10.1002/qj.3803.

[12] I. M. Howat, C. Porter, B. E. Smith, M.-J. Noh, and P. Morin, ‘The Reference Elevation Model of Antarctica’, The Cryosphere, vol. 13, no. 2, pp. 665–674, Feb. 2019, doi: https://doi.org/10.5194/tc-13-665-2019.

[13] E. Rignot, J. Mouginot, and B. Scheuchl, ‘MEaSUREs InSAR-based Antarctica ice velocity map, version 2’, Boulder, CO: NASA DAAC at the National Snow and Ice Data Center, 2017.

[14] P. Mayewski and I. Goodwin, ‘Antarctic’s role pursued in global climate change’, Eos, Transactions American Geophysical Union, vol. 80, no. 35, pp. 398–400, 1999.

[15] M. A. Fahnestock, T. A. Scambos, and R. A. Bindschadler, ‘Semi-automated ice velocity determination from satellite imagery’, Eos, vol. 73, p. 493, 1992.

[16] T. A. Scambos, M. J. Dutkiewicz, J. C. Wilson, and R. A. Bindschadler, ‘Application of image cross-correlation to the measurement of glacier velocity using satellite image data’, Remote sensing of environment, vol. 42, no. 3, pp. 177–186, 1992.

4.3 Article "Megadunes in Antarctica: migration and characterization from remote and in situ observations" (Traversa et al., 2023)

Giacomo Traversa [1,2], Davide Fugazza [3], and Massimo Frezzotti [4]

[1] Institute of Polar Sciences, National Research Council of Italy, 20125 Milano, Italy

[2] Department of Physical Sciences, Earth and Environment (DSFTA), Università Degli Studi Di Siena, 53100 Siena, Italy;

[3] Department of Environmental Science and Policy (ESP), Università Degli Studi Di Milano, 20133 Milan, Italy;

[4] Department of Science, Università Degli Studi Roma Tre, 00146 Rome, Italy

Abstarct: Megadunes are peculiar features formed by the interaction between the atmosphere and cryosphere and are known to be present only on the East Antarctic Plateau and other planets (Mars and Pluto). In this study, we have analysed the glaciological dynamic of megadunes, their spectral properties and morphology on two sample areas of the East Antarctic Plateau where in the past international field activities were carried out (EAIIST, East Antarctic International Ice Sheet Traverse; It-ITASE, Italian International Trans-Antarctic Scientific Expedition). Using satellite images spanning 7 years, we analysed the spatial and temporal variability in megadune surface characteristics, i.e. near-infrared (NIR) albedo, thermal brightness temperature (BT) and slope along the prevailing wind direction (SPWD), useful for mapping them. These parameters allowed us to characterize and perform an automated detection of the glazed surfaces, and we determined the influence of the SPWD by evaluating different combinations of these parameters. The inclusion of the SPWD significantly increased the accuracy of the method, doubling it in certain analysed scenes. Using remote and field observations, for the first time we surveyed all the components of upwind migration (absolute, sedimentological and ice flow), finding an absolute value of about 10 m a−1. The analysis shows that the migration is driven by the snow accumulation on the crest and trough prograding upwind on the previous windward flanks characterized by glazed surface. Our results present significant implications for the surface mass balance estimation, paleo-climate reconstruction using ice cores, and the measurements using optical and radar images/data in the megadune areas.

1. Introduction

Antarctic climate and mass balance have been highlighted by the Special Report on the Ocean and Cryosphere in a Changing Climate (Meredith et al., 2019) by the Intergovernmental Panel on Climate Change (IPCC) among the main uncertainties for the climate system and sea level projections. Surface mass balance (SMB) is the net balance between the processes of snow precipitation and loss on a glacier surface and provides mass input to the surface of the Antarctic Ice Sheet. Therefore, it

represents an important control on the ice sheet surface mass balance and resulting contribution to global sea level change. Ice sheet SMB varies greatly across multiple scales of time (hourly to decadal) and space (metres to hundreds of kilometres), and it is notoriously challenging to observe and represent in atmospheric models (e.g. Agosta et al., 2019; Lenaerts et al., 2019). Moreover, given the difficulties in accessing the interior of the ice sheet, only limited field observation on past and current conditions exists. The southern part of the East Antarctic ice divide, from Concordia and Vostok stations to the South Pole, is the coldest and driest area on Earth and presents unique features called megadunes, which extend for more than 500 000 km^2 (Fahnestock et al., 2000). The drivers of megadune formation are uncommon snow accumulation and redistribution processes driven by wind scouring that remain relatively unexplained (Fahnestock et al., 2000; Frezzotti et al., 2002a, b; Courville et al., 2007; Scambos et al., 2012; Dadic et al., 2013; Ekaykin et al., 2015). Ground surveys of megadunes show that snow is removed from their leeward slopes where a specific erosional type of snow, “glazed surface” or “wind crust”, is formed as a result. In contrast, snow accumulation is increased on the windward slopes that are characterized by the depositional types of the snow microrelief termed “sastrugi”. Glazed surfaces form because wind and sublimation can ablate much more snow/firn than is accumulated by annual solid precipitation, causing a persistent SMB close to zero or which is negative. The stability of climatic conditions could play a key role in megadune formation, since snow precipitation is very low, while katabatic wind intensity and direction are stable; these conditions affect snow sintering and a high grade of snow metamorphism (Albert et al., 2004; Courville et al., 2007; Scambos et al., 2012; Dadic et al., 2013). Megadunes are oriented perpendicular to the slope along the prevailing wind direction (SPWD); wave amplitudes are small (up to 8 m); wavelengths range from 2 to over 5 km; and megadune crests are nearly parallel, extending from tens to hundreds of kilometres (Swithinbank et al., 1988; Fahnestock et al., 2000; Frezzotti et al., 2002a, b; Arcone et al., 2012a, b). The angle between the katabatic wind direction and the direction of general surface slope at a regional scale can differ up to 50∘ due to the interaction between the topographic slope driving gravity and the Coriolis force (Fahnestock et al., 2000; Frezzotti et al., 2002b).

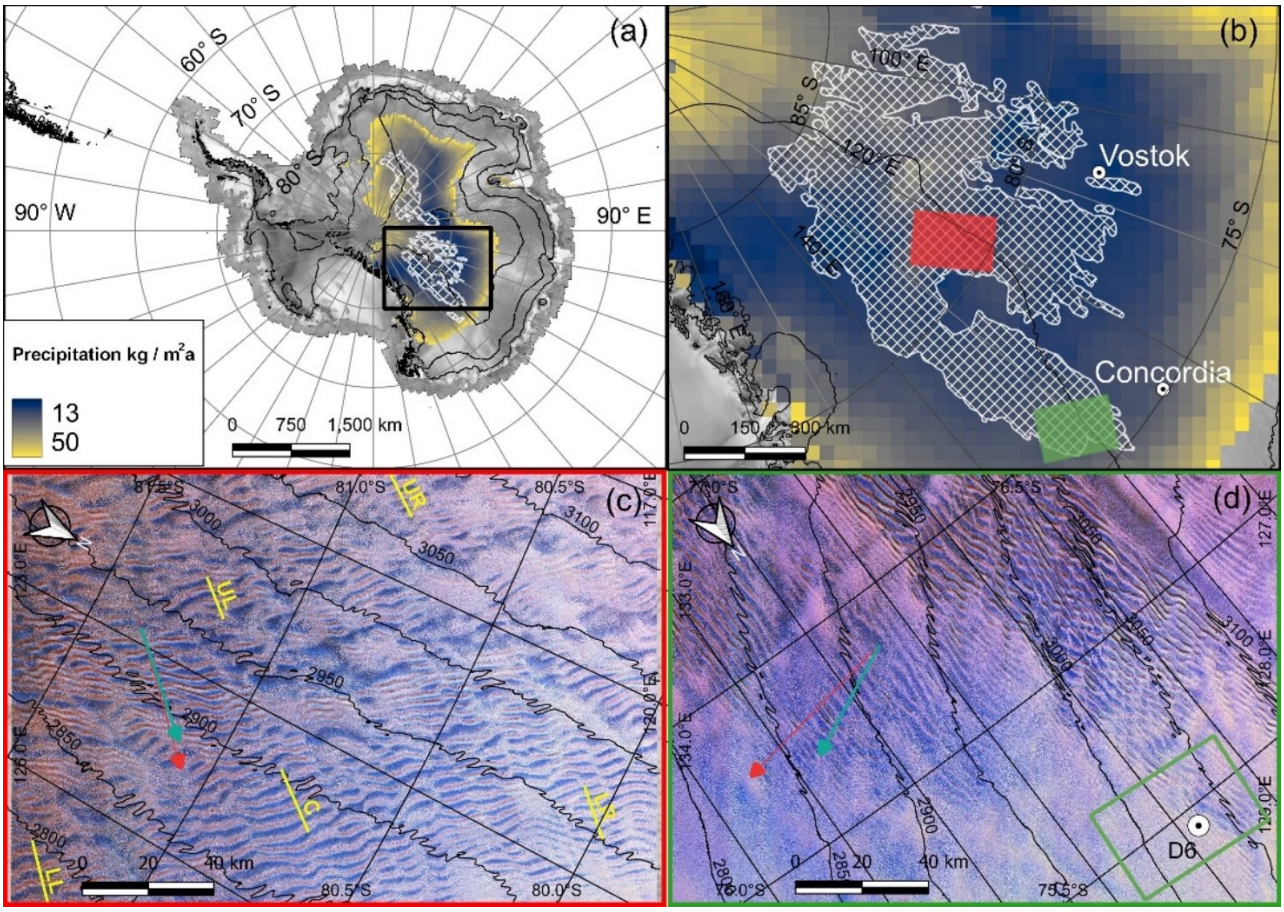

Figure 1. Location map of megadune area. (a) Satellite image map of the Antarctic continent (Jezek, 1999) with elevation contour lines at 1000 m a.s.l. intervals; megadune regions are shown as cross-hatched white areas (Fahnestock et al., 2000), with snow precipitation by RACMO (Regional Atmospheric Climate Model) in colour for areas with precipitation < 50 kg m^2 a^{-1} (Van Wessem et al., 2014) (black rectangle, b). (b) The megadune field with two study sites, EAIIST (red rectangle, c) and It-ITASE (green rectangle, d). (c) Landsat 8 OLI (Operational Land Imager) image in false colour (scene 069119 on 17 December 2015) of the EAIIST area. (d) Landsat 8 OLI image in false colour (scene 081114 on 18 December 2014) of the It-ITASE area and D6 core site; the green rectangle shows the location of Fig. 4. In panels (c) and (d), red arrows represent ERA5 wind direction and green arrows represent sastrugi-based wind direction, while the yellow lines show the location of the transects studied.

Based on previous studies, the SMB of megadunes ranges between 25 % (leeward faces, glazed surfaces) and 120 % (windward faces, covered by huge sastrugi up to 1.5 m in height) of accumulation in adjacent non-megadune areas (Frezzotti et al., 2002b). The sedimentary structure of buried megadunes examined via ground-penetrating radar (GPR) and the Global Positioning System (GPS) suggests that the sedimentary morphology of the windward face (sastrugi) migrates upwind with time, burying the glazed surface of the leeward face (Frezzotti et al., 2002b; Ekaykin et al., 2015), with typical “antidune” processes similar to those observed on fluvial and ocean bedforms (Prothero and Schwab, 2004). This uphill migration is caused by the difference in accumulation between windward (high-accumulation) and leeward (near-zero or negative-accumulation) sides, also leading to

differences in snow features and surface roughness (Fahnestock et al., 2000; Frezzotti et al., 2002a; Albert et al., 2004; Courville et al., 2007). Megadunes appear to be formed by an oscillation in the katabatic airflow, leading to a wave-like variation in net accumulation; the wind waves are formed at the change in SPWD, in response to the buoyancy force, favouring the standing-wave mechanism (Fahnestock et al., 2000; Frezzotti et al., 2002b). Dadic et al. (2013) based their analysis on the surficial-flow theory for sediments in water (Núñez-González and Martín-Vide, 2011), and atmospheric-flow modelling, persistent katabatic winds, strong atmospheric stability and spatial variability in surface roughness are the primary controllers of upwind accumulation and migration of megadunes, where the latter represents the main factor that influences their velocity. The surface waveforms of megadunes with regular bands of sastrugi and glazed surfaces allow for surveying the megadunes by satellite observations because of differences in albedo and microwave backscatter (Fahnestock et al., 2000; Frezzotti et al., 2002a; Scambos et al., 2012) between these features and surrounding snow. Spectral differences also lead to an effect on temperature, which is on average higher over glazed surfaces than on the snow surface (Fujii et al., 1987). In spite of the importance of the glazed surfaces of megadunes for the SMB of Antarctica, a remote sensing characterization of their physical properties and spatial distribution and a quantitative analysis of their migration are currently lacking. The aim of the study is to provide a detailed survey of the spatial and temporal variability in two megadune areas using remote sensing data (Landsat 8 and Sentinel-2), high-resolution elevation models (Reference Elevation Model of Antarctica, REMA; Howat et al., 2019) and climatic conditions using atmospheric reanalysis data (ERA5) in addition to past in situ measurement data (firn core, GPR and GPS) to explore spectral, thermal and windward slope relationships with a view towards generating an algorithm for their automatic detection. Moreover, we provide for the first time the first measurements of the absolute megadune movement and its different components: ice flow and sedimentological progradation. The analysis of absolute megadune movement has important implications on the remote sensing ice dynamic measurements, in particular on ice-flow measurements and elevation changes. Our work constitutes substantial progress towards the survey of ablation areas on SMB at small spatial scales over ice sheets using surface morphology (SPWD) and albedo detection by satellite. A clear understanding of these interactions is of primary importance for the climatic interpretation of ice records and for the assessment of processes and rates of wind scouring and its SMB implications.

2 Study Area

Megadune fields on the Antarctic continent extend along 10∘ in latitude (75–85∘ S, about 1100 km) and 30∘ in longitude (110–140∘ E, about 300–600 km). The climatic conditions of the area are characterized by extremely low temperatures (mean annual temperatures from −45 to −60 ∘C), extremely low snow precipitation (< 30 mm w.e. a−1, water equivalent per year; Van Wessem et al., 2014; Agosta et al., 2019) and nearly constant katabatic wind direction and wind speed (6–12 m s−1; Courville et al., 2007). Analysis of data acquired by the Cloud-Aerosol Lidar and Infrared Pathfinder Satellite Observation (CALIPSO) satellite has enabled the construction of a 12-year climatology of blowing snow over Antarctica, showing that the greatest frequency of blowing-snow events, approaching 75 % of observations, is seen in the megadune region (Palm et al., 2019), which includes the study areas of the present work. This research focuses on two megadune areas that were crossed and surveyed by two snow traverse expeditions: EAIIST (East Antarctic International Ice Sheet Traverse) in 2018–2019 and It-ITASE (Italian International Trans-Antarctic Scientific Expedition) in 1998–1999. The EAIIST area is situated 300 km east of Vostok Station (centred at 80° 47’ S, 122° 19’ E) and It-ITASE area 150 km east of Concordia Station (centred at 75° 54’ S, 131° 36’ E; Fig. 1). The survey data of the first area (EAIIST, https://www.ige-grenoble.fr/EAIIST-project-a-scientific-raid, last access: 15 January 2023) are being processing, whereas the in situ observations of the second traverse It-ITASE are available (Frezzotti et al., 2002a, b, 2004, 2005; Proposito et al., 2002; Vittuari et al., 2004). The EAIIST area is in the middle of the megadune area; thus, megadunes are well defined and continuous on satellite images in optical and microwave bands, whereas the It-ITASE area is at the north-eastern limit of the megadune field, where this morphology is discontinuous and disappears, thus representing the developing threshold of the environmental conditions (morphology, climatology, glaciology) determining megadune formation.

Topographically, the two study areas are in a relative sloping zone where the altitude decreases moving from SW to NE and the elevation ranges from 2700 to 3200 m a.s.l. Thus, the topographic aspect (the direction that a topographic slope faces) is generally east (∼ 80∘, It-ITASE; ∼ 70∘, EAIIST). The regional topographic slope (10 km scale) is on average 1.5 and 1.8 m km−1 for the It-ITASE and EAIIST areas, respectively. The katabatic wind direction is nearly constant with wind blowing from SW in both areas.

3 Data and Methods

3.1 Data

In order to study the megadune areas, we combined three main datasets (satellite images; meteorological data from reanalysis products; digital elevation model, DEM) to create a method for the automatic detection of snow glazed surfaces. We tested two methods, one by creating five sample transects in the EAIIST area (Fig. 1c) and visually identifying thresholds of albedo, thermal brightness temperature (BT) and SPWD to discriminate between glazed surfaces and surrounding snow. The five transects were created in different areas of the megadune field, and they show relatively different wind directions and topographic aspect and slope, with the aim of representing the widest possible range of SPWD values. For the second method, i.e. a maximum likelihood supervised classification, we created 30 polygons in the glazed-snow area and 30 for firn, which were used to train the classification algorithm.

3.1.1 Satellite datasets

Two sources of satellite imagery were used: Landsat 8 OLI (EROS Center, 2013) satellite images (tile area: ~ 38 000 km^2) and Sentinel-2 (ESA, 2022) images (tile area: ~ 12 000 km^2), both downloaded from EarthExplorer portal (https://earthexplorer.usgs.gov/, last access: 24 December 2022). Landsat 8 OLI and Sentinel-2 provide data in several spectral bands, including panchromatic, visible, very near-infrared, short-wave infrared and thermal-infrared bands, with different spatial resolution from 10 to 100 m. Satellite images from Landsat 8 OLI (Table A1) were chosen at dates close to the first stripe acquisitions of the REMA DEM (2013, Table A2). The megadune area is subject to blowing-snow events (more than 75 % of the time; Palm et al., 2019) and cloud cover. Moreover, in the morning a strong atmospheric inversion layer develops 70 % of the time during summer on the Antarctic Plateau (Pietroni et al., 2014) with the formation of fog, which is not homogeneously distributed on the area surveyed by satellite images and is difficult to detect. Therefore, we excluded from our dataset all images with cloud cover > 10 % of land surface, visible blowing-snow and fog events and images with solar zenith angle (SZA) ≥ 75∘ (because of the effect on the albedo, as demonstrated by Picard et al., 2016) and obtained 17 images from Landsat 8 from 2013 to 2020 and 4 images from Sentinel-2 from 2018 to 2021 (Table A1), 11 for the EAIIST site and 6 for It-ITASE. To map glazed surfaces on megadunes, we used Landsat 8 OLI data as the method that rely on the calculation of the albedo, which have been thoroughly validated for Landsat 8 OLI (Traversa et al., 2021a). Additionally, Landsat 8 OLI is available for a longer period of time compared to Sentinel-2, allowing us to investigate temporal evolution of the megadune area. In the megadune

area, the difference between snow glazed surfaces and snow is higher considering near-infrared (NIR) spectral albedo and BT (Traversa et al., 2021b). A “higher” amount of solar radiation absorbed by the glazed surface also corresponds to a different BT on snow glazed surfaces (Fujii et al., 1987; Scambos et al., 2012, and references therein). In fact, these zones show a higher BT compared to the upwind part of the dune characterized by the snow surface. In detail, we used the Landsat 8 OLI near-infrared band (NIR band 5, with a ground resolution of 30 m) to calculate NIR albedo and thermal-infrared (Thermal Infrared Sensor, TIRS 1) band 10 to calculate BT (with a ground resolution of 100 m, provided and resampled to 30 m). To perform the megadune migration analysis (Sect. 2.2.2), we used the panchromatic band of Landsat 8 OLI, as this band has a higher resolution (15 m) compared to the other spectral bands of Landsat. For comparison, Sentinel-2 images were also used, specifically NIR band 8 (10 m spatial resolution), which allows for better observing differences between snow and glazed surfaces compared to the other visible and infrared bands.

3.1.2 Atmospheric reanalysis dataset

We extracted wind direction from the ERA5 atmospheric reanalysis global climate dataset (Hersbach et al., 2020) and by identification of sastrugi based on Landsat (Sect. 2.2.1). In particular, we used ERA5 hourly data (https://doi.org/10.24381/cds.adbb2d47, Hersbach et al., 2018) of wind speed and direction at 10 m above the surface averaged over a 20-year temporal period, from 2000 to 2019. Beside using all wind speed observations, we further divided wind speed into five classes, only considering wind speed values above specific thresholds, i.e. wind speed > 3, > 5, > 7 and > 11 m s−1. These thresholds were chosen based on the interactions between wind and snow: snow transportation by saltation (within 0.3 m in elevation) at wind speeds between 2 and 5 m s−1, transportation by suspension (drift snow) at velocities > 5 m s−1 (within 2 m), and blowing snow (snow transportation higher than 2 m) at velocities between 7 and 11 m s−1 (see Frezzotti et al., 2004, and references therein). The threshold wind speed at which the sublimation of blowing snow starts to contribute substantially to katabatic flows in a feedback mechanism appears to be 11 m s−1 (Kodama et al., 1985; Wendler et al., 1993).

3.1.3 Topographic dataset (DEM)

In order to obtain the aspect and slope of the surface for the SPWD calculation and perform topographic correction for the calculation of albedo, we used a mosaic of REMA tiles (Howat et al., 2019, 2022). These are constructed from thousands of individual stereoscopic DEMs at high spatial

resolution (8 m). Each individual DEM was vertically registered to satellite altimetry measurements from CryoSat-2 and ICESat (Ice, Cloud, and land Elevation Satellite), resulting in absolute uncertainties of less than 1 m and relative uncertainties of decimetres. REMA is based mainly on imagery acquired during the austral summer period (December–March), and at the two sites, the temporal period is from 2008 to 2017, although 87.5 % of stripes were acquired in 2013–2017 (Table A2).

3.2 Methods

The study includes four main processing steps: Landsat 8 OLI image processing for the calculation of NIR albedo, extraction of thermal BT from Landsat thermal band 10, SPWD calculation from ERA5 and satellite sastrugi-based wind direction, estimation of the surface velocity and migration of megadunes using feature tracking (2014–2021), and comparison of GPR–GPS measurements from 1999 with the REMA DEM from 2014 (specific strip on the area). The first three steps were the basis of the automatic detection of the glazed-snow areas.

3.2.1 Automatic detection of snow glazed surfaces

By using spectral datasets and topographic data, we consider for the automatic detection of the glazed areas the following parameters: NIR albedo, thermal BT and SPWD. NIR albedo (α) was here estimated using Landsat 8 OLI imagery, following the method first proposed by Klok et al. (2003) and recently tested and validated in Antarctica by Traversa et al. (2021a). We used NIR albedo as opposed to broadband albedo owing to the higher detection ability of NIR albedo, which stems from the fact that broadband albedo obtained by using the Liang conversion algorithm (Liang, 2001) considers the visible area of the spectrum and the short-wave infrared. In fact, in broadband albedo it is hardly possible to recognize the differences between glazed and unglazed areas, which in the visible wavelengths look very similar (Warren, 1982). Following the methodology proposed by Traversa et al. (2021a) and Traversa and Fugazza (2021), the images were processed through three main steps: (1) conversion of radiance to top-of-atmosphere (TOA) reflectance by using per-pixel values of the SZA available through the Landsat solar zenith band. This conversion allows for applying a more accurate per-pixel correction for the SZA, useful in our study considering the average high SZA (always $\geq 59^{\circ}$, Table A1) and its strong effect on albedo (Pirazzini, 2004; Picard et al., 2016; Traversa et al., 2019). Also included are (2) atmospheric correction and (3) topographic correction. To retrieve the thermal BT, we employed band 10 of Landsat 8. To estimate the TOA thermal BT received at the

satellite, spectral radiance in the thermal band was converted using the thermal constants in the Landsat metadata (Zanter, 2019). For the SPWD, the wind directions were extracted at low spatial resolution (30 km) using ERA5 and validated by identifying sastrugi and deriving wind directions from them using Landsat 8 OLI at 30 m spatial resolution (Mather, 1962; Parish and Bromwich, 1991). The identification of sastrugi was performed on the Landsat 8 OLI NIR band (band 5) by applying the Canny edge detection algorithm (i.edge in GRASS GIS, Geographic Resources Analysis Support System geographic information system; Canny, 1986). Prior to edge detection, each image was pre-processed by using a high-pass filter with a length scale of 150 m implemented through a fast Fourier transform to highlight the sastrugi. This process was applied on seven Landsat scenes from the spring and summer months, i.e. November, December and January of the period 2013–2020. To further estimate the SPWD based on the wind direction from ERA5 and Landsat-derived sastrugi, we used the approach of Scambos et al. (2012); i.e. we calculated the dot product between the slope derived from the REMA DEM and the wind direction. The algorithm was applied to ERA5 and sastrugi-based wind directions resampled at 120 m spatial resolution, and the REMA DEM was resampled to match ERA5 and sastrugi-based wind directions using bilinear interpolation. The resulting SPWD has units of metres per kilometre. Due to the small difference in NIR albedo and BT of glazed surfaces (leeward) and sastrugi (windward) and the different illumination and meteorological conditions of the satellite images, the analysis of the variability in SPWD, NIR albedo and BT was conducted in detail on the five transects perpendicular to megadunes. The comparisons were conducted using the albedo and temperature values and normalized using mean and standard deviation for each transect. Moreover, we determined the strength of the relationship between SPWD and NIR albedo and between SPWD and thermal BT (applied on the moving averages of 11 pixels weighted based on the distance from the central point) using linear regression. The comparison analysis was conducted at seasonal scale for the 2013–2014 (4 images) and at multi-annual scale on 17 images distributed over 8 years. With the aim of providing an automatic methodology for distinguishing the glazed snow from the surrounding firn surface and evaluating the role of SPWD in the classification, we applied and compared two different approaches: a supervised classification (maximum likelihood) and a self-defined-threshold approach. In both cases, we considered SPWD, NIR albedo and thermal BT. The analysed images were the one from 17 December 2015, which was one of the best available images in terms of cloud cover (~ 0 %), presenting no blowing snow/fog and the lowest SZA (67°) for the EAIIST site and the closest date to the REMA DEM in the area (January–October 2016), and the four scenes available for the 2013–2014 season (i.e. 25 November 2013, 11 December 2013, 27 December 2013 and 28 January 2014). For the self-defined-threshold method, we applied a conditional evaluation (i.e. output result for each pixel based on whether the pixel value is assessed as true or

false in a set conditional statement) to automatically map glazed snow. The thresholds were visually identified and iteratively adjusted to obtain a best fit as follows: SPWD > 1 m km−1, with the aim of considering the leeward flanks only, NIR albedo < 0.82 and thermal BT > 246.5 K. In order to evaluate the role of each parameter, with particular attention to the SPWD, we repeated the two approaches by using individual parameters (NIR, SPWD, BT) and combinations of them (i.e. NIR–SPWD, NIR–BT, BT–SPWD and NIR–BT–SPWD). Finally, we calculated the accuracy for each case, by creating a set of random points (100 points, following the density used in Azzoni et al., 2016) as ground truth (visually assigned on the false-colour image) and comparing the results through a confusion matrix. The accuracy was calculated not only for methodologies in their entireness (identifying and distinguishing glazed snow and the surrounding firn surface) but also with respect to their specific ability in detecting glazed snow.

3.2.2 Megadune movement estimation

Frezzotti et al. (2002b) and Ekaykin et al. (2015), based on the sedimentary structure of buried megadunes (using GPR and GPS), pointed out that the megadune migration and ice sheet surface flow show a similar intensity but opposite directions and that megadunes migrate upwind with time, burying the glazed surface of the leeward face. Here, by using different satellite images and field data, we are able to provide and quantify megadune migration components: ice-flow (If) direction, which is correlated mainly to topographic slope; sedimentological migration (Ms), caused by sedimentological processes linked to deposition (on the upstream dune flank); ablation (on the downstream dune flank) of snow; and the result of these processes, the absolute migration (Ma):

$$\overrightarrow{M_a} = \overrightarrow{M_s} + \overrightarrow{If} \quad (1)$$

During the It-ITASE traverse at the D6 site, megadunes were surveyed by means of GPR–GPS to measure ice velocity, surface elevation, and internal layering of present and buried megadunes. We compared these measurements with the REMA DEM derived by satellite images acquired in 2014 to estimate the change in surface morphology due to sedimentological migration of the megadunes. With the aim of calculating the surface velocity and direction of megadune movement, the feature-tracking module IMCORR (Scambos et al., 1992) was run in the System for Automated Geoscientific Analyses (SAGA GIS). This algorithm performs image correlation based on two images providing the displacement of each pixel between the second and first image (Jawak et al., 2018). Prior to feature tracking, each image pair was pre-processed by using a low-pass filter with a length scale of 150 m implemented through a fast Fourier transform to smooth out the sastrugi and leave megadune features

for tracking. Finally, by dividing the displacement values obtained through IMCORR by the corresponding time period, we obtained the absolute migration of the megadunes in metres per year. For comparison, we also employed another method to evaluate the megadune migration. By using Landsat 8 OLI imagery, similarly to what was already done for the detection of sastrugi and applying an edge detection on band 5 (NIR), it is possible to identify the megadune crest and trough at the edges between leeward (glazed snow) and windward (sastrugi) zones. The obtained direction raster was manually cleaned from errors and artefacts (angles: < 200 and $> 240\circ$, intensity: < 5 m a-1) and then vectorized after thinning, i.e. reducing the number of cells used to represent the width of the features to 1 pixel. Comparing the obtained velocity fields in different years, we could observe the absolute migration of the megadunes. We considered the widest temporal interval between two pairs of cloud-free images of Landsat 8 (four pairs) and Sentinel-2 (two pairs), which were in a similar period of the year, to avoid relevant differences in the SZA that could confound the feature-tracking algorithm (Table 1).

Zone	Satellite	t_o	t_1	t span (a)	Mean M_a (m a^{-1})	SD M_a (m a^{-1})	Features
It-ITASE	L8	2 Dec 2014	30 Nov 2019	5	14.0	3.9	30 073
It-ITASE	L8	2 Dec 2014	2 Dec 2020	6	12.8	3.4	30 538
It-ITASE	S2	13 Dec 2016	27 Dec 2020	4	11.4	3.8	537 304
EAIIST	L8	27 Dec 2013	28 Dec 2019	6	11.9	3.6	316 951
EAIIST	L8	17 Dec 2015	30 Dec 2020	5	14.2	3.4	139 622
EAIIST	S2	10 Jan 2018	2 Jan 2021	3	10.5	4.1	1 329 648

Table 1. Results of the absolute migration of megadunes calculated from IMCORR based on Landsat 8 OLI (L8), with a tile area of ~ 38 000 km^2, and Sentinel-2 (S2), with a tile area of ~ 12 000 km^2. Imagery at the It-ITASE and EAIIST sites.

The results from IMCORR and GPS observations were compared with the MEaSUREs (Making Earth System Data Records for Use in Research Environments) ice-flow velocity product (Rignot et al., 2017), which provides the highest-resolution (450 m) digital mosaic of ice motion in Antarctica (assembled from multiple satellite interferometric synthetic-aperture radar (SAR) systems, mostly between 2007–2009 and 2013–2016), showing for each pixel the direction and the velocity of ice flow with a mean error of 3 %–4 %.

4 Results

4.1 Megadune characterization and automatic detection

On average, in the five analysed transects NIR albedo ranges from 0.81 to 0.86 (α) in the upwind area (snow sastrugi) and from 0.73 to 0.81 (α) downwind (glazed surfaces), with differences inside the transects of about 0.07 (α) with a maximum value of 0.1 (α). The maximum contrast of NIR albedo between glazed surfaces and snow sastrugi usually occurs at springtime (October–November) and decreases during the summer season (Fig. 2). Our remote sensing observations agree with previous analysis that pointed out that in late summer, radiative cooling of the uppermost surface layer leads to formation of surface frost, by condensation of local atmospheric vapour onto the snow surface; this gives the glazed surface a more diffuse specular reflection than in spring and changes its appearance in albedo and BT (Scambos et al., 2012, and references therein). Along the transects, the correlation of NIR albedo from the different images is high (R^2: up to 0.99) during the spring season (24 November 2013, 27 December 2013) and decreases by the end of the summer and in comparison with the following years, with an R^2 of 0.7 only after 2 years (17 December 2015) and up to 0.6 after 6 years (December 2019). A similar decrease in correlation occurs from the comparison of the SPWD and NIR albedo from 2013 (R^2: 0.66) to 2019 (R^2: 0.39).

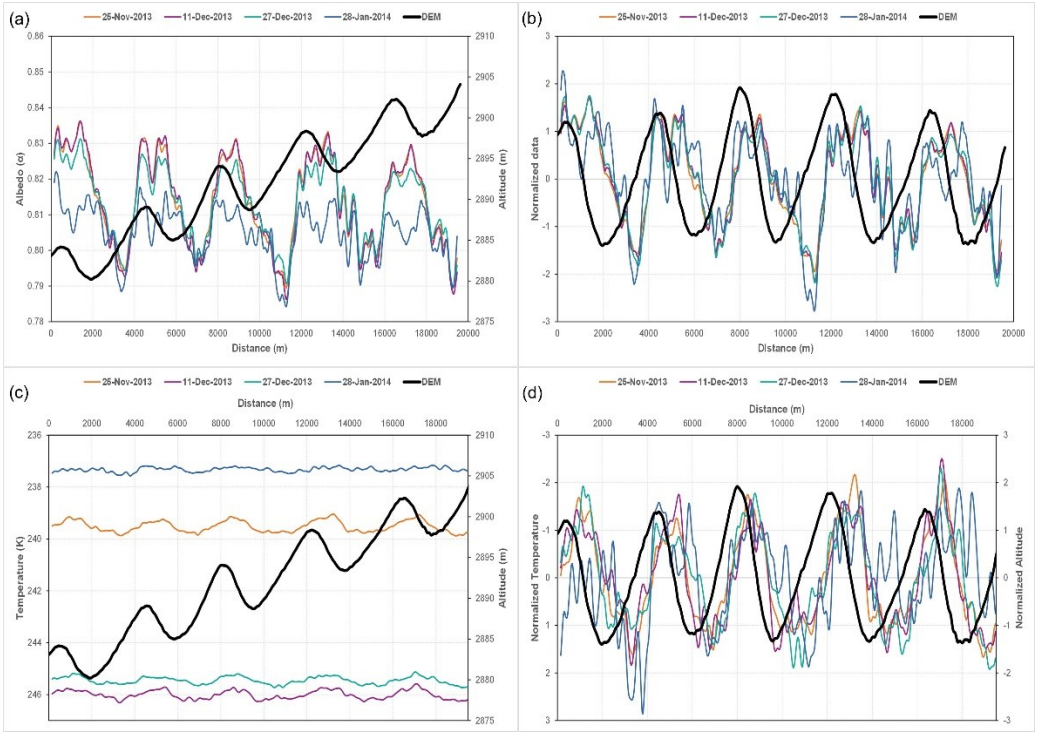

Figure 2. Moving averages (based on 11 transect pixels) of (a) NIR albedo and (c) thermal BT TIRS1 between November 2013 and February 2014 for transect C at the EAIIST site (see Fig. 1c for location) and elevation from the REMA DEM. Corresponding normalized moving averages of (b) NIR albedo and (d) thermal BT TIRS1 during the austral summer season 2013–2014 for transect C and elevation from the REMA DEM (detrended topography).

For the thermal BT, we observed an intra-seasonal trend on all transects: in fact, while thermal BT remains ≥ 244 K during the middle of the summer (11 and 27 December 2013), it decreases moving away from the summer solstice. Temperatures range between 238 and 240.5 K on 25 November 2013, 26 d from the solstice. The difference increases on the date farthest from the solstice, 28 January 2014 (38 d from the solstice), with the lowest values ranging between 236 and 239 K. The BT varies up to 1.5 K for each transect but up to 3–4 K within individual images. Intra-annually, the difference between glazed surfaces and snow is higher during the spring (max 1 K in November) and tends to decrease over time, becoming lower than 0.5 K at the end of summer (January), where differences between the two surfaces are hardly detectable and the correlation between the two parameters frequently decreases drastically. These differences are directly correlated to the ones observed in NIR albedo, as a higher quantity of energy is absorbed on glazed surfaces. High correlations are found between NIR albedo and thermal BT with an R^2 of up to 0.67 (95 % confidence interval) and between SPWD vs. NIR albedo and thermal BT (R^2=0.44 and 0.57 at 95 % confidence interval, respectively) calculated along all the transects (Fig. 3). The comparison between thermal BT and SPWD shows the same pattern observed for the NIR albedo but is proportionally inverse with respect to SPWD (Fig. 3), with higher temperatures corresponding to the glazed part of downwind areas of the dunes and conversely, lower values related to snow sastrugi in the upwind zones.

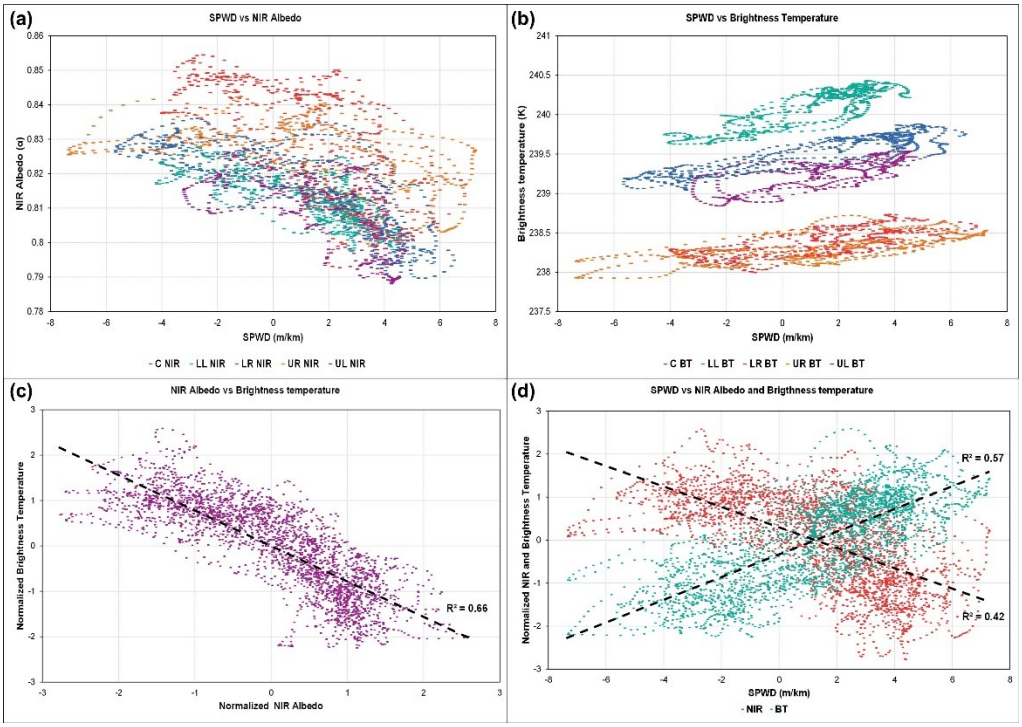

Figure 3. Diagram plots of transects at the EAIIST site from a Landsat 8 image acquired on 25 November 2013: (a) SPWD (slope along the prevailing wind direction) compared within each transect (C, LL, LR, UL, UR; Fig. 1 for location) with NIR spectral albedo and (b) thermal BT; (c) normalized NIR albedo of all transects compared with BT with linear regression; and (d) SPWD compared with normalized NIR albedo and thermal BT for all transects with linear regression.

Based on the transects, the variability in NIR albedo at a seasonal (spring–summer) to pluriannual scale is observed to be twice as large in the snow accumulation area on the upwind flank and the bottom of the leeward flank (Fig. 2) compared to the glazed-surface NIR albedo (0.7 % compared to 0.3 % NIR albedo variability), which remains more stable and more highly correlated at a seasonal (spring–summer) and pluriannual scale. The analysis of sastrugi direction using seven Landsat scenes from the spring and summer months during the period 2013–2020 show small differences in direction within each image and in repeated imagery (< 5∘), confirming the stability in direction of sastrugi landforms and thus the persistence of katabatic wind. The comparison of the results of wind direction obtained using sastrugi direction by satellite (resampled using bilinear interpolation) and ERA5 present similar values for both areas, with a lower difference in the EAIIST area (differences of 1∘ in average values) compared to It-ITASE (9–14∘; see Table A3). At the regional scale (30 km spatial resolution), the entire megadune field has an average SPWD of 1.2 m km−1, when calculated using sastrugi-based wind direction, and 1.1 m km1 when using ERA5, in agreement with previous studies (e.g. Frezzotti et al., 2002b). To distinguish between leeward (glazed surface) and windward flanks of the dunes for the two sites, the SPWD based on sastrugi was further resampled to 120 m using bilinear interpolation. For the SPWD on megadunes at a local scale (100 m), we found a mean value of 5.6 ± 1.0 m km−1 for the leeward side and negative SPWD values, with a mean of -4.2 ± 1.6 m km−1 on the windward flanks. The application of the supervised classification and the self-defined-threshold methodology on the different combination of the analysed parameters for the 2013–2014 season and on the 17 December 2015 scene showed contrasting results (Table 2).

Date	NIR	BT–SPWD	NIR–SPWD	NIR–BT	NIR–BT–SPWD
25 Nov 2013	32 %	57 %	55 %	9 %	55 %
11 Dec 2013	27 %	52 %	50 %	32 %	55 %
27 Dec 2013	9 %	43 %	50 %	9 %	45 %
28 Jan 2014	23 %	43 %	45 %	23 %	50 %
Season average	23 ± 9 %	49 ± 6 %	50 ± 3 %	18 ± 10 %	51 ± 4 %
17 Dec 2015	78 %	48 %	83 %	70 %	78 %

Table 2. Accuracy assessment (%) in the detection of glazed snow using a supervised classification applied on NIR, BT and SPWD and their combination over the four scenes of the 2013–2014 summer season and on 17 December 2015. The results of BT and SPWD (alone) are not reported, as they present the same result in all cases (i.e. 0 % for BT and 30 % for SPWD).

In fact, even if the general accuracy in distinguishing firn and glazed surfaces was on average high (mostly > 80 %), with the highest values on the scene from 17 December 2015 (up to 94 % and 98 % in the combination of NIR–SPWD for supervised and self-defined thresholds, respectively), lower

values and higher differences were found when comparing the accuracy in detecting only glazed snow. There, the inclusion of SPWD in the classification significantly improves the ability to detect these surfaces, with a doubling of the accuracy during the season 2013–2014 (between 0 % and 30 % for single parameters or combination without SPWD to around 50 % of season average in the other cases and up to 55 % for the NIR–BT–SPWD combination). The increase is also observed for the 17 December 2015 scene, from 78 % of NIR alone to 83 % for NIR–SPWD (which becomes 95 % in the case of NIR–SPWD for the self-defined-threshold methodology, the highest calculated value of accuracy in detecting glazed snow). Summarizing, the impact of the inclusion of the SPWD is evident, both applying the supervised classification and self-defined-threshold methodology, as the SPWD doubles the accuracy compared to the cases with no SPWD. We further observed issues in using BT in these approaches because of its high heterogeneity at a high scale (i.e. entire Landsat scene), as BT presents strong variations across the image; the strong improvement in using a scene (i.e. 17 December 2015) with no interferences (e.g. fog, clouds, "low" SZA) and close in time to the REMA DEM (stripes from January to October 2016), leading to a significant increase in accuracy of the method (from highest values of ∼ 50 % of scenes from season 2013–2014 to over 80 %); and the higher accuracy when applying a self-defined-threshold approach.

4.2 Megadune migration

The absolute megadune movement calculated using feature tracking on optical satellite image pairs spans from 3 to 6 years and presents small differences in the two study areas, ranging between 10.5 and 14.2 m a−1 overall, with no detected significant trends over time. The average values are similar when using different datasets (Landsat 8 OLI and Sentinel-2) but with Sentinel-2 velocities showing slightly lower average values compared to Landsat 8. Moreover, due to the slightly higher spatial resolution (10 m vs. 15 m), the number of features tracked using Sentinel-2 is an order of magnitude higher than that of Landsat 8 OLI (Table 1), even if the number of pixels is higher (with a ratio of 1.4) in Landsat scenes. The direction of the migration does not differ much across the different datasets, showing opposite values compared to wind direction. The second method used to calculate the migration velocity is the ridge vectorization and tracking for the same image pairs. This method shows slightly higher velocities (16.7 ± 3 m a−1) than IMCORR tracking of megadune features (11.9 ± 3.6 m a−1) at the EAIIST site for the period 2013–2019 but within the error. At the D6 It-ITASE site, five GPR–GPS transects were surveyed on megadunes (Frezzotti et al., 2002b); the comparison between GPS elevations (3 January 1999) and the REMA DEM (2 February 2014) provides information about the relative change in elevation at high resolution (decametre level) of the

megadunes during the past 15 years. On the five transects, we observe an almost stable elevation in correspondence with glazed surface/leeward flank, whereas the maximum difference in elevation (from +1.2 to +1.9 m, with an average maximum value of +1.4 m) occurs always in the snow accumulation/upwind flank on the correspondence of the trough (Fig. 4). By projecting the transects along the prevalent wind direction (239∘), based on the surrounding sastrugi orientation, we were able to evaluate the megadune migration using the relative change in elevation. Using the crest/trough position of each dune, we calculated an average displacement of 11 ± 5.2 m a^{-1} from all transects (Fig. 4). The migration of the dunes is evident in all transects with the upwind migration of the crest over the upstream flank and of the trough on the upstream flank of the previous megadune. In contrast, the glazed surfaces on the downwind flank remained generally stable in elevation over time (Fig. 4) but are clearly buried at the upstream flank foot and migrate at the crest. At the D6 site, Vittuari et al. (2004) measured an ice velocity of 1.46 ± 0.04 m a^{-1} with a direction of 97∘ using repeated GPS measurement between 1999 and 2001. The closer value of MEaSUREs ice flow at the D6 site is 2.2 ± 1.1 m a^{-1} with a direction of 89∘, in agreement with GPS measurements. At the EAIIST site, MEaSUREs data show an ice flow of 6.1 ± 3.4 m a^{-1} with a direction of ∼ 65∘. Both velocity directions agree with the topographic slope at the site. Applying Eq. (1) for the calculation of megadune migration components, we obtained a sedimentological migration of 18.4 ± 6.7 m a^{-1} (229∘) at EAIIST and 15.4 ± 4.7 m a^{-1} (246∘) at It-ITASE using Landsat 8 OLI data and 16.0 ± 7.3 m a^{-1} (230∘) at EAIIST and 13.6 ± 4.9 m a^{-1} (245∘) at It-ITASE with Sentinel-2.

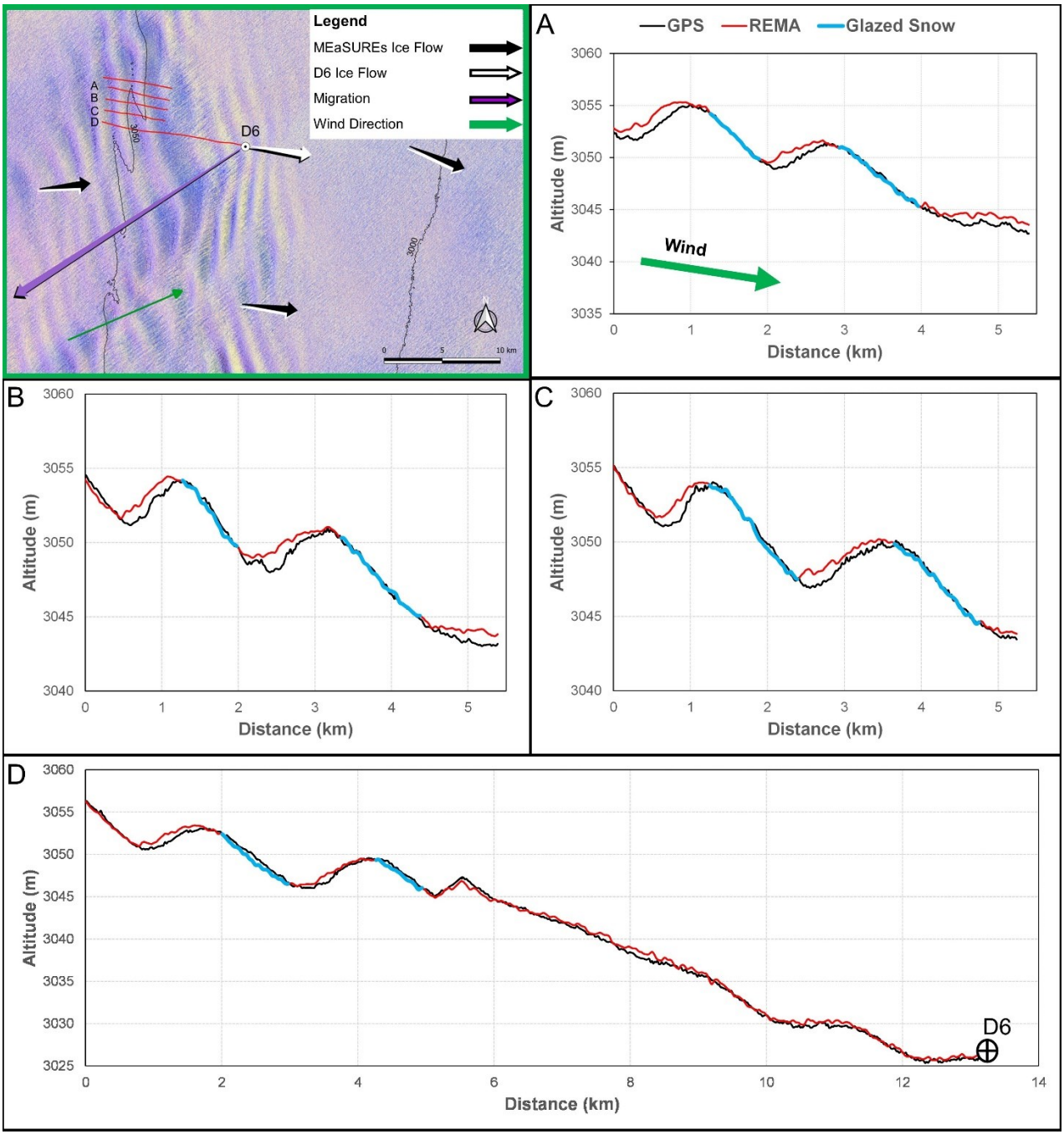

Figure 4. Location of the GPS transects (red) at the It-ITASE site with a false-colour Landsat 8 OLI image in the background (18 December 2014). Universal Transverse Mercator (UTM) projection. Topographic section of four transects (A, B, C, D), with the black lines representing elevation from in situ GPS observations (1999), red lines from the REMA DEM (2014) and blue lines from glazed snow detected on the Landsat image from 18 December 2014.

5 Discussion

5.1 Application of the automatic detection of glazed snow on megadune fields

In this study, we showed the possibility of calculating the SPWD based on wind direction from ERA5 and Landsat-derived sastrugi. At both investigated sites, the direction of the wind from ERA5 at a

velocity higher than 11 m s−1 was found to be closer to the direction of sastrugi surveyed by satellite. The small difference between the two datasets could be correlated to the formation of sastrugi, as wind speed ≥ 11 m s−1 was previously reported by Kodama et al. (1985) and Wendler et al. (1993) to be required for the formation of sastrugi. While the EAIIST site shows similar average directions to ERA5, in the other study area (It-ITASE) a slightly higher difference was found between the two datasets for wind velocity slower than 11 m s−1. The direction retrieved from Landsat is strongly dependent on high-velocity prevailing winds (katabatic winds), which shape the sastrugi and direction, while ERA5 also takes into account wind directions other than the katabatic. In addition, this difference could be caused by the different spatial and temporal resolutions between the satellite and ERA5 (30 m vs. 30 km, scene-based vs. average of 20 years), as well as inaccuracies in the ERA5 wind direction. The larger difference in wind direction using the various datasets (ERA5, sastrugi detected by satellite, sastrugi measured on the field) at the It-ITASE site could also be attributed to the higher variability in the katabatic wind direction; in fact, this site is at the northern limit of megadune field (Fig. 1), and a relatively high variability in katabatic wind direction (> 10–15∘) could be among the threshold factors that does not allow for the formation of megadunes in the northern part. However, with the aim of applying this methodology at a large scale using ERA5 data, e.g. the whole continent, the differences between the two sources can be significant (e.g. at the It-ITASE site) and could produce errors in the SPWD calculation. Therefore, the use of sastrugi could be a more accurate way to interpret the prevalent wind direction with high wind speed (≥ 11 m s−1) compared to ERA5. The SPWD is the only parameter that could be considered almost constant at a 10 km scale, in consideration of the stability of the direction of the katabatic wind, driven mainly by surface slope and the Coriolis force. In contrast, albedo and above all thermal BT change both temporally, annually and during seasons, and spatially across the satellite scene. In fact, NIR albedo significantly varies because of surface changes of up to 0.1 α and between the beginning, the middle and the end of the summer season in relation to the SZA by ±0.01–0.02 α. Frezzotti et al. (2002b) pointed out the presence of huge sastrugi (up to 1.5 m in height) located on the windward flank and alternation of sastrugi (up to 40 cm) and glazed surfaces located at the bottom of the interdune area. The observed change on NIR albedo and BT on the windward flank is correlated to the sastrugi formation and deterioration during the season and their relative change in shadow (Warren, 1982). In addition, thermal BT varies from a higher temperature near the summer solstice to lower values in late spring and summer, in the range ±5–10 K. In both cases, the differences between leeward flanks where glazed surfaces are located and windward flanks of megadunes are not high enough to overcome the seasonal variability and thus a constant range for albedo and temperature is impossible to determine. Spatially, the satellite-derived NIR and thermal BT show large variability inside the same satellite

images, in particular for thermal BT, but strong correlation among the two parameters up to an R^2 of 0.99 along each transect. The observed variabilities could be related to the different illumination condition and meteorological conditions with development of surface hoar crystal due to fog and under calm sunny weather with a downward as well as an upward vapour source to the near-surface layer. The growth of surface hoar crystals dramatically changes the snow structure, specific surface area and density, as well as surface roughness, leading to significant changes in albedo and therefore surface temperature (Gallet et al., 2014). For these reasons, different thresholds can not only be required when investigating an entire tile of Landsat in the case of self-defined-threshold methodology but also can explain the inability of supervised classification based only on BT to distinguish between glazed snow and firn. With BT, in fact, the difference in values across the images is higher than the mean spectral difference between these two surfaces at these wavelengths. For the same reasons, the classification approaches including BT present, in most cases, lower accuracy than the other cases, suggesting against using it to map glazed snow at a large scale. On the other hand, NIR albedo does not show this sort of problem and instead demonstrates good ability in distinguishing between the two surfaces, with a good accuracy even when used alone (especially in the 17 December 2015 case, Table 2). Additionally, it is evident how the implementation of SPWD is fundamental in aiding the detection of glazed snow, together with the NIR band, particularly by improving the detection even when the other parameters present more uncertainties (owing to e.g. SZA and fog). In fact, in all the combinations where SPWD is included, the accuracy in the distinction between glazed snow and firn shows more constant results and minimum and maximum accuracy across the analysed season is similar. Finally, our results point out the importance of using satellite images with no interferences (e.g. clouds, fog, high SZA), with the aim of automatically detecting glazed snow, as the accuracy of the method drastically increases (17 December 2015 compared to the other cases) and also that the self-defined-threshold approach provides better results in terms of accuracy than the supervised classification. Nevertheless, even if the self-defined-threshold model shows a higher accuracy, supervised classification allows for overcoming the issue of defining accurate thresholds across a certain season, providing good accuracy results especially on good quality images, as calculated on 17 December 2015. By using the classifications with the highest accuracy in the EAIIST area achieved based on the scene from 17 December 2015 (NIR–SPWD combination), where approximately 75 % of the area is covered by megadunes, we could calculate that the glazed surfaces cover around 43 % of this specific dune area, i.e. ~ 80 % of leeward flanks. In conclusion, the detection of glazed surface/ablation area by satellite images is challenging because of differences in illumination and meteorological conditions (cloud cover, blowing snow, etc.) among different satellite images. Nevertheless, the high-resolution digital terrain model (REMA) allows for

calculating an SPWD with unprecedented detail, similar to the resolution of optical satellites (Landsat 8–9, Sentinel), and significantly improves the detection of glazed/ablation surfaces at 10 m scale across the continent; therefore, it could significantly improve research on the SMB of the Antarctic Ice Sheet.

5.2 Megadune upwind migration

The absolute position of the megadune crest and trough are driven mainly by two processes: snow ablation/accumulation processes and ice sheet surface flow. GPS and GPR profiles along the It-ITASE traverse show the presence of paleo-megadunes buried up to the investigation depth of 20 m (Frezzotti et al., 2002b). Analysis of the D6 firn core allowed for detecting the Tambora eruption signal (1816 CE) at 15.36 m depth with an average snow accumulation of 36 ± 1.8 mm w.e. a−1, whereas an average value of 29 ± 7 mm w.e. a−1 of spatial variability in SMB at D6 site was evaluated by GPR calibrated using accumulation at three firn cores (Frezzotti et al., 2005). The elevation changes during 15 years observed using GPS and REMA show a relative increase in accumulation on the windward flank with the maximum value at the trough compared to the glazed-surface area from 29 to 46 mm w.e. a−1 with an average value of 34 mm w.e. a−1, using a density of 360 kg m3 in the first 2 m. This value is very close to the estimated change in accumulation in the megadune area from 7 to 35 mm w.e. a−1 provided by Frezzotti et al. (2002b) using the variability in GPR internal layering at the megadune site. The minimum value represents a decrease in accumulation of up to 75 % or more on glazed surfaces. The relative stability of glazed surfaces with respect to elevation change and NIR albedo confirms the extremely stable SMB low value of the glazed surfaces with respect to accumulation areas, due to the long-term hiatus in SMB forced by wind scouring processes. Using the isochrone distance of 1.5–1.8 km between the 180-year-old paleo-crest detected by GPR and the recent crest from GPS observations (1998–1999 CE), we can evaluate the windward migration of the paleo-megadune crest at about 8–10 m a−1. This vector from field observations summed with an ice flow from GPS of 1.46 ± 0.04 m a−1 with a direction of 97∘ produced an absolute migration of 10.3 m a−1 with a direction of 214∘. This value is in very good agreement with absolute migration calculated using the elevation comparison between GPS and REMA (11 ± 5.2 m a−1) and with satellite tracking (from 11.4 to 14.0 m a−1), in particular with Sentinel-2 images (11.4 m a−1, Table 1). At the D6 site, the movement components show different intensity with an order of magnitude of difference: 1–2 m a−1 for ice flow vs. 13.6–15.4 m a−1 for sedimentological migration. The components present nearly opposite directions: 97∘ for ice flow and 245∘ for sedimentological migration. The results allowed us to calculate all the components of migration and to conclude that

for a megadune with a wavelength of 3 km we could calculate an absolute migration of approximately 10 m a−1. This burying process of snow on glazed surfaces takes about 300 years, with a overlap of the crest to the trough and glazed to sastrugi surface as observed by GPR internal layering. These results are strongly in accordance with Courville (2007), who determined a burial rate of 330 years based on a firn core drilled in 2003/04 and migration rates of approx. 12 m a−1 (from AVHRR data; Advanced Very High Resolution Radiometer) at a field located at 80° 47' S, 124° 29' E in the megadune region of the EAIIST site. The megadune migration on the upwind part observed by elevation change and tracking is also confirmed by the comparison of NIR and BT along the studied transects. These parameters remain relatively stable during the observed time on the glazed surface on the leeward flank, whereas the positive SMB upwind flank and bottom trough area change significantly not only at a pluriannual scale but also at a seasonal scale. Hence, we observe a general overestimation of sedimentological and absolute migration using remote sensing with a mean difference of +1.9 m a−1 for Sentinel-2 (uncertainties of 19 % for sedimentological migration and 10 % for absolute migration). Using Landsat 8 OLI images, larger differences were found, with an average overestimation of 3.8 m a−1. This difference could be caused by spatial variability in processes: with remote sensing we analysed a much wider area, as opposed to in situ observations which were acquired in transects on a limited section of the megadune field. Finally, the spatial resolution and geolocation (Mouginot et al., 2017) could affect the satellite data, as demonstrated by the worse results obtained using Landsat images at 15 m spatial resolution against 10 m resolution of Sentinel-2. The ice velocity of MEaSUREs is based on SAR images and is in very good agreement with GPS measurement, and the tracking methods of IMCORR using optical images and crest displacement are in agreement with the migration of morphologies observed from the comparison between change in elevation by GPS and REMA. Based on our analysis, the sedimentological processes are analogous at the It-ITASE and EAIIST sites. At the second site, a faster ice-flow motion was observed by MEaSUREs, and the velocity of absolute migration is reduced by almost 35 %, compared to the initial sedimentological-migration velocity. The ice velocity based on SAR images presents a phase centre that penetrates up to 10 m on dry and cold firn (Rignot et al., 2001) and provides information on ice flow and not surface features. In contrast, using feature tracking on optical images (Landsat and Sentinel-2), it is possible to estimate the absolute migration (migration + ice flow) of surface features that could be significantly different from ice flow as for the megadunes.

6 Conclusions

This study significantly improved the previous knowledge on the temporal/spatial variability in Antarctic megadunes and glazed surfaces, measurements of their sedimentation/migration, and their interaction with the atmosphere and ice sheet surface. The snow accumulation distribution/variability processes that allow megadune formation have important consequences concerning the choice of sites for ice coring and SMB evaluation, since orographic variations of a few metres per kilometre have a significant impact on the snow accumulation process. Furthermore, these new results represent a new ground truth and foundation of knowledge for ice sheet mass balance research, in particular for satellite altimeter and ice velocity derived by remote sensing measurements (e.g. radar vs. optical/lidar). The new results confirm and quantify the previous hypotheses and provide new relevant information on different aspects of these peculiar landforms showing that the megadune is a dynamic feature at different spatial and temporal scales. The glazed-surface/megadune survey has revealed previously unknown large spatial variability in ice sheet SMB, superimposed on the large-scale gradients in SMB from the coast to the interior. On smaller scales (< 1 km), SMB varies considerably as well, driven by surface topography undulations (SPWD) and consequent wind-driven snow ablation and redistribution, which challenges the spatial representativeness of stake and firn/ice core records. Moreover, this small-scale variability is not represented by regional climate model systems used for SMB evaluation (e.g. Agosta et al., 2019; Lenaerts et al., 2019), which currently operate at horizontal resolutions of typically 25 km for East Antarctica. Previous studies have pointed out that glazed areas are extensive enough to have a significant impact on current estimates of SMB and therefore overall mass balance using the mass budget method (Frezzotti et al., 2004; Das et al., 2013; Scambos et al., 2012). The scale of the overestimation is of the same order of magnitude as the total error reported for East Antarctica and a large fraction of the currently reported error bars for Antarctic-wide mass balance (Rignot et al., 2019). Considering the characteristics of megadunes, the leeward glazed flanks show a lower NIR albedo (up to 0.1) and higher BT (up to 1.5 K) compared to windward snow-covered sides within each of the five transects analysed. NIR albedo and thermal BT, combined with the SPWD, allowed us to produce a method for automatically detecting glazed surfaces. High correlations were found between SPWD and NIR albedo and thermal BT with an R^2 of up to 0.44 and 0.57, respectively, calculated along the whole transect examined in 2013–2014, with differences between spring and the end of summer. The correlations between SPWD and NIR albedo on the transects decrease to 0.39 in comparison with the image from December 2019. Moreover, the high correlation of NIR albedo between images decreases over time by up to 60 % between November 2013 and December 2019. Our results support the importance of SPWD (especially when sufficiently synchronous with spectral imagery, in consideration of the migration of megadunes) for megadune

snow characterization. Together with NIR albedo, the SPWD was found to be more important than BT in the classification and to provide a higher accuracy than spectral data only, by allowing accuracy > 80 % in detecting glazed snow. Further research might consider other parameters to automatically detect snow glazed surfaces, including snow grain size or the normalized difference snow index. Finally, we provided for the first time an estimation of megadune migration from field and remote observations at the It-ITASE site. The results obtained using field measurements and remote observations allow for calculating all the components of megadune migration, absolute (11–14 m a−1), sedimentological migration (13–15 m a−1) and the ice flow (1–2 m a−1), and to conclude that for megadunes with a wavelength of 3 km and migration of approximately 10 m a−1, the burying process of snow on glazed surfaces takes about 300 years, with an overlap of the crest to the trough and glazed to sastrugi surface. The reconstruction of paleo-climate based on firn/ice cores drilled in the megadune or downstream area is very complex; the distortion of recordings is characterized by a snow accumulation/hiatus periodicity of about hundreds of years. The length of periodic variations due to mesoscale relief and/or megadunes depends on ice velocity, megadune migration and snow accumulation and can therefore vary in space and time within the 500 000 km^2 of the megadune field and downstream area. In the end, our work points out the importance of antidune sedimentological processes in megadune fields with an almost opposite direction between the migration of surface features and ice flow derived, respectively, from feature tracking of optical images and SAR. These results present significant implication for surface measurements using radar/lidar altimetric satellite and measurements of ice flow using optical and SAR images in the megadune area. Moreover, our results point out the different elevation behaviour at a pluriannual scale of the stable elevation and NIR albedo of glazed surface, while the snow-covered surface changes elevation and NIR albedo, with a higher accumulation/elevation in correspondence with the previous trough, decreasing from the trough towards the windward crest. The wind-driven process greatly affects the SMB of the megadune area, which implies that all or most of the regional accumulation (as determined by RACMO and other models) is gathered in the accretionary faces, whereas in the downwind area the SMB is near zero with a long hiatus in snow accumulation.

Appendix A

Sensor	Tile	Scene	Solar zenith (°)	Azimuth (°)
OLI	069119	25 Nov 2013	69	89
OLI	069119	11 Dec 2013	67	91
OLI	069119	27 Dec 2013	67	93
OLI	069119	28 Jan 2014	72	95
OLI	069119	28 Nov 2014	68	89
OLI	069119	17 Dec 2015	67	92
OLI	069119	18 Jan 2016	70	95
OLI	069119	4 Nov 2017	74	87
OLI	069119	10 Nov 2019	72	88
OLI	069119	28 Dec 2019	67	93
OLI	069119	29 Jan 2020	73	95
OLI	081114	31 Oct 2014	68	62
OLI	081114	2 Dec 2014	61	65
OLI	081114	18 Dec 2014	60	67
OLI	081114	6 Jan 2016	62	69
OLI	081114	30 Nov 2019	62	65
OLI	081114	17 Jan 2020	64	70
S2	T51CWL	10 Jan 2018	67	87
S2	T51CWL	2 Jan 2021	66	84
S2	T52CEA	13 Dec 2016	59	59
S2	T52CEA	27 Dec 2020	59	61

Table A1. Landsat (OLI) and Sentinel-2 (S2) images in the EAIIST (069119 and T51CWL tiles for L8OLI and S2, respectively) and It-ITASE (081114 and T52CEA tiles for L8OLI and S2, respectively) areas used in the study with corresponding solar zenith and azimuth angles from the Landsat/Sentinel metadata.

	It-ITASE		EAIIST	
Year	No. of stripes	Percentage of the total	No. of stripes	Percentage of the total
2008	5	0.4 %	5	0.5 %
2009	13	0.9 %	11	1.2 %
2010	27	1.9 %	27	2.9 %
2011	128	9.0 %	44	4.7 %
2012	27	1.9 %	16	1.7 %
2013	110	7.7 %	89	9.5 %
2014	217	15.2 %	184	19.6 %
2015	136	9.5 %	61	6.5 %
2016	593	41.6 %	398	42.5 %
2017	169	11.9 %	102	10.9 %

Table A2. Frequency of the REMA DEM stripes at the EAIIST and It-ITASE sites from different years, based on the REMA strip index.

EAIIST				It-ITASE			
Dataset	Average	Max	Min	Dataset	Average	Max	Min
Landsat 8	224°	232°	212°	Landsat 8	240°	250°	215°
ERA5 $\geq 0\,m\,s^{-1}$	225°	230°	220°	ERA5 $\geq 0\,m\,s^{-1}$	227°	236°	215°
ERA5 $\geq 3\,m\,s^{-1}$	225°	229°	220°	ERA5 $\geq 3\,m\,s^{-1}$	226°	233°	217°
ERA5 $\geq 5\,m\,s^{-1}$	225°	229°	220°	ERA5 $\geq 5\,m\,s^{-1}$	226°	234°	217°
ERA5 $\geq 7\,m\,s^{-1}$	225°	235°	220°	ERA5 $\geq 7\,m\,s^{-1}$	227°	236°	218°
ERA5 $\geq 11\,m\,s^{-1}$	223°	229°	216°	ERA5 $\geq 11\,m\,s^{-1}$	231°	240°	223°

Table A3. Wind direction statistics (average, maximum and minimum values) for the considered datasets: Landsat 8 at 30 m spatial resolution and ERA5 at 30 km spatial resolution (divided into five sub-datasets according to wind speed) at the EAIIST and It-ITASE sites.

Data availability

Data used for the aims of the present study are available from different repositories. Landsat 8 and Sentinel-2 imagery are available at https://doi.org/10.5066/P9OGBGM6 (Earth Resources Observation And Science (EROS) Center, 2013) and https://doi.org/10.5270/S2_-znk9xsj (European Space Agency, 2022). ERA5 data are available at https://doi.org/10.24381/cds.adbb2d47 (Hersbach et al., 2018). The REMA DEM is available at https://doi.org/10.7910/DVN/X7NDNY (Howat et al., 2022). Field data were obtained from previously published papers, i.e. Frezzotti et al. (2002a, b) and Vitturari et al. (2004).

Author contributions

GT and MF conceived the idea of this work. GT and DF developed the procedure and processed the satellite image and data. All authors contributed to the writing of the final manuscript.

Competing interests

The contact author has declared that none of the authors has any competing interests.

Disclaimer

Publisher's note: Copernicus Publications remains neutral with regard to jurisdictional claims in published maps and institutional affiliations.

Acknowledgments

The authors are thankful to the PNRA (National Antarctic Research Program) and MNA (National Antarctic Museum) of Italy (fellowship and PhD scholarship to Giacomo Traversa, respectively) and

Levissima Sanpellegrino S.p.A. (post-doc fellowship to Davide Fugazza). This study was supported by the EAIIST project (no. ANR-16-CE01-0011), the Institut Polaire Français Paul-Émile Victor (IPEV), the National Antarctic Research Program (PNRA), the French National Research Agency, the Department of Science of the Università degli Studi Roma Tre (Minister of University and Research Italy, Dipartimenti Eccellenza 2023–2027) and the Department for Regional Affairs and Autonomies (DARA). The authors would like to warmly thank all the participants of the It-ITASE and EAIIST traverses for their tremendous field contributions allowing for the collection of the crucial in situ measurements used in this study. Finally, the authors thank the editor, Ted Scambos, Stef Lhermitte and an anonymous referee for having revised the paper; their suggestions have strongly improved the quality of the research.

Financial support

The research has been supported by Levissima Sanpellegrino S.P.A. (grant no. LIB_VT17GDIOL, postdoc fellowship to Davide Fugazza).

Review statement

This paper was edited by Olaf Eisen and reviewed by Ted Scambos, Stef Lhermitte, and one anonymous referee.

References

Agosta, C., Amory, C., Kittel, C., Orsi, A., Favier, V., Gallée, H., van den Broeke, M. R., Lenaerts, J. T. M., van Wessem, J. M., van de Berg, W. J., and Fettweis, X.: Estimation of the Antarctic surface mass balance using the regional climate model MAR (1979–2015) and identification of dominant processes, The Cryosphere, 13, 281–296, https://doi.org/10.5194/tc-13-281-2019, 2019.

Albert, M., Shuman, C., Courville, Z., Bauer, R., Fahnestock, M., and Scambos, T.: Extreme firn metamorphism: impact of decades of vapor transport on near-surface firn at a low-accumulation glazed site on the East Antarctic plateau, Ann. Glaciol., 39, 73–78, https://doi.org/10.3189/172756404781814041, 2004.

Arcone, S. A., Jacobel, R., and Hamilton, G.: Unconformable stratigraphy in East Antarctica: Part I. Large firn cosets, recrystallized growth, and model evidence for intensified accumulation, J. Glaciol., 58, 240–252, https://doi.org/10.3189/2012JoJ11J044, 2012a.

Arcone, S. A., Jacobel, R., and Hamilton, G.: Unconformable stratigraphy in East Antarctica: Part II. Englacial cosets and recrystallized layers, J. Glaciol., 58, 253–264, https://doi.org/10.3189/2012JoG11J045, 2012b.

Azzoni, R. S., Senese, A., Zerboni, A., Maugeri, M., Smiraglia, C., and Diolaiuti, G. A.: Estimating ice albedo from fine debris cover quantified by a semi-automatic method: the case study of Forni Glacier, Italian Alps, The Cryosphere, 10, 665–679, https://doi.org/10.5194/tc-10-665-2016, 2016.

Canny, J.: A computational approach to edge detection, IEEE T. Pattern Anal. Mach. Intell., PAMI-8, 679–698, 1986.

Courville, Z. R.: Gas diffusivity and air permeability of the firn from cold polar sites, PhD thesis, Dartmouth College, 3341626, https://www.proquest.com/openview/67a457ce9973e10b601ba324a525b3f0/1?cbl=18750&pq-origsite=gscholar&parentSessionId=UpZ4V8N6xSPAcKTOy9xE7le%2FzOB69XIB%2FSnUxdEWmwk%3D (last access: 15 January 2023), 2007.

Courville, Z. R., Albert, M. R., Fahnestock, M. A., Cathles, L. M., and Shuman, C. A.: Impacts of an accumulation hiatus on the physical properties of firn at a low-accumulation polar site, J. Geophys. Res., 112, F02030, https://doi.org/10.1029/2005JF000429, 2007.

Dadic, R., Mott, R., Horgan, H. J., and Lehning, M.: Observations, theory, and modeling of the differential accumulation of Antarctic megadunes: accumulation of Antarctic megadunes, J. Geophys. Res.-Earth, 118, 2343–2353, https://doi.org/10.1002/2013JF002844, 2013.

Das, I., Bell, R. E., Scambos, T. A., Wolovick, M., Creyts, T. T., Studinger, M., Frearson, N., Nicolas, J. P., Lenaerts, J. T. M., and van den Broeke, M. R.: Influence of persistent wind scour on the surface mass balance of Antarctica, Nat. Geosci., 6, 367–371, https://doi.org/10.1038/ngeo1766, 2013.

Earth Resources Observation And Science (EROS) Center: Collection-2 Landsat 8-9 OLI (Operational Land Imager) and TIRS (Thermal Infrared Sensor) Level-2 Science Products, Earth Resources Observation And Science (EROS) Center [data set], https://doi.org/10.5066/P9OGBGM6, 2013.

Ekaykin, A. A., Lipenkov, V. Ya., and Shibaev, Yu. A.: Spatial Distribution of the Snow Accumulation Rate Along the Ice Flow Lines Between Ridge B and Lake Vostok, Ice Snow, Journal of ice and snow, 52, 122, https://doi.org/10.15356/2076-6734-2012-4-122-128, 2015.

European Space Agency: Sentinel-2 MSI Level-2A BOA Reflectance, European Space Agency [data set], https://doi.org/10.5270/S2_-znk9xsj, 2022.

Fahnestock, M. A., Scambos, T. A., Shuman, C. A., Arthern, R. J., Winebrenner, D. P., and Kwok, R.: Snow megadune fields on the East Antarctic Plateau: Extreme atmosphere-ice interaction, Geophys. Res. Lett., 27, 3719–3722, https://doi.org/10.1029/1999GL011248, 2000.

Frezzotti, M., Gandolfi, S., Marca, F. L., and Urbini, S.: Snow dunes and glazed surfaces in Antarctica: new field and remote-sensing data, Ann. Glaciol., 34, 81–88, https://doi.org/10.3189/172756402781817851, 2002a.

Frezzotti, M., Gandolfi, S., and Urbini, S.: Snow megadunes in Antarctica: Sedimentary structure and genesis, J. Geophys. Res.-Atmos., 107, ACL 1-1–ACL 1-12, https://doi.org/10.1029/2001JD000673, 2002b.

Frezzotti, M., Pourchet, M., Flora, O., Gandolfi, S., Gay, M., Urbini, S., Vincent, C., Becagli, S., Gragnani, R., and Proposito, M.: New estimations of precipitation and surface sublimation in East Antarctica from snow accumulation measurements, Clim. Dynam., 23, 803–813, https://doi.org/10.1007/s00382-004-0462-5, 2004.

Frezzotti, M., Pourchet, M., Flora, O., Gandolfi, S., Gay, M., Urbini, S., Vincent, C., Becagli, S., Gragnani, R., and Proposito, M.: Spatial and temporal variability of snow accumulation in East Antarctica from traverse data, J. Glaciol., 51, 113–124, https://doi.org/10.3189/172756505781829502, 2005.

Fujii, Y., Yamanouchi, T., Suzuki, K., and Tanaka, S.: Comparison of the Surface Conditions of the Inland Ice Sheet, Dronning Maud Land. Antarctica. Derived from Noaa AVHRR Data with Ground Observation, Ann. Glaciol., 9, 72–75, https://doi.org/10.3189/S0260305500000410, 1987.

Gallet, J.-C., Domine, F., Savarino, J., Dumont, M., and Brun, E.: The growth of sublimation crystals and surface hoar on the Antarctic plateau, The Cryosphere, 8, 1205–1215, https://doi.org/10.5194/tc-8-1205-2014, 2014.

Hersbach, H., Bell, B., Berrisford, P., Biavati, G., Horányi, A., Muñoz Sabater, J., Nicolas, J., Peubey, C., Radu, R., Rozum, I., Schepers, D., Simmons, A., Soci, C., Dee, D., and Thépaut, J.-N.: ERA5 hourly data on single levels from 1959 to present, Copernicus Climate Change Service (C3S) Climate Data Store (CDS) [data set], https://doi.org/10.24381/cds.adbb2d47, 2018.

Hersbach, H., Bell, B., Berrisford, P., Hirahara, S., Horányi, A., Muñoz-Sabater, J., Nicolas, J., Peubey, C., Radu, R., Schepers, D., Simmons, A., Soci, C., Abdalla, S., Abellan, X., Balsamo, G., Bechtold, P., Biavati, G., Bidlot, J., Bonavita, M., Chiara, G., Dahlgren, P., Dee, D., Diamantakis, M., Dragani, R., Flemming, J., Forbes, R., Fuentes, M., Geer, A., Haimberger, L., Healy, S., Hogan,

R. J., Hólm, E., Janisková, M., Keeley, S., Laloyaux, P., Lopez, P., Lupu, C., Radnoti, G., Rosnay, P., Rozum, I., Vamborg, F., Villaume, S., and Thépaut, J.: The ERA5 Global Reanalysis, Q. J. Roy. Meteor. Soc., 146, qj.3803, https://doi.org/10.1002/qj.3803, 2020.

Howat, I. M., Porter, C., Smith, B. E., Noh, M.-J., and Morin, P.: The Reference Elevation Model of Antarctica, The Cryosphere, 13, 665–674, https://doi.org/10.5194/tc-13-665-2019, 2019.

Howat, I., Porter, C., Noh, M.-J., Husby, E., Khuvis, S., Danish, E., Tomko, K., Gardiner, J., Negrete, A., Yadav, B., Klassen, J., Kelleher, C., Cloutier, M., Bakker, J., Enos, J., Arnold, G., Bauer, G., and Morin, P.: The Reference Elevation Model of Antarctica – Strips, Version 4.1, Harvard Dataverse, V1 [data set], https://doi.org/10.7910/DVN/X7NDNY, 2022.

Jawak, S. D., Kumar, S., Luis, A. J., Bartanwala, M., Tummala, S., and Pandey, A. C., Evaluation of Geospatial Tools for Generating Accurate Glacier Velocity Maps from Optical Remote Sensing Data, Proceedings, 2, 341, https://doi.org/10.3390/ecrs-2-05154, 2018.

Jezek, K. C.: Glaciological properties of the Antarctic ice sheet from RADARSAT-1 synthetic aperture radar imagery, Ann. Glaciol., 29, 286–290, https://doi.org/10.3189/172756499781820969, 1999.

Klok, E. L., Greuell, W., and Oerlemans, J.: Temporal and spatial variation of the surface albedo of Morteratschgletscher, Switzerland, as derived from 12 Landsat images, J. Glaciol., 49, 491–502, https://doi.org/10.3189/172756503781830395, 2003.

Kodama, Y., Wendler, G., and Gosink, J.: The effect of blowing snow on katabatic winds in Antarctica, Ann. Glaciol., 6, 59–62, https://doi.org/10.3189/1985AoG6-1-59-62, 1985.

Lenaerts, J. T., Medley, B., van den Broeke, M. R., and Wouters, B.: Observing and modeling ice sheet surface mass balance, Rev. Geophys., 57, 376–420, 2019.

Liang, S.: Narrowband to broadband conversions of land surface albedo I: Algorithms, Remote Sens. Environ., 76, 213–238, https://doi.org/10.1016/S0034-4257(00)00205-4, 2001.

Mather, K. B.: Further observations on sastrugi, snow dunes and the pattern of surface winds in Antarctica, Polar Rec., 11, 158–171, https://doi.org/10.1017/S0032247400052888, 1962.

Meredith, M., Sommerkorn, M., Cassotta, S., Derksen, C., Ekaykin, A., Hollowed, A., Kofinas, G., Mackintosh, A., Melbourne-Thomas, J., and Muelbert, M. M. C.: Polar Regions, chap. 3, IPCC Special Report on the Ocean and Cryosphere in a Changing Climate, https://doi.org/10.1017/9781009157964.005, 2019.

Mouginot, J., Rignot, E., Scheuchl, B., and Millan, R.: Comprehensive annual ice sheet velocity mapping using Landsat-8, Sentinel-1, and RADARSAT-2 data, Remote Sens., 9, 364, https://doi.org/10.3390/rs9040364, 2017.

Núñez-González, F. and Martín-Vide, J. P.: Analysis of antidune migration direction, J. Geophys. Res.-Earth, 116, F02004, https://doi.org/10.1029/2010JF001761, 2011.

Palm, S. P., Yang, Y., and Kayetha, V.: New Perspectives on Blowing Snow in Antarctica and Implications for Ice Sheet Mass Balance, in: Antarctica – A Key To Global Change, edited by: Kanao, M., Toyokuni, G., and Yamamoto, M., IntechOpen, https://doi.org/10.5772/intechopen.81319, 2019.

Parish, T. R. and Bromwich, D. H.: Continental-scale simulation of the Antarctic katabatic wind regime, J. Climate, 4, 135–146, https://doi.org/10.1175/1520-0442(1991)004<0135:CSSOTA>2.0.CO;2, 1991.

Picard, G., Libois, Q., Arnaud, L., Verin, G., and Dumont, M.: Development and calibration of an automatic spectral albedometer to estimate near-surface snow SSA time series, The Cryosphere, 10, 1297–1316, https://doi.org/10.5194/tc-10-1297-2016, 2016.

Pietroni, I., Argentini, S., and Petenko, I.: One year of surface-based temperature inversions at Dome C, Antarctica, Bound.-Lay. Meteorol., 150, 131–151, 2014.

Pirazzini, R.: Surface albedo measurements over Antarctic sites in summer, J. Geophys. Res., 109, D20118, https://doi.org/10.1029/2004JD004617, 2004.

Proposito, M., Becagli, S., Castellano, E., Flora, O., Genoni, L., Gragnani, R., Stenni, B., Traversi, R., Udisti, R., and Frezzotti, M.: Chemical and isotopic snow variability along the 1998 ITASE traverse from Terra Nova Bay to Dome C, East Antarctica, Ann. Glaciol., 35, 187–194, https://doi.org/10.3189/172756402781817167, 2002.

Prothero, D. R. and Schwab, F.: Sedimentary geology, Macmillan, ISBN 978-1-4292-3155-8, 2004.

Rignot, E., Echelmeyer, K., and Krabill, W.: Penetration depth of interferometric synthetic-aperture radar signals in snow and ice, Geophys. Res. Lett., 28, 3501–3504, https://doi.org/10.1029/2000GL012484, 2001.

Rignot, E., Mouginot, J., and Scheuchl, B.: MEaSUREs InSAR-based Antarctica ice velocity map, version 2, Boulder CO NASA DAAC Natl. Snow Ice Data Cent. [data set], https://doi.org/10.5067/D7GK8F5J8M8R. 2017.

Rignot, E., Mouginot, J., Scheuchl, B., van den Broeke, M., van Wessem, M. J., and Morlighem, M.: Four decades of Antarctic Ice Sheet mass balance from 1979–2017, P. Natl. Acad. Sci. USA, 116, 1095–1103, https://doi.org/10.1073/pnas.1812883116, 2019.

Scambos, T. A., Dutkiewicz, M. J., Wilson, J. C., and Bindschadler, R. A.: Application of image cross-correlation to the measurement of glacier velocity using satellite image data, Remote Sens. Environ., 42, 177–186, 1992.

Scambos, T. A., Frezzotti, M., Haran, T., Bohlander, J., Lenaerts, J. T. M., Van Den Broeke, M. R., Jezek, K., Long, D., Urbini, S., Farness, K., Neumann, T., Albert, M., and Winther, J.-G.: Extent of low-accumulation "wind glaze" areas on the East Antarctic plateau: implications for continental ice mass balance, J. Glaciol., 58, 633–647, https://doi.org/10.3189/2012JoG11J232, 2012.

Swithinbank, C., Ferrigno, J. G., Williams, R. S., and Chinn, T. J.: Antarctica, Geological Survey professional paper , 1386-B. U.S. G.P.O., Washington, DC, https://hdl.handle.net/2027/uc1.31210020769210 (last access: 13 January 2023), 1988.

Traversa, G. and Fugazza, D.: Evaluation of Anisotropic Correction Factors for the Calculation of Landsat 8 OLI Albedo on the Ice Sheets, Geogr. Fis. Din. Quar., 44, 91–95, https://doi.org/10.4461/GFDQ.2021.44.8, 2021.

Traversa, G., Fugazza, D., Senese, A., and Diolaiuti, G. A.: Preliminary results on Antarctic albedo from remote sensing observations, Geogr. Fis. Din. Quat., 42, 245–254, https://doi.org/10.4461/GFDQ.2019.42.14, 2019.

Traversa, G., Fugazza, D., Senese, A., and Frezzotti, M.: Landsat 8 OLI Broadband Albedo Validation in Antarctica and Greenland, Remote Sens., 13, 799, https://doi.org/10.3390/rs13040799, 2021a.

Traversa, G., Fugazza, D., and Frezzotti, M.: Analysis of Megadune Fields in Antarctica, in: 2021 IEEE International Geoscience and Remote Sensing Symposium IGARSS, 5513–5516, https://doi.org/10.1109/IGARSS47720.2021.9554827, 2021b.

Van Wessem, J. M., Reijmer, C. H., Morlighem, M., Mouginot, J., Rignot, E., Medley, B., Joughin, I., Wouters, B., Depoorter, M. A., Bamber, J. L., Lenaerts, J. T. M., Van De Berg, W. J., Van Den Broeke, M. R., and Van Meijgaard, E.: Improved representation of East Antarctic surface mass balance in a regional atmospheric climate model, J. Glaciol., 60, 761–770, https://doi.org/10.3189/2014JoG14J051, 2014.

Vittuari, L., Vincent, C., Frezzotti, M., Mancini, F., Gandolfi, S., Bitelli, G., and Capra, A.: Space geodesy as a tool for measuring ice surface velocity in the Dome C region and along the ITASE traverse, Ann. Glaciol., 39, 402–408, https://doi.org/10.3189/172756404781814627, 2004.

Warren, S. G.: Optical properties of snow, Rev. Geophys., 20, 67–89, https://doi.org/10.1029/RG020i001p00067, 1982.

Wendler, G., André, J. C., Pettré, P., Gosink, J., and Parish, T.: Katabatic winds in Adélie coast, in: Antarctic Meteorology and Climatology: Studies Based on Automatic Weather Stations, edited by: Bromwich, D. H. and Stearns, C. R., 61, 23–46, https://doi.org/10.1029/AR061p0023, 1993.

Zanter, K.: Landsat 8 (L8) data users handbook, Landsat Sci. Off. Website, https://d9-wret.s3.us-west-2.amazonaws.com/assets/palladium/production/s3fs-public/atoms/files/LSDS-1574_L8_Data_Users_Handbook-v5.0.pdf (last access:13 January 2023), 2019.

4.4 Conclusion of the chapter

In conclusion, Chapter 4 intended to provide a deep analysis of snow dunes in Antarctica in different points of view. Using different remote sensing sources and in-situ measurements acquired during past Antarctic campaigns, it was possible to update previous knowledge about Antarctic megadunes and demonstrate and quantify previous hypotheses. A precise calculation of albedo properties of leeward and windward flanks of the dunes was carried out, to which is added a detailed analysis of thermal brightness temperature using Landsat 8 OLI-TIRS images. It has been then demonstrated the lower values of broadband albedo on leeward glazed snow in respect to firn windward flanks of the dunes by 0.02α (0.04α in the NIR wavelengths). Additionally, the higher mean BT on these ablation areas than on surrounding snow was confirmed and quantified. Then, taking advantage of wind direction obtained from ERA5 reanalysis data and vectorization of sastrugi, combined with the high spatial resolution REMA DEM, SPWD at high resolution was calculated, being one of the parameters mostly significant for characterization of megadune fields. Finally, the combination of spectral information (albedo and BT) and topographic data (SPWD) allowed the automatic detection of glazed surfaces with an accuracy higher than 80%. In addition to these detailed spectral analyses which allowed a characterization and detection of glazed snow, the dune migration was investigated with a combination of in-situ and remote datasets. Using both satellite Sentinel-2 and Landsat 8 imagery, to which was applied a feature tracking module, as well as GPS (It-ITASE 1999) and REMA-DEM transects over a megadune field, the dune migration and its components were analysed and quantified, providing a final 10 ma^{-1} mean displacement and confirming their anti-dunal formation. Future efforts would focus on the application of indices for glazed snow identification, as well as their analysis through hyperspectral sensor for a better characterization. Regarding the morphology and processes of megadune fields, their presence would be analysed in relation with bedrock topography, with the aim of investigating not only surficial features, but also deeper characterization.

Chapter 5: Blue ice areas

5.1 Presentation of the chapter

In this chapter a preliminary analysis of the second type of ablation areas is carried out, i.e., blue ice areas (BIAs). In detail, using MCD43A3 product of the Moderate Resolution Imaging Spectroradiometer (MODIS), which combine acquisitions from both Terra and Aqua satellites in a 16-day data temporally weighted to the ninth day, the research focused on 2000-2020 period firstly at continental scale and then on a specific sample area of the Antarctic continent, the Amery Ice Shelf in the Mac. Robertson Land. The use of MODIS, and in particular the broadband and NIR narrowband albedo, allowed to detect with good precision the BIAs and analyse their spatial variation in time. Additionally, taking advantage of temperature and wind in-situ measurements from an AWS, the relation among these parameters and spatial evolution was investigated in order to find a possible dependence. This research is part of a published article: "Traversa, G., Zappetti M. and Senese A. (2021), Spring and Summer Spatial Evolution of Blue Ice Areas in Antarctica, Geografia Fisisca e Dinamica Quaternaria, 44, 70-90, https://doi.org/10.4461/GFDQ.2021.44.7" (Sec. 5.2).

5.2 Article "Spring and Summer Spatial Evolution of Blue Ice Areas in Antarctica" (Traversa et al., 2021c)

Giacomo Traversa[1,2*], Marta Zappetti[2] & Antonella Senese[2]

[1] Department of Physical Sciences, Earth and Environment (DSFTA), Università Degli Studi Di Siena, 53100 Siena, Italy;

[2] Department of Environmental Science and Policy (ESP), Università Degli Studi Di Milano, 20133 Milan, Italy.

Abstract: Blue ice areas (BIAs) are relevant ablation surfaces present on the Antarctic continent, mainly located in proximity of the coast or mountainous zones, in sloping areas. Featuring negative values of surface mass balance, in a continent where this parameter is averagely positive, their study gains of importance, in particular regarding their evolution in time and space and the reasons of their variations. Therefore, taking advantage of remote sensing techniques and satellite products, we analysed the intra-annual BIA variation in 2000-2021 spring-summer periods. Basing the detection on topographic slope and albedo values from MCD43A3 product of Moderate Resolution Imaging Spectroradiometer (MODIS), trends are detected for all the analysed seasons, showing a steady and significant increase from the spring to the summer and only in half of the cases a final decrease in early autumn. Comparing these areal patterns with meteorological parameters (i.e., air temperature and wind speed) acquired by an automatic weather station located on the Amery Ice Shelf (Eastern Antarctica), a relation between positive temperatures and BIA increase was found ($R = 0.60$), possibly due to snow melting or sublimation processes, which expose the beneath bare blue ice. In addition, weak relations between area increase and high and steady wind speed conditions are detected. Finally, the areal decrease in early autumn observed in a certain number of seasons could be explained with intense phenomena of melting, as a result of continuing days of positive air temperatures, which lead to the formation of drainage systems, or with extreme solid precipitation events. In both the cases, water and snow cover the BIAs, making them impossible to be detected from remote techniques.

1. Introduction

One of the most challenging and long research in the cryosphere sciences regards the reconstruction of processes and factors which control the mass balance in Antarctica, in relation with climate change. A relevant feature is represented by the blue ice, a surface type peculiar of the Antarctic continent. In fact, blue ice areas (BIAs) are known to be ablation areas, i.e., zones featuring a negative surface mass balance (SMB), where net annual ablation exceeds accumulation, in contradiction with the rest of the continent where it is mainly positive (Agosta & alii, 2019). Therefore, it has an important control on ice sheet mass balance (Bintanja & Van Den Broeke, 1995), contributing to the global sea level change (Van den Broeke & alii, 2011). Thus, an eventual increasing of these areas could bring to a relevant mass loss in future, leading to consequences to the global climatic system. BIAs are one

of the few areas in Antarctica presenting an anomalous SMB, as well as the wind crust or glazed snow surfaces, which, however, show a near-zero SMB and have a significant lower extent (Scambos & alii, 2012; Traversa & alii, 2021a). Both these ablation areas are shaped by the effect of the wind scouring phenomenon (Das & alii, 2013), i.e., the interaction of snow (and its morphogenic stage transition), steady catabatic winds and peculiar topographic conditions, which lead to mass loss by melting, evaporation, sublimation and wind erosion. BIAs covers approximately 1-1.7% of Antarctic continent (Bintanja, 1999; Winther & alii, 2001; Hui & alii, 2014) and they are usually located in proximity of the coast or mountainous zones, in sloping areas (Winther & alii, 2001). Historically, the first glaciological and geomorphological surveys on BIAs were carried out in the early fifties in Dronning Maud Land (van Autenboer, 1964; Worsfold, 1967; Juckes, 1972), but then their interest increased significantly after the discovery of several meteorites trapped inside (Yoshida & alii, 1971), which show ages up to 2.5 Ma and are mainly located at altitudes over 2000 m a.s.l., suggesting that high-altitude BIAs are also the most stable ones (Cassidy & alii, 1992). Geomorphologically, we can distinguish four types of BIAs (Bintanja, 1999): i) associated to nunataks or located on the edge of barriers which help the snow accumulation, with lengths that can be 50-100 times higher than barrier height (Takahashi & alii, 1992); ii) located along valley glaciers, emerging by the effect of catabatic wind erosion; iii) located on relatively sloping surfaces where a wind effect similar to type ii is encountered; iv) located at the bottom of mountains and due to the effect of wind acceleration which removes/sublimate snow/firn/ice from the surface. In general, most of the BIAs in Antarctica are of type i, even if other types show averagely wider areas. Their formation can be divided into four main phases (Bintanja, 1999): i) rock is in depth below ice and does not have any influence on the surface, ii) ice-flow is affected by topographic slope and downstream glacier surface melts becoming steeper, then katabatic winds become stronger eroding snow and exposing bare ice, iii) nunatak emerges and on its leeward flank ice thickness decreases and blue ice enlarges by effect of snow erosion and sublimation, iv) further ice lowering releases completely the nunatak, increasing turbulences, sublimation and snow transport. In addition, progressive loss of blue ice mass is owed to its lower albedo (0.50-0.70, Bintanja & Van Den Broeke, 1995; Bintanja, 1999; Reijmer & alii, 2001) than surrounding snow (0.80-0.85, Grenfell & Warren, 1994), increasing the available energy for sublimation/melting. An increase in wind action on leeward flanks can additionally lead to an enlargement of their surface. After a first field approach (van Autenboer, 1964; Worsfold, 1967; Juckes, 1972), BIAs started to be studied via remote sensing (Orheim & Lucchitta, 1990) and the present study intends to analyse their distribution taking advantage of these techniques. In detail, images from satellites Terra and Aqua of the product Moderate Resolution Imaging Spectroradiometer (MODIS) in the spring-summer seasons (October-February) of period 2000-2021

were used, in particular data of albedo. After a first methodological validation on a sample area of Victoria Land by comparing MODIS data with higher resolution Landsat 8 OLI images (calculated using the recent model proposed by Traversa & alii, 2021b), a preliminary continental scale analysis of variation in space and time of the BIAs was carried out. Then, a local study on the BIAs on the Amery Ice-Shelf region (East Antarctica) is proposed, with an analysis of their extent as a function of the altitude and finally the so calculated trends were compared with meteorological measurements (i.e., temperature and wind speed) collected by an Automatic Weather Station (AWS).

2. Data and Methods

Two significant parameters fundamental for the automatic detection of BIAs were used: topographic slope and albedo. As regards the slope, it was calculated from the Reference Elevation Model of Antarctica (REMA, Howat & alii, 2019), the highest spatial resolution Digital Elevation Model (DEM) available for this continent (with a resolution of 8 m). For the albedo product, since the aim of the work is an analysis of the entire Antarctica, a middle-resolution dataset was chosen (500 m), i.e., MODIS imagery from Terra (EOS AM) and Aqua (EOS PM) satellites, which acquire daily data since 2000 and 2002 respectively in 36 bands having a 0.4-14.4 μm of spectral resolution. In fact, products with higher resolution would entail more storage space and working time. In detail, we tested three products of MODIS, in order to find the best one for our objectives: MOD10A1 (Terra), MYD10A1 (Aqua) and MCD43A3 (Terra and Aqua). For MOD10A1 and MYD10A1 products, we used the broadband albedo layer, defined as the albedo integrated over the entire solar spectrum. Regarding the MCD43A3 product, we considered the Near Infrared (NIR) spectral albedo (i.e. reflectance for specific wavelengths bands) and the broadband black sky albedo (i.e., the directional hemispherical reflectance, that is inherent to specific locations and is linked with the structure and optical properties of the land cover, Schaaf & alii, 2011), since mostly clear-sky conditions are here considered as suggested by Tedesco & alii (2016) and Traversa & alii (2019). The main difference between these products is that MOD10A1 and MYD10A1 provide daily data and MCD43A3 uses 16-day (of Terra and Aqua MODIS data) temporally weighted to the ninth day. The choice fell on MCD43A3 since, mainly, it provides a more complete albedo map per each scene, with less no-data values due to cloud cover, as the values are based on 16 days instead of one. Additionally, MOD10A1 and MYD10A1 seem to present a latitudinal gradient of albedo values, which makes the albedo increase moving towards the South Pole, even on constant snow surfaces (possibly due to Solar Zenith Angle, SZA, effect, see Pirazzini, 2004). MCD43A3 allowed to analyse the BIAs from 2000 and we focused on the spring and summer (October-February) seasons, detailly on 9 scenes per season with 16 days of display (corresponding to MCD43A3 data-weight time), i.e., 14/10, 31/10, 17/11, 04/12,

21/12, 07/01, 24/01, 10/02 and 27/02 (dd/mm), thus analysing the period from 14/10/2000 to 27/02/2021. Finally, in order to validate the MCD43A3 product in BIA automatic detection, we used also albedo calculated from Landsat 8 OLI imagery (calculated through the methodology validated by Traversa & alii, 2021b), which present a higher spatial resolution of 30 m from the visible to shortwave infrared (SWIR) wavelengths (0.43-2.29 µm). Then, we decided to compare the variations of the BIA with the variations of temperature and wind speed, as a preliminary way to better understand their evolution in time and the reasons of these changes. In order to do so, we focused on an AWS located at 84 m a.s.l. on the Amery Ice Shelf on the East Antarctic Ice Sheet (EAIS), area characterized by a vast cover of blue ice (Budd, 1966; Markov & alii, 2019). The AWS is part of the Australian Antarctic Data Centre (AADC) and is named Amery G3, coordinates: 70° 53' 31" S, 69° 52' 21" E, and distant about 50 km from the nearest BIA (fig. 1). It provides several data, including hourly data of air temperature and wind speed at 2 m from the surface. Air temperature is available from 1999 to 2011, while wind speed data are provided only until 2008. Therefore, we compared only the first eight seasons (i.e., from 2000-2001 to 2007-2008) with corresponding area evolution.

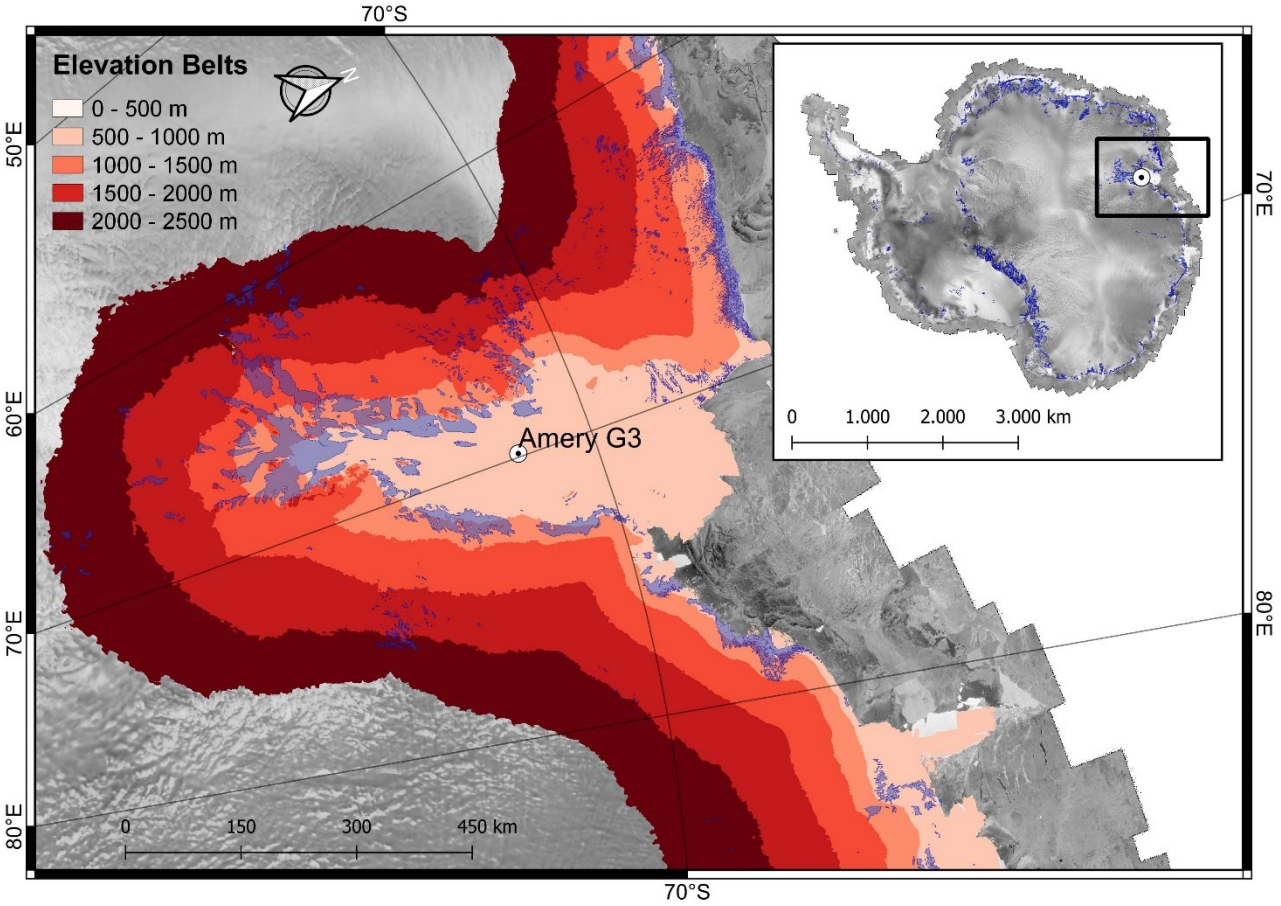

Fig. 1 - Amery Ice Shelf divided in elevation belts and the location of the Amery G3 AWS, with BIAs (Hui & alii, 2014) in blue and RAMP RADARSAT mosaic (Jezek, 1999) in the background. Location of the Amery Ice Shelf area in the zoom out.

BIA automatic detection and MCD43A3 albedo product validation

In order to automatically detect and map the BIAs on the entire Antarctic continent, four remote-sensing products and two parameters were considered, i.e., albedo and topographic slope. As regards the albedo, we used both the broadband and NIR spectral albedo, taking advantage of the thresholds given by Bintanja (1999) and Hui & alii (2014) (i.e., 0.50-0.70 for broadband albedo and 0.30-0.70 for NIR albedo). For the topographic slope, we followed Hui & alii (2014) who stated that almost 97% of Antarctic BIAs are in areas with a slope ≤ 5°. Finally, in order to automatically exclude nunataks from the analyses, Making Earth System Data Records for Use in Research Environment (MEaSUREs) Bedmachine product (Morlighem, 2020; Morlighem & alii, 2020) was taken into account, since this raster classifies the continent based on surface types, including rock outcrops. Then, using a conditional calculation based on the previous thresholds, we could automatically detect the BIAs and vectorize the so obtained raster map. However, in our survey, NIR albedo thresholds appeared to be slightly overestimated for MCD43A3 product of MODIS, and thus we calculated a new useful range starting from ten sample polygons on certain blue ice surfaces (manually digitalized using the Landsat Image Fig. 1 - Amery Ice Shelf divided in elevation belts and the location of the Amery G3 AWS, with BIAs (Hui & alii, 2014) in blue and RAMP RADARSAT mosaic (Jezek, 1999) in the background. Location of the Amery Ice Shelf area in the zoom out. Mosaic of Antarctica, LIMA at 15 m spatial resolution as background, Bindschadler & alii, 2008). The new calculated NIR albedo range was 0.20-0.50. Once the MODIS product and thresholds useful for the automatic detection were selected, we compared the use of MCD43A3 product of MODIS in BIA detection with a higher resolution satellite imagery (i.e., Landsat 8 OLI with 30 m of spatial resolution). The classification of the surface was processed using the same methodology followed for MCD43A3, i.e., conditional calculation based on slope and albedo (both NIR spectral and broadband). In order to calculate the dataset of albedo, both broadband and NIR spectral, from Landsat 8 imagery, the methodology proposed by Traversa & alii (2021b) was followed, which permits to derive reliable albedo values for the ice-sheets by four main process steps: zenith, atmospheric and topographic corrections and spectral to broadband albedo conversion using the Liang algorithm (Liang, 2001). For this reason, bands 2-4-5-6-7 of Landsat 8 (i.e., blue, red, NIR and SWIRs) were used. In this case, the range for BIAs of broadband albedo proposed by Hui & alii (2014, 0.30-0.70) was applied. With the aim of comparing the obtained results, a sample area was chosen (~100,000 km^2), located in Victoria Land (EAIS), in proximity of Mario Zucchelli Italian station, since a large presence of blue ice occurs in this zone (Folco & alii, 2006). Three consecutive scenes (same path) of Landsat 8 acquired on 31/12/2013 date (which presented almost no cloud cover above all the sample area) were used and compared to the corresponding date for MCD43A3. After having validated the MCD43A3 product,

an additional step was added to the dataset processing, fundamental for the intra-annual analysis: the cloud-mask application. In fact, focusing on the entire continent and calculating trends in time based on the amount of BIA surfaces, the effect of cloud cover could be relevant and removing those areas interested by this phenomenon was essential. Thus, a specific cloud-mask per each year was calculated, in order to exclude all those pixels presenting cloud-coverage in at least one analysed scene. This allowed to always compare the same cloud-free areas (pixels) during all a certain season and obtain a more significant areal trend in time. The cloud-mask was calculated using a conditional calculation which took into account the no-data pixels of each MCD43A3 scene, corresponding to cloud-covered pixels. A summarize of the image processing and the steps adopted for BIAs identification is showed in a workflow (fig. 2).

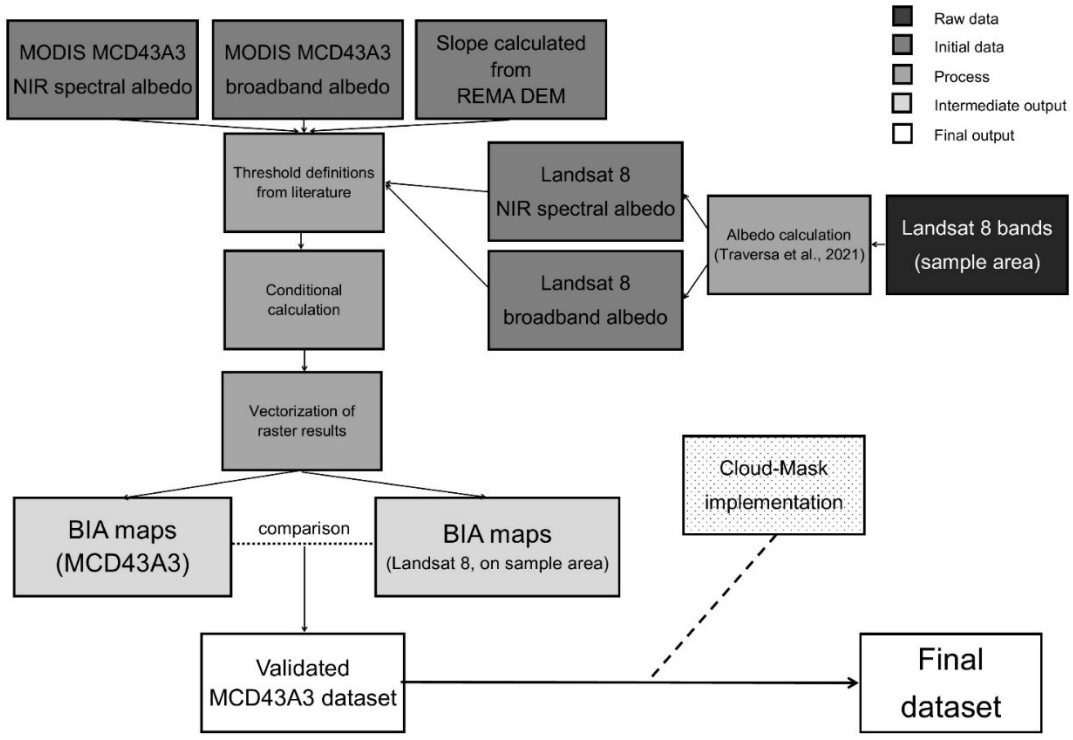

Fig. 2 - Workflow of the methodology used to calculate BIAs.

BIA distribution as a function of the altitude

Once having analysed the intra-annual trends of BIAs over the entire continent, we investigated a possible relation between BIA extension and the altitude, focusing on the area of the Amery Ice Shelf, where the AWS Amery G3 is located. In this context, starting from the REMA DEM (Howat & alii, 2019), we classified the area of the Amery Ice Shelf into five sub-zones of altitude (fig. 1), taking also advantage of its big extension in terms of height, as here the ice shelf and the blue ice extend from the sea level to around 2500 m a.s.l. (in accordance with REMA DEM, Howat & alii, 2019). The five zones are defined every 500 m as follows: between 0 and 500 m a.s.l., between 500 and 1000

m a.s.l., between 1000 and 1500 m a.s.l., between 1500 and 2000 m a.s.l. and between 2000 and 2500 m of altitude. In doing so, we assigned the corresponding zone to the BIA polygons and analysed the aerial trends in time for each zone.

Temperature and wind measurements from the Automatic Weather Station

In order to better understand the BIA evolution, we investigated the factors driving the BIA genesis or exposition. In fact, as reported above, the BIAs of the previous year can be covered by snow and then return to be exposed once the snow has completely melted. For the BIAs genesis we considered wind conditions following Bintanja & Van Den Broeke (1995), where it stated that a wind speed higher than 8 m s^{-1} can initiate the BIAs formation provided no mass is being imported into the region other than the background mass balance. Regarding snow melt, we evaluated thermal conditions affecting the melt processes: air temperature higher than 0 °C. In particular, we counted the number per day of hours with wind speed data higher than 8 m s^{-1}. Similarly, we counted the number per day of hours with positive temperature data. We performed the comparison between these meteorological parameters and BIA extent only over the elevation belt 0-500 m a.s.l., since the AWS is geographically located in this area (height of 84 m).

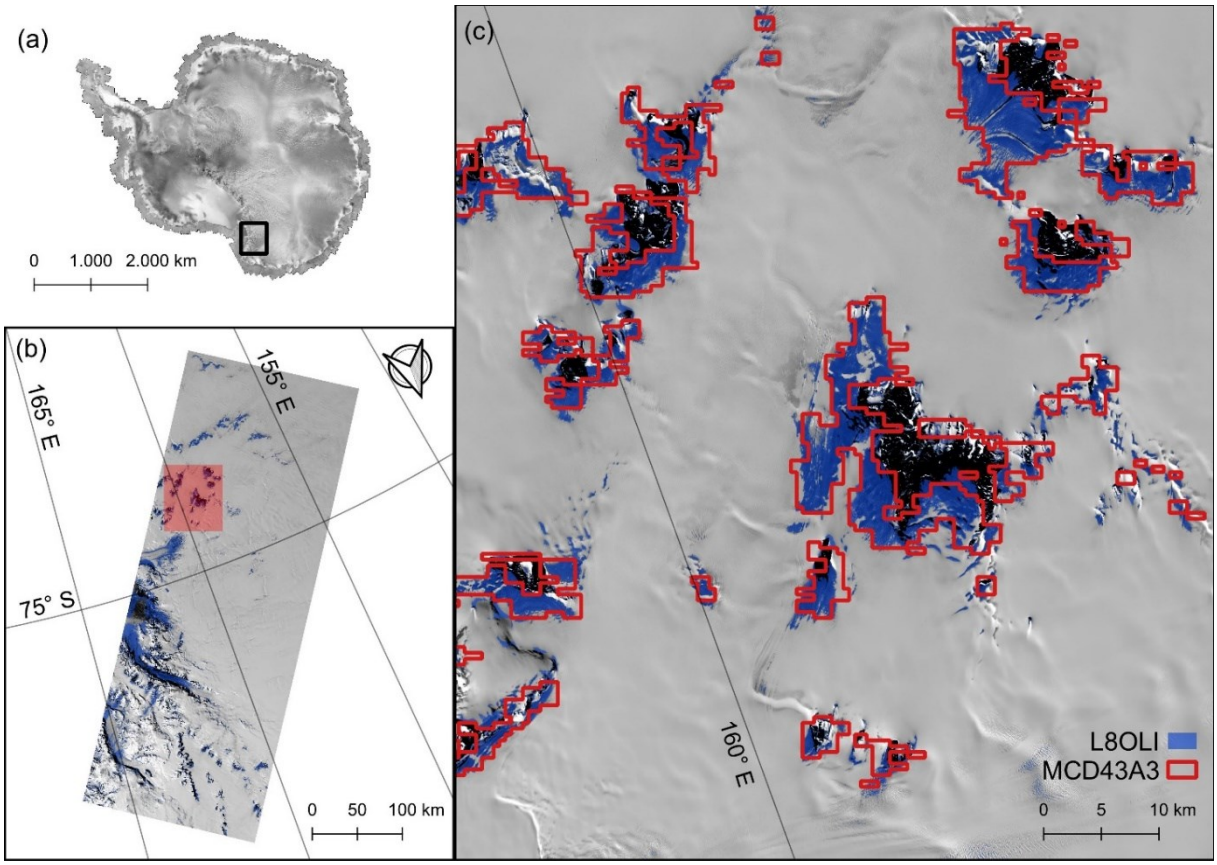

Fig. 3 - a) RAMP RADARSAT mosaic (Jezek, 1999) with b) the zoom in of the sample area on Victoria Land (Landsat scene on 31/12/2013) and in c) a focus of it, showing the comparison between BIAs calculated from Landsat 8 OLI imagery (blue polygons) and MCD43A3 of MODIS (red perimeters).

3. Results

At first, in order to quantify the error in mapping BIAs, we compared the results obtained from MCD43A3 of MODIS and Landsat 8 OLI (on 31/12/2013, fig. 3). We found about 8% areal overestimation of automatic detection using MCD43A3 of MODIS (~5600 km^2 out of a ~100,000 km^2 of analysed surface) if compared to the results obtained using Landsat 8 OLI (~5200 km^2), probably due to the large difference in spatial resolution (500 m and 30 m, respectively). Nevertheless, considering that the aim of this study is to analyse the entire continent, such an overestimation can be considered acceptable and therefore MCD43A3 can be considered suitable for the next analyses. Once validated the dataset, the results are here presented in three sections, corresponding to the three subsections of Data and Methods section: i) an initial overview of seasonal blue ice surface variability in time at continental scale, ii) the focus on Amery Ice Shelf region where the division as a function of the altitude was applied, and iii) the results of temperature and wind obtained from the Amery G3 AWS located on the ice shelf. In general, the maximum extent per year of BIAs is, on average, approximately equal to 1.1% of Antarctica (~150,000 km^2), similar to the value obtained by Bintanja (1999, 1%), and significantly lower if compared to the one of Hui & alii (2014, 1.7%).

Intra-annual analysis of BIA variability at continental scale

In order to find a trend in time of areal evolution of BIAs in Antarctica, an intra-annual or seasonal analysis is here calculated for each spring-summer season from 2000-2001 to 2020-2021 period (20 seasons), moving from 14/10 to 27/02 scenes of MODIS MCD43A3 product. In every studied season, nine dates were considered with 16-day span. For all the analysed seasons, a positive areal trend in time is found from the beginning of the spring (October) to the end of the summer (February). Generally, two types of trends are found. In 9 seasons (i.e., 2005-2006, 2011-2012, 2012-2013, 2013-2014, 2014-2015, 2015-2016, 2018-2019, 2019-2020 and 2020-2021) the increasing of blue ice area in time is constant and the maximum of extent is reached at the end of February. In 12 seasons (i.e., 2000-2001, 2001-2002, 2002-2003, 2003-2004, 2004-2005, 2006-2007, 2007-2008, 2008-2009, 2009-2010, 2010-2011, 2016-2017 and 2017-2018) the increasing is steady until the end of December and averagely between January and February turnarounds are detected, with the area that tends to decrease in the last considered scenes. Two examples of these two kinds of trends are in fig. 4 (2019-2020 season for the first type, and 2016-2017 season for the second one). These trends were found both applying or without applying the cloud-mask on the original data and the evolution in time remains approximately the same in both the cases. It is interesting to note that most of the seasons of the first type (i.e., steady increase during all the period) are mostly encountered in the second decades of analysis (i.e., 2011-2021) and the second type is mostly detected in the first decade (i.e., 2000-

2011), with just three exceptions in total. In general, the BIAs result to be doubled or more in terms of extension from the beginning to the end of the season (increasing of 150% on average) and therefore their percentage on the total of Antarctic surface varies significantly, from about 0.4% to 1.1% of the total area.

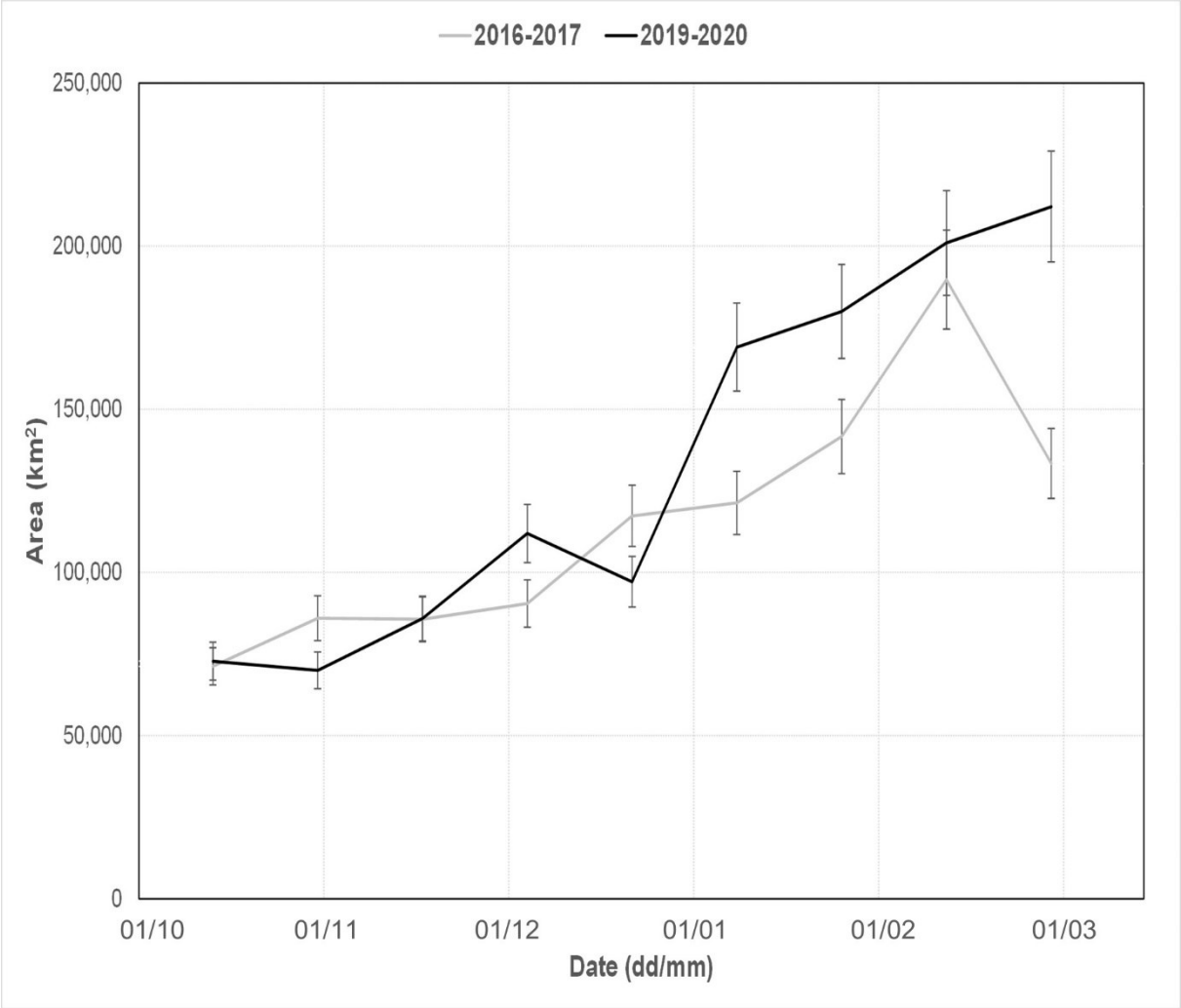

Fig. 4 - Variations of BIA extents at continental scale during 2016-2017 and 2019-2020 spring-summer seasons. Percentage-error bars of 8% are shown.

Intra-annual analysis of BIA as a function of the altitude in Amery Ice-Shelf region

In this section, an analysis of the BIA variation in time for the different altitudinal areas is provided, on the area of the Amery Ice Shelf, the largest ice shelf of the EAIS, SW of Prydz bay in Mac land. Here, generally, on average 20,000-30,000 km^2 of BIA are detected at their seasonal maximum extent, in accordance with previous studies (Liu & alii, 2006; Yu & alii, 2012). The altitudinal areas are five from 0 to 2500 m a.s.l., each of 500 m range (fig. 1). Spatially, the distribution of the BIAs is evidently influenced by the altitude, as a decrease is found moving from the coast to the highest zones. In fact, on average 70% of the total is located in the first 500 m of height. Then, in 500-1000 m a.s.l. and

1000-1500 m a.s.l. areas respectively 16% and 11% are observed. The remaining 3% is in the last two higher zones, subdivided in 2.6% and 0.4% in 1500-2000 and 2000-2500 m a.s.l. areas, respectively. Moving to the temporal variation in blue ice extent in each elevation belt, we found a positive trend for all the years in the first belt (0-500 m a.s.l.) with similar patterns to the ones described for the entire continent. In most of the cases, the major increase in area happened between the end of December and the beginning of January. In fact, on average an increase of +15,000 km^2 along the summer season was detected, with maximum value of +25,000 km^2 on 2004-2005 and minimum +9,000 km^2 on 2001-2002. In certain seasons, the decrease at the end of season was detected, being on average -9,500 km^2 from the peak, with maximum decrease again on 2004-2005 showing -17,000 km^2 (thus, 2004-2005 resulted to be most heterogenous analysed season), and minimum decrease on 2006-2007 (-2,000 km^2). As regards the second belt (500-1000 m a.s.l.), no well-defined trends are detected and they change year by year, even if some seasons present a decrease from December after an initial increase (e.g., 2006-2007, 2011-2012, 2012-2013, 2013-2014), so an opposite behaviour in respect to the previous cases. The third belt (1000-1500 m a.s.l.) present a different general trend, with the area decreasing in the middle of the analysed period (December) and then it increases at the end of the summer, reaching values similar to the initial ones. Regarding the last two elt (1500-2000 and 2000-2500 m a.s.l.), no particular trends are detected, and the obtained values tend to be more constant with slight variations during the spring and summer.

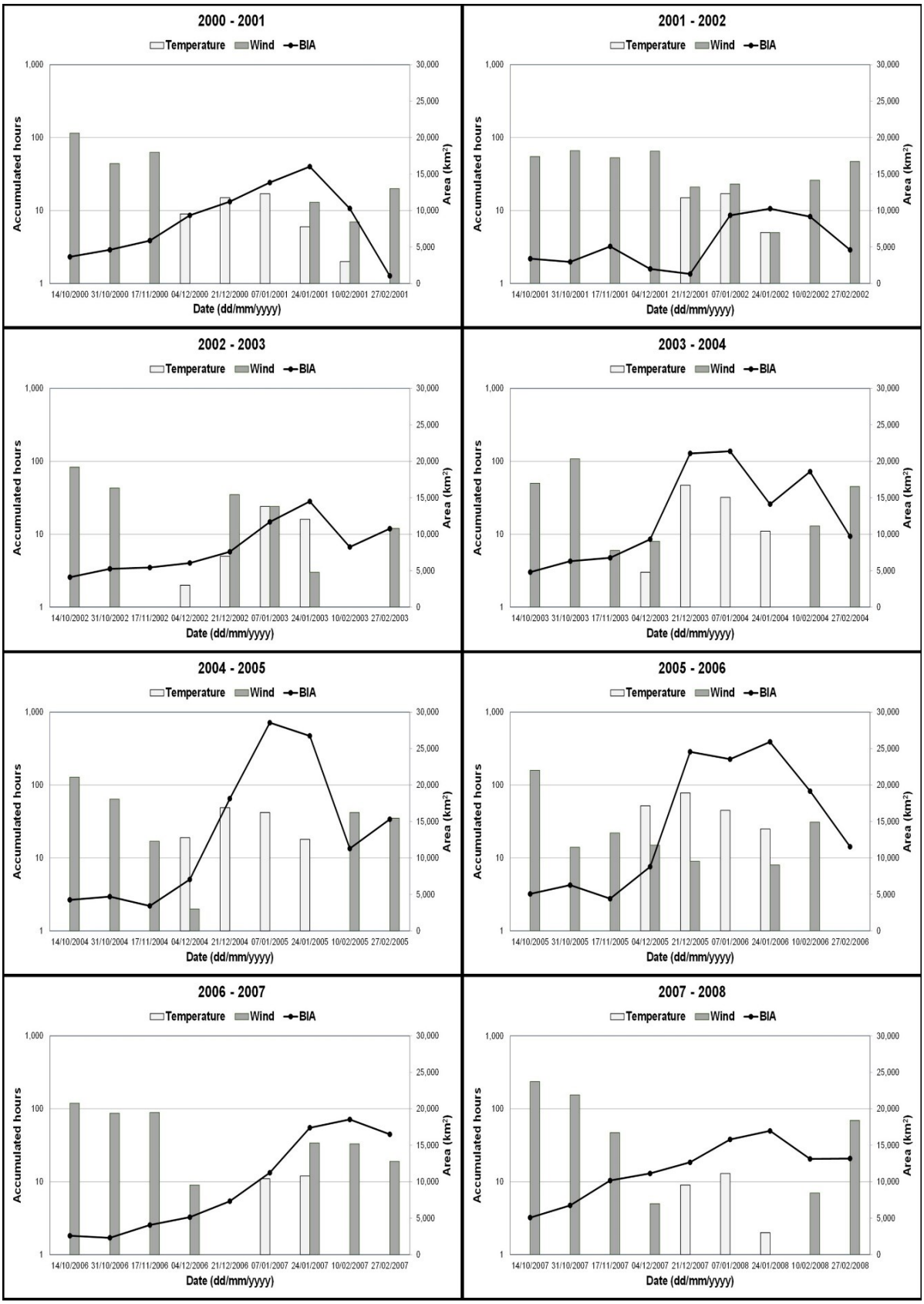

Fig. 5 - Seasonal variations of BIA extents in Amery Ice-Shelf area at the lowest altitude belt (0-500 m a.s.l.) in 2000-2008 period. Corresponding accumulated (16-day temporally weighted to the ninth day) hours above the thresholds of temperature and wind speed from Amery G3 AWS are shown (for a better representation, a logarithmic scale is applied to these two parameters).

Temperature and wind speed present two opposite trends in time (fig. 5). In fact, on the one hand, the temperature is positive only in the middle of the summer (i.e., December and January) with the highest number of hours showing positive values between the end of December and the beginning of January, when the average maximum is about 9 hours per day ranging from 4 hours in 2007-2008 to 14 hours in 2005-2006. The only two exceptions are represented by 2006-2007 and 2007-2008 seasons, where the peaks are slightly postponed in time, mostly located only in January. At the same time, these last two seasons are also the two with the lowest values of positive-temperature hours (with 2000-2001 season), as they present peaks around 5 hours, in contradiction with the other five seasons which present values that are even more than doubled. On the other side, the wind speed presents a different pattern, with the highest number of hours per day with values > 8 m s^{-1} located during the spring, mainly October (with three seasons, i.e., 2004-2005, 2005-2006 and 2007-2008, having entire days always over the threshold). The wind speed tends to decrease in the middle of the study period, when the temperature presents its peaks, reaching no-data with speed higher than 8 m s^{-1}, especially in between December and January (the only exception is represented by 2001-2002 season, which shows mostly positive values). The wind speed then starts to increase again showing high values at the end of the studied season, in February, even if these peaks result to be lower if compared to October ones (averagely, 21 hours in October and 15 hours in February).

4 Discussion

In the present work, we detected a maximum extent of BIA per year of about 150,000 km^2 at continental scale with a low inter-annual variability, corresponding to 1.1% of the Antarctic surface, in agreement with previous findings (Bintanja, 1999). However, the strong difference between our results and the one by Hui & alii (2014, 1.7% of Antarctica) could depend on the different satellite dataset used, as in the previous effort also Landsat imagery (i.e., with higher spatial resolution) was used and thus more precise results could have been obtained, as demonstrated by the 8% of overestimation calculated in the Victoria Land using MODIS. In addition, the application of the cloud mask could have significantly underestimated the final amount of detected BIA, as well as the vectorization of the raster maps of BIA detection, in consideration of the included simplification step in polygon conversion procedure. Last but not least, the difference could be affected by an overestimation of BIA in the work by Hui & alii (2014), who detected as BIA also other surface features, such as glazed snow (albeit shows higher albedo values compared to blue ice, Traversa & alii, 2022). Nevertheless, good agreements are found for the Amery Ice-Shelf area, where on average

20,000-25,000 km^2 of BIA are detected in 2000-2008 period, extremely similar to other works at even higher spatial resolutions (Liu & alii, 2006; Yu & alii, 2012).

Seasonal variation interpretation and comparison between areal and meteorological features

Analysing the variation of spatial distribution of BIAs in Antarctic continent during the spring-summer seasons, we found a general increase of area in every intra-annual analysis, from 2000-2001 to 2020-2021. The only difference between the seasons stands the general trends, which show two main types: steady increase from October to February (the entire analysed period) or increase of the area until December/January and then a decrease in the last scenes. These two kinds of trends are approximately equally subdivided in the twenty analysed seasons, as nine are characterized by the first case (steady increase) and eleven by the second one (turnaround in December/January). Additionally, the two categories are also well divided in the two studied decades, as from 2000-2001 to 2010-2011 the second type is dominant and from 2012-2013 to 2020-2021 the first one results to be more predominant. However, in general, despite of these differences, the detected increase in terms of extent of the BIAs during all the studied seasons is relevant, as the evolution in time leads to a doubled area or more. As a first attempt to explain this relevant increase, we could consider the melting of the snow which covers the BIAs as a main reason, since in most of the years the final extent results to be almost unvaried. This could mean that the BIA tends to remain mainly the same through years and what gives the variability from a remote approach is the snow layer, which covers the blue ice in certain frames of the season. Additionally, summer melting of the covering snow could also be suggested by an increase in temperature in Antarctic coastal area during the last 50 years (Turner & alii, 2005), where a significant number of the BIAs are located. On the other hand, the final decrease in blue ice extent in certain seasons cloud be explained by increasing snowfall events, which are temporally anticipated before autumn-winter seasons and quantitatively more significant, according to Medley & alii (2018) and Medley & Thomas (2019). Nevertheless, some points remain unexplained, e.g., the presence or not of the turnaround in some analysed seasons, and thus a more deepen analysis is required. Taking advantage of the Amery G3 AWS, we can focus on the coastal portion of the Amery Ice Shelf, where these trends are detected as well as at continental scale. In order to do so, we compared 8 seasons of areal distributions, from 2000-2001 to 2007-2008, corresponding to the AWS data time span with sufficient data to reproduce a significant meteorological analysis. From the trends of temperature and wind speed above a certain threshold, as described in Results section, we can detect the exact time when melting and sublimation respectively could take place. Looking at the comparison between blue ice extent and daily cumulative positive temperatures (fig. 5), it is evident the correlation between these two parameters, as the major increases

of BIA happen in concomitance with the first dates with positive temperatures and significant increases take place when daily positive temperatures last for 3-5 hours or more. In fact, the BIAs increases or their major increases are detected during December and January, exactly when the temperatures become positive, promoting melting processes of the overlying snow.

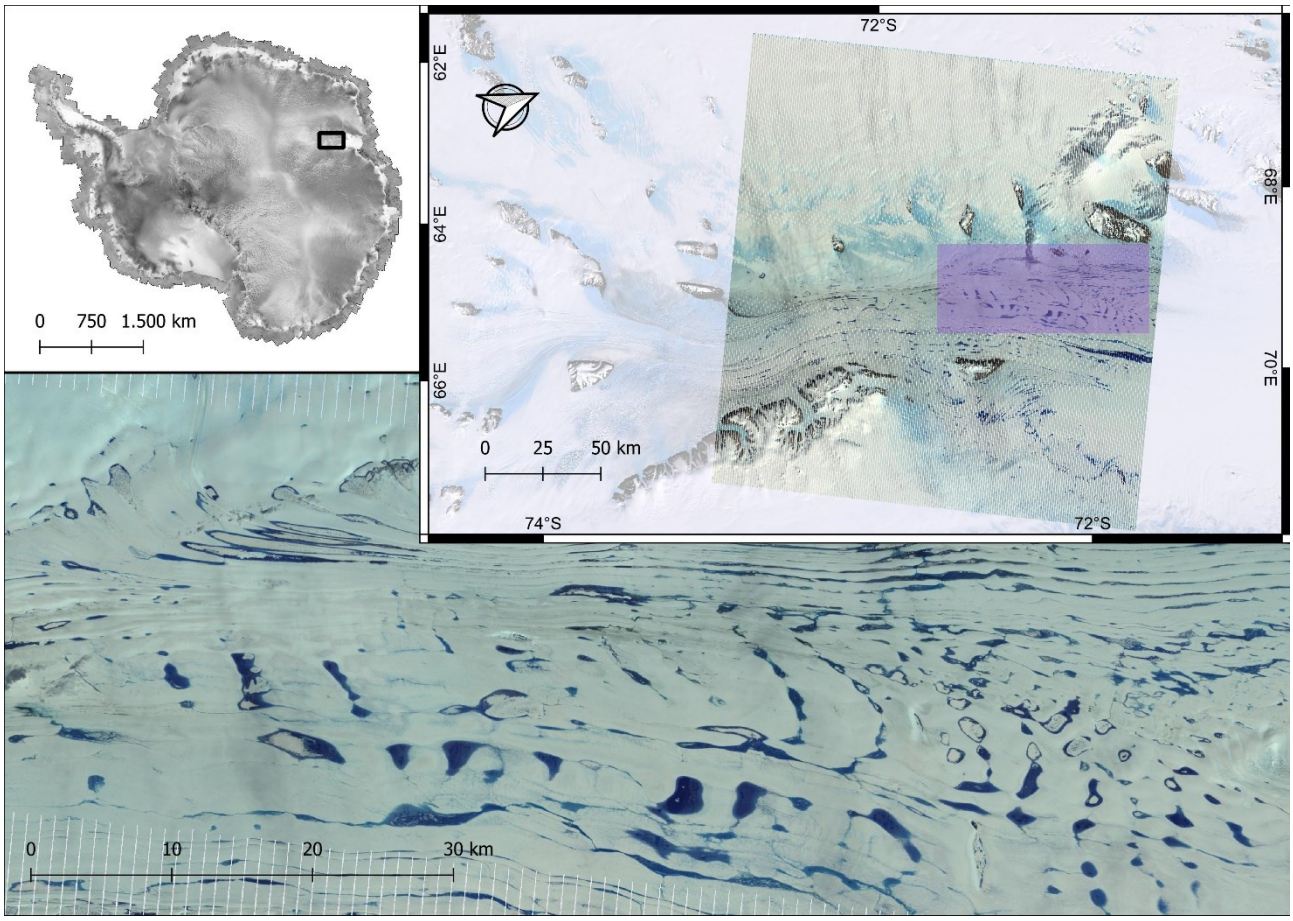

Fig. 6 - Zoom in of a drainage system of supraglacial lakes and canals on Amery Ice Shelf on 25/01/2005. Landsat 7 ETM+ image; RAMP RADARSAT mosaic (Jezek, 1999) and Landsat Image Mosaic of Antarctica (LIMA, Bindschadler & alii, 2008) as backgrounds.

On the other hand, wind speed values higher than 8 m s^{-1} occur mainly at the beginning (October-November) and the end (February) of the analysed period, with highest cumulative peaks at the beginning of the period (21 hours versus 15 hours per day above the threshold). In this second case, the increase in area of blue ice is evidently less related with an increase in wind speed if compared to positive temperatures. However, periods of strong and persistent wind (i.e., at least 10 hours with wind speed > 8 m s^{-1}) could suggest a relation with weak increase in BIA at the end of the spring (November) or beginning of the autumn (February), by erosion phenomena of snow which expose the beneath blue ice (Scambos & alii, 2007; Lenaerts & alii, 2017). The first increase (November) is evident in all the 8 analysed seasons, and it cannot be related with melting due to the temperature effect, as no continuative melting periods can be detected. In addition, this initial increase becomes

more relevant when many strong windy days are continuously found (e.g., 2006-2007 and 2007-2008 seasons). In this view, also the final increase in blue ice extent of 2004-2005 season could be explained by the presence of many consecutive days with high wind speed. We could then conclude that both temperature and wind could have an impact on BIA extent by increasing it with higher values, but temperature presents certainly a higher control on its exposure. In this context, in order to statistically support this control, a linear regression between area variations and the two meteorological parameters was calculated, finding a multiple R of 0.61, even if the corrected R2 resulted to be lower (0.35). However, it was statistically proved the higher role of temperature ($R = 0.60$) in respect to wind ($R = -0.12$), being also the only significative ($p < 0.05$) parameter in the correlation. It should be noted that in certain seasons, i.e., 2002-2003, 2003-2004 and 2007-2008, the corrected R^2 increases to > 0.50 values. Therefore, we could explain the variations of BIAs with the calculated trends of temperature and wind speed, especially the link with temperature variations, and possibly the not so high statistical correlation (0.35) could be due to the use of a single AWS, explaining the huge 0-500-m-belt area of the Amery Ice Shelf. Additionally, our approach did not consider another relevant aspect, i.e., the different location and the related topographic characteristics of BIA that are on the ice shelf or in sloping areas at higher altitudes. In fact, some issues could arise applying this approach. The AWS is located at lower altitudes and in a flatter area, compared to BIAs that are mostly in steep high zones. For this reason, the meteorological conditions, both temperature and wind, could not be completely representative of all the BIAs. Nevertheless, Amery G3 AWS seems to be the unique station providing available data in the area. Then, we decided to consider only this AWS, since this methodology represents a preliminary way to interpret the relation between BIA extent and the meteorological parameters. Finally, as we detected along all the 8 studied spring-summer seasons a decrease in the last period (end of summer-beginning of autumn), taking advantage of the meteorological parameters already analysed, we could provide two possible scenarios. Firstly, the decrease sometimes corresponds to the absence of days with hourly positive temperatures, corresponding to no melting conditions. Therefore, the BIA decrease could be due to snowfalls in this time frame, since blue ice becomes covered by snow that will not melt. In fact, Amery Ice Shelf area is known to be interested by extreme solid precipitation events which are concentrated in less than 10 days, mainly in autumn (50% of annual precipitations, Turner & alii, 2019). In general, this sort of events concern all the Antarctic continent and are the main factor in controlling the interannual variability in snow accumulation (Turner & alii, 2019) and thus could also explain the detected inter-annual variability and the presence of two distinct trends at the end of the studied seasons. Nevertheless, in certain cases (i.e., 2000-2001, 2003-2004, 2004-2005 and 2007-2008) the final decrease corresponds to many consecutive days with possible melting by positive temperature effect.

In accordance with previous works (Phillips, 1998; Zhou & alii, 2019; Spergel & alii, 2021), who reported the presence of supraglacial drainage systems composed by lakes and canals on the Amery Ice Shelf at the end of the summer season, we could explain the decrease of BIA with the hypothesis of a water coverage which makes the blue ice undetectable from space, by decreasing its albedo. In this context, we visually checked the presence of bodies of water at the end of 2004-2005 summer season (25/01/2005) with a higher spatial-resolution satellite image (natural colour composite from Landsat 7 ETM+) on the Amery Ice Shelf (fig. 6). There we easily detected huge drainage systems covering the blue ice, confirming then our hypothesis. Also at continental scale drainage systems are knowingly present on BIA (Kingslake & alii, 2017; Lenaerts & alii, 2017) and therefore the decrease in blue ice exposure at the end of the summer after many melting days at continental scale could be explained. Nevertheless, accordingly to Tuckett & alii (2021), these meltwater areas reach their maximum in January and then decrease in February for freezing over. Therefore, the very final areal decrease in February could be reasonably depending on snow cover, and not on the meltwater area formations.

5. Conclusion

In the present study an analysis of spatial distribution of BIAs in the Antarctic continent is carried out, focusing on their variations in time by means of remote-sensing applications. Taking advantage of an automatic detection based on albedo (broadband and NIR from MODIS product MCD43A3) and topography (topographic slope calculated from REMA DEM, Howat & alii, 2019), we analysed the intra-annual evolutions of BIAs of Antarctica in 2000- 2021 period from October to February. With a percentage on the total Antarctic of 1.1% (150,000 km^2 on average), we detected an evident trend in areal increase along the season for all the analysed years, with change in surface of about +150% or more from the end of the autumn to the summer. However, in half of the analysed periods a turnaround in tendency was detected, with the steady increase of area reaching its maximum in December/January followed by a final decrease in February. Then, moving to the Amery Ice-Shelf region, where the Amery G3 AWS is, we first divided the area in 5 elevation belts, and we detected the same trends found at continental scale in the ones closer to the coast, especially in the first belt (0-500 m a.s.l.), where most of the BIA are located. In order to explain these trends, we evaluated thermal and windy conditions focusing on the first belt, where the Amery G3 AWS is located. An evident relation was found between the increase of BIA in the middle of the season and the dates presenting melting phenomena (i.e., air temperature higher than 0 °C; R = 0.60), especially explaining the strong increase in extension, peculiar of December and January. The other weaker increases can be explained by the effect of wind, which presents high values of accumulated hours with wind speed

higher than 8 m s^{-1}, suggesting the occurrence of erosion of superficial snow cover (Scambos & alii, 2007; Lenaerts & alii, 2017). In both cases, the areal variations can be explained by a higher portion of BIA which becomes uncovered by the snow, due to melting/sublimation or erosional phenomena. As concerns the decrease of BIA mainly at the end of the seasons, it could be explained by snow or water cover above the blue ice, caused by intense events of snowfall (Turner & alii, 2019) or by the creation of relevant drainage systems owed to snow and blue ice melting (Phillips, 1998; Zhou & alii, 2019; Spergel & alii, 2021). Future efforts could focus on BIA variations in different sectors or specific areas of Antarctica in order to confirm the present results or to find areal discrepancies across the continent, possibly taking advantage of other AWSs located in proximity or above BIA and in gullies of katabatic wind flow. In addition, also a differentiation of BIA based on type and topographic location could be a better approach in respect to our preliminary methodology based on the altitude. Data of snow cover (especially fresh snow) measured by an AWS could also be useful in order to detect extreme snowfall events leading to the observed BIA decrease. In addition, an inter-annual analysis of continental BIA based on the proposed methodology could be considered.

References

Agosta C., Amory C., Kitt el C., Orsi A., Favier V., Gallée H., van den Broeke M.R., Lenaerts J.T.M., van Wessem J.M., van de Berg W.J. & Fettw eis X. (2019) - Estimation of the Antarctic surface mass balance using the regional climate model MAR (1979-2015) and identification of dominant processes. The Cryosphere, 13 (1), 281-296. doi: 10.5194/tc-13-281-2019

Bindschadler R., Vornberger P., Fleming A., Fox A., Mullins J., Binnie D., Paulsen S., Granneman B. & Gorodetzk y D. (2008) - The Landsat Image Mosaic of Antarctica. Remote Sensing of Environment, 112 (12), 4214-4226. doi: 10.1016/j.rse.2008.07.006 89

Bintanja R. & Van Den Broeke M.R. (1995) - The surface energy balance of Antarctic snow and blue ice. Journal of Applied Meteorology and Climatology, 34 (4), 902-926.

Bintanja R. (1999) - On the glaciological, meteorological, and climatological significance of Antarctic blue ice areas. Reviews of Geophysics, 37 (3), 337-359.

Budd W. (1966) - The dynamics of the Amery ice shelf. Journal of Glaciology, 6 (45), 335-358.

Cassidy W., Harvey R., Schutt J., Delisle G. & Yanai K. (1992) – The meteorite collection sites of Antarctica. Meteoritics, 27 (5), 490-525.

Das I., Bell R.E., Scamb os T.A., Wolovick M., Creyts T.T., Studinger M., Frearson N., Nicolas J.P., Lenaerts J.T.M. & van den Broeke M.R. (2013) - Influence of persistent wind scour on the surface mass balance of Antarctica. Nature Geoscience, 6 (5), 367-371. doi: 10.1038/ngeo1766

Folco L., Welten K.C., Jull A.J.T., Nishiizumi K. & Zeoli A. (2006) - Meteorites constrain the age of Antarctic ice at the Frontier Mountain blue ice field (northern Victoria Land). Earth and Planetary Science Letters, 248 (1), 209-216. doi: 10.1016/j.epsl.2006.05.022

Grenfell T.C., Warren S.G. & Mullen P.C. (1994) - Reflection of solar radiation by the Antarctic snow surface at ultraviolet, visible, and near-infrared wavelengths, Journal of Geophysical Research, Journal of Geophysical Research, Atmospheres, 99 (D9), 18669-18684.

Howat I.M., Porter C., Smith B.E., Noh M.-J. & Morin P. (2019) - The Reference Elevation Model of Antarctica. The Cryosphere, 13 (2), 665-674. doi: 10.5194/tc-13-665-2019

Hui F., Ci T., Cheng X., Scamb os T.A., Liu Y., Zhang Y., Chi Z., Huang H., Wang X. & Wang F. (2014) - Mapping blue-ice areas in Antarctica using ETM+ and MODIS data. Annals of Glaciology, 55 (66), 129-137.

Jezek K.C. (1999) - Glaciological properties of the Antarctic ice sheet from RADARSAT-1 synthetic aperture radar imagery. Annals of Glaciology, 29, 286-290. doi: 10.3189/172756499781820969

Juckes L.M. (1972) - The geology of north-eastern Heimefrontfjella, Dronning Maud Land. British Antarctic Survey, Scientific Reports, 65, 41 pp.

Kingslake J., Ely J.C., Das I. & Bell R.E. (2017) - Widespread movement of meltwater onto and across Antarctic ice shelves. Nature, 544 (7650), 349-352.

Lenaerts J.T.M., Lhermitt e S., Drews R., Ligt enberg S.R.M., Berger S., Helm V., Smeets C., Van Den Broeke M.R., Van De Berg W.J. & Van Meijg aard E. (2017) - Meltwater produced by wind-albedo interaction stored in an East Antarctic ice shelf. Nature climate change, 7 (1), 58-62.

Liang S. (2001) - Narrowband to broadband conversions of land surface albedo I: Algorithms. Remote sensing of environment, 76 (2), 213-238. doi: 10.1016/S0034-4257(00)00205-4

Liu H., Wang L. & Jezek K.C. (2006) - Automated delineation of dry and melt snow zones in Antarctica using active and passive microwave observations from space. IEEE Transactions on Geoscience and Remote Sensing, 44 (8), 2152-2163. doi: 10.1109/TGRS.2006.872132

Markov A., Polyakov S., Sun B., Lukin V., Popov S., Yang H., Zhang T., Cui X., Guo J., Cui P., Zhang L., Greenbaum J., Mirakin A., Voyevodin A., Boronina A., Sukh anova A., Deshovykh G., Krekh ov A., Zarin S., Semyonov A., Soshchenko V. & Mel'nik A. (2019) - The conditions of the formation and existence of "Blue Ice Areas" in the ice flow transition region from the Antarctic ice sheet to the Amery Ice Shelf in the Larsemann Hills area. Polar Science, 22, 100478. doi: 10.1016/j.polar.2019.08.004

Medley B., McConnell J.R., Neumann T.A., Reijm er C.H., Chellman N., Sigl M. & Kipfstuhl S. (2018) - Temperature and snowfall in western Queen Maud Land increasing faster than climate model projections. Geophysical Research Letters, 45 (3), 1472-1480.

Medley B. & Thomas E.R. (2019) - Increased snowfall over the Antarctic Ice Sheet mitigated twentieth-century sea-level rise. Nature Climate Change, 9 (1), 34-39. doi: 10.1038/s41558-018-0356-x

Morlighem M., Rignot E., Binder T., Blankenship D., Drews R., Eagles G., Eisen O., Ferraccioli F., Forsberg R., Fretwell P., Goel V., Greenbaum J.S., Gudmundsson H., Guo J., Helm V., Hofstede C., Howat I., Humb ert A., Jokat W., Karlsson N.B., Lee W.S., Matsuoka K., Millan R., Mouginot J., Paden J., Patt yn F., Roberts J., Rosier S., Ruppel A., Seroussi H., Smith E.C., Steinhage D., Sun B., Broeke M.R. van den, Omm en T.D. van, Wessem M. van & Young D.A. (2020) - Deep glacial troughs and stabilizing ridges unveiled beneath the margins of the Antarctic ice sheet. Nature Geoscience, 13 (2), 132-137. doi: 10.1038/s41561-019-0510-8

Morlighem M. (2020) - MEaSUREs BedMachine Antarctica, Version 2. NASA National Snow and Ice Data Center DAAC. doi: 10.5067/E1QL9HFQ7A8M

Orheim O. & Lucchitt a B. (1990) - Investigating climate change by digital analysis of blue ice extent on satellite images of Antarctica. Annals of Glaciology, 14, 211-215.

Phillips H.A. (1998) - Surface meltstreams on the Amery Ice Shelf, East Antarctica. Annals of Glaciology, 27, 177-181.

Pirazzini R. (2004) - Surface albedo measurements over Antarctic sites in summer. Journal of Geophysical Research, 109 (D20), D20118. doi: 10.1029/2004JD004617

Reijm er C.H., Bintanja R. & Greuell W. (2001) - Surface albedo measurements over snow and blue ice in thematic mapper bands 2 and 4 in Dronning Maud Land, Antarctica. Journal of Geophysical Research: Atmospheres, 106 (D9), 9661-9672.

Scambos T.A., Haran T.M., Fahnestock M.A., Painter T.H. & Bohlander J. (2007) - MODIS-based Mosaic of Antarctica (MOA) data sets: Continent-wide surface morphology and snow grain size. Remote Sensing of Environment, 111 (2-3), 242-257. doi: 10.1016/j.rse.2006.12.020

Scambos T.A., Frezz ott i M., Haran T., Bohlander J., Lenaerts J.T.M., Van Den Broeke M.R., Jezek K., Long D., Urbini S., Farness K., Neumann T., Albert M. & Winth er J.-G. (2012) – Extent of low-accumulation ‘wind glaze’ areas on the East Antarctic plateau: implications for continental ice mass balance. Journal of Glaciology, 58 (210), 633-647. doi: 10.3189/2012JoG11J232

Schaaf C.L.B., Liu J., Gao F. & Strahler A.H. (2011) - MODIS albedo and reflectance anisotropy products from Aqua and Terra. Land Remote Sensing and Global Environmental Change: NASA's Earth Observing System and the Science of ASTER and MODIS, 11, 549-561.

Spergel J.J., Kingslake J., Creyts T., van Wessem M. & Fricker H.A. (2021) - Surface meltwater drainage and ponding on Amery Ice Shelf, East Antarctica, 1973-2019. Journal of Glaciology, 1-14. doi: 10.1017/jog.2021.46

Takahashi S., Endoh T., Azuma N. & Meshida S. (1992) - Bare ice fields developed in the inland part of Antarctica. Proceedings of the NIPR Symposium on Polar Meteorology and Glaciology, 5, 128-139.

Tedesco M., Doherty S., Fettw eis X., Alexander P., Jeyaratnam J. & Stroeve J. (2016) - The darkening of the Greenland ice sheet: trends, drivers, and projections (1981-2100). The Cryosphere, 10 (2), 477-496.

Traversa G., Fugazz a D., Senese A. & Diolaiuti G.A. (2019) – Preliminary results on Antarctic albedo from remote sensing observations. Geogr. Fis. Din. Quat, 42 (2), 245-254. doi:10.4461/GFDQ.2019.42.14

Traversa G., Fugazz a D. & Frezz ott i M. (2021a) - Analysis of Megadune Fields in Antarctica. IEEE, 2021 IEEE International Geoscience and Remote Sensing Symposium IGARSS, 5513-5516. doi:10.1109/IGARSS47720.2021.955482790

Traversa G., Fugazz a D., Senese A. & Frezz ott i M. (2021b) – Landsat 8 OLI Broadband Albedo Validation in Antarctica and Greenland. Remote Sensing, 13 (4), 799. doi: https://doi.org/10.3390/rs13040799

Traversa G., Fugazz a D. & Frezzotti M. (2022) - Megadunes in Antarctica: migration and evolution from remote and in situ observations. The Cryosphere Discussions, 1-30. doi: https://doi.org/10.5194/tc-2022-11

Tuckett P.A., Ely J.C., Sole A.J., Lea J.M., Livingstone S.J., Jones J.M. & van Wessem J.M. (2021) - Automated mapping of the seasonal evolution of surface meltwater and its links to climate on the Amery Ice Shelf, Antarctica. The Cryosphere, 15 (12), 5785-5804. doi: 10.5194/tc-15-5785-2021

Turner J., Colwell S.R., Marshall G.J., Lachlan-Cope T.A., Carleton A.M., Jones P.D., Lagun V., Reid P.A. & Iagovkina S. (2005) - Antarctic climate change during the last 50 years. International Journal of Climatology, 25 (3), 279-294.

Turner J., Phillips T., Thamb an M., Rahaman W., Marshall G.J., Wille J.D., Favier V., Winton V.H.L., Thomas E., Wang Z., van den Broeke M., Hosking J.S. & Lachlan-Cope T. (2019) – The Dominant Role of Extreme Precipitation Events in Antarctic Snowfall Variability. Geophysical Research Letters, 46 (6), 3502-3511. doi: 10.1029/2018GL081517

van Autenboer T. (1964) - The Geomorphology and Glacial Geology of the Sør-Rondane, Dronning Maud Land, Antarctica. In: Adie R.J. (Ed.), Antarctic Geology, 81-103. North Holland Publishing Company, Amsterdam.

Van den Broeke M.R., Bamb er J., Lenaerts J. & Rignot E. (2011) – Ice Sheets and Sea Level: Thinking Outside the Box. Surveys in Geophysics, 32 (4), 495-505. doi: 10.1007/s10712-011-9137-

Winth er J.-G., Jespersen M.N. & Liston G.E. (2001) - Blue-ice areas in Antarctica derived from NOAA AVHRR satellite data. Journal of Glaciology, 47 (157), 325-334. doi: 10.3189/172756501781832386

Worsfold R.J. (1967) - Physiography and glacial geomorphology of Heimefrontfjella, Dronning Maud Land. British Antarctic Survey Bulletin, 11, 49-57.

Yoshida M., Omoto K., Naruse R. & Ageta Y. (1971) - Discovery of meteorites near Yamato mountains, east Antarctica. 南極資料, 39, 62-65.

Yu J., Liu H., Wang L., Jezek K.C. & Heo J. (2012) - Blue ice areas and their topographical properties in the Lambert glacier, Amery Iceshelf system using Landsat ETM+, ICESat laser altimetry and ASTER GDEM data. Antarctic Science, 24 (1), 95-110. doi: 10.1017/S0954102011000630

Zhou C., Zheng L., Sun Q. & Liu R. (2019) - Amery Ice Shelf surface snowmelt detected by ASCAT and Sentinel-1. Remote Sensing Letters, 10 (5), 430-438. doi: 10.1080/2150704X.2018.1553317

5.3 Conclusion of the chapter

Concluding the chapter about BIA analysis using remote sensing techniques, yearly maps of blue ice at continental scale are provided, based on broadband albedo, NIR narrowband albedo and topographic slope. Even if no significant trends were found inter-annually, seasonally a constant evolution through years was detected, with increase of blue ice surface up to +150% from the end of spring. A turnaround at the end of the summer, i.e., decrease of BIA extent, is also detected. In order to interpret these results, a correlation with temperature and wind speed from AWS on the Amery Ice Shelf is provided, finding a good correlation (R) with temperature, equal to 0.60, then explaining almost two third of BIA variation only with temperature. Further research would focus on other Antarctic areas as comparison and compare snowfall or water presence as main reason of seasonal evolution of blue ice surfaces.

Chapter 6: Further work

The present chapter is intended to be a report of on-going projects at early- or mid-stage of the research. In detail, the two projects are developed in collaboration with two research groups, the first one with Dr. R. Pirazzini from the Finnish Meteorological Institute (Meteorological Research, 00560 Helsinki, Finland), regarding the analyses of reflectance and albedo at Aboa Station (Dronning Maud Land, Section 6.1), and secondly with Prof. L. Sironi and R. Scodellaro from the University of Milano-Bicocca (Physics Department "G. Occhialini", 20126 Milano, Italy, Section 6.2) for a comparison of feature-tracking methods for glacier-velocity evaluation.

6.1 Analyses of reflectance and albedo at Aboa Station (Dronning Maud Land)

Over the Antarctic Ice Sheet (AIS) snow represents the main cover of continental surface and then the albedo (or bi-hemispherical reflectance, Schaepman-Strub et al, 2006) has an important impact on the surface energy balance, leading to a mean high albedo value at continental scale (above 0.80α, Traversa et al., 2019). Albedo and in general surficial reflectance were investigated both from the field and in remote. In details, the study area of the present study, which is the snowy area in proximity of the Finnish Aboa Station in the Dronning Maud Land (Antarctica, coordinates: 73º03' S, 13º25' W, Fig. 6a), was spectrally surveyed continuously in the period 2006-2011 during six Finnish Antarctic campaigns over six austral summers (December – January), and then in the 2014-2015 and 2018-2019 expeditions for a total of eight analysed summer seasons. Remotely, despite of the recent efforts that have allowed to estimate with high precision albedo of snow surfaces in Antarctica using Landsat-mission satellites (Traversa et al., 2021a, b), a calibration and validation of spectral reflectance obtained using this recent proposed methodology on Landsat had not been carried out and now, taking advantage of spectral data obtained during these Finnish campaigns, the present study will fill this relevant gap. In fact, a validated methodology to estimate spectral reflectance at different wavelengths, i.e., VIS-IR, will be of relevance for future energy-balance research, considering the role of snow in Polar Region energy balance, as well as in the determination of certain indices which are useful in snow property determination (Kokhanovsky et al., 2019, 2022).

The data utilized in this study are both from in-situ, using automatic weather stations (AWSs) in the area of Aboa Station, and remote, using mainly Landsat-mission satellites (at the present stage of the analyses) and also Sentinel-2 and PRISMA imagery.

Two AWS datasets are analysed from two different stations, i.e., *AWS5* and *Snow Station* and, at the present, both the datasets refer to 2014-2015 campaign for December-January period and furtherly the other campaigns will be analysed. AWS5 is located close to the Aboa Station and Snow Station

little southern in respect to it. Both the AWSs are mounted over snow surface and carry Kipp&Zonnen CMP pyranometers (CNR4), CGR pyrgeometers and SPN1 sunshine pyranometer for the radiation setup, to which is added a dual-axes inclinometer (BEIsensors INC-080-2-SV00-HH2) (Fig. 1).

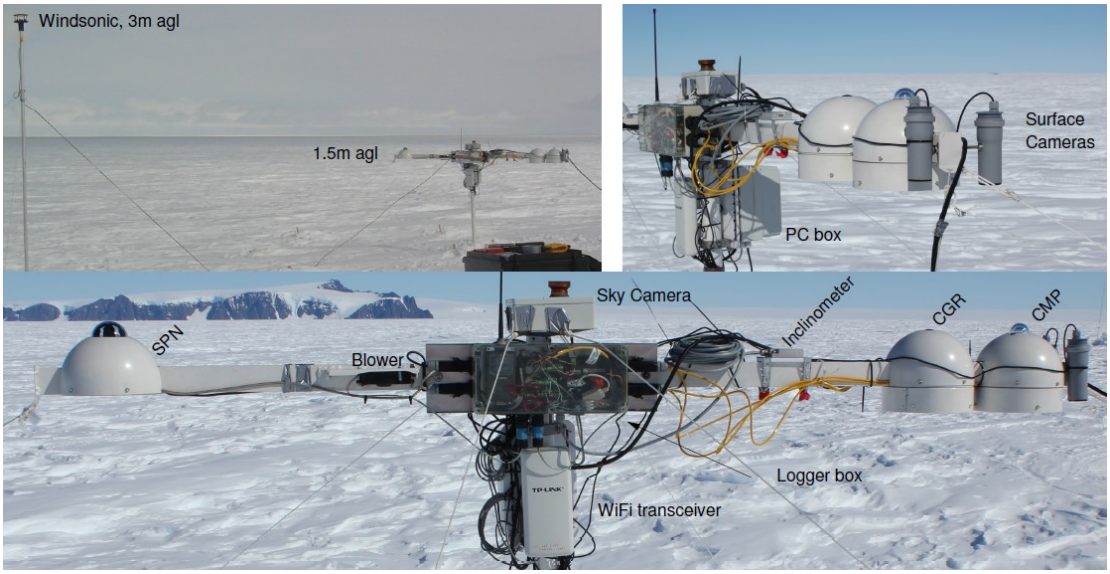

Figure 1: The radiation station setup (Kouznetsov et al., *Notes on measurements at Aboa 2014-2015*).

Therefore, starting from these observations, spectral information at second time scale such as shortwave (SW) and longwave (LW) components are acquired, useful to calculate broadband albedo (percental ratio between SWout and SWin), as well as spectral radiance between 300 and 2800 nm. On the other side, satellite imagery is used to be calibrated and validated using AWS observations. In details, the multi-spectral satellite Sentinel-2 from the European Space Agency (ESA) and the hyper-spectral satellite PRISMA (PRecursore IperSpettrale della Missione Applicativa) from the Italian Space Agency (ASI) will be used in this context. Sentinel-2 presents 13 bands covering VNIR and SWIR areas of the electromagnetic spectrum with different spatial resolution (10, 20 and 60 m) and PRISMA two hyperspectral cubes, a Visible-Near InfraRed (VNIR) cube including 67 bands and a Short-Save InfraRed (SWIR) cube (167 bands), both with 30 m spatial resolution. Nevertheless, these satellites were launched and started to acquire images later than January 2015 and then could be useful for the more recent campaign only (2018-2019) or as an asynchronous comparison, considering the strong stability and homogeneity of the area. However, at the present stage of the analyses, only Landsat 8 OLI images were taken into account (providing data in several spectral bands, including panchromatic, visible, near infrared, short-wave infrared, and thermal infrared bands, with different spatial resolution from 15 to 100 m) and particularly 6 image albedo was compared with in-situ measurements, i.e.: 15-Dec-2014, 17-Dec-2014, 24-Dec-2014, 11-Jan-2015, 25-Jan-2015 and 27-Jan-2015, acquired between 9.05 AM and 9.23 AM UTC. The choice fell on these images as they are all the available cloud-free scenes over the AWS areas in the period of AWS acquisitions.

In order to have a comparable albedo from satellite to be used in pair with AWS measurements, different steps were required. In fact, Landsat raw data are dimensionless and following the methodology of Traversa et al. (2021a, b) a first conversion to radiance and then to Top of Atmosphere (TOA) reflectance was needed (using per-pixel values of the SZA available through the Landsat solar zenith band). Then two corrections were applied, i.e., atmospheric and topographic correction (using REMA DEM, Howat et al., 2019). Doing so, spectral reflectance of blue, green, red, NIR, SWIR and cirrus wavelengths (435-2294 nm) were obtained. Finally, in order to obtain broadband albedo values, Liang algorithm (Liang, 2001) was applied, which requires blue, green, NIR and SWIR band reflectance to be calculated.

Moving to the early results, the in-situ measurements could be classified into two statements, which are: i) day-cloudless situation with no disturbance of clouds over the field-acquisitions and ii) cloud presence in certain time span of the selected day, except of e.g., sensing-acquisition time of the satellite. In detail, the first two scenes, i.e., 15-Dec-2014 and 17-Dec-2014 resulted to be daily cloud free and all the other analysed days presented cloud presence. In addition, to this problem affecting field measurements, both the AWSs were affected by effect of artificial disturbances which could be identified in must shadows at certain times, depending on solar azimuth angles (SAA), and artificial snow accumulation at the base of the must, that influence the cone area of spectral acquisition. All these natural and artificial factors forced a daily average calculation to the final results in order to have a more significant comparison with satellite results not affected by disturbances. However, in certain days when the disturbance was temporally restricted and easily detectable, only those portions of the dataset was removed from the final daily average. In the other cases, when this identification was not possible, the average was based on the entire day acquisition.

At the present stage of the research, only the comparison of broadband albedo results was carried out, finding a MAE in both the AWSs equal to 0.019, strongly near to the 0.020 MAE obtained for Antarctica in Traversa et al. (2021b) research. The so calculated MAE is the result of values between 0.000 (three times over the entire dataset) and 0.005 (only once). In respect to the previous efforts (Traversa et al., 2021b, c), in this case the albedo differences between the remote and in-situ datasets can be explained, having photos and notes about field acquisitions which are of fundamental help for data interpretation. Therefore, the differences can be explained with the fact that field measurements are affected by known issues (e.g., clouds, must shadows or artificial snow accumulations in the cone acquisition) and then the final data is a daily mean, compared to a satellite image acquired at a specific time. Then, it is also possible to suppose that the MAE obtained in the previous research, very analogous to the one obtained now, could have a similar interpretation. Finally, it is to be noted the low value of MAE between remote and in-situ broadband albedo observations, even if the second are

daily means, supporting the methodology proposed in Traversa et al. (2021b, c). Next results from spectral reflectance will be fundamental to evaluate the methodology over single bands (narrowband albedo), as well as on its applicability on other satellites, e.g., Sentinel-2.

6.2 Comparison of feature-tracking methods for glacier-velocity evaluation in different regions of the Earth

The second on-going project regards feature tracking methods for glacier velocity calculations, which have been proposed in the recent years for the increasing interest in these features, being the most significant signals of Climate Change. In this work, we compare three modules from different periods, i.e., IMCORR feature tracking module (Scambos et al., 1992, see Section 2.2.3), Image GeoRectification and Feature Tracking toolbox – ImGRAFT (Messerli and Grinsted, 2015) and Glacier Image Velocimetry – GIV (Van Wyk de Vries and Wickert, 2021). ImGRAFT is an open-source package developed in MATLAB, whose processing is based on different steps, i.e., template matching (feature tracking between image pairs using the NCC algorithm as a measure of template similarity, Heid and Kääb, 2012), georectification and displacement and velocity calculation. Finally, the recent GIV toolkit (that is provided in a dedicated application) is a GUI-based feature tracking module (co-registration) using a frequency cross correlation. Here, both the chip and search area are converted to the frequency domain using a fast Fourier transform (FFT), allowing the calculation of these two-matrix pointwise product and the conversion of the resulting similarity matrix to the spatial domain using the inverse FFT. In respect to the other modules, GIV can easily process several image pairs, instead of a single pair as IMCORR and ImGRAFT. However, GIV is not programmed to obtain subpixel displacement, as the other two do (bi-cubic intensity interpolation in the case of ImGRAFT module).

Now to these three existing modules, a new Machine Learning-based method is proposed for testing and comparing, which couples rigid image registration and correlation methods in order to disentangle the real glaciers movement from the artifacts caused by the image acquisition and provide an accurate estimation of the glacier velocity and direction. The evaluation of this last model and the cross-comparison with the previous methodologies is possible by validation with field available data, in four regions of the Earth: Antarctica (David Glacier, Frezzotti et al., 1998), Italy (Miage G., unpublished data), Chile (Exploradores G., unpublished data) and Pakistan (Baltoro G., Quincey et al., 2009). To these in-situ measurements, the different methods are also tested on a dataset made up of artificial synthetic images which simulate several types of distortions (e.g., linear, circular, etc.). These comparisons allow to evaluate existing feature tracking modules in a controlled environment

where movements are known (synthetic case), as well as in different regions of our planet, periods and satellite (Landsat-family, Sentinel-2 and ASTER imagery) sources and to provide and validate a new method from Machine Learning techniques.

References

Bernstein, R.: Image geometry and rectification, Manual of Remote Sensing (R. N. Colwell, Ed.), 881–884, 1983.

Frezzotti, M, Capra A. and Vittuari L.: Comparison between glacier ice velocities inferred from GPS and sequential satellite images, Annals of Glaciology, 27, 54-60, 1998.

Heid, T. and Kääb, A.: Evaluation of existing image matching methods for deriving glacier surface displacements globally from optical satellite imagery, Remote Sens. Environ., 118, 339–355, 2012.

Howat, I. M., Porter, C., Smith, B. E., Noh, M.-J., and Morin, P.: The Reference Elevation Model of Antarctica, The Cryosphere, 13, 665–674, https://doi.org/10.5194/tc-13-665-2019, 2019.

Kokhanovsky, A., Lamare, M., Danne, O., Brockmann, C., … and Box, J.: Retrieval of Snow Properties from the Sentinel-3 Ocean and Land Colour Instrument, Remote Sensing, 11(9), 2280, https://doi.org/10.3390/rs11192280, 2019.

Kokhanovsky, A., Di Mauro B. and Colombo R.: Snow surface properties derived from PRISMA satellite data over the Nansen Ice Shelf (East Antarctica), Frontiers in Environmental Science, 1420, 2022.

Liang, S.: Narrowband to broadband conversions of land surface albedo I: Algorithms, Remote sensing of environment, 76, 213–238, https://doi.org/10.1016/S0034-4257(00)00205-4, 2001.

Messerli, A. and Grinsted, A.: Image georectification and feature tracking toolbox: ImGRAFT, Geoscientific Instrumentation, Methods and Data Systems, 4, 23–34, 2015.

Quincey, D. J., Copland, L., Mayer, C., Bishop, M., Luckman, A., and Belò, M.: Ice velocity and climate variations for Baltoro Glacier, Pakistan, Journal of Glaciology, 55, 1061–1071, 2009.

Scambos, T. A., Dutkiewicz, M. J., Wilson, J. C., and Bindschadler, R. A.: Application of image cross-correlation to the measurement of glacier velocity using satellite image data, Remote Sensing of Environment, 42, 177–186, https://doi.org/10.1016/0034-4257(92)90101-O, 1992.

Schaepman-Strub G., Schaepman M.E., Painter T.H., Dangel S. & Martonchik J.V.: Reflectance quantities in optical remote sensing—Definitions and case studies, Remote sensing of environment, 103 (1), 27-42. doi: 10.1016/j.rse.2006.03.002, 2006.

Traversa, G., Fugazza, D., Senese, A., and Diolaiuti, G. A.: Preliminary results on Antarctic albedo from remote sensing observations, Geogr Fis Din Quat, 42, 245–254, http://dx.doi.org/10.4461/GFDQ.2019.42.14, 2019.

Traversa, G., Fugazza, D., Senese, A., and Frezzotti, M.: Landsat 8 OLI Broadband Albedo Validation in Antarctica and Greenland, Remote Sens., 13, 799, https://doi.org/10.3390/rs13040799, 2021a.

Traversa, G. and Fugazza, D.: Evaluation of Anisotropic Correction Factors for the Calculation of Landsat 8 OLI Albedo on the Ice Sheets, Geogr Fis Din Quar, 44, 91-95, http://dx.doi.org/10.4461/GFDQ.2021.44.8, 2021b.

Van Wyk de Vries, M. and Wickert, A. D.: Glacier Image Velocimetry: an open-source toolbox for easy and rapid calculation of high-resolution glacier velocity fields, The Cryosphere, 15, 2115–2132, https://doi.org/10.5194/tc-15-2115-2021, 2021.

Chapter 7: Conclusions

The present PhD thesis, in conclusions, focused on the ablation areas in Antarctica and on their related landforms, i.e., blue ice, glazed snow and the linked megadune fields. These features in fact have important consequences concerning the choice of sites for ice coring (megadunes) and are the only zones in Antarctica showing a value of SMB ≤ 0 kg m^{-2} a^{-1}, acquiring then a high relevance in mass balance and sea-level rise research.

The first efforts of the research focused on albedo and its determination using satellite remote sensing. However, only the MODIS products, such as MCD43A3 (used in BIA analysis), provide it already calculated and the other higher spatial resolution satellites as Landsat-mission and Sentinel-2 needed to be processed before showing a reliable albedo data. Then, the first step focused on albedo determination for Landsat 8-9 OLI and, taking advantage of previous models applied at mid-latitudes (Klok et al., 2003; Fugazza et al., 2016). A new adapted model for the ice-sheets has been validated (Section 3.2). This method includes different steps, i.e., radiometric calibration (with zenith angle correction), atmospheric and topographic correction. Then, a narrowband to broadband albedo correction was required and Liang algorithm (Liang, 2001) resulted to have better statistics than Knap (Knap et al., 1999). The so resulted MAE value, based on 75 comparisons between satellite acquisitions and AWS measurements in both Antarctica and Greenland, is equal to ±0.02. The use of anisotropic correction resulted to be unsuggested with the present correction factors, because of SZA effect (Section 3.3). Further research (Section 6.1) will focus on evaluating this model at narrowband scale for each band of the satellite at VIS-NIR wavelengths.

Based on this relevant improvement in spectral properties of surfaces at high latitudes, a characterization of glazed snow areas over the leeward flanks of megadunes was possible (Section 4.2), finding that these surfaces present an albedo 0.02α lower than surrounding firn, which become -0.04α considering the spectral NIR albedo. In addition to albedo, also BT and SPWD were investigated on megadune fields and these three parameters were used to automatically map glazed snow surfaces (Section 4.3). The detection resulted in an accuracy higher than 80% and allowed to determine that glazed snow cover circa 40% of dunal areas, which correspond to 80% of leeward side of each dune. The analysis of megadunes fields where past traverses were conducted provided also for the first time a calculated quantification of dune migration (and of all its components), equal to 10 ma^{-1} circa, demonstrating also their anti-dunal formation, where leeward flanks characterised by the presence of glazed surfaces remain stable in time and the sedimentation happens on the windward side with an opposite direction in respect to ice flow (Section 4.3).

A similar approach of automatic detection was also applied for BIA identification (Section 5.2), but by using a different source of albedo, i.e., MCD43A3 product of MODIS. Here, no significant trends

through years were identified, but seasonally a strong evolution in time was detected. In order to explain this trend, the relation of blue ice extent was investigated together with meteorological parameters, i.e., temperature and wind intensity. From R results, the dependence of BIA evolution to these parameters was demonstrated for the area of Amery Ice Shelf, even if the effect of temperature has a dominant role on their expansion. However, further analyses of other parameters, such as snowfall or water coverage would be significant to better analyse BIA evolution in time.

On the base of the efforts carried out in the present PhD thesis, certain key issues about ablation areas in Antarctica were provided, especially regarding the megadune fields and glazed snow surfaces, and other important outcomes will be at the base of future research of these relevant areas which characterise the Antarctic continent and its role in the global climate system.

List of conference presentations

- Megadunes in Antarctica: Updated Properties and Genesis by Remote-Sensing (oral presentation), 24th Alpine Glaciology Meeting (AGM), Online, 25-26 March 2021.
- Satellite broadband albedo validation on the ice sheets through in-situ validation (oral presentation), Students in Polar and Alpine Research conference (SPARC) 2021, Online, 3-4 May 2021.
- Analysis of Megadune Fields in Antarctica (oral presentation), International Geoscience and Remote Sensing Symposium (IGARSS) 2021, Online, 12-14 July 2021.
- Spatial and temporal variability of blue ice areas in Antarctica (oral presentation), 1st Student-led Conference on Polar Environment (SCOPE), Longyearbyen (NO), 15 October 2021.
- Variazione delle aree di ablazione nel continente Antartico (oral presentation), 3° Convegno Nazionale APECS Italia, Siena (I), 9-10 November 2021.
- Glacier foreland characterization in Lombardy region, North Italy (oral presentation), 25th Alpine Glaciology Meeting (AGM), Munich (D), 24-25 March 2022.
- Comparison of feature-tracking methods for glacier-velocity evaluation in Polar and Alpine regions (poster presentation), Living Planet Symposium 2022, Bonn (D), 23-27 May 2022.
- Migration and characterization of snow megadunes in Antarctica (poster presentation) 10th SCAR Open Science Conference, Online, 1-10 August 2022.
- A multidisciplinary approach for the characterization of a rockfall-affected river catchment (poster presentation), Geosciences for a sustainable future, Torino (I), 19-21 September 2022.
- Migrazione e caratterizzazione delle megadune in Antartide (oral presentation), 4° Convegno Nazionale APECS Italia, Bologna (I), 19-20 October 2022.

Other manuscripts

In addition to main PhD thesis themes, G. Traversa was involved in other projects and published further papers. In this appendix, the two manuscripts where G. Traversa had the main role are presented, to which are added two other publications (no leading role) not shown in the present section, i.e., “Immersive and Virtual Tools to See and Understand Climate Change Impacts on Glaciers: A New Challenge for Scientific Dissemination and Inclusive Education, Geografia fisica e dinamica quaternaria. 44.1 (2021): 67–77” (Diolaiuti et al., 2021) and “An empirical melt model of a small Alpine debris-covered glacier: the case study of Amola Glacier (Italy)” (Fugazza et al., in revision). In detail, the two manuscripts here present are: “Preliminary Results on Antarctic Albedo from Remote Sensing Observations, Geografia fisica e dinamica quaternaria. 42.2: 245–254” (Traversa G. et al., 2019; Appendix 1.1) and “Characterization of glacial foreland areas in Lombardy Region (North Italy) and their spatial variation in the last 70 years” (Traversa et al., in preparation; Appendix 1.2).

Appendix 1.1: Article "Preliminary results on Antarctic albedo from remote sensing observations" (Traversa et al., 2019)

Giacomo Traversa [1,2], Davide Fugazza [2], Antonella Senese [2*] and Guglielmina A. Diolaiuti [2]

[1] Department of Physical Sciences, Earth and Environment (DSFTA), Università Degli Studi Di Siena, 53100 Siena, Italy;

[2] Department of Environmental Science and Policy (ESP), Università Degli Studi Di Milano, 20133 Milan, Italy;

* Corresponding author: A. Senese (antonella.senese@unimi.it)

Abstract: The aim of the study is to analyse the surface albedo of the Antarctica and investigate eventual signals of variations in space and time between summer 2000/2001 and 2011/2012 by means of the GLASS albedo product. We followed a step-by-step procedure from micro- to macro-scale. At first, we analysed 95 glaciers around the continent, and we found limited temporal variability. Then, looking at spatial variations, we divided Antarctica based on oceanic basins and by continentality. We found spatial signals, since mean albedo values range between 0.79 (Pacific and Atlantic basins) and 0.82 (Indian basin) and between 0.76 (along the shore) and 0.81 (inner continent). An increasing variability was found from the inner continent to the shore, and heterogeneous patterns among the basins, most likely due to meteorological and environmental conditions (mainly: temperature, precipitation, katabatic winds). Finally, the general patterns observed (considering the specific glaciers, the three basins and the three continentality sectors) were verified by the analysis of the whole continent and we did not find a significant change of summer averages over time, as they range between 0.79 and 0.80.

1. Introduction

Antarctica is the fourth continent by width and is almost entirely covered by snow and ice (King & Turner, 1997). The inner continent presents almost entirely snow as superficial cover and the coastline shows only 5% (1656 km) of rock surface (Drewry, 1983). Antarctica is one of the widest and most reflective surfaces of the planet and thus an eventual variation of its albedo could be a crucial issue in the Earth energy balance, by controlling the absorption of solar radiation at the surface, leading to significant effects on sea level. The continent is a heat sink for the Southern Hemisphere and thus exerts considerable control over the circulation of the atmosphere at high and mid-latitudes (King & Turner, 1997). Unlike the high latitude landmasses of the Northern Hemisphere, characterized by large areas of seasonal snow cover, and thus a rapid response to temperature changes, the Antarctica is covered by a permanent highly reflective surface. For these reasons, albedo is an important feature that needs to be investigated in detail, considering its relations with surface variations from a spatial and temporal point of view. In particular, here light-absorbing impurities are few, and thus snow

albedo is mostly determined by the size of snow grains (Grenfell & alii, 1994; Gay & alii, 2002; Warren & alii, 2006; Gallet & alii, 2011; Picard & alii, 2016), regulated by snow metamorphism (i.e. the process of grain coarsening). In addition, the effects of various morphologies owing to strong and persistent winds (e.g. sastrugi, snow dunes and wind glaze areas), or the presence of blue ice, can considerably affect the surface albedo (Frezzotti & alii, 2002; Scambos & alii, 2012; Das & alii, 2013). In turn, the rate of snow metamorphism is influenced by temperature, relative humidity and wind (Pirazzini, 2004; Picard & alii; 2012; Lenaerts & alii, 2017). The first measurements of Antarctic surface albedo date back to the past century; in fact, direct surveys of the incoming solar radiation and albedo were performed during the US-IGY-Antarctic Expedition 1957/58. During this campaign, measurements of the albedo at the South Pole and at Byrd Station (80° S, 120° W, 1515 m a.s.l.) gave a mean value of 0.89, with a range between 0.84 and 0.93 (Hoinkes, 1960). Since these first surveys, several field campaigns have been carried out; among others, field observations showed mean albedo values of 0.76 at Faraday (1963-1982), 0.82 at Halley (1963-1982) and 0.85 at Vostok (1963-1972) (King & Turner, 1997), 0.80-0.85 at Scott South Pole and Vostok stations (average of spectral albedo in summer 1985-1986 and 1990-1991, Grenfell & alii, 1994), 0.58-0.82 at Hells Gate, Neumayer, Concordia and Reeves Névé stations (between 1994 and 1998, Pirazzini & alii, 2004), 0.80-0.90 on the Antarctic Plateau (Dalrymple & alii, 1966; Dolgina & alii, 1976; Gardiner & Shanklin, 1989). Presently, the best way to acquire albedo data over wide areas of Antarctica is via remote sensing, which also allows investigating longer periods of time. However, few studies have actually used remote sensing for this purpose: Laine (2008) found a range of 0.75-0.90 for the entire Ice Sheet between 1981 and 2000 from AVHRR Pathfinder data; Gallet & alii (2011) found values of 0.79-0.83 from MODIS MCD43C3 along a transect from Dome C to Dumont d'Urville. Considering the scarcity of existing literature, the aim of this study is to analyse the variability of Antarctic albedo in space and time with remote sensing, focusing on inter and intra-annual variations, from summer 2000-2001 to summer 2011-2012, and across different sub-zones, to obtain a complete overview of the continent. Firstly, starting from a micro-scale analysis, we investigated a subsample of glaciers (fig. 1A) in order to investigate temporal variability in detail; then, dividing the continent based on oceanic basins (i.e. Indian, Pacific and Atlantic) and continentality (i.e. continent, transition and shore), see fig. 1B, we analysed changes in space to verify the presence of spatial signals. Several existing global albedo products are available, but we chose to discard most of them for different reasons: CLARA-A2 has a coarse resolution (25 km), MCD43A3 and MOD10A1 are affected by data gaps owing to clouds; in addition, while it is also possible to retrieve the albedo from Landsat or Sentinel-2 satellites (e.g. Fugazza & alii, 2019), the fine resolution and low spatial coverage of single scenes imply a long processing time, which was unsuitable for our large scale preliminary analysis. Thus, for the aims of

this study, the GLASS product derived from MODIS was chosen as the main data source. In fact, considering its spatial and temporal resolutions (described in detail in Methods and Data section), we considered GLASS as the most suitable product for our research, also thanks to its efficient cloud screening algorithm (Liang & alii, 2012; Zhao & alii, 2013).

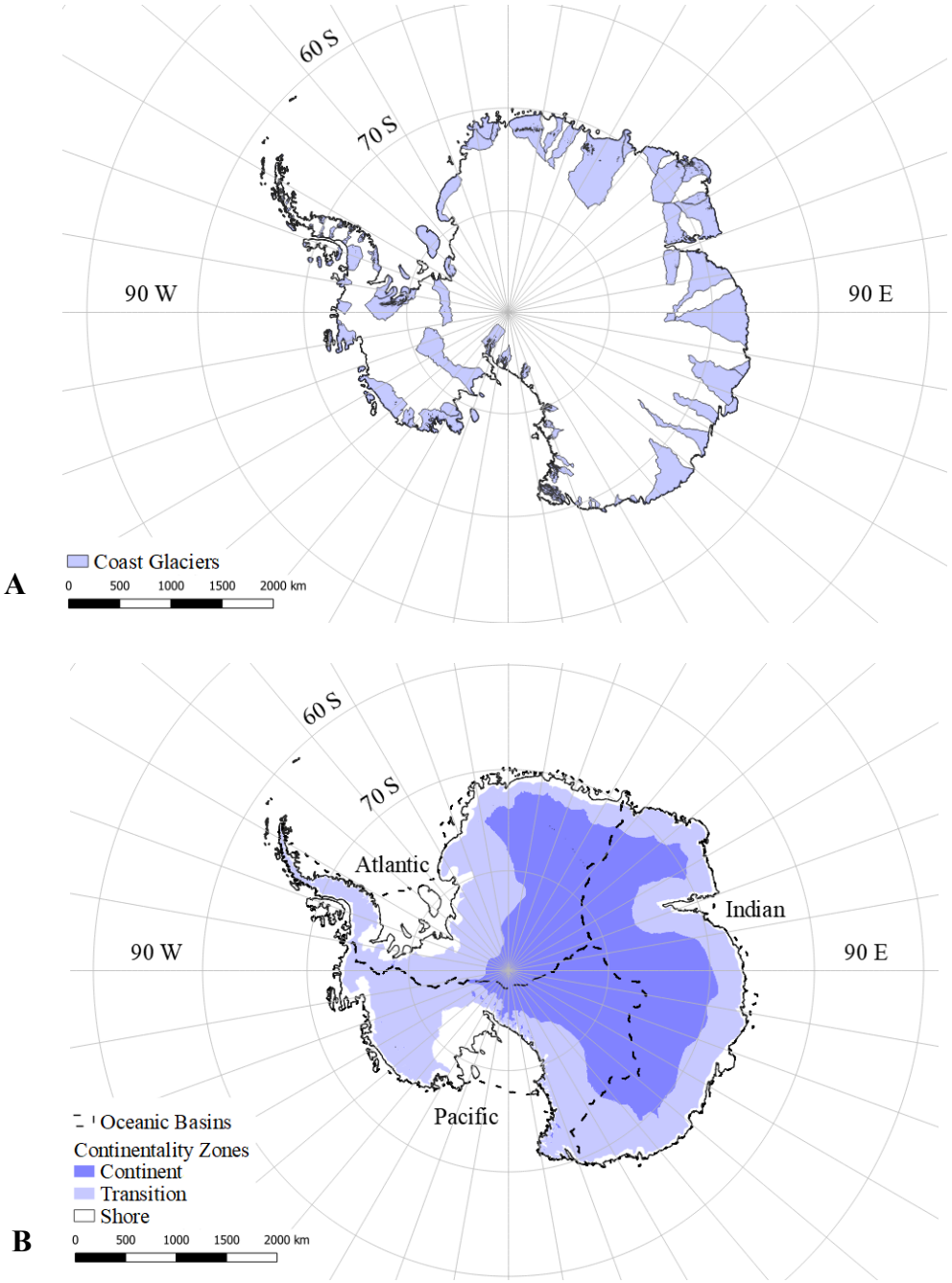

Figure 1. The 95 investigated glaciers, including Dovers and Cosgrove g. (1), Darwin g. (2) and Evans. (3) (A) and Antarctica divided into the 3 oceanic basins by the dashed lines and into continentality zones by different coloured areas (B).

2. Methods and Data

To obtain the albedo values, we used the GLASS product (Liang & alii, 2012), derived from MODIS.

This product had an 8-day temporal resolution between 2000 and 2012 and a spatial resolution of 5.6 km for the continental zone (ice shelves and sea ice are not included). GLASS is based on pre-processed MODIS data (i.e. MOD09A1, MOD09GA, MCD43B3 and MOD02), with the addition of a snow- and cloud-mask used to identify different pixels and remove cloud and cloud-shadows effect to increase the overall quality. Each GLASS scene is obtained by merging the 1-day broadband albedo derived from top-of-atmosphere directional reflectance, corrected for the solar/view angle dependence of the surface in a 16-day window through a Statistics-Based Temporal Filtering algorithm (Zhao & alii, 2013). We analysed 16 images per season from November 2000 to February 2012. From the original products, downloaded from the GLCF (Global Land Cover Facility), we extracted black-sky albedo (or directional hemispherical reflectance, DHR, that is inherent to specific locations and is linked with the structure and optical properties of the land cover; Schaaf & alii, 2011), as proposed by Tedesco & alii (2016). Each layer was extracted and cut, considering only the South Polar region (coordinates: C1 (180° W, 60° S); C2 (180° E, 90° S)) and then re-projected into the Antarctic Polar Stereographic coordinate system. The uncertainty of individual pixels as reported in the quality control layer of the GLASS product is ±0.10. GLASS products have already been tested using spatial quality verification processes, consisting of different components (Zhao & alii, 2013): a spatial quality check-up (i.e. screening for missing data or bands, spatial discontinuity problems) and a numerical accuracy assessment (i.e. comparison between the GLASS product with data measured on the ground). For each date and each of the following analysis steps, i.e. glacier subsample, basin and continentality division, and whole Antarctica, we applied zonal statistics in QGIS software to obtain mean, median, maximum, minimum and standard deviation of all the considered pixels. In addition, we calculated the uncertainty for each average albedo estimate, using the standard error of the mean (σ_x) (Fugazza & alii, 2019), as:

$$\sigma_x = \frac{\sigma}{\sqrt{n}}$$

where σ is the standard deviation of albedo values (for each date and each step) and n is the number of pixels considered. Firstly, to investigate temporal variability, 95 coastal glaciers were randomly selected from the ice features catchments polygon shapefile by the British Antarctic Survey (BAS). In particular, we analysed 46 glaciers of the Atlantic basin, 30 of the Pacific one and 19 of the Indian one (fig. 1A). We chose a different number of glaciers in each ocean basin to consider approximately the same total glacier area for every basin. In fact, even if the area of the widest glacier for each basin

has the same magnitude, ranging between 140,000 km^2 (Pacific) and 300,000 km^2 (Atlantic), the Atlantic basin also presents much smaller glaciers, with areas of 150 km^2, compared to the Pacific and Indian sectors, where the smallest glaciers average 1,200 km^2. Then, in order to divide the Antarctica into the 3 oceanic basins (dashed lines in fig. 1B), we used i) the shapefile of the Antarctic drainage system from Zwally & alii (2012), which separates the continent by drainage basins, ice sheets and ice shelves and ii) a shapefile by Natural Earth Data, separating the world waters into individual oceans and seas. Although previous studies used a simpler approach based on longitude zones (Brandt & alii, 2005; Laine, 2008), we chose to consider drainage basins for a more accurate subdivision. Considering the continentality zones (i.e. continent, transition and shore), we classified a DEM (Cryo Sat DEM of Antarctica created by the CPOM - Centre for Polar Observation and Modelling, Helm & alii, 2014), based on altitude: shore below 800 m a.s.l., transition between 800 and 2500 m a.s.l. and continent above 2500 m a.s.l. (coloured areas in fig. 1B). These altitude ranges are based on the morphology of the surface. In fact, the elevation belt between 800 and 2500 m a.s.l. is characterized by significant changes in topography, with very steep slopes encircling the continent and marking the separation of the inner area from the coast. By combining information on continentality and oceanic basins, we obtained a polygon of the Atlantic basin divided into continentality zones. Finally, to extract the albedo of the whole Antarctica, we used the coastline shapefile provided by the SCAR (Scientific Committee on Antarctic Research). The climatological dataset RACMO2.3 (an update of Regional Atmospheric Climate MOdel 2) described by Van Wessem & alii (2014a, b) was used to investigate the influence of meteorological conditions on albedo values, by calculating correlation with our albedo data. RACMO2.3 includes 5 different raster maps at 35 km spatial resolution available at https://www.npolar.no/quantarctica/, providing the climatic mean 1979-2011 of: i) annual cumulative precipitation (rain and snow) in kg m-2 yr^{-1}, ii) annual total (surface and drifting snow) sublimation rate in kg m-2 yr^{-1} where positive values indicate sublimation and negative ones indicate deposition, iii) annual surface mass balance in kg m-2 yr^{-1}, iv) annual average temperature in K 2 m above the surface, and v) annual average wind speed in m s^{-1} 10 m above the surface. Our albedo maps were resampled to 35 km spatial resolution by averaging albedo values in the finer grid. Correlation was calculated using Pearson's r between each climatological parameter and separate albedo datasets using every pixel of the raster maps, with significance calculated using a two-tailed student's T-test. Specifically, for each correlation we considered the mean albedo of: i) entire season (November-February), ii) beginning of summer (November), iii) central summer period (December-January), and iv) end of summer (February). Every mean considers the whole period 2000-2012.

3. Results

The results are shown here following 5 steps, from micro- to macro-scale. Thus, the initial analysis at the scale of individual glaciers allowed us to identify the presence or absence of temporal variations and provided insights into more relevant spatial trends, which were then evaluated in more detail at the macro-scale. In all the analyses, the standard error is low ($\sigma_x < 0.001$), which suggests that all the albedo variations are statistically significant.

Analysis of individual glaciers

We analysed individual glaciers that presented a portion of their outlines directly exposed to the sea or ice shelves. Hence, we randomly chose 95 glaciers around the continent, studying their albedo variations. As concerns temporal trends of the entire period (average albedo from November 2000 to February 2012), none is evident for any of the glaciers, since the albedo changes are <0.0005 y^{-1} and significance is below the 95% confidence level. However, focusing on a spatial pattern, we found a general low variability in albedo of the Indian glaciers (with a range of 0.03 and an average of 0.79, tab. 1) compared to the other two oceanic basins. Glaciers in the Pacific basin feature an albedo range of 0.10 (with a mean albedo of 0.76) and in the Atlantic basin a range of 0.18 (with a mean albedo of 0.74), which make it the most heterogeneous basin and with the lowest values. The standard deviation confirms this variability: 0.01 (Indian), 0.03 (Pacific) and 0.04 (Atlantic).

Table 1. Mean, maximum, minimum and standard deviation (StD) of albedo of analysed individual glaciers, divided into the three oceanic basins (i.e. Indian, Pacific and Atlantic).

	Mean	Maximum	Minimum	StD
Indian	0.79	0.81	0.78	0.01
Pacific	0.76	0.80	0.70	0.03
Atlantic	0.74	0.80	0.62	0.03

Analysing in more details one representative glacier of each basin provides more information supporting our results. For example, observing the albedo of the Dovers and Cosgrove glacier (fig. 2A), about 400 km away from the Amery Ice Shelf (Indian basin, fig. 1A), we did not identify any significant variation over time and the values are always high (mean of 0.81, ranging from 0.79 to 0.84). Conversely, the time series of the Darwin glacier (fig. 2B), in the proximity of the Ross Ice Shelf (Pacific basin), is more heterogeneous with lower albedo values compared to Dovers and Cosgrove glacier, a mean of 0.7 and an absolute range of 0.13 (0.63-0.76). Here it is also possible to

observe, intra-annually, a weak seasonal cycle, where the albedo tends to increase in early summer, with the maximum generally at the end of November, followed by a period of decrease until the end of summer. Finally, in the Atlantic basin, a notable glacier is Evans (fig. 2C) in the Antarctic Peninsula, 50 km from the Larsen Ice Shelf. This glacier provides evidence of the sea proximity effect: the range of values is particularly wide, ranging from 0.6 to 0.83, reaching albedo values typical of blue ice (Bintanja, 1999). In addition, the seasonal cycle is stronger for this glacier.

Analysis by Oceanic basins

Now, focusing on the study of spatial variations, we started by dividing Antarctica in its 3 oceanic basins: Indian, Pacific and Atlantic (fig. 3). The first one shows a higher mean albedo (0.81) compared to the other two basins, a maximum of 0.82 (17/11/2001) and a minimum of 0.79 (26/02/2007). The seasonal cycle of the Indian basin mimics the one previously observed for individual glaciers. Compared to the Indian basin, the Pacific and Atlantic basins show different patterns, but similar between each other. The mean albedo of the Pacific basin is 0.79, the maximum is 0.81 (25/11/2001) and the minimum is 0.76 (06/02/2001), confirming the higher variability also seen for Darwin glacier. Unlike in the analysis of individual glaciers, the Atlantic basin is more homogeneous than Pacific one, with an average albedo of 0.79, and lower range between maximum and minimum (0.80 on 25/11/2001 and 0.77 on 26/02/2007). The seasonal cycle replicates the previous ones, but the inter-annual variation shows larger heterogeneity among the different summers (e.g. summer 2009-2010 when the range is much lower than the previous and following summer). In summary, we found higher values in the Indian basin and a similar range in the Pacific and Atlantic basins, with larger variability in the Pacific one. In comparison, Laine (2008) found the highest average albedo values in the Indian and Pacific basins (average of 0.85) between 1981 and 2000, with slightly higher variability in the Indian basin. Lower values were instead found in the Weddell Sea (WS), Ross Sea (RS) and Bellingshausen-Amundsen Sea (BS) with 0.84, 0.80 and 0.78, respectively. The differences with respect to our results can be explained by the different definitions of basins used by Laine (2008), e.g. our definition of the Pacific includes RS and BS, lowering the overall albedo.

Analysis by continentality sectors

For this analysis, we divided the data based on the three continentality sectors (fig. 4): continent, transition and shore. We did not observe significant inter-annual trends in any sector, but we found evidence of intra-annual patterns, with all three continentality zones showing an albedo range typical of snow (King & Turner, 1997; Picard & alii, 2012). The first sector has limited absolute variations, with a maximum of 0.83 (17/11/2001), a minimum of 0.79 (26/02/2009) and a mean value of 0.81. The albedo has the same seasonal cycle as found for the previous analyses, with a second local

maximum between January and February (excluding the summer 2009-2010). In the transition sector, maximum, minimum and mean albedo are 0.02 lower compared to the values of the continental sector: the maximum is 0.81 (25/11/2001), the minimum 0.77 (26/02/2007) and the mean value 0.79. The transition sector has the same seasonal pattern as the continental one, but the second peak has a lower duration, limited to January, and does not involve all the summers. The coastal sector shows the lowest values compared to the other sectors: 0.77 (09/11/2001), 0.73 (26/02/2007) and 0.76 for maximum, minimum and average albedo, respectively. The intra-annual variability is similar to the two other sectors, in particular to the continental one, showing a pronounced second peak in January-February.

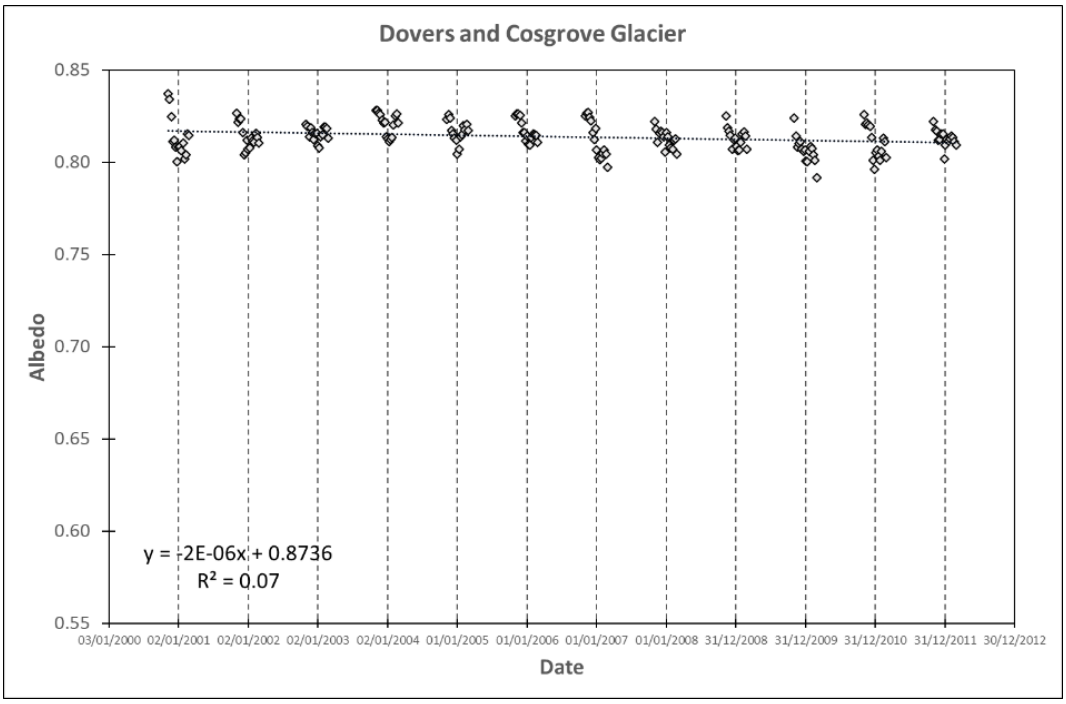

A

B

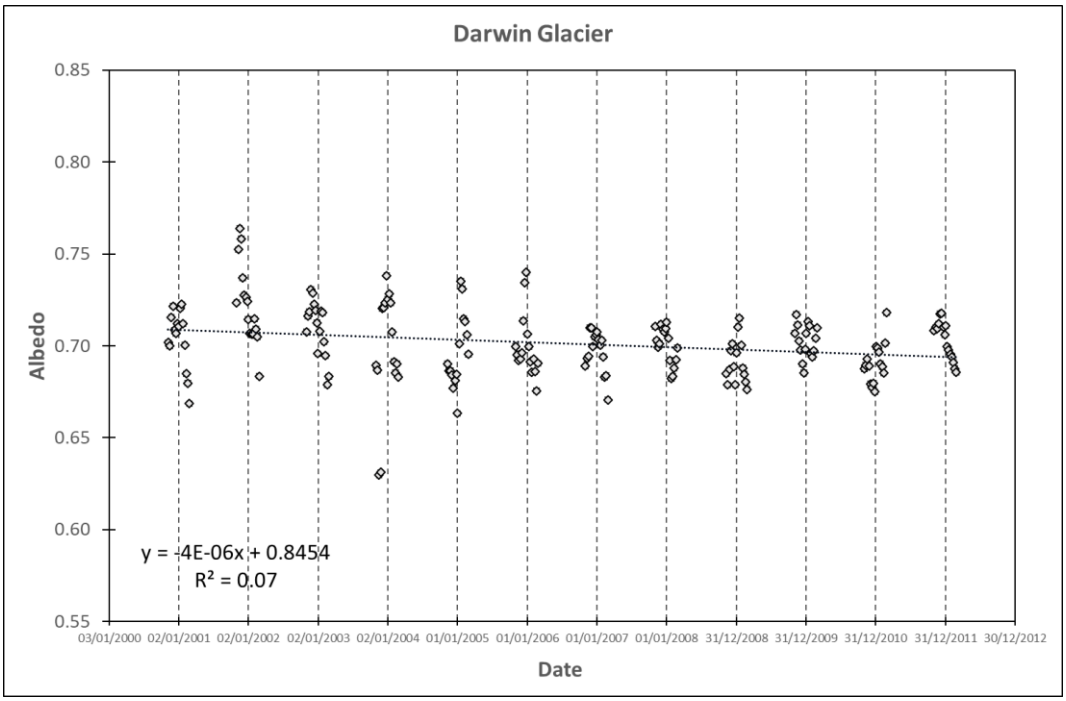

C

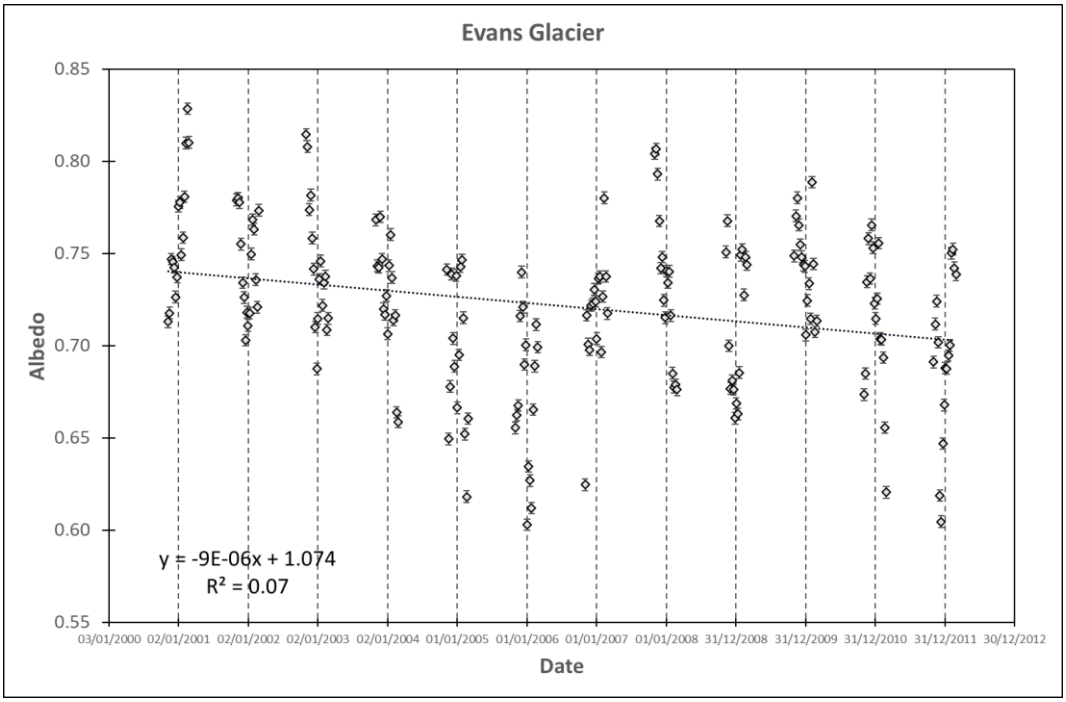

Figure 2. Albedo values of Antarctica from 08/11/2000 to 26/02/2012 of Dovers and Cosgrove glacier in the Indian basin (A), Darwin glacier in the Pacific basin (B) and Evans Glaciers in the Atlantic basin (C). Error bars represent the standard error of the mean.

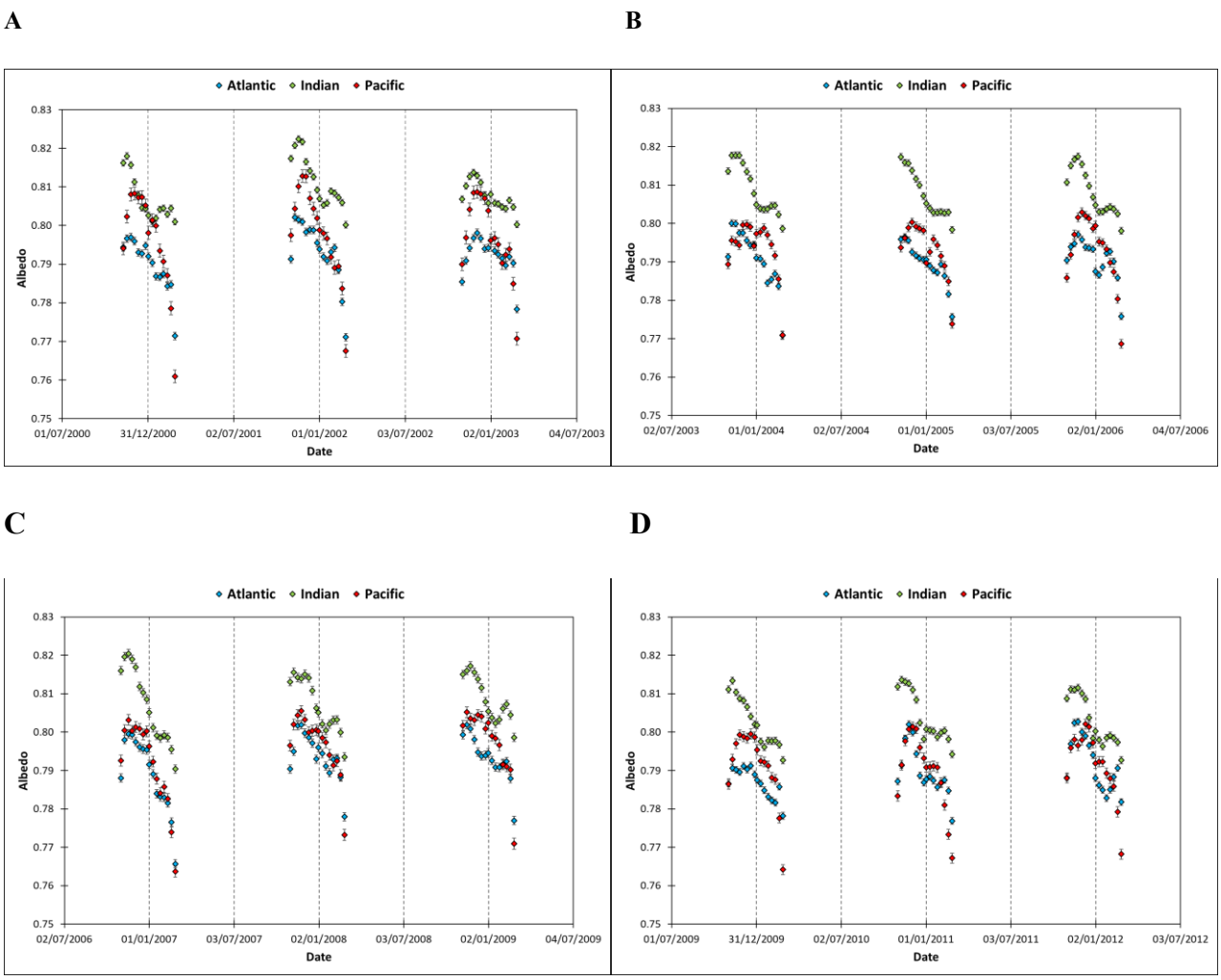

Figure 3. Albedo values from 08/11/2000 to 26/02/2012 of Antarctica, divided by oceanic basins: from summer 2000/2001 to 2002/2003 (A), from summer 2003/2004 to 2005/2006 (B), from summer 2006/2007 to 2008/2009 (C) and from summer 2009/2010 to 2011/2012 (D). Error bars represent the standard error of the mean.

Analysis of the Atlantic basin by continentality sectors

Since the Atlantic basin is found to be the most heterogeneous analysing individual glaciers but not at macro-scale, we studied this basin in more detail, dividing it into the three continentality sectors. The continental sector of the Atlantic basin shows a very similar range to the continental sector of the entire Antarctica. We found a mean of 0.81, the same maximum of 0.83 (17/11/2001) and a minimum of 0.78 (26/02/2004), -0.01 lower than the value for continental Antarctica. Here, we observed the same seasonal cycle as the continental sector for the whole Antarctica, again with the exception of summer 2009/2010 when the values are on average lower. Also in the Atlantic transition sector, we did not find a different cycle, but similar patterns to the transition sector of Antarctica. In addition, the mean is once more equal to 0.79, the maximum, dated 25/11/2001, is almost the same with a value of 0.8. Conversely, the minimum is slightly lower than the whole continent transition sector, with a value of 0.75 (26/02/2007). Finally, the Atlantic coastal sector shows a different picture with a higher

heterogeneity. It shows the same mean value (0.76) and the same maximum (0.77, on 17/11/2011) of the Antarctic coastal sector and a similar minimum (0.74, on 26/02/2007). Unlike the three continentality sectors, oceanic basins, and Atlantic continental and transition sectors, the intra-annual cycle of the Atlantic shore is not well defined. This might be explained by the very variable climate on the Western side of the Antarctic peninsula (King & Turner, 1997).

Analysis of the entire continent

In the last step, we analysed the albedo variations of the whole Antarctica. We did not find a significant change of the summer averages over time; in fact, the values ranged between 0.79-0.81, with an average of 0.8. Again, the seasonal cycle previously observed is present. Inter-annually, no significant trends are seen between 2000 and 2012. The absolute maximum, for the entire period 2000-2012, occurred on 25/11/2001 with an albedo value of 0.81 and the absolute minimum, on 26/02/2007, with a value of 0.77. The albedo of the whole continent is thus slightly lower than the "Snow on the plateau" albedo range (Dalrymple & alii, 1966; Dolgina & alii, 1976; Gardiner & Shanklin, 1989).

A **B**

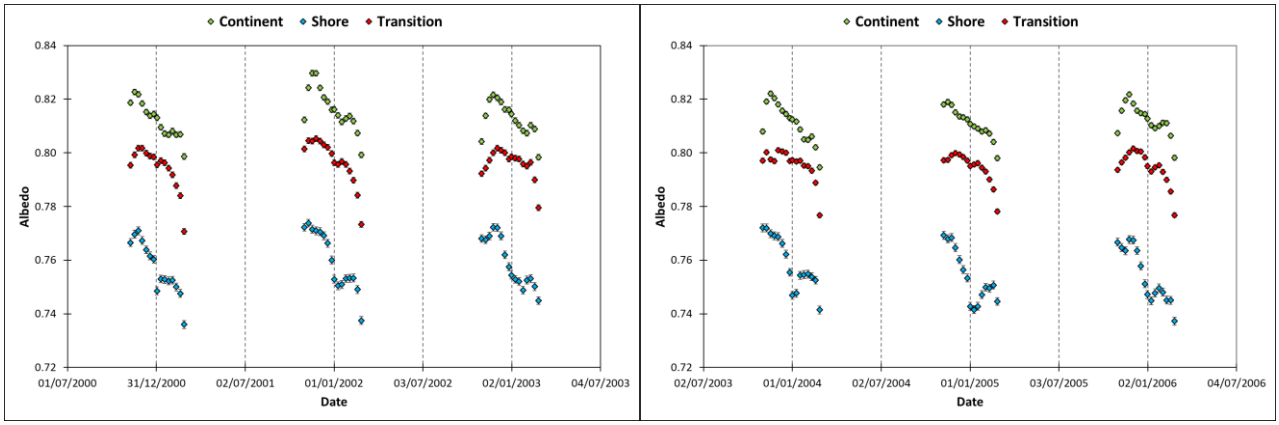

C **D**

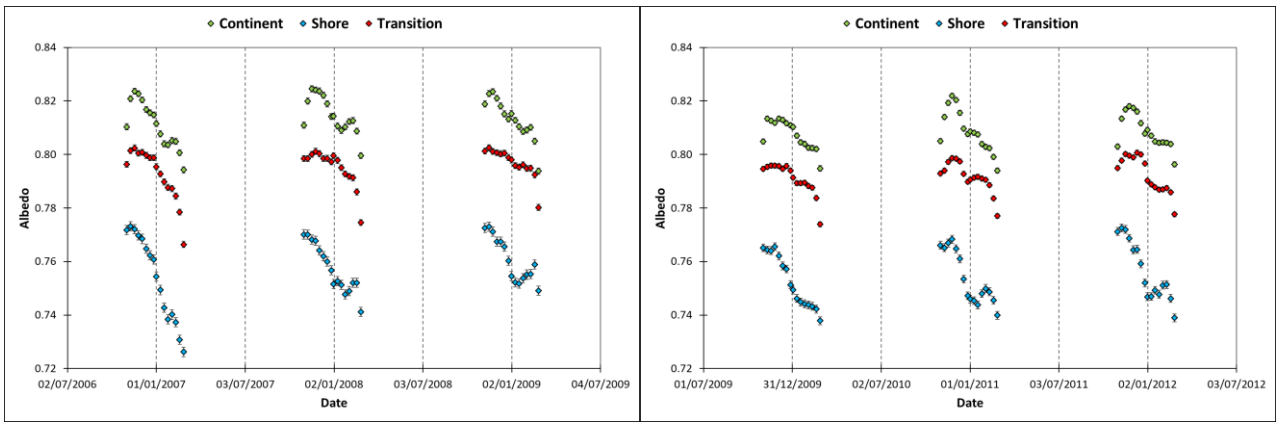

Figure 4. Albedo of Antarctic sectors based on continentality from November 2000 to February 2012: from summer 2000/2001 to 2002/2003 (A), from summer 2003/2004 to 2005/2006 (B), from summer 2006/2007 to 2008/2009 (C) and from summer 2009/2010 to 2011/2012 (D). Error bars represent the standard error of the mean.

4. Discussion

In our analysis, we found limited temporal variability which does not lead to significant trends and a larger spatial variability. In fact, we observed changes from a basin to another and from the continental sector to the shore. In particular, we identified i) a pattern from homogeneous and higher albedo in the Indian basin to more heterogeneous and lower values in the Pacific and Atlantic basins, and ii) an evident decreasing of albedo from inland (i.e. continental zone) to the coastal sector, through the transition zone. In each case, a typical seasonal cycle is observed (increasing albedo in the first half of summer, followed by a decrease during the last months). This seasonal albedo cycle might be due to the dependence of the albedo on the solar zenith angle (SZA). For instance, Picard & alii (2016) found an inverse relationship between albedo and SZA in Antarctica from the analysis of automatic weather station data. A similar relationship was found by Cao & alii (2010) by using seven satellite datasets, including Landsat 7 ETM+, MODIS and AVHRR. Therefore, the SZA causes a seasonal albedo cycle, as observed by Pirazzini (2004), since it is higher at the beginning and end of summer. Consequently, the albedo cycle observed in our datasets is probably due to the SZA influence on raw data acquired by MODIS and used in the GLASS algorithm. As concerns spatial variations, the differences among the basins can be explained from a meteorological and environmental point of view. The results of the correlation analysis between albedo and climatological parameters from RACMO2.3, presented in tab. 2, show negative correlations (except wind speed), with the strongest r between albedo and temperature (from -0.52 to -0.62). All correlations are significant at the 99% confidence level. Considering the central summer period, the correlations generally become stronger, especially with precipitation with a value of -0.46. All other correlations, including wind speed and sublimation rate are always lower than ±0.2. The only positive correlation is between albedo and wind speed thus suggesting that an increase of wind speed would lead to increasing albedo. We also calculated correlations for specific dates, obtaining again similar values (see example in tab. 2). It has to be noted that RACMO2.3 provides only means of yearly observations, and correlation indexes might become higher when comparing e.g. the average of summer climatological data with mean summer albedo. The strongest controls on the albedo at the continent scale, where local conditions are negligible, are therefore temperature (-0.56) and precipitation (-0.39). In fact, the albedo generally depends on the temperature, which controls the morphogenesis stage of snow and ice, and on precipitation, which regulates the presence of fresh snow on the surface (Nakamura & alii, 2001).

Table 2. Correlation indexes between albedo (α) and Wind-Speed (WS), Precipitations (P), Sublimation Rate (SR), Surface Mass Balance (SMB) and Temperature (T). All correlations are significant at the 99% confidence level.

	α - WS	α - P	α - SR	α - SMB	α – T
Entire summer season	0.15	-0.39	-0.19	-0.31	-0.56
19/12/2011	0.13	-0.44	-0.21	-0.36	-0.55
Beginning of the summer	0.18	-0.38	-0.13	-0.32	-0.52
Central summer period	0.14	-0.46	-0.24	-0.38	-0.62
End of the summer	0.13	-0.39	-0.17	-0.31	-0.56

At the local scale, however, other meteorological and environmental factors become important. Concerning continentality, the proximity to the oceans appears to affect Antarctic albedo. Cloudiness, originated from the offshore persistence of low-pressure systems (King & Turner, 1997), has been proposed as an explanation for higher variability in albedo measured at weather stations on the shore (Pirazzini, 2004). However, this assumption cannot be valid in our study as GLASS images are cloud-free. Again, the effect of ocean proximity can be traced back to temperature and precipitation. To further confirm that, we compared the three sectors with the climate zones found by Wagner & alii (2018), who divided Antarctica into 12 temperature zones and 5 precipitation zones. The zones with temperatures lower than -43 °C and precipitation lower than 25 mm correspond approximately to the continental sector defined in our study, while the areas with temperatures above -18 °C and precipitation above 500 mm are in agreement with our coastal sector. In addition, wind, for which contrasting effects have been reported, can also have an important role. Pirazzini (2004) showed that katabatic winds (i.e. winds with very high speed) can increase albedo by limiting snow metamorphism, above all when the absence of warm temperature does not lead to snowmelt. However, most studies report a lowering effect of wind speed on the albedo. In fact, a higher frequency and intensity of katabatic winds can decrease albedo: i) by shaping snow on sloping surfaces and creating sastrugi (i.e. meter-scale longitudinal erosional features, whose axes align with the direction of strong winds, Warren & alii, 1998; Frezzotti & alii, 2002); ii) by increasing surface melt, and iii) by exposing blue ice through snow erosion (e.g. Victoria Land area, in proximity to David glacier) (Winther & alii, 2011). Lenaerts & alii (2017) focused on the double role of katabatic winds near the grounding zone of ice shelves. They found that katabatic winds increase near-surface temperatures by 3 K through disruption of the surface-based temperature inversion, leading to a doubling of surface melt; these

winds continuously scour the surface exposing blue ice and firn. Further still, katabatic winds can also shape the surface, creating wind glaze areas that show lower albedo than snow (e.g. in mega-dune fields, on the Antarctic plateau, associated also with sastrugi) (Frezzotti & alii, 2002; Scambos & alii, 2012; Das & alii, 2013). From the positive correlation index between wind speed and albedo, we can hypothesize that, at the macro-scale (i.e. 35 km spatial resolution in our case), the effect of limiting metamorphism by strong katabatic winds leads to an increase of albedo, taking over all other negative effects. An example of local scale effects is instead on the coast of Ross Sea, where temperatures near the melting point and the decreased intensity and frequency of katabatic winds during the summer allow a strong metamorphism of the snow (Pirazzini, 2004), lowering the albedo. Meteorological and environmental factors also explain the differences seen among the oceanic basins. For instance, the Indian sector includes the Antarctic plateau, with a high average altitude, thus lower temperatures and reduced snow metamorphism. The Pacific basin consists of the area to the west of the Transantarctic Mountains with a wide coastal zone, including the Ross coast, where Pirazzini (2004) found high albedo variability. The Atlantic basin is characterized by slightly different albedo values compared to the Pacific one. This might be due to the combination of two opposite factors: i) the presence of the Antarctic Peninsula, which reaches the lowest latitude of the continent and thus shows the highest temperatures, and ii) the occurrence of cyclones and easterly winds, producing frequent snowfall and almost continuous drifting snow, which supply the surface with small and highly reflective snow grains (Pirazzini, 2004). Finally, as regards the analysis of the Atlantic basin by continentality zones, we observed a similar variation in the albedo of the continental and transition zone and a different situation in the Atlantic coastal zone. This difference could be due to the mixing of the heterogeneous meteorological and geographical conditions (e.g. temperature, precipitation, wind speed, proximity to the ocean, etc.) occurring in the Atlantic coastal zones, unlike the other sectors. Values seen in the Atlantic coastal zone however do not affect patterns in the other areas: the whole Atlantic basin, the whole shore sector and the whole continent.

5. Conclusion

In this study, we analysed the surface albedo of Antarctica between summer 2000/2001 and summer 2011/2012 by means of the GLASS product. We found limited temporal variability from the micro-scale analysis of individual glaciers. Considering the spatial variability, mean albedo ranges from 0.79 (Pacific and Atlantic basins) to 0.82 (Indian basin) and from 0.76 (shore) to 0.81 (continent). This decrease in albedo from the inner areas to the shore can be explained by sea proximity and larger meteorological variability (in temperature, precipitation and wind speed influencing the presence of fresh snow and its metamorphism; Nakamura & alii, 2001). This is further demonstrated by the

comparison between GLASS albedo dataset and RACMO2.3 climatological product (Van Wessem & alii, 2014a, 2014b), where we found good correlations especially with temperature and precipitation. Other factors might include the presence of exposed ice or nunataks close to the coast (Stenmark & alii, 2014), lowering albedo at the scale of GLASS pixels and topography (less constant on the shore than on the Antarctic plateau). These findings permit to assess a spatial pattern but not a trend over time. In fact, the relationship between albedo, oceanic basins and continentality points to heterogeneous patterns among the basins and an increasing variability from the inner continent to the shore. In general, our albedo values are: i) slightly lower than the typical range of "snow on the plateau" (0.80-0.90, Dalrymple & alii, 1966; Dolgina & alii, 1976; Gardiner & Shanklin, 1989); ii) in agreement with field data from Hells Gate, Neumayer, Concordia and Reeves Névé stations (0.58-0.82, Pirazzini, 2004); iii) slightly lower than values of 0.80-0.85 found by Grenfell & alii (1994) at Scott South Pole and Vostok stations. However, for some glaciers the albedo reaches values equal or lower than blue ice (0.56-0.69 according to King & Turner, 1997; Bintanja, 1999; Reijmer & alii, 2001; Hui & alii, 2014). In future research, the results obtained by means of GLASS products should be compared with other remote- sensing albedo datasets (e.g. MOD10A1, CLARA-A2, bearing in mind that MOD10A1 needs cloud filtering and CLARA-A2 has a much coarser resolution). This would allow to i) ensure the reliability of GLASS; ii) increase the period of observations, from the 1980s up to the present, and investigate longer-term trends in Antarctic albedo, iii) assess the impact of albedo variations on the energy budget at the local and global scale.

References

Bintanja R. (1999) - On the glaciological, meteorological, and climatological significance of Antarctic blue ice areas. Reviews of Geophysics, 37 (3), 337-359.

Brandt R.E., Warren S.G., Worby A.P. & Grenfell T.C. (2005) – Surface albedo of the Antarctic sea ice zone. Journal of Climate, 18 (17), 3606-3622.

Cao C., Uprety S., Xiong J., Wu A., Jing P., Smith D., Chander G, Fox N. & Ungar, S. (2010) - Establishing the Antarctic Dome C community reference standard site towards consistent measurements from Earth observation satellites. Canadian Journal of Remote Sensing, 36 (5), 498-513.

Dalrymple P.C., Lettau H. & Wollaston S. (1966) - South Pole Micrometeorology Program. In: RUBIN M.J. (Ed.), Studies in Antarctic Meteorology. Antarctic Research Series, V. 9, American Geophysical Union, Washington, 13-57.

Das I., Bell, R. E., Scambos T.A., Wolovick M., Creyts T.T., Studinger M., Frearson N., Nicolas J.P., Lenaerts J.T.M. & Van Den Broeke M.R. (2013) - Influence of persistent wind scour on the surface mass balance of Antarctica. Nature Geoscience, 6 (5), 367-371.

Dolgina I.M., Marshunova M.A. & Petrova L.S. (1976) – Reference Book of the Climate of Antarctica. Volume 1. Radiation, Arctic and Antarctic Scientific Research Institute, Leningrad, 213 pp. (In Russian).

Drewry D.J. (1983) - Antarctica: Glaciological and geophysical folio. Scott Polar Research Institute, University of Cambridge, Cambridge.

Frezzotti M., Gandolfi S., La Marca F. & Urbini S. (2002) – Snow dunes and glazed surfaces in Antarctica: New field and remote sensing data. Annals Glaciology, 34, 81-88.

Fugazza D., Senese A., Azzoni R.S., Maugeri M., Maragno D. & Diolaiuti G.A. (2019) - New evidence of glacier darkening in the Ortles-Cevedale group from Landsat observations. Global and Planetary Change 178, 35-45. doi: 10.1016/j.gloplacha.2019.04.014

Gallet J.C., Domine F., Arnaud L., Picard G. & Savarino J. (2011) - Vertical profile of the specific surface area and density of the snow at Dome C and on a transect to Dumont D'Urville, Antarctica-albedo calculations and comparison to remote sensing products. The Cryosphere, 5, 631-649.

Gardiner B.G. & Shanklin J.D. (1989) - Measurements of Solar and Terrestrial Radiation at Faraday and Halley. British Antarctic Survey, Cambridge, 45 pp.

Gay M., Fily M., Genthon C., Frezzotti M., Oerter H. & Winther J.G. (2002) - Snow grain-size measurements in Antarctica. Journal of Glaciology, 48 (163), 527-535.

Grenfell T.C., Warren S. & Mullen P.C. (1994) - Reflection of solar radiation by the Antarctic snow surface at ultraviolet, visible, and nearinfrared wavelengths. Journal of Geophysical Research, 99, 18,669-18,684.

Helm V., Humbert A. & Miller H. (2014) - Elevation and elevation change of Greenland and Antarctica derived from CryoSat-2. The Cryosphere, 8 (4), 1539-1559.

Hoinkes H.C. (1960) - Studies of solar radiation and albedo in the Antarctic. Archiv für Meteorologie, Geophysik und Bioklimatologie, Serie B, 10 (2), 175-181.

Hui F., Ci, T., Cheng X., Scambo T.A., Liu Y., Zhang Y., Chi Z., Huang H., Wang X., Wang F., Zhao C., Jin Z. & Zhao C. (2014) - Mapping blue-ice areas in Antarctica using ETM+ and MODIS data. Annals of Glaciology, 55 (66), 129-137.

King J.C. & Turner J. (1997) - Antarctic meteorology and climatology. Cambridge University Press, 409 pp.

Laine V. (2008) - Antarctic ice sheet and sea ice regional albedo and temperature change, 1981-2000, from AVHRR Polar Pathfinder data. Remote Sensing of Environment, 112 (3), 646-667.

Lenaerts J.T.M., Lhermitte S., Drews R., Ligtenberg S.R.M., Berger S., Helm V., Smeets C.J.P., Van Der Broeke M.R., Van Der Berg W.J., Van Meijgaard E., Eijkelboom M., Eisen O. & Pattyn F. (2017) - Meltwater produced by wind–albedo interaction stored in an East Antarctic ice shelf. Nature climate change, 7 (1), 58-62.

Liang S. & Liu Q. (2012) - Global Land Surface Products: Albedo Product Data Collection (1985-2010). Beijing Normal University. doi:10.6050/ glass863.3001.db

Nakamura T., Abe O., Hasegawa T., Tamura R. & Ohta T. (2001) - Spectral reflectance of snow with a known grain-size distribution in successive metamorphism. Cold Regions Science and Technology, 32, 13-26.

Picard G., Domine F., Krinner G., Arnaud L. & Lefebvre E. (2012) - Inhibition of the positive snow-albedo feedback by precipitation in interior Antarctica. Nature Climate Change, 2, 795-798.

Picard G., Libois Q., Arnaud L., Vérin G. & Dumont M. (2016) – Estimation of superficial snow specific surface area from spectral albedo time-series at Dome C, Antarctica. The Cryosphere Discussion, 10.5194/tc-2015-213

Pirazzini R. (2004) - Surface albedo measurements over Antarctic sites in summer. Journal of Geophysical Research, 109, D20118. doi: 10.1029/2004JD004617.

Reijmer C. H., Bintanja R. & Greuell W. (2001) - Surface albedo measurements over snow and blue ice in thematic mapper bands 2 and 4 in Dronning Maud Land, Antarctica. Journal of Geophysical Research: Atmospheres, 106 (D9), 9661-9672.

Scambos T.A., Frezzotti M., Haran T., Bohlander J., Lenaerts J.T.M., Van Den Broeke M.R., Jezek, K., Long, D., Urbini, S., Farness K., Neumann T., Albert M., & Winther J.G. (2012) – Extent of low-accumulation'wind glaze'areas on the East Antarctic plateau: implications for continental ice mass balance. Journal of Glaciology, 58 (210), 633-647.

Schaaf C.L.B., Liu J., Gao F. & Strahler A.H. (2011) - MODIS albedo and reflectance anisotropy products from Aqua and Terra. Land Remote Sensing and Global Environmental Change: NASA's Earth Observing System and the Science of ASTER and MODIS, 11, 549-561.

Stenmark A., Hole L.R., Voss P., Reuder J. & Jonassen M.O. (2014) - The influence of nunataks on atmospheric boundary layer convection during summer in Dronning Maud Land, Antarctica. Journal of Geophysical Research, Atmospheres, 119 (11), 6537-6548.

Tedesco M., Doherty S., Fettweis X., Alexander P., Jeyaratnam J. & Stroeve J. (2016) - The Darkening of Greenland ice sheet: trends, drivers, and projections (1981-2100). The Cryosphere, 10, 477-496.

Van Wessem, J. M., Reijmer, C. H., Lenaerts, J. T. M., Van De Berg, W. J., Van Den Broeke, M. R. & Van Meijgaard E. (2014a) – Updated cloud physics in a regional atmospheric climate model improves the modelled surface energy balance of Antarctica. The Cryosphere, 8, 125-135.

Van Wessem J.M., Reijmer C.H., Morlighem M., Mouginot J., Rignot E., Medley B., Joughin I., Wouters B., Depoorter M.A., Bamber J.L., Lenaerts J.T.M., Van De Berg W.J., Van Den Broeke M.R. & Van Meijgaard E. (2014b) - Improved representation of East Antarctic surface mass balance in a regional atmospheric climate model. Journal of Glaciology, 60 (222), 761-770.

Wagner M., Trutschnig W., Bathke A.C. & Ruprecht U. (2018) – A first approach to calculate BICLIM variables and climate zones for Antarctica. Theoretical and Applied Climatology, 131, 1397-1415.

Warren S.G., Brandt R.E. & O'rawe Hinton P. (1998) - Effect of surface roughness on bidirectional reflectance of Antarctic snow. Journal of Geophysical Research, Planets, 103 (E11), 25789-25807.

Warren S.G., Brandt R.E. & Grenfell T.C. (2006) - Visible and near-ultraviolet absorption spectrum of ice from transmission of solar radiation into snow. Applied Optics, 45 (21), 5320-5334.

Winther J.G., Jespersen M.N. & Liston G.E. (2001) - Blue-ice areas in Antarctica derived from NOAA AVHRR satellite data. Journal of Glaciology, 4 (157), 325-334.

Zhao X., Liang S., Liu S., Yuan W., Xiao Z., Liu Q., Zhou G., Xu S. Yu K. (2013) - The Global Land Surface Satellite (GLASS) remote sensing data processing system and products. Remote Sensing, 5, 2436-2450.

Zwally H.J., Giovinetto M.B., Beckley M. A. & Saba J.L. (2012) - Antarctic and Greenland drainage systems. GSFC Cryospheric Sciences Laboratory.

Appendix 1.2: Characterization of glacial foreland areas in Lombardy Region (North Italy) and their spatial variation in the last 70 years

Giacomo Traversa[1,2], Davide Fugazza[2*], Davide Maragno[2], Guglielmina A. Diolaiuti[2] & Manuela Pelfini[3]

[1] Department of Physical Sciences, Earth and Environment (DSFTA), Università Degli Studi Di Siena, 53100 Siena, Italy;

[2] Department of Environmental Science and Policy (ESP), Università Degli Studi Di Milano, 20133 Milan, Italy;

[3] Department of Earth Sciences "A. Desio", Università degli Studi di Milano, 20133 Milan, Italy

Abstract: Glacier foreland areas are not well known in Alpine area, especially in Lombardy region in the North of Italy. Therefore, the present study intends to provide new and updated information about periglacial zones in this zone, focusing on spatial variation in time (1989-2015 period) and surface characterization, taking advantage of a remote approach based on various techniques and materials of remote sensing (e.g., Sentinel-2 and PRISMA satellites). Additionally, updated information about glacier retreats in Lombardy are here reported. As regards glaciers, a reduction of about 30% of area is here detected in the 26 years of study, even if the highest retreat is meanly located in 1999-2007 period and the lowest values in the most recent years and no evident trend in time is found. The major loss, both cumulative and yearly rate, is showed by the biggest mountain sectors (i.e., Adamello, Ortles – Cevedale and Bernina – Disgrazia) and a high correlation between glacier extensions and retreat rates are calculated. However, the smallest sectors present the highest cumulative and annual values in percentage (on the total initial area). On the other side, the same results and trends are then detected for foreland progression, which shows a tripled extension from 1989 to 2015. Focusing on glacier-foreland characterization, we mapped four types of surfaces, i.e., bare rock, unconsolidated debris, water and vegetation. Being on average at high altitudes (always > 2000 m), we found a predominance of the first two surfaces, which cover almost 99% of the total. Finally, general aspect dominances for water and vegetation coverages are here detected, with N for water (and generally foreland areas as well) and E for vegetation.

1. Introduction

The current rapid glacier recession, from Alpine areas (Haeberli and Beniston,1998) to Antarctica (Rott et al. 1996, Cook et al. 2005; Frezzotti and Orombelli, 2014), is largely considered the most clear and unambiguous signal of global warming (Oerlemans 2005). The volume and area loss of mountain glaciers in response to climate change has been reported at both high and low latitudes (Kaser et al., 2006; Wang et al., 2011; Rabatel et al., 2013; Falaschi et al., 2013; Gardent et al., 2014; Diolaiuti et al; 2019; Paul et al; 2020). Glacier retreat started at the end of the Little Ice Age (LIA), but over the last decades glaciers have been melting at rates that cannot be explained only by natural climate variability (Dyurgerov and Meier, 2000; IPCC, 2013). In the southernmost parts of Europe

(Balkans, Spain, and the Apennines of Italy), glacier retreat since the LIA has been particularly rapid compared to other areas of the Planet (González Trueba et al., 2008; D'Orefice et al., 2000; Hughes, 2009; 2010; Branda et al., 2010). This strong recession dramatically decreased the glacier presence in such areas, which currently show only a mere relic of the past ice coverage. Glacier retreat is also particularly strong in the Alpine region, and it is likely driven by the rapid rise in air temperature occurred in the last few decades (IPCC, 2013). In the Alps, the increase in air temperature was found to be more than double the global mean value over the last 5 decades (Böhm et al. 2001, Casty et al. 2005; Leonelli et al., 2016). Terminus fluctuation records of Alpine glaciers collected over the past 2 centuries permitted to analyse the retreating trend which characterized this period. The cumulative decrease in glacier length was found varying from several hundreds of metres (in the case of smaller ice bodies, Cannone et al; 2008) to a few kilometres (in the case of wider glaciers, Hoelzle et al., 2003; Citterio et al., 2007; Diolaiuti and Smiraglia, 2010). This retreating trend had only one meaningful pause: between the 1950s and 1990s a significant number of glaciers all over the World were found advancing (Patzel, 1985; Wood, 1988), including 85% of the Italian glaciers (Citterio et al., 2007). At the end of this period, the receding trend restarted (Hoelzle et al., 2003). Glacier area changes are considered the most useful geometry feature to evaluate glacier recession and its magnitude; Maisch (2000) reported a general decrease in the area of Alpine glaciers by 27% from 1850 to 1975, with even stronger losses in some subregions of the Alps. Glacier outlines to compute changes are generally available through glacier inventories (Paul & alii, 2004; 2007; 2011; Pfeffer et al., 2014). Glacier inventories should be carried out at time intervals compatible with the characteristic response time of mountain glaciers (a few decades or less in the case of small glaciers), and the currently observed glacier down-wasting calls for frequent updates of inventories (Paul et al; 2020). During the past two decades, several regional inventories were developed and published describing glacier changes with a consistent spatial resolution in the individual Alpine countries (Paul et al, 2004; Gardent et al; 2014; Diolaiuti et al; 2019). With the launch of the first Sentinel-2 (S2) satellite in 2015, it became possible to create a consistent, Alpine-wide (international) glacier inventory with an unprecedented spatial resolution of 10 m (Paul et al; 2020). Paul et al. (2020) used the S2 images from 2015-2017 as a base for the compilation of a new Alpine-wide glacier inventory in a collaborative international team effort. Overall, the total glacier area was 1806±60 km^2 when considering 4395 glaciers with an area greater than 0.01 km^2. This value, compared to the cumulative Alpine glacier extent in 2003 (based on Landsat imagery) permitted to quantify glacier area changes of -14 %, which implies a rate of −1.2 % per year, thus underlying the continuation of glacier shrinkage in the Alps since the mid-1980s. This increasing glacier recession leads to a widening of glacier forelands. In fact, the retreat of the glacier termini drives the exposure of lands which were

covered by ice in the past. In these pristine environments, exogenous phenomena can operate through mass wasting action, melting and running water and gravitative processes (Pelfini and Bollati, 2014). The widening of glacier forelands in some cases permitted the retrieval of wood remnants which are crucial to reconstruct the past climate history (Pelfini et al., 2014; St-Hilayre & Smith, 2017;). The responses of the environmental systems to the retreat of the glacier termini are not simple and show contributions from several biotic and abiotic elements. These newly exposed lands experience rapid variations and evolution (Staines et al., 2015) and therefore represent key sites for analysing the effects of paraglacial and periglacial processes on the landscape, and to detect phenomena triggering environmental hazard and risk conditions (Mergili et al., 2012). These latter are mainly due to the unconsolidated sediments (which may also contain heterogenic ground ice) located on the glacier forelands, which are vulnerable to rapid changes depending on the magnitude and rates of climate warming and influence both geomorphic processes and sediment supply down valley (Bosson et al., 2015; D'Agata et al; 2019); furthermore, melting waters as well as ground water may affect depositional landforms in the glacier forelands (Levy et al., 2015). Proglacial lakes and water ponds can also develop and undergo variations (Geilhausen et al., 2003; Salerno et al., 2014; Fugazza et al., 2020) with relevant biological effects (Sommaruga, 2015). The newly exposed areas show the beginning of soil development (Egli et al 2006; D'Amico et al., 2015), both on sparse till deposits and on well-shaped moraine ridges (Kabala and Zapart, 2012); the chrono-sequences on the glacier forelands also represent favourable substrates for biological colonization; these pristine areas show successions of: arthropods (Gobbi et al., 2007; Brambilla and Gobbi, 2014), bacterial communities (Meola et al 2014), plants (Cannone et al, 2008) and trees (Garavaglia et al., 2010). A recent study on Alpine glacier forelands and their evolution was performed by D'Agata et al. (2019). The authors analysed the recent recession of a representative subset of glaciers within the Italian Alps, the Bernina group, where small glaciers are experiencing considerable shrinking, leading to a rapid expansion of glacier forelands. They analysed high resolution aerial photos and orthophotos to calculate glacier area changes from 1954 to 2007 and perform a geomorphological analysis. D'Agata et al. (2019) estimated that glacier area changes during 1954-2007 were -36.5% (with respect to the glacier coverage in 1954). The rate of area changes increased in recent years; in fact, the glacier retreat during 1981-1954 (27 years) was -0.205 km^2/y, against -0.387 km^2/y during 1981-2003 (22 years), and -0.534 km^2/y during 2007-2003 (4 years). Over the same periods, the forelands experienced a rather continuous widening trend: they expanded by about 4 km^2 from 1954 to 1981, and the whole area abandoned by glacier ice was about 14.7 km^2 in the period 1954-2007. 82% of the newly exposed areas were characterized by unconsolidated till deposits, which makes them subject to the action of meltwater and gravitative processes; thus, they represent unstable and potentially rapidly changing

environments. Following the recent study of D'Agata et al (2019), we analyse the evolution of glacier forelands of the whole Lombardy Region, a representative subset of the Italian Alps, where several glaciers are located and many studies on glacier recession have already been performed (among others Citterio et al; 2007; Diolaiuti et al; 2012). The period of observation was 1989-2015, and we used remote sensing-based analysis to investigate the extent and features of glacier forelands in Lombardy.

2. Materials and methods

The present research analyses the glacier forelands in Lombardy region over the period 1989-2015. The period of analysis was chosen owing to the availability of high-resolution aerial orthophotos over the Lombardy region, i.e., 1989, 1999, 2003, 2007, 2012 and 2015 (https://www.terraitaly.it/), with a spatial resolution of 0.5 m. Starting from these images, the glaciers of Lombardy were manually digitalized into shapefiles, which allowed to calculate the glacier foreland extension in different periods by subtracting each polygon surface in GIS software (across the entire period and between an orthophoto and the subsequent one), after manually removing nunataks and rock outcrops. A detailed analysis was carried out on the foreland areas which developed from 1989 to 2015. Different datasets and approaches were used: in addition to the aerial orthophotos, we also analysed multispectral (Sentinel-2) and hyperspectral (PRecursore IperSpettrale della Missione Applicativa PRISMA of the Italian Space Agency ASI; Guarini et al., 2017) imagery (respectively at 10 m and 30 m spatial resolution) and the Digital Terrain Model (DTM) of Lombardy region (https://www.geoportale.regione.lombardia.it/, ed. 2015) at 5 m spatial resolution. Sentinel-2 images were used to estimate the presence of vegetation and water through the calculation of spectral indices, i.e. NDVI (Normalized Difference Vegetation Index) and NDWI (Normalized Difference Water Index); PRISMA imagery was used to validate vegetation mapping from Sentinel-2. The DTM was used to estimate ruggedness (Riley et al., 1999), used to estimate bare rock coverage. Finally, unconsolidated debris was detected by subtracting vegetation, water and bare rock surfaces from the total glacier foreland areas over the period 1989-2015. The list of the datasets used is presented in Table 1. The correlation coefficients (R, or Cc) between foreland areas and their expansion rates are calculated as presented in Traversa et al. (2021).

Dataset	Date	Spatial resolution (m)
Orthophoto	1989	0.5
Orthophoto	1999	0.5
Orthophoto	2003	0.5
Orthophoto	2007	0.5
Orthophoto	2012	0.5
Orthophoto	2015	0.5
Sentinel-2	03/09/2020 (T32TPS + T32TNS)	10
PRISMA	03/09/2020	30

Table 1. satellite and aircraft images used in the analyses with their acquisition date

2.1 Calculation of Sentinel-2-based indices

In order to identify vegetated and water areas, Sentinel-2 imagery was used. Sentinel-2 presents 13 bands covering VNIR and SWIR areas of the electromagnetic spectrum with different spatial resolution (10, 20 and 60 m). A pair of images (T32TNS and T32TPS tiles) acquired on the same day (03/09/2020 as dd/mm/yyyy) were used to cover the entire Lombardy alpine region. In detail, the NDVI and NDWI were calculated to obtain the vegetation and water surfaces of the forelands, respectively. These indices were calculated as follows:

$$NDVI=(B8-B4)/(B8+B4)$$

$$NDWI=(B3-B8)/(B3+B8)$$

where B8 is the NIR band, B4 the Red and B3 the Green bands of Sentinel-2 (10 m spatial resolution). Both indices range between -1 and +1 and the value of the index increases with higher concentration of water (NDWI) and vegetation (NDVI). In general, the NDWI threshold we selected to classify water areas was 0.4 (pixels with NDWI > 0.4 were classified as water), slightly higher than the one proposed by McFeeters (2013) (>0.3). The reason for the higher threshold is to avoid snow covered areas, which show NDWI values between 0.3 and 0.4, very common in glacier forelands.

2.2 PRISMA imagery for foreland vegetation

The PRISMA hyperspectral sensor, whose data is available from 2019, was used as comparison and validation of NDVI calculated from Sentinel-2 images to detect vegetation in glacier forelands. In fact, it allows for a better discrimination of several vegetation types, increasing the performance of vegetation mapping when the complication of the classification system also increases (Vangi et al., 2021). PRISMA presents two hyperspectral cubes, a Visible-Near InfraRed (VNIR) cube including 67 bands and a Short-Save InfraRed (SWIR) cube (167 bands), both with 30 m spatial resolution. Only one cloud-free PRISMA image was available for the alpine region of Lombardy (eastern part, Ortles-Cevedale area) on 3 September 2020, compared to a much larger number of images from Sentinel-2, which started acquiring data in 2015. EarthBIT software by Planetek was used to analyse PRISMA satellite images. The software allows evaluating which hyperspectral band of the sensor presents the highest reflectance response for a specific pixel of the image. Thus, we calculated the response on vegetation pixel (identified on the field) on Forni glacier foreland (Ortles-Cevedale group, Fig. 1). We selected this glacier since it was one of the widest of Lombardy Region and for it several field data to calibrate and validate remote sensing investigations are available. The highest reflectance was found in SWIR-cube band 32, with a wavelength of 1263 nm, and a threshold of ≈14.000 was selected to detect vegetation. Such band was therefore used to calibrate the NDVI from Sentinel-2. The corresponding pixels presented NDVI values ≥ 0.3, which were then considered as vegetated.

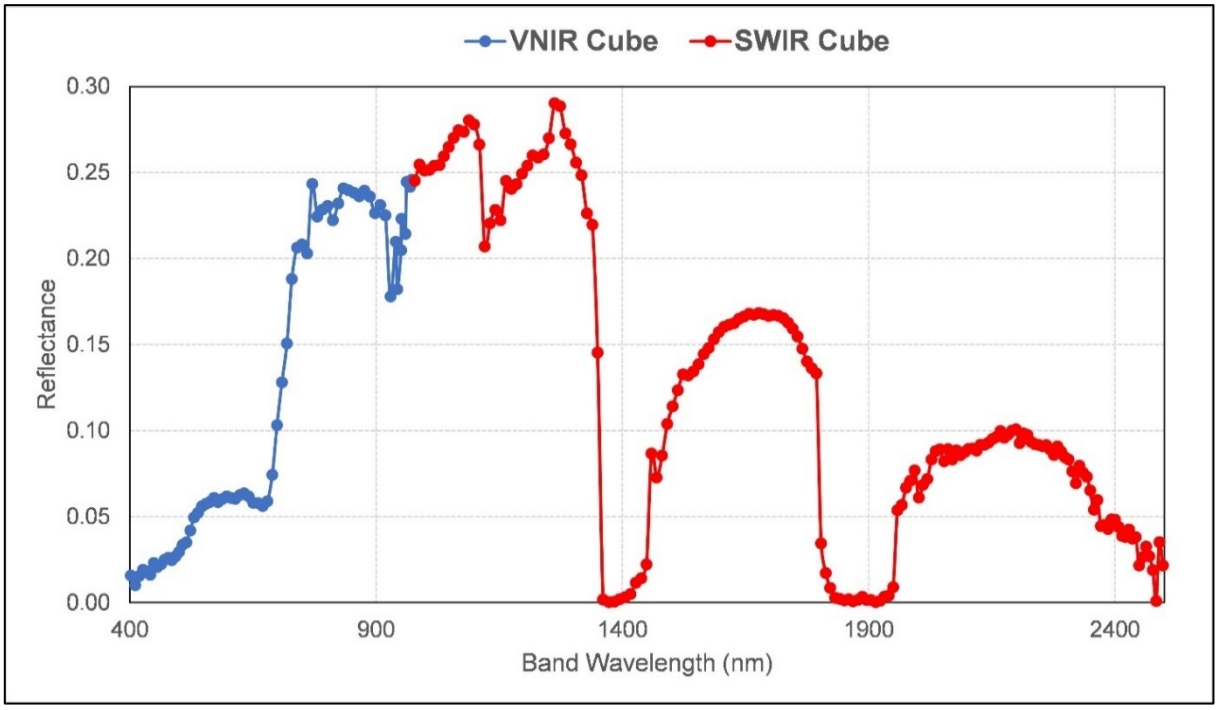

Figure 1. reflectance response of PRISMA bands in a vegetation pixel of Forni glacier foreland.

2.3 Bare rock identification through the ruggedness index

Bare rock areas were detected by taking advantage of the terrain ruggedness index, which calculates the maximum height difference between a pixel and the surrounding cells (Riley et al., 1999). With the aim of detecting the range of ruggedness for bare rock surfaces, we used for calibration the well-known area of Forni glacier foreland (Diolaiuti and Smiraglia, 2010; Fugazza et al; 2015; Azzoni et al., 2018;) and created 25 sample polygons of pure bare rock surfaces to determine their statistical properties. The average ruggedness of the polygons was 5; thus, we selected a threshold of 5 and classified pixels above this threshold as bare rock.

3 Results

The results are here presented firstly focusing on glacier retreat and subsequently on the progression of glacier foreland in Lombardy region, showing both the areas and yearly rates (both on the entire period and from the comparison between single orthophotos). This analysis is also carried out in different mountain sectors. In these results, only glacier polygons which are always present in all the datasets are considered. Finally, the glacier foreland surface characterization is provided with details about debris thickness and the topographic characteristics of water and vegetated areas.

3.1 Glacier foreland progression and glacier retreat

By using the glacier outlines digitized from orthophotos corresponding to different acquisition times, we calculated the evolution over time of the glacier forelands. The area of glaciers in Lombardy Region continuously decreased from 1989 to 2015 (Fig. 2); in 1989, the total glacier area was 115.3 km^2; since then, glaciers reduced at the regional scale by almost 30%, as the total glacier extent in 2015 was 81.0 km^2.

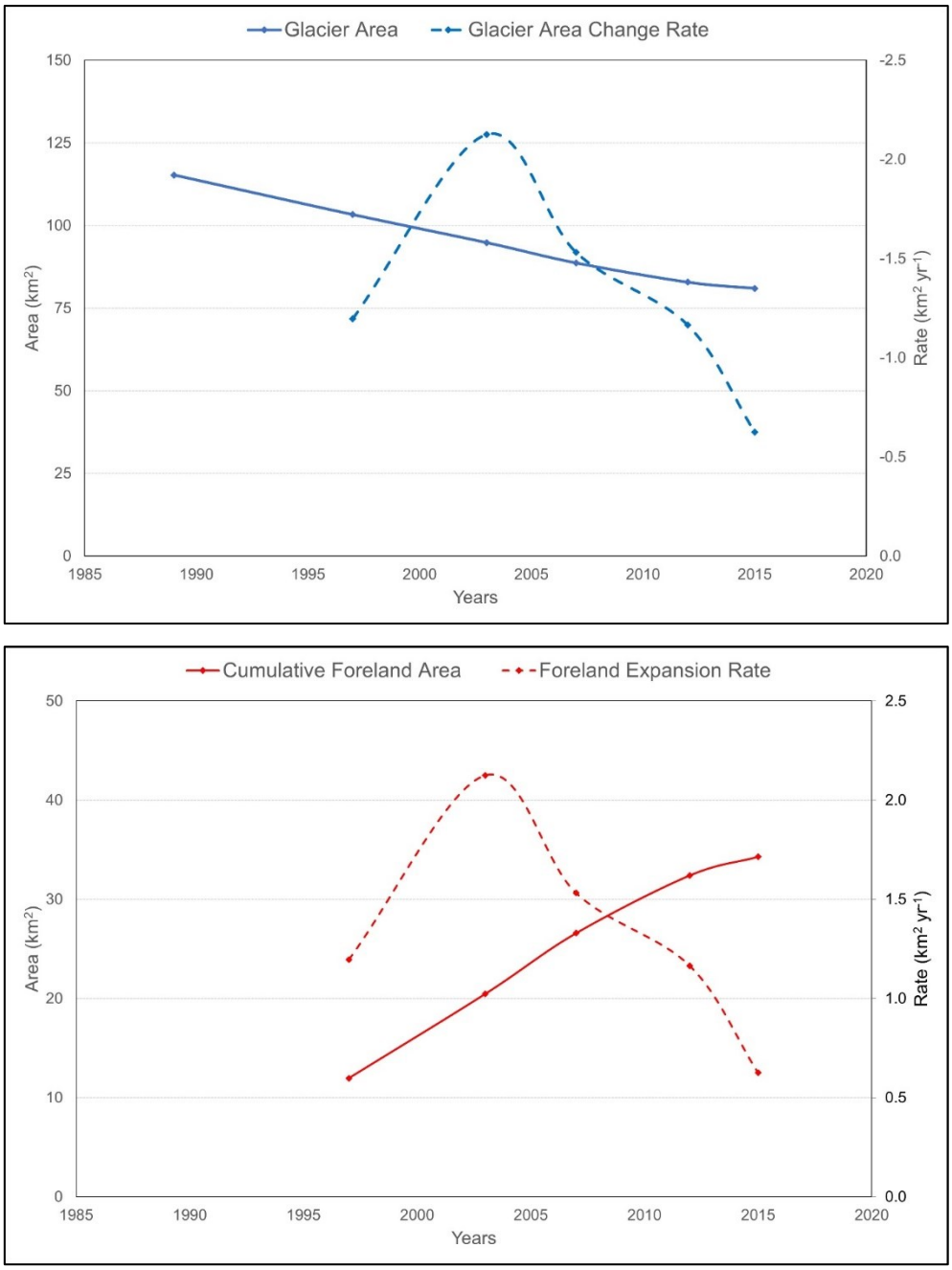

Figure 2: evolution of glacier (a) and glacier foreland (b) areas and their change/expansion rates over 1989 - 2015.

The glacier area loss in 26 years is –34.3 km^2 which results in a rate of -1.3 km^2 yr^{-1} (-1.1 % yr^{-1}). As a consequence, glacier forelands significantly increased their area by almost three times (287%) - the initial foreland developed over 1989-1999 was 12.0 km^2 which increased by 22.3 km^2 with a resulting foreland area of 34.3 km^2 in 2015. Looking at the rate calculated from each pair of orthophotos (i.e., 1989-1999, 1997-2003, 2003-2007, 2007-2012 and 2012-2015; Fig. 2), we found an increase in glacier retreat until 2003, which then decreases in the last decade and glacier foreland expansion which decreases during all the period of observation. In fact, glacier retreat has its maximum from 1999 to 2003 with a rate of -2.1 km^2 yr^{-1} (-2.1% yr^{-1}), and its minimum from 2012 to 2015, with a

rate of -0.6 km^2 yr^{-1} (-0.8% yr^{-1}). As regards the glacier forelands, maximum and minimum rate are respectively: +2.1 km^2 yr^{-1} (+17.8% yr^{-1}, 1999-2003) and +0.6 km^2 yr^{-1} (+1.9% yr^{-1}, 2012-2015). Nevertheless, if we consider the expansion rate of individual glacier forelands over time, we find a very strong correlation between foreland areas in 2015 and their expansion rate in the 26 years of analysis (R = 0.86; Fig. 3). For example, Adamello and Forni glacier forelands, which present the widest surfaces, also show the two highest expansion rates, with 15 km^2 and +0.09 km^2 yr^{-1} in Adamello and 7.7 km^2 and +0.09 km^2 yr^{-1} in Forni glacier, respectively.

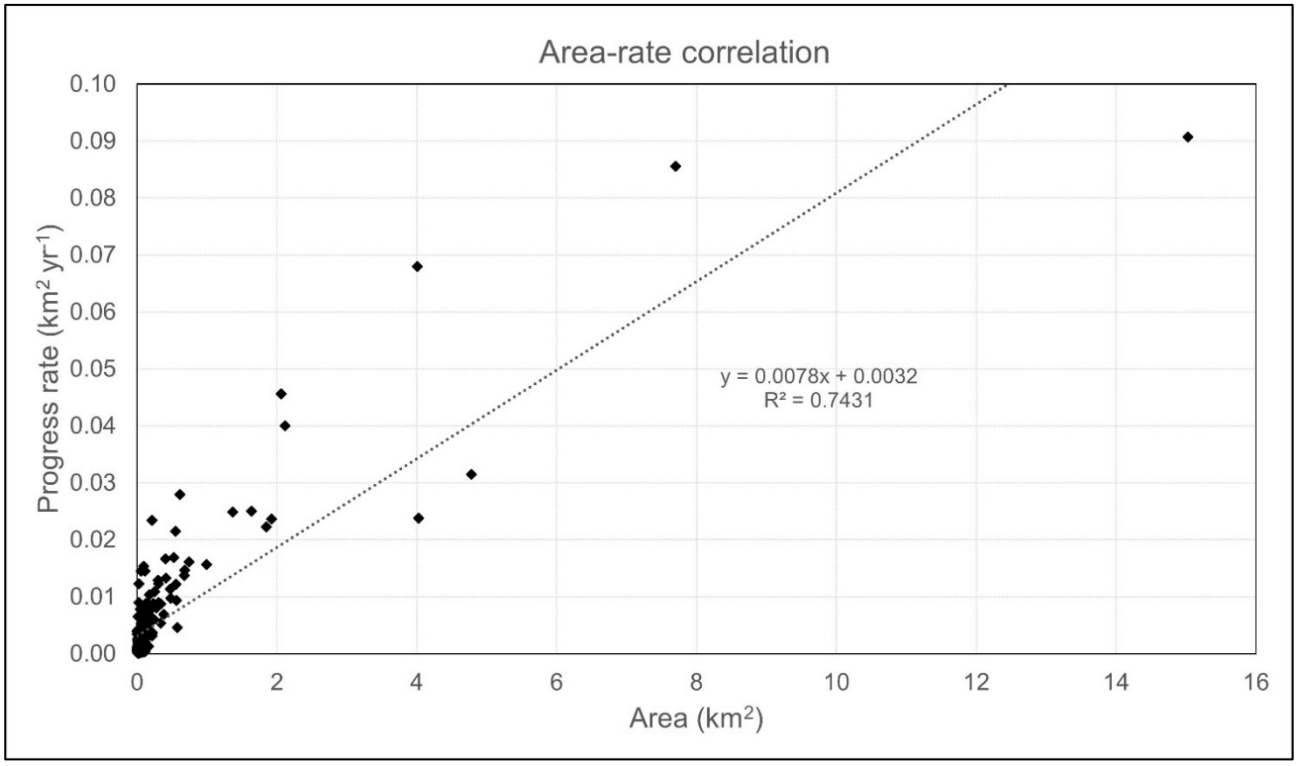

Figure 3: Correlation between the area of the glacier forelands and their expansion rate per year.

In contrast, the smallest glacier in Lombardy, i.e., Cima della Manzina, with an area lower than 0.001 km^2, presents one of the lowest expansion rates, equal to 0.0004 km^2 yr^{-1}. This confirms that the largest glaciers, e.g. Adamello and Forni, are also the ones most subjected to glacier retreat with a large amount of glacierized areas that are lost every year. Spatially, i.e., taking into consideration the mountain sectors corresponding to glacier forelands, we can evaluate the areas and expansion rates of the 6 represented sectors (Tab. 2).

Sectors	Adamello	Bernina Disgrazia	Orobie	Ortles Cevedale	Piazzi Campo	Tambo Stella
Glacier retreat Area 1989-2015 (km^2)	-5.08	-11.89	-0.81	-11.74	-2.94	-1.83
Rate 1989-2015 (% yr^{-1})	-0.77	-1.15	-1.13	-1.21	-1.75	-2.09
Rate 1989-1999 (% yr^{-1})	-0.47	-1.11	-1.98	-0.92	-1.94	-3.28
Rate 1999-2003 (% yr^{-1})	-1.24	-2.51	-1.47	-2.04	-3.02	-2.27
Rate 2003-2007 (% yr^{-1})	-0.76	-1.85	-2.20	-1.62	-3.29	-3.24
Rate 2007-2012 (% yr^{-1})	-1.13	-1.11	-3.81	-1.45	-1.33	-1.98
Rate 2012-2015 (% yr^{-1})	-1.12	0.12	8.96	-1.76	-1.68	-1.47

(a)

Sectors	Adamello	Bernina Disgrazia	Orobie	Ortles Cevedale	Piazzi Campo	Tambo Stella
Glacier foreland Area 1989-2015 (km^2)	5.08	11.89	0.81	11.74	2.94	1.83
Rate 1989-2015 (% yr^{-1})	12.59	6.45	1.83	9.37	5.15	2.51
Rate 1999-2003 (% yr^{-1})	25.40	20.06	5.94	20.25	12.53	4.65
Rate 2003-2007 (% yr^{-1})	7.33	7.35	6.75	8.16	7.99	5.08

Rate 2007-2012 (% yr^{-1})	8.20	3.16	8.40	5.15	2.12	2.25
Rate 2012-2015 (% yr^{-1})	5.40	-0.29	-11.28	4.61	2.27	1.35

(b)

Table 2. total glacial (a) and proglacial (b) area and percentual annual rates between 1989 and 2015 of glacier forelands in the 6 mountain sectors in Lombardy region.

The expansion rates are on average (considering all sectors) +0.14 km^2 yr^{-1}, where Bernina-Disgrazia and Ortles-Cevedale groups have the highest rates (both around 0.30 km^2 yr^{-1}), Orobie, Piazzi-Campo and Tambò-Stella the lowest (always lower than 0.1 km^2 yr^{-1}) and Adamello sector similar to the average. However, the percent rates show a slightly different situation, as the highest value is represeted by Adamello group (12.6% yr^{-1}) and Piazzi-Campo presents a higher value (5.2% yr^{-1}) in respect to Orobie and Tambò-Stella sectors. Additionally, if we consider the relationship between the foreland areas in 2015 and the glacierised areas in 1989 for each sector, the statement is even more different. In fact, Adamello shows the lowest foreland area in respect to its wide glacier area, being the relationship slightly lower than 20%. On the contrary, Piazzi-Campo and Tambò-Stella present the highest relationship of 50% circa (which means they lost around half of their glacierised area in 1989-2015 period). The remaining sectors instead, present values similar to the general mean (circa 30%). Nevertheless, the correlation between the glacier areas of each sector and its foreland expansion rate remains very high (R = 0.98), confirming the relation between these two parameters.

3.2 Glacier foreland surface characterization

On the over 39 km^2 of glacier foreland areas in Lombardy region which were left free from ice between 1989 and 2015, we calculated the relative area of four different types of surfaces: bare rock, unconsolidated debris, vegetation and water (lakes, ponds). The first surface, i.e., bare rock, is the most represented one with 25.9 km^2 of area, corresponding to about 65.3% of the total (on areas located at average altitudes higher than 2800 m a.s.l.). Secondly, we found a 13.3 km^2 coverage of debris (33.6%), which can correspond to a volume of 0.007-0.013 km3, considering an average thickness of 0.5-1 m (D'Agata et al., 2020). The last two features represent only a small part of the total foreland areas, with coverages of 0.1 km^2 (vegetation, 0.3%) and 0.3 km^2 (water, 0.8%). However, their environmental and ecological roles make them relevant even despite their small area.

In detail, water is included in 27 forelands of different glaciers, although only 30 of these lakes/ponds have an area higher than 0.001 km^2 and only two, the Pisagana West (Adamello sector) and Fellaria East (Bernina – Disgrazia sector) glacier lakes reach 0.1 km^2. Topographically, we provided a detailed analysis of water and vegetation areas by taking into consideration the altitude, slope and aspect of these surfaces. In general, the glacier foreland altitudes range between ≈2000 and 3900 m a.s.l. on average; however, both water and vegetation areas are located at the lowest edges of these zones, i.e. 2640±3 m a.s.l. and 2514±3 m a.s.l., on average respectively, and in general never at elevations higher than 2700 m a.s.l.. As regards slope, the forelands areas average 33±11° and again, water and vegetation are present on flatter surfaces, with slopes of 28±3° and 24±3°, respectively. Finally, regarding the aspect, if we consider the number of areas (Fig. 4a), the picture is more heterogeneous: water areas show similar values to the general foreland areas, mostly heading towards N-NW (71% of the polygons).

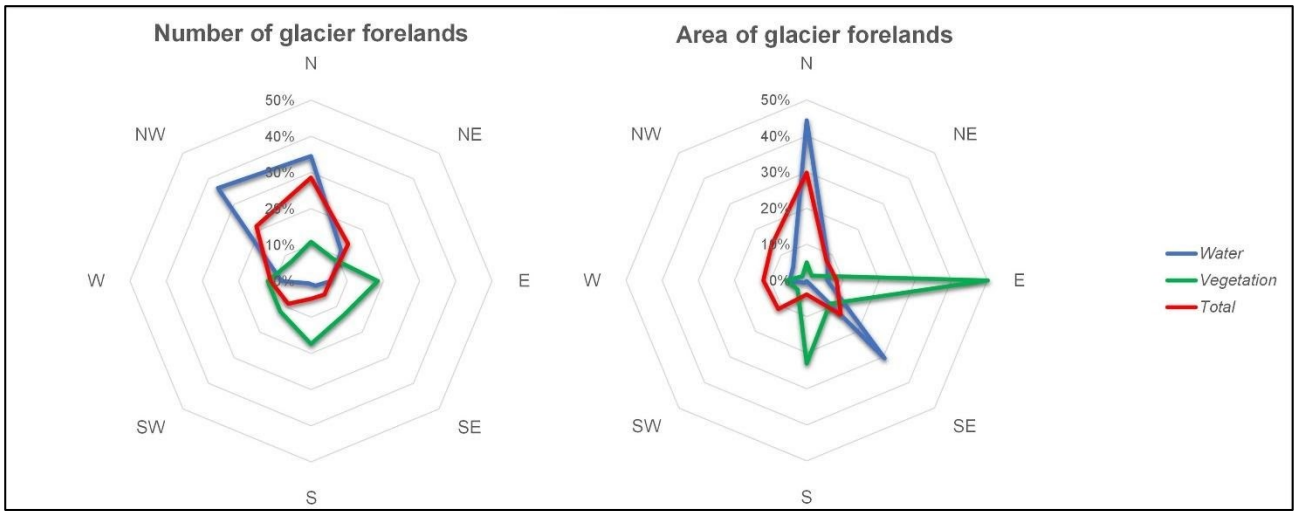

Figure 4: Radar plots of aspect distribution of water, vegetation and total foreland areas, in percentage based on the number of foreland areas (a) and their surface area (b).

In contrast, vegetated zones mainly head towards E-SE-S with 51% of the areas. However, if we consider the areas of the forelands and each surface type, (Fig. 4b), the situation is quite different. In fact, even if the glacier forelands face N (30%), water zones are equally distributed in the N and SE aspect on average (44% and 30% respectively) and vegetation areas face E and S (50% and 23%). These differences, above all for water, are explained by the presence of some large areas which have a higher impact on the area-based classification compared to the number-based classification. For example, just two lakes have a SE aspect, but one of these is the Fellaria E glacier lake, the largest in Lombardy.

4 Discussion

In accordance with several previous studies (Rabatel et al., 2013; Falaschi et al., 2013; Gardent et al., 2014; Diolaiuti et al; 2019; Paul et al; 2020), we found a relevant retreat of glaciers in Lombardy Alps in all its sectors, both considering the area reduction and its rate per year. A general average retreat of all sectors in 1989-2015 period resulted to be equal to almost –30%, from 115 km^2 (1989) to 81 km^2 (2015), slightly higher than the –24% of extension for Lombardy region in 1959-2011 (Smiraglia et al., 2015) and in line with –15% for all the Alps in half of the period (2003-2015, Paul et al., 2020). In addition, our results for retreat rate in percentage are in accordance with Paul et al. (2004, 2020), where they found around –1.1% yr^{-1} for Swiss and entire Alps as well. However, in contrast with previous studies on Bernina Alps (D'Agata et al., 2019), we did not detect any increase in glacier retreat in recent years. In fact, the highest retreat rate occurred meanly from 1999 to 2007, especially in 1999-2003 period, and the lowest one in the most recent period (2012-2015). To this glacier retreat corresponds an expansion in foreland areas in the entire Lombardy region and furthermore, a very high correlation between the final area in 2015 and the yearly progression rate of these areas was found. This demonstrates that to larger glaciers corresponds a higher retreat rate and thus a higher rate of foreland area formation. For example, the two largest Lombardy glaciers (Adamello and Forni glaciers) also present the two highest values of progression rate in terms of foreland areas and glacier retreat. Nevertheless, looking at the yearly retreat rate in percentage, the smallest sectors, i.e., Orobie, Piazzi – Campo and Tambò - Stella sectors have the lowest negative values (Tab. 2). Thus, in absolute terms the largest sectors present the highest retreat rates, but smallest sectors show the highest retreats in respect to their original areas. Probably, the turnaround with positive values (advance instead of retreat) of Orobie and Bernina – Disgrazia sectors in the last period are due to an error of glacier detection caused by snow presence, above all for Orobie (Paul et al., 2020), where little glaciers are covered in snow in their entirety also during summer seasons. Therefore, these two results need to be taken with caution and they could have also affected the final averaged results of all 1989-2015 span, wrongly increasing the values. Additionally, on the other hand, talking about foreland progression, from the results we see an apparent decrease of the progressions for every sector through the different periods. However, the first results (1999-2003 period) appear to be higher as they are the first results after the starting point in 1989, which was stated to be with 0 km^2 of foreland area (because previous extensions are unknown). For this reason, probably these values are overestimated and not representative in order to detect a trend in time. Then, if we focus on the surface characterization of the glacier foreland, being located at very high altitudes, these recent forelands present a majority of bare rock and debris coverage, that altogether make up 98.9% of the surfaces. The remaining 1.1% is unequally subdivided in water and vegetation, where

the first one covers most of the area. Such a low coverage of vegetation can be explained by the relative mean altitude, which relegates plants (represented by grass or shrub, identified by inspecting the detected vegetated areas on Forni glacier foreland based on a 2014 orthophoto acquired with a UAV, Fugazza et al., 2015) at the lowest edges of the surface left recently free from glaciers. Also, the water areas, represented mainly by lakes and ponds, are located at very low altitudes and most of the times correspond to the lower parts of the glacier forelands. The presence of lakes or vegetation could instead depend on the orientation of the interested area. In fact, looking at their local aspects (Fig. 4), we discovered almost opposite orientation between these two kinds of surfaces. If water areas present on average a N-NW aspect, which correspond to the general one of the foreland areas, vegetation shows an opposite S-E orientation. The mountain landscape of Lombardy Alps is deeply changing owing to glacier retreat; in fact, Lombardy Alps are expected to show features and forms now visible in the Pyrenees (where the present glaciation is a relic of the previous one, see Gonzalez Trueba et al., 2008) and, in a second phase to resemble the Apennines (where only the Calderone Glacier is located, see Branda et al., 2010). Geodynamically a transition is presently occurring from the glacial to the paraglacial system (Ballantyne and Benn, 1994;1996; Curry and Ballantyne; 1999). The areas where in the recent past the main shaping and driving factors have been glaciers are now subject to the action of melting water, slope evolution and dynamics and periglacial processes. Under such changing environmental features, the new territories are available for plant and trees colonization as observed in the Ortles-Cevedale Group (Garavaglia et al 2010), and at the Forni glacier forefield where in the last years saples are germinating after just very few years after the glacier margin retreat (Pelfini, unpublished data). The melting of glaciers not only has obvious impacts on the surrounding ecosystems, but it also has adverse consequences upon the value of the sites where they are located, in the context of natural heritage. Heritage is an irreplaceable source of life and inspiration, it is humankind's legacy from the past, with which we live in the present and pass on to future generations (UNESCO, 2007). Also, the GEO-Heritage (Bosson and Reynard, 2012) properties could be exposed to the unfavourable effects of changing climate and this is particularly the case of mountain glaciers, which are among the most fascinating elements of the high elevation environment. In fact, the consequences of glacier retreat on the natural and cultural heritage of the Alps have not been investigated in detail, and only few studies have been carried out (among the others, UNESCO, 2007; Haeberli, 2008; Diolaiuti and Smiraglia, 2010; Garavaglia et al, 2010; Bollati et al., 2013; 2017; Pelfini and Bollati, 2014). Our study, applying remote sensing techniques on recent satellite images and also using a semi-automatic approach shows results consistent with field observations performed in selected locations of the Lombardy Alps (Diolaiuti and Smiraglia, 2010; Garavaglia et al, 2010; Bollati et al., 2013; 2017; Pelfini and Bollati, 2014) and suggests that the

method could be estended to the whole Italian Alps, taking advantages from the recent national glacier inventories (Diolaiuti et al; 2019; Paul et al; 2020) to obtain data and information on the extent and features of these newly exposed pristine territories, which are important for both geomorphological processes and the development of ecological systems.

5 Conclusion

The present study intends to analyse the glacier foreland areas in Lombardy region, focusing on their spatial variation in time and surface characterization. In order to do so, different datasets were used, i.e., six Lombardian glacier inventories from several years (1989, 1999, 2003, 2007, 2012 and 2015), all based on orthophotos at high spatial resolutions (0.5 m, https://www.terraitaly.it/). Firstly, analysing the glacier evolutions in 1989-2015 period, we found a general decrease in surface or glacier retreat in accordance with previous studies (Diolaiuti et al; 2019; Paul et al; 2020), with a loss of about 30% in 26 years (-34.3 km^2), even if the mountain sectors presenting the smallest glacier (e.g., Orobie, Tambò - Stella) show the highest loss in percentage (on the total of initial extent), both in absolute and as annual retreat. On the other hand, hugest sectors show the highest decrease in area and annual retreat (not percentage). However, in contradiction with previous studies (D'Agata et al., 2019), we did not detect any relevant increase in ice loss in the recent years, which in contradiction present the lowest rates. The highest rates are located instead in 1999-2007 period. These trends are also reflected in glacier-foreland progressions, which present an area almost tripled in 1999-2015 span (+287%). Again, no particular trends in time are here detected, but a relevant correlation between foreland areas for each glacier and the corresponding progression rate is calculated (Fig. 3). Moving to foreland characterization, we took advantage of different approaches, corresponding to the different kinds of surfaces: bare rock (ruggedness index), unconsolidated debris (as result from the subtraction of all the other surfaces from the total), vegetation (NDVI validated with PRISMA hyperspectral data) and water (lakes, ponds; NDWI). The first two surfaces are prevalent in all the region, being the 98.9% (65.3% of bare rock and 33.6% of debris). The remaining part is composed by 0.8% of water and 0.3% of vegetation. Such a small cover of water and especially vegetation could be explained considering that foreland areas formed from 1989 are located at high altitude (> 2000 m) and in fact all these two surfaces are in proximity of foreland edges (2500-2600 m on average). On the contrary, previous studies on foreland lakes (Viani et al., 2016) based on areas created from 1927 and thus at lower altitudes, found larger water cover in Aosta Valley region, i.e., 1.4 km^2 in 2012 against 0.3 km^2 in 2015 in the present study (even if the glacier surfaces in Aosta Valley is only 30% circa more than in Lombardy, Smiraglia et al., 2015). Finally, we discovered an evident prevalence of aspects for water and vegetation covers. In fact, water areas, as well as generally the

foreland areas, present a N exposure, and vegetation shows an E predominant aspect (Fig. 4). In conclusion, a better understanding of glacier forelands could be possible by enlarging the study period, moving back in time further than 1989, in order to gain a more significative trend of spatial variation. In addition, an analysis in space and time of different surface types, i.e., water and vegetation, as done by Viani et al. (2016) in Aosta Valley region, could provide a better understanding of these feature evolutions in a warming world statement.

References

Azzoni, R.S., Fugazza, D., Zerboni, A., Senese, A., D'Agata, C., Maragno, D., Carzaniga, A., Cernuschi, M., Diolaiuti, G.A., 2018. Evaluating high-resolution remote sensing data for reconstructing the recent evolution of supra glacial debris: A study in the Central Alps (Stelvio Park, Italy). Progress in Physical Geography: Earth and Environment 42, 3–23

Diolaiuti, G., Bocchiola, D., D'agata, C. et al. Evidence of climate change impact upon glaciers' recession within the Italian Alps. Theor Appl Climatol 109, 429–445 (2012). https://doi.org/10.1007/s00704-012-0589-y

Böhm R, Auer I, Brunetti M, Maugeri M, Nanni T and Schöner W (2001) - Regional temperature variability in the European Alps: 1760–1998 from homogenized instrumental time series. International Journal of Climatology 21, 1779-1801.

Bosson, JB, Deline P, Bodin X, Schoeneich P, Baron L, Gardent M and Lambiel, C,(2015) - The influence of ground ice distribution on geomorphic dynamics since the Little Ice Age in proglacial areas of two cirque glacier systems, Earth Surface Processes And Landforms, 40, 5, 666-680, DOI: 10.1002/esp.3666.

Brambilla M and Gobbi M (2014) - A century of chasing the ice: delayed colonisation of ice-free sites by ground beetles along glacier forelands in the Alps, Ecography, 37, 1, 33-42, DOI: 10.1111/j.1600-0587.2013.00263.x

Branda E, Turchetti B, Diolaiuti G, Pecci M, Smiraglia C and Buzzini P (2010) - Yeast and yeast-like diversity in the southernmost glacier of Europe (Calderone Glacier, Apennines, Italy). FEMS Microbiology Ecology 1-16.

Casty C, Wanner H, Luterbacher JL, Esper J and Böhm R (2005) - Temperature and Precipitation variability in the European Alps since 1500. International Journal of Climatolology 25, 1855- 1880.

Cannone N, Diolaiuti G, Guglielmin M and Smiraglia C (2008) - Accelerating climate change impacts on alpine glacier forefield ecosystems in the European Alps. Ecol Appl 18(3):637–648

Citterio M, Diolaiuti G, Smiraglia C, D'Agata C, Carnielli T, Stella G and Siletto GB (2007) - The fluctuations of Italian glaciers during the last century: a contribution to knowledge about Alpine glacier changes. Geografiska Annaler: Series A Physical Geography 89, 164-182

Cook AJ, Fox AJ, Vaughan DG, Ferrigno JG (2005) Retreating glacier fronts on the Antarctic Peninsula over the past half-century. Science 308, 541-544.

D'Agata C., G. Diolaiuti, D. Maragno, C. Smiraglia & M. Pelfini (2020) Climate change effects on landscape and environment in glacierized Alpine areas: retreating glaciers and enlarging forelands in the Bernina group (Italy) in the period 1954–2007, Geology, Ecology, and Landscapes, 4:1, 71-86, DOI: 10.1080/24749508.2019.1585658

D'Amico ME, Freppaz M, Leonelli G, Bonifacio E and Zanini, E (2015) Early stages of soil development on serpentinite: the proglacial area of the Verra Grande Glacier, Western Italian Alps, Journal Of Soils And Sediments, 15, 6, 1292-1310, DOI: 10.1007/s11368-014-0893-5

Diolaiuti, G., Smiraglia, C., 2010. Changing glaciers in a changing climate: how vanishing geomorphosites have been driving deep changes in mountain landscapes and environments. Géomorphologie: relief, processus, environnement 16, 131–152.

Diolaiuti G.A., Azzoni R.S., D'Agata C., Maragno C, Fugazza D., Vagliasindi M., Mortara G., Perotti L.,Bondesan A., Carton A., Pecci M., Dinale R.,Trenti A., Casarotto C., Colucci R.R., Cagnati A., Crepaz A. and Smiraglia (2019) - Present extent, features and regional distribution of Italian glaciers. La Houille Blanche 2019, 5-6, 159–17. Https://doi.org/10.1051/lhb/2019035

D'Orefice M, Pecci M, Smiraglia C and Ventura R (2000) - Retreat of Mediterranean glaciers since the Little Ice Age: Case study of Ghiacciaio del Calderone, Central Apennines, Italy. Arctic, Antarctic and Alpine Research 32: 197-201.

Dyurgerov MB, Meier MF (2000) Twentieth Century Climate Change: Evidence from Small Glaciers. Proceedings of the National Academy of Sciences 97, 1406-1411.

Egli, M, Wernli, M, Kneisel, C, Haeberli, W (2006) Melting glaciers and soil development in the proglacial area Morteratsch (Swiss Alps): I. Soil type chronosequence, Arctic Antarctic And Alpine Research, 38, 4, 499-509

Falaschi, D, Bravo, C, Masiokas, M, Villalba, R, Rivera, A, (2013) - First Glacier Inventory and Recent Changes in Glacier Area in the Monte San Lorenzo Region (47 degrees S), Southern Patagonian Andes, South America, Arctic Antarctic And Alpine Research., 45, 1, 19-28, DOI: 10.1657/1938-4246-45.1.19

Frezzotti, M, Orombelli, G (2014) - Glaciers and ice sheets: current status and trends, Rendiconti Lincei-Scienze Fisiche E Naturali, 25, 1, 59-70, DOI: 10.1007/s12210-013-0255-z

Fugazza D., A. Senese, R S Azzoni, C Smiraglia, M Cernuschi, D Severi & G A Diolaiuti (2015) - High-resolution mapping of glacier surface features. the UAV survey of the Forni Glacier (Stelvio National Park, Italy). Geogr. Fis. Dinam. Quat. 38 (1),25-33. DOI 10.4461/GFDQ.2015.38.03

Garavaglia V., Pelfini M. & Motta E. (2010b) - Glacier stream activity in the proglacial area of an italian debris covered glacier: an application of dendroglaciology. Geografia Fisica e Dinamica Quaternaria, 33 (1) 2010, 15-24

Gardent, M, Rabatel, A , Dedieu, JP, Deline, P (2014) - Multitemporal glacier inventory of the French Alps from the late 1960s to the late 2000s, Global And Planetary Change, 120, 24-37 DOI: 10.1016/j.gloplacha.2014.05.004

Geilhausen, M, Morche, D, Otto, JC, Schrott, L, (2012) - Sediment discharge from the proglacial zone of a retreating Alpine glacier. Zeitschrift Fur Geomorphologie, 57(2), 29-53, DOI: 10.1127/0372-8854/2012/S-00122

Gobbi M., Rossaro B., Vater A., De Bernardi F., Pelfini M. & Brandmayr P. (2007) - Environmental features influencing Carabid beetle (Coleoptera) assemblages along a recently deglaciated area in the Alpine region. Ecological Entomology, 32, 282-289

González Trueba JJ, Martín Moreno R, Martínez de Pisón E, Serrano E (2008) - "Little Ice Age" glaciation and current glaciers in the Iberian Peninsula. The Holocene 18, 551-568

Guarini, R., Loizzo, R., Longo, F., Mari, S., Scopa, T., Varacalli, G., 2017. Overview of the prisma space and ground segment and its hyperspectral products, in: 2017 IEEE International Geoscience and Remote Sensing Symposium (IGARSS). IEEE, pp. 431–434.

Haeberli W. and Beniston M (1998) - Climate change and its impacts on Glaciers and Permafrost in the Alps. Ambio 27, 258-265.

Hoelzle M, Haeberli W, Dischl M, Peschke W (2003) - Secular glacier mass balances derived from cumulative glacier length changes. Global and Planetary Change 36, 295-306.

Hughes PD (2009) - Twenty-first Century Glaciers in the Prokletije Mountains, Albania. Arctic, Antarctic and Alpine Research 4, 455-459.

Hughes PD (2010) - Little Ice Age glaciers in Balkans: low altitude glaciation enabled by cooler temperatures and local topoclimatic controls. Earth Surface Processes and Landforms 35, 229-241

Kabala C and Zapart J (2012) - Initial soil development and carbon accumulation on moraines of the rapidly retreating Werenskiold Glacier, SW Spitsbergen, Svalbard archipelago, Geoderma, 175, 9-20, DOI: 10.1016/j.geoderma.2012.01.025

Kaser G, Cogley JC, Dyurgerov MB, Meier MF and Ohmura A (2006) - Mass balance of glaciers and ice caps: Consensus estimates for 1961-2004. Geophys. Res. Lett., 33, L19501, doi:10.1029/2006GL027511.

IPCC (2013) - Summary for Policymakers. In: Climate Change 2013: The Physical

Science Basis Contribution of. Working Group I to the Fifth Assessment Report . Available on line at: http://www.climatechange2013.org/images/report/WG1AR5_SPM_FINAL.pdf

Leonelli G, Coppola A, Baroni C, Salvatore MC, Maugeri M, Brunetti M, Pelfini M (2016) - Multispecies dendroclimatic reconstructions of summer temperature in the European Alps enhanced by trees highly sensitive to temperature. Climatic Change, Volume 137, Issue 1–2, 275–291.

Levy, A, Robinson, Z, Krause, S, Waller, R, Weatherill, J, (2015) - Long-term variability of proglacial groundwater-fed hydrological systems in an area of glacier retreat, Skeioararsandur, Iceland, Earth Surface Processes And Landforms, 40, 7, 981-994, DOI: 10.1002/esp.3696

Maisch, M (2000) - The longterm signal of climate change in the Swiss Alps. Glacier retreat since the Little Ice Age and future ice decay scenarios. Geografia Fisica e Dinamica Quaternaria 23, 139–52.

McFeeters, S.K., 2013. Using the Normalized Difference Water Index (NDWI) within a Geographic Information System to Detect Swimming Pools for Mosquito Abatement: A Practical Approach. Remote Sensing 5, 3544–3561. https://doi.org/10.3390/rs5073544

Meola, M, Lazzaro, A, Zeyer, J (2014) - Diversity, resistance and resilience of the bacterial communities at two alpine glacier forefield safter a reciprocal soil transplantation, Environmental Microbiology, 16, 6, 1918-1934, DOI: 10.1111/1462-2920.12435

Mergili M, Kopf C and Muellebner B. (2012) - Changes of the cryosphere and related geohazards in the high-mountain areas of Tajikistan and Austria: a comparison, Geografiska Annaler Series A-Physical Geography Volume: 94A Issue: 1 Special Issue: SI Pages: 79-96

Oerlemans J (2005) - Extracting a climate signal from 169 glacier records. Science 308, 675-677.

Patzelt, G (1985) - The period of glacier advances in the Alps, 1965 to 1980. Zeitschrift für Gletscherkunde und Glazialgeologie 21: 403-407.

Paul F, Kääb A, Maisch M, Kellenberger T, Haeberli, W (2004) - Rapid disintegration of Alpine glaciers observed with satellite data, Geophysical Research Letters 31, L21402, doi:10.1029/2004GL020816.

Paul F, Kääb A and Haeberli W (2007) - Recent glacier changes in the Alps observed from satellite: Consequences for future monitoring strategies. Global and Planetary Change. doi:10.1016/j.gloplacha.2006&07.007.

Paul F, Frey H and Le Bris R (2011) - A new glacier inventory for the European Alps from Landsat TM scenes of 2003: challenges and results. Annals of Glaciology, 52(59), 144-152.

Paul, F., Rastner, P., Azzoni, R. S., Diolaiuti, G., Fugazza, D., Le Bris, R., Nemec, J., Rabatel, A., Ramusovic, M., Schwaizer, G., and Smiraglia, C.: Glacier shrinkage in the Alps continues unabated as revealed by a new glacier inventory from Sentinel-2, Earth Syst. Sci. Data, 12, 1805–1821, https://doi.org/10.5194/essd-12-1805-2020, 2020

Pelfini M. & Bollati I. (2014) - Landforms and geomorphosites ongoing changes: concepts and implications for geoheritage promotion Quaestiones Geographicae 33(1) , 131 – 143

Pelfini M., Leonelli G.,Trombino L., Zerboni A.,Bollati I.,Merlini A., Smiraglia C. & Diolaiuti G. (2014)- New data on glacier fluctuations during the climatic transition at similar to 4,000 cal. year BP from a buried log in the Forni Glacier forefield (Italian Alps) Rendiconti Lincei-Scienze Fisiche e Naturali, 25 (4), 427-437

Pfeffer WT, Arendt AA, Bliss A, Bolch T, Cogley JG, Gardner AS, Hagen JO, Hock R, Kaser G, Kienholz C, Miles ES, Moholdt G, Mölg N, Paul F, Radic´ V, Rastner P, Raup BH, Rich J, Sharp MJ and The Randolph Consortium (2014) - The Randolph Glacier Inventory: a globally complete inventory of glaciers, Journal of Glaciology, 60 (221), 537-552

Rabatel A. Francou, B, Soruco, A, Gomez, J, Caceres, B, Ceballos, JL, Basantes, R, Vuille, M, Sicart, JE, Huggel, C More (2013) - Current state of glaciers in the tropical Andes: a multi-century

perspective on glacier evolution and climate change, The Cryosphere, 7, 1, 81-102, DOI: 10.5194/tc-7-81-2013

Riley, S.J., DeGloria, S.D., Elliot, R., 1999. Index that quantifies topographic heterogeneity. intermountain Journal of sciences 5, 23–27.

Rott H., Skvarca P, Nagler T (1996) - Rapid collapse of northern Larsen Ice Shelf, Antarctica. Science 271, 788-792.

Salerno F, Gambelli S, Viviano G,Thakuri S,Guyennon N, D'Agata C, Diolaiuti G, Smiraglia C, Stefani F and Bocchiola, D (2014)- High alpine ponds shift upwards as average temperatures increase: A case study of the Ortles-Cevedale mountain group (Southern Alps, Italy) over the last 50 years, Global And Planetary Change, 120, 81-91, DOI: 10.1016/j.gloplacha.2014.06.003

Smiraglia, C., Azzoni, R. S., D'Agata, C. A. R. L. O., Maragno, D., Fugazza, D., & Diolaiuti, G. A. (2015). The evolution of the Italian glaciers from the previous data base to the New Italian Inventory. Preliminary considerations and results. Geografia Fisica e Dinamica Quaternaria, 38(1), 79-87.

Sommaruga, R (2015) - When glaciers and ice sheets melt: consequences for planktonic organisms, Journal Of Plankton Research, 37, 3, 509-518, DOI: 10.1093/plankt/fbv027

Staines, KEH, Carrivick, JL, Tweed, FS, Evans, AJ, Russell, AJ, Johannesson, T, Roberts, M (2015)- A multi-dimensional analysis of pro-glacial landscape change at Solheimajokull, southern Iceland, Earth Surface Processes And Landforms, 40, 6, 809-822, DOI: 10.1002/esp.3662

St-Hilaire VM &Smith DJ. (2017)- Holocene glacier history of Frank Mackie Glacier, northern British Columbia Coast Mountains Canadian Journal Of Earth Sciences, 54 (1) 76-87

Traversa, G., Fugazza, D., Senese, A., Frezzotti, M., 2021. Landsat 8 OLI Broadband Albedo Validation in Antarctica and Greenland. Remote Sensing 13, 799.

Vangi, E., D'Amico, G., Francini, S., Giannetti, F., Lasserre, B., Marchetti, M., Chirici, G., 2021. The new hyperspectral satellite PRISMA: Imagery for forest types discrimination. Sensors 21, 1182.

Viani, C., Giardino, M., HuGGel, C., Perotti, L., & Mortara, G. (2016). An overview of glacier lakes in the Western Italian Alps from 1927 to 2014 based on multiple data sources (historical maps, orthophotos and reports of the glaciological surveys). Geografia Fisica e Dinamica Quaternaria, 39(2), 203-214.

Wang X , Siegert F, Zhou AG and Franke J (2013)- Glacier and glacial lake changes and their relationship in the context of climate change, Central Tibetan Plateau 1972-2010, Global And Planetary Change, 111, 246-257, DOI: 10.1016/j.gloplacha.2013.09.011

Wood F (1988) - Global alpine glacier trends 1960s to 1980s. Artic, Alpine and Antarctic Research 20, 404-413.